UNIVERSIDAD NACIONAL DE COLOMBIA

Hamiltonian formulation of the full vectorial Helmholtz equation for modeling the interaction between ME composites and optical fiber immersed in electromagnetic fields from high voltage power systems

Raúl Esteban Jiménez Mejía

Universidad Nacional de Colombia
Facultad de Ciencias, Escuela de Física
Medellín, Colombia
2019

Hamiltonian formulation of the full vectorial Helmholtz equation for modeling the interaction between ME composites and optical fiber immersed in electromagnetic fields from high voltage power systems

Raúl Esteban Jiménez Mejía

Thesis dissertation submitted in partial fulfillment of the requirements for the degree of :
Doctor en Ciencias - Física

Major Professors:
Rodrigo Acuña Herrera, Ph.D. and Chiu Tai Law, Ph.D.

Research line:
Fiber Optic Sensors

Research Groups:
Grupo de Investigación en Fotónica y Optoelectrónica
Laboratory of Smart Composites, Department of Electrical Engineering and Computer Science at University of Wisconsin-Milwaukee

Universidad Nacional de Colombia, Sede Medellín
Facultad de Ciencias, Escuela de Física
Medellín, Colombia
2019

Acknowledgements

There are many persons and institutions that I am very grateful with. Firstly, I want to offer my gratitude to my major advisors during this academic process. I would like to thank to Professor Dr. Rodrigo Acuña for allowing me being part of his research group and my sincere acknowledgments to Professor Dr. C.T. Law, who opened to me his laboratory doors and offered me his experience in magnetostriction and magnetostrictive composites. Besides, I want to express thankfulness to the University of Wisconsin-Milwaukee for having me as a visiting scholar and offered me high quality facilities for the development of most of the experimental part of this work. I also would like to thank the continuous advising and helpful discussions offered to me by Professor Dr. Pedro Torres during this research, who always was opened to offer theoretical backgrounds to support the experimental results. My sincere gratitude should be expressed the Universidad Nacional de Colombia, for being the institution that have prepared me as a researcher, where I have met several colleagues and friends that have contributed to my academic conception of science and life. I particularly appreciate the financial support of the Departamento Administrativo de Ciencia, Tecnología e Innovación (Colciencias) during the years of the development of this work, as well as to give thanks to the Fulbright scholarship and Sapiencia-Enlazamundos program for their support during the internship.

Abstract

This thesis deals with the proposal, analytical background and practical implementation of fiber optic based sensors for measuring electrical variables in high voltage systems. The thesis presents the physical and mathematical formulation for each of the sensing principles that were tackled in the proposition and develops the theoretical backgorund for each particular application. Three main contributions should be highlighted from the obtained results: Firstly, the formulation of the interaction characteristics with optical fibers by extending the coupled theory mode through a Hamiltonian formulation of the Helmholtz equation to account for transverse perturbations into the propagation characteristics of propagating light. Secondly, the proposition of a numerical method for predicting the magnetic characteristics of magnetostrictive-powder/epoxy composites with arbitrary shapes. Finally, the proposition of two fiber-based sensor for sensing electric variables (magnetic field and voltage magnitudes) from high voltage systems. Proposed sensors were implemented in practice and their results were contrasted to the theoretical expected performance leading to very good agreements. Future work is proposed based on the main opportunities discovered during the analytical and practical implementation of the sensors.

Key Words: Optical Fibers, Magnetostriction, Piezoelectric, Terfenol-D, magnetostrictive composites, Piezoelectric Bimorph.

Contents

List of Figures

Chapter 1

Introduction

Measurement of electrical variables such as voltage and currents are of great importance in the control and operation of power systems. In high voltage systems, sensors are required to present high standards of reliability and insulation levels for avoiding undesired outages of services, as well as the minimum required maintenance. Power lines are currently controlled and operated by using very mature technology in current and voltage measurements known as Current and Potential Transformers (CTs and PTs). However, in some situations these sensors present some limitations related to its operational principles, maintenance requirements, low flexibility and portability. Smart Grids is a new tendency in power-systems which consists in giving flexibility and maximum reliability to power-grids. This tendency is becoming mandatory in the operation and control of power-systems due to the increasing and exigent demand. Therefore, more measurements points with higher flexibility and portability are required in this growing industry in order to provide more information about the power-lines condition, as well as to propose more effective protective coordination schemes and reliable power-system operation under contingency maneuvers caused by faults or lightning strikes. Based on this fact, the usage of optical sensors for the electrical variables in high voltage systems has been seen as a very interesting alternative to attend this measurement necessity. These sensors present more flexible systems and in some cases relatively lower costs. Besides, optical systems have enormous advantages when compared with the traditional elements, particularly, its immunity to electromagnetic noise and high dielectric strength; this latter of especial benefit in practical implementations because it allows eliminating those sophisticated and large size insulation elements that are required in high-voltage applications, enabling the usage of lightweight optical-based devices. This interest have motivated the proposal of novel techniques for measuring electrical variables from overhead lines based on the usage of fiber optic technology.

Overhead transmission and distributions lines are the dominant technology to transport energy from generator plants and deliver electric power to industries and homes [40]. Typical operation of the overhead lines is normally performed at 50/60Hz. Figure 1.1(a) presents a conceptual schematic of a single-phase overhead line.

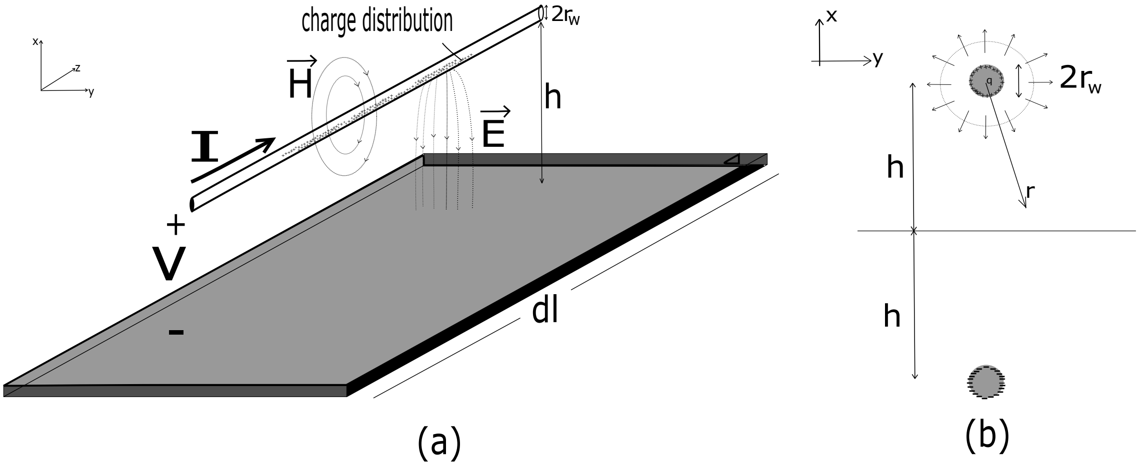

Figure 1.1: Overhead Line Conceptualization. (a) single-phase overhead line over perfectly conducting ground (b) Image method

The fundamental assumption for finding typical transmission line equations and the corresponding magnitudes of the electric and magnetic field is the consideration of transversal fields, i.e. the electric field intensity vector, $\vec{\mathbf{E}}_{\text{ext}}(\vec{\mathbf{r}},t)$, and the magnetic field intensity vector, $\vec{\mathbf{H}}_{\text{ext}}(\vec{\mathbf{r}},t)$, lie on the transversal plane to the direction of propagation (the x-y plane in Fig. 1.1). Subscripts ***ext*** have been included to these fields to distiguish them as the fields associated to the overhead line. Transversal electromagnetic field (TEM) assumption allows to solve the propagation equations for both current and voltage along the transmission lines. This assumption will be considered here for deriving the electric and magnetic field intensities for a single-phase overhead line. Maxwell's equations for homogeneous, linear and isotropic medium can be written by:

$$\nabla \times \vec{\mathbf{E}}_{\text{ext}}(\vec{\mathbf{r}},t) = -\mu_0 \frac{\partial \vec{\mathbf{H}}_{\text{ext}}(\vec{\mathbf{r}},t)}{\partial t} \tag{1.1a}$$

$$\nabla \times \vec{\mathbf{H}}_{\text{ext}}(\vec{\mathbf{r}},t) = \sigma \vec{\mathbf{E}}_{\text{ext}} + \epsilon \frac{\partial \vec{\mathbf{E}}_{\text{ext}}(\vec{\mathbf{r}},t)}{\partial t} + \vec{\mathbf{J}}_{\mathbf{fr}}(\vec{\mathbf{r}},t) \tag{1.1b}$$

$$\nabla \cdot \vec{\mathbf{D}}_{\text{ext}}(\vec{\mathbf{r}},t) = \rho_{\text{fr}} \tag{1.1c}$$

$$\nabla \cdot \vec{\mathbf{E}}_{\text{ext}}(\vec{\mathbf{r}},t) = 0, \tag{1.1d}$$

where σ, μ and ϵ are the conductivity, magnetic permeability and electric permittivity of the medium respectively. $\vec{\mathbf{D}}_{\text{ext}}(\vec{\mathbf{r}}, t)$ is the displacement vector. ρ_{fr} and $\vec{\mathbf{J}}_{\mathbf{fr}}(\vec{\mathbf{r}}, t)$ represents any free-charge and free-current density in the region of analysis.
We want to derive the nature of the electromagnetic field in the region between the ground plane and the overhead conductor. Assuming no conductivity or air, neither free sources within this region, we can write $\sigma = 0$, $\rho_{\text{fr}} = 0$ and $\vec{\mathbf{J}}_{\mathbf{fr}}(\vec{\mathbf{r}}, t) = 0$. Displacement vector will be linearly related with the electric field, $\vec{\mathbf{D}}_{\text{ext}} = \epsilon\vec{\mathbf{E}}_{\text{ext}}$. Additionally, we are considering transversal fields only, i.e. $\vec{\mathbf{E}}_{\text{ext}_z} = 0$ and $\vec{\mathbf{H}}_{\text{ext}_z} = 0$. Besides, ∇ operator can be divided by: $\nabla = \nabla_t + \nabla_z$, where ∇_t operates over transversal field components and ∇_z over longitudinal ones. Operating upon Eqs. 1.1 we can obtain for transversal fields the following equations:

$$\nabla_t \times \vec{\mathbf{E}}_{\text{ext}_t}(\vec{\mathbf{r}}_t, t) = 0 \tag{1.2a}$$

$$\nabla_t \times \vec{\mathbf{H}}_{\text{ext}_t}(\vec{\mathbf{r}}_t, t) = 0 \tag{1.2b}$$

This result shows that under TEM considerations, electric and magnetic fields obey the same equations as in the electrostatic and magnetostatic case. Therefore, we can find the magnitudes of the electric field by defining a scalar potential, $\phi(\vec{r}_t)$ such as $\vec{\mathbf{E}}_{\text{ext}_t}(\vec{\mathbf{r}}_t) = -\nabla\phi(\vec{r}_t)$ and magnetostatic approaches can be also proposed for finding the magnetic fields. In order to find the magnitudes of electric and magnetic fields, we can take advantage of the method of images [40] in order to convert the infinite wire over a ground conducting plane to an equivalent two-wire problem as shown in Fig. 1.1(b). Under the assumption of uniform distribution of charges in the conductor wires and a voltage V given between ground plane and conductor wire, it can be shown that charge on the overhead conductor and radial electric field magnitude. [40]:

$$E_r = \frac{V}{r \ln\left(\frac{2h}{r_w}\right)}. \tag{1.3}$$

A typical radius for conductor wires used in distribution and transmission lines is about $r_w = 1$[cm]. Therefore, approximated electric field intensities can be calculated depending on the wire height. Assuming typical heights about $h = 12$[m], $h = 17$[m], $h = 18$[m] for voltage levels about $V = 44$[kV], $V = 132$[kV], $V = 275$[kV] we can obtained the electric field magnitudes in terms of distance to the conductor wire. Fig. 1.2(a) shows the estimated results for the radial electric field magnitude by using Eq. 1.3. As it can be seen from Fig. 1.2(a), maximum field strengths are obtained at the conductor radius, then decreases rapidly over the first centimeters. Maximum electric field intensities were about $|\vec{\mathbf{E}}| = 565$[kV/m], $|\vec{\mathbf{E}}| = 1623$[kV/m], $|\vec{\mathbf{E}}| = 3358$[kV/m]

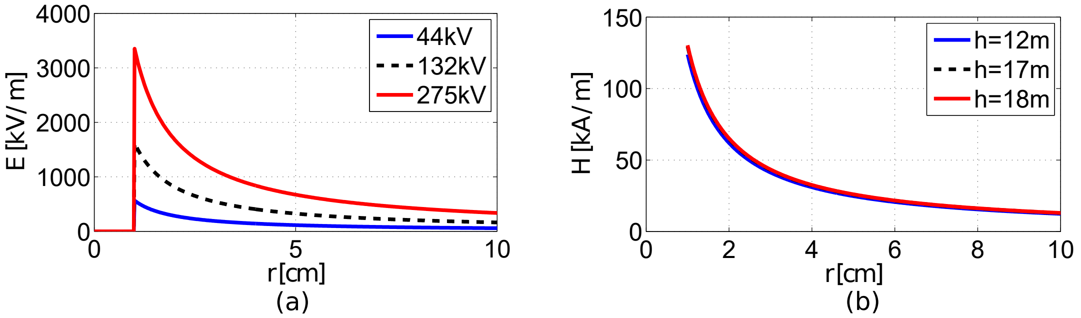

Figure 1.2: (a)Electric field radial component distribution for typical overhead lines in high voltage systems. (b)Magnetic field azimuthal component from overhead lines with $\mathbf{I} = 1$[kA] and different heights of conductor wires

from lower to higher voltage level respectively. On the other hand, magnetic field intensity from overhead lines can be also quantified under magnetostatic assumption, in this case we will have for the azimuthal component:

$$H = \frac{\mathbf{I}}{2\pi r} \ln\left(\frac{2h}{r_w}\right) \tag{1.4}$$

In contrast to the voltage in overhead lines, current magnitude will depend on the electric load, hence a definite value can not be given. However, nominal currents can be established depending on the electric power that the overhead line will transport. Considering an electric apparent power of $S = 100$[MVA], we can calculate the magnitude of the current in terms of the overhead line voltage. For the three cases under analysis, currents through overhead line conductors will be about $\mathbf{I} = 2$[kA], $\mathbf{I} = 757$[A] and $\mathbf{I} = 363$[A], for voltages from 44[kV], 132[kV] and 275[kV] respectively. It is worth noting that unity power factor was used for calculating the current magnitude from apparent power. Additionally, since the power was assumed to be constant, current magnitudes for lower voltages are much higher than those for high voltages. Nevertheless, in practice as higher voltage is used for transmission and distribution lines as higher power is transported, thus currents are also increased. Fig. 1.2(b) plots the intensity of magnetic field from the conductor wire surface when a current of $\mathbf{I} = 1$[kA] is assumed and different heights of conductor wires are considered. As can be seen from Fig. 1.2(b), intensity of magnetic field is much more dependent on the current magnitude than the overhead line height. This results allows to estimate the expected magnetic field intensity based on typical primary currents. As in the case of electric field intensity (Fig. 1.2(a)), we will find higher magnitudes near the conductor surface and will decrease with the inverse of distance.

This thesis presents two approaches based on optical fibers that can indirectly measure these electrical variables from the overhead lines. Current magnitude can be estimated through measuring the magnetic field around the conductor and voltage can be estimated from the associated electric field magnitude and geometrical aspects of the overhead line. The strategies that were selected to explore in the current thesis were based on the use of magnetostriction and piezoelectric properties of certain materials to transfer mechanical strains to optical devices based on the electric and magnetic field magnitudes, such as the external magnitude of interest can be estimated through the modulation of light guided in an optical fiber.

Chapter 2

Scope of the thesis

This thesis is focused on the theoretical description and practical implementation of magnetostrictive and piezoelectric sensors for magnetic field and voltage measurements. This thesis proposes two sensor arrangements for inferring external magnetic field and voltage magnitude by modulating light in an optical fiber. The analysis of both sensors are supported theoretically based on the known prior art, as well as some novel developments are proposed for describing the experimental results. Fig. 2.1 presents the scope of the thesis in a methodological diagram where the main physical interactions in the measurement of electrical variables in high voltage systems are highlighted. Light is sent from the ground level by using an optical fiber as a waveguide, light propagating in the optical fiber interacts with magnetostrictive and piezoelectric materials that are driven by the electromagnetic fields generated from the overhead line. This interaction allows to determine a sensing principle for

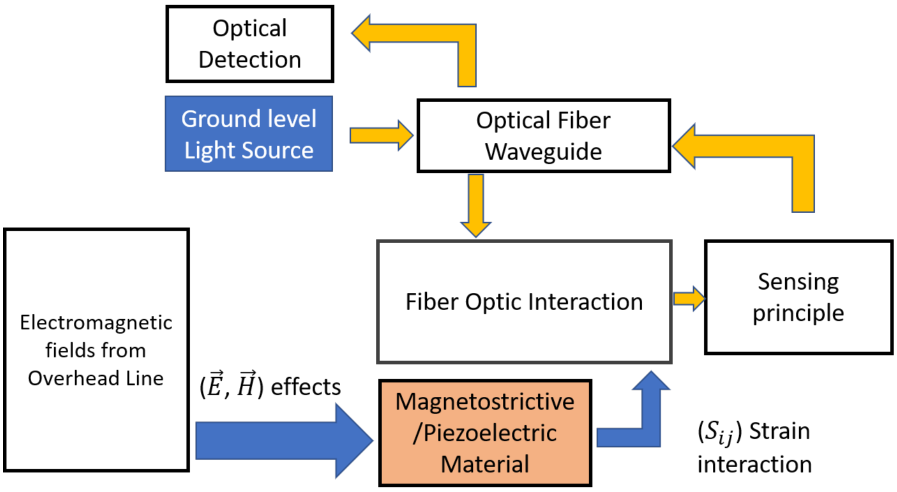

Figure 2.1: Methodological diagram of the interactions analyzed in this document

each of the variable that enables its inference through an optical detection. This document is organized in the following chapters: **Chapter 3** presents the strategies to transfer the strain due to the external perturbations into light modulation. This chapter presents a mathematical framework for extending the well known Coupled Mode Theory (CMT) through a Hamiltonian Formulation of the Helmholtz equation for accounting, in the propagation characteristics of few-mode fibers, additional perturbations across transverse spatial distribution of the propagating mode. As a particular case, this chapter considers the Fiber Bragg Gratings (FBGs) as one of the techniques to transfer the mechanical strain due to the external perturbations for altering the characteristics of the propagating light throughout the optical fiber. **Chapter 4** presents the characteristics of magnetized bodies due to an external magnetic field. This chapter describes the effects of geometry in the behavior of the demagnetization field, as well as discusses the difference of full vectorial solutions of the magnetization problem for finite length bodies against approached solutions that considers only magnetization along the external field direction. This chapter presents the most used methods for accounting non linearity, hysteresis and magnetostrictive effects due to the magnetization process.

After dealing with the physical description of magnetization and magnetostriction in continuum bodies, **Chapter 5** deals with the description of magnetostrictive composites. In this chapter, a novel numerical description of magnetic composites is presented and discussed in terms of previous literature reports and experimental results. The proposed method models the magnetic powder particles in the composite as individual cuboids, which allows to calculate a closed solution for the magnetic vector potential as well as controlling the geometric aspect ratio for each particle in the composite. This chapter presents some theoretical comparisons based on the magnetic powder particle size and its spatial distributions against magnetization of monolithic bodies, showing and highlighting the role that plays the demagnetization field of each of the particles in the overall magnetostrictive response of the composite body. Once magnetostrictive effects have been addressed in the previous chapters, **Chapter 6** presents the basics of piezoelectric devices modeling, especially the theoretical background of piezoelectric bi-morph and uni-morph actuators. Simplified analytical approaches are compared to Finite Element Method (FEM) results.

Once both sensing principles: magnetostriction and piezoelectric effects have been addressed, **Chapter 7** presents the experimental implementations for sensing magnetic and electric field by using magnetostrictive and piezoelectric devices and its coupling methods to optical fibers. Reported results present the capability of the implemented type of sensors to use the advantages of optical fiber to develop sensors in power systems. Some of the found drawbacks are also discussed and their limitations are explained. As a last section, **Chapter 8** presents the concluding remarks of the thesis and proposes future work based on the achieved results.

Chapter 3

Propagating light characteristics in optical fiber waveguides

In this chapter, the properties of propagating light into an optical fiber are analyzed with the aim to provide a background for the interaction between external perturbations and propagating light into the waveguide. First section of the chapter presents the most important characteristics of the light that propagates throughout an optical fiber. **Appendix A** presents a more detailed explanation of the used equations in this chapter. Main properties of propagating modes are considered for accounting their interaction with the external perturbations, which in the scope of this thesis will be associated to external strains transferred by magnetostrictive and piezoelectric effects. Secondly, one of the most used theory for mode interaction analysis, the Coupled Mode Theory (CMT), is discussed focused on its definition of orthogonality relationship between modes and modal expansion criteria. Since CMT formulation does not describe explicitly the effects of transverse perturbations upon the propagating mode characteristics, a Hamiltonian formulation of the Helmholtz equation (HFHE) is developed to provide a mathematical framework for computing the distortions over the spatial distribution of the propagating modes under some transverse perturbation. Discussed framework supports the application of the perturbation theory for few-mode fibers and its possible applications in modal conversion. Finally, as a particular case of a longitudinal perturbation, the Fiber Bragg Grating (FBGs) are addressed to be used as the optical device that allows the modulation of light by means of mechanical strain into its grating distribution.

3.1 Electromagnetic Fields in a Optical Fiber Waveguide

The description of electromagnetic waves that propagates through an optical fiber waveguide are in general described by the Maxwell's equations in a source-free medium:

$$\nabla \times \mathbf{E} = -j\omega\mu\mathbf{H} \tag{3.1}$$

$$\nabla \times \mathbf{H} = j\omega\varepsilon\mathbf{E}, \tag{3.2}$$

where $\mathbf{E}$ and $\mathbf{H}$ are complex vectors. There is a very well known decomposition of the electric and magnetic field components into transverse ($\mathbf{E_t}$,$\mathbf{H_t}$) and longitudinal direction ($\mathbf{E_z}$,$\mathbf{H_z}$), where this latter is considered as the direction of propagation of the resultant propagating waves (in this particular case z-axis has been defined as the propagating direction). By means fo this decomposition transverse fields can be found such as they satisfy the boundary conditions imposed by the waveguide. Afterwards, longitudinal components can be also found such as the total electromagnetic field can be determined for the waveguide. A more detailed explanation can be found in **appendix A** and Reference [38]. Once the electromagnetic field is known, the optical power carried by the electromagnetic field can be calculated from the Poynting vector definition, this latter is given by: $\vec{\mathcal{S}} = \mathbf{E} \times \mathbf{H}$, and relates the associated electric and magnetic energy of the electromagnetic wave [38]. Assuming a waveguide oriented through z-direction, averaged z-component of the Poynting vector is given by:

$$< \mathcal{S}_z >= \frac{1}{4}\left(\mathbf{E}_t^* \times \mathbf{H}_t + \mathbf{E}_t \times \mathbf{H}_t^*\right) \tag{3.3}$$

being $\mathbf{E}_t$ and $\mathbf{H}_t$ tangential components of the field. Based on this result, the total power through the cross-section of the waveguide can be calculated by:

$$P_{tz} = \frac{1}{4}\iint \left(\mathbf{E}_t^* \times \mathbf{H}_t + \mathbf{E}_t \times \mathbf{H}_t^*\right) \cdot d\vec{A}. \tag{3.4}$$

This result enables the calculation of the total power carried out by a propagating mode into a determined waveguide.

Since depending on the characteristics of the waveguide there can exist several propagating modes, an orthogonality relationship can be established between two of these solutions [28]. Assume two solutions to the Maxwell's equation in a waveguide, i.e. $\mathbf{E}_1$,$\mathbf{H}_1$,$\mathbf{E}_2$ and $\mathbf{H}_2$ and their conjugated vectors $\mathbf{E}_1^*$,$\mathbf{H}_1^*$,$\mathbf{E}_2^*$ and $\mathbf{H}_2^*$. It can be shown that the orthogonality relationship that holds for these two propagating modes is given by (details are presented in appendix **A**):

$$-j(\beta_1 - \beta_2)\iint \left(\mathbf{E}_{1t} \times \mathbf{H}_{2t}^* + \mathbf{E}_{2t}^* \times \mathbf{H}_{1t}\right) \cdot d\vec{A} = 0. \tag{3.5}$$

where β_1 and β_2 are the propagating constants for each mode, and $\mathbf{E}_{1t}$, $\mathbf{H}_{1t}$, $\mathbf{E}_{2t}$, $\mathbf{H}_{2t}$, are the transverse field spatial distribution of the electromagnetic fields. This orthogonality relation supports the Coupled Mode Theory (CMT) and establishes the power-mode independence between transversal solutions of propagating modes in waveguides [28]. Based on this orthogonality relationship, a modal expansion can be proposed for an arbitrary tangential field in terms of forward ($\hat{e}_{\nu t}(x,y)$, $\hat{h}_{\nu t}(x,y)$) and backward modes ($\hat{e}_{-\nu t}(x,y)$, $\hat{h}_{-\nu t}(x,y)$) by:

$$\mathbf{E}_t(x,y) = \sum_\nu a_\nu \hat{e}_{\nu t}(x,y) + \sum_\nu b_\nu \hat{e}_{-\nu t}(x,y) \tag{3.6}$$

$$\mathbf{H}_t(x,y) = \sum_\nu a_\nu \hat{h}_{\nu t}(x,y) + \sum_\nu b_\nu \hat{h}_{-\nu t}(x,y). \tag{3.7}$$

such as the forward and backwards amplitudes: a_ν, b_ν, can be found for each element in the expansion. When there is a perturbation in the permittivity ($\Delta\varepsilon_t$, $\Delta\varepsilon_z$), propagating modes can present energy interactions. Including the external perturbation and taking advantage of the current orthogonality relationship, we can define tangential and longitudinal coupling coefficients by:

$$K^t_{\nu\mu} = \omega \iint \hat{e}^*_{t\mu}(x,y)\Delta\varepsilon_t \hat{e}_{\nu t}(x,y)dA \tag{3.8a}$$

$$K^z_{\nu\mu} = \omega \iint \hat{e}^*_{z\mu}(x,y)\frac{\Delta\varepsilon_z\varepsilon}{(\varepsilon+\Delta\varepsilon_z)}\hat{e}_{\nu z}(x,y)dA \tag{3.8b}$$

such as it is possible to write for the forward and backward amplitudes (see **appendix A** for details):

$$a'_\mu(z) + j\beta_\mu a_\mu(z) = -j\sum_\nu \left[a_\nu(z)\left(K^t_{\nu\mu} + K^z_{\nu\mu}\right) + b_\nu(z)\left(K^t_{\nu\mu} - K^z_{\nu\mu}\right)\right] \tag{3.9}$$

$$b'_\mu(z) - j\beta_\mu b_\mu(z) = j\sum_\nu \left[a_\nu(z)\left(K^t_{\nu\mu} - K^z_{\nu\mu}\right) + b_\nu(z)\left(K^t_{\nu\mu} + K^z_{\nu\mu}\right)\right] \tag{3.10}$$

CMT theory allows to find the amplitudes of the expansion coefficients by solving the resultant equations. There are some typical situations where the CMT theory allows to find explicit solutions for the unknown coefficients when initial conditions for the amplitudes and modal characteristics are given. It is the case of co-directional and counter-directional coupling, where interaction modes are predefined in direction of propagation and propagation constant.

It should be noticed that CMT theory does not impose orthogonality between the modes spatial distribution themselves, but the power they carry out. As it was shown, the orthogonality relationship holds for propagating modes that present different propagation constants and propagation directions but there is no way to find

out the effects upon the propagation constant due to the perturbation neither the modifications of the spatial distributions of the transverse field.
Next section proposes an alternative formulation for calculating the corrections to the propagation constant as well as the transverse modal distortion due to an external perturbation.

3.2 Hamiltonian formulation for the Helmholtz equation in optical fibers

In optical fibers, those electromagnetic fields should be attached to appropriated boundary conditions which imposes additional conditions to the propagation constant. Assuming harmonic time dependence, i.e. $\exp(j\omega t \pm j\beta z)$, solutions for radiated and guided modes in Eqs. (3.1) can be found by solving an eigen-value problem, written in terms of the propagation constant β. Eigenfunctions that solve this problem are characterized by a specific set of parameters to describe the propagation characteristics as an unique entity, such as: spatial distribution for each field component, an effective refractive index and the optical power distribution for each of the propagating modes [47, 38, 8]. Closed form solutions has been extensively studied to solve for the transverse electric field distributions in basic dielectric profiles $\varepsilon_t(\vec{r}_\perp)$, such as rectangular slabs and cylindrical waveguides. However, interaction with external phenomena can lead to more complex transverse dielectric distributions and numerical techniques should be implemented. Perturbation theory is an analytical approximation that proposes a solution for the complex problem spanning the perturbed scenario through a linear combination of the unperturbed solutions[9]. This approach, in contrast to numerical simulation solutions, keeps most of the physical basis of the initial problem which helps much more in the understanding the effects of perturbation upon the propagating modes. In order to implement the perturbation theory to optical waveguides in the same fashion as in the Hamiltonian eigenproblem in quantum mechanics [9], a Hamiltonian formulation of the Maxwell's equations can be proposed [27, 44, 45, 46]. In this formulation, the propagating parameters of a waveguide with perturbed transverse dielectric profile $\tilde{\varepsilon}_t(\vec{r}_\perp)$ are calculated from the unperturbed waveguide $\varepsilon_t(\vec{r}_\perp)$, assuming that the perturbed dielectric profile can be considered as small change from the unperturbed one as: $\tilde{\varepsilon}_t(\vec{r}_\perp) = \varepsilon_t(\vec{r}_\perp) + \Delta\varepsilon_t(\vec{r}_\perp)$. References [44, 46] writes Maxwell's equation by means of two operators. A first operator $\hat{\mathbf{B}}$ acting as a longitudinal projector, and a second one $\hat{\mathbf{A}}$, that includes the transverse characteristics of the waveguide [44]. By using this procedure, corresponding equations can be written as a generalized eigenproblem, that expressed in Dirac's notation, can be written by means of the standard perturbation theory by:

$$\hat{\mathbf{A}}\left|\Psi\right\rangle = \beta\hat{\mathbf{B}}\left|\Psi\right\rangle \tag{3.11a}$$

$$\left|\Psi\right\rangle = \left[\begin{array}{c}\mathbf{E}_t\\ \mathbf{H}_t\end{array}\right], \tag{3.11b}$$

with the same power orthogonality condition presented in the section before, such as between two eigenkets this relationship is given by:

$$(\beta_i - \beta_j)\iint(\mathbf{E}_{it}\times\mathbf{H}_{jt}^{*} + \mathbf{E}_{jt}^{*}\times\mathbf{H}_{it})\cdot\hat{i}_z dA = 0, \tag{3.12}$$

where β_i and β_j are non-degenerate propagation constants, and $\mathbf{E}_{it}$, $\mathbf{H}_{it}$, $\mathbf{E}_{jt}$ and $\mathbf{H}_{jt}$ are their corresponding transverse mode distributions. Orthogonality expression in Eq.(3.12) is the same one used in the Coupled Mode Theory (CMT) widely discussed in previous section [29, 47]. Formulation in Eq.(3.11) allows the application of the stationary perturbation theory considering the eigenkets as a composition of the tangential electric and magnetic field (as stated in Eq.(3.11b)), this strategy implies that perturbation expansion coefficients will involve both fields instead of dealing with them individually. Helmholtz equation, in contrast to Maxwel equations, has the advantage of writing relationships for each tangential field independently. Evaluation of perturbation effects over the electric and magnetic field in a separated way constitutes an advantage in the analysis of dielectric waveguides, particularly for the electric field which can be modified not only in its propagation characteristics but also in its transverse distributions when immersed in dielectric profile perturbations.

In the attempt to deal with decoupled Maxwell equations as independent eigenproblems, (Eq.(3.13a) and Eq.(3.13b) written here again for readability), only Eq.(3.13b) satisfies hermiticity condition for the resultant operator [46], but perturbation terms associated to linear and non-linear contributions due to the polarization vector cannot be included into the formulation [46].

$$\nabla\times(\nabla\times\mathbf{E}(\vec{r})) = \mu_0\omega^2\mathbf{D}(\vec{r}) \tag{3.13a}$$

$$\nabla\times\left(\frac{1}{\varepsilon(\vec{r})}\nabla\times\mathbf{H}(\vec{r})\right) = \mu_0\omega^2\mathbf{H}(\vec{r}) \tag{3.13b}$$

$$\nabla\cdot\mathbf{D}(\vec{r}) = 0 \tag{3.13c}$$

$$\nabla\cdot\mathbf{H}(\vec{r}) = 0, \tag{3.13d}$$

On the other hand, Eq.(3.13a) includes polarization vector effects, but resultant operator does not satisfy hermiticity [44, 46].

In the following, a theoretical background of an analytical approach for dealing with the non-hermiticity of Eq.(3.13a) is presented, such as propagation parameters, as well as the distortions on the transverse electric field distribution can be calculated from a perturbation due to a polarization vector. This fact offers a main advantage of over conventional methods based on the CMT theory, because instead of considering the whole transversal field in expansion coefficients, proposed formulation calculates based on the electric field distribution in the cross section, which can be naturally connected to the polarization vector. In the proposed formulation completeness requirement is relaxed by means of a reduced basis analysis where both conditions can be achieved, which in some cases could be enough to describe the perturbed scenario. In practice, few-mode fibers are highly suitable for this type of analysis inasmuch as only some propagating modes can be excited. A set of numerical experiments for fiber optics waveguides are discussed to show the accuracy of the proposed method when different types of perturbation terms such as: inhomogeneities, anisotropies and nonlinearities are included. Results obtained through this formulation shows an excellent agreement with FEM simulations and results reported previously in literature.

Consider a z-directed propagating waves with propagation constant β. By using the vectorial identity $\nabla\times(\nabla\times\mathbf{A}) = \nabla(\nabla\cdot\mathbf{A}) - \nabla^2\mathbf{A}$, the eigenproblem in Eq.(3.13a) can be written as:

$$\left(\nabla_\perp^2 + k_0^2(1+\chi) - \beta^2 + \hat{\mathbf{W}}_\mathbf{t}\right)\mathbf{E}(\vec{\mathbf{r}}_\perp) = 0 \tag{3.14a}$$

$$\hat{\mathbf{W}}_\mathbf{t} = \nabla\left(-\frac{\nabla\varepsilon(\vec{\mathbf{r}}_\perp)}{\varepsilon(\vec{\mathbf{r}}_\perp)}\cdot\right) + \frac{\omega^2\Delta\hat{\chi}^{(1)}}{c^2} + \tag{3.14b}$$

$$\frac{\omega^2}{c^2}\left(\hat{\chi}^{(2)} : \mathbf{E}(\vec{\mathbf{r}}_\perp) + \hat{\chi}^{(3)}\mathbf{E}(\vec{\mathbf{r}}_\perp) : \mathbf{E}(\vec{\mathbf{r}}_\perp) + ...\right),$$

where $k_0 = \omega/c$ is the wavenumber, c the speed of light in vacuum; $\beta = n_{\mathrm{eff}}k_0$ the propagation constant through the waveguide with n_{eff} the mode effective refractive index; χ is the linear, homogeneous, and isotropic susceptibility. Additional term $\hat{\mathbf{W}}_\mathbf{t}$ includes any inhomogeneity associated to the spatial distribution of the permittivity and polarization vector effects. Linear anisotropies are included through the term $\Delta\hat{\chi}^{(1)}$ and the nonlinearities are taken into account according to the electric field dependence [8]. This mathematical artifice casts Helmholtz equation into a Hamiltonian eigenvalue problem in quantum mechanics [9], where unperturbed case is determined by isotropic, linear and lossless material, which reduces Eq. (3.14) to the Helmholtz equation for the electric field:

$$\left(\nabla_\perp^2 + k_0^2 n^2 - \beta^2\right) \mathbf{E}\left(\vec{\mathbf{r}}_\perp\right) = 0 \tag{3.15a}$$

$$\nabla_\perp^2 \mathbf{E}\left(\vec{\mathbf{r}}_\perp\right) = k_e^2 \mathbf{E}\left(\vec{\mathbf{r}}_\perp\right), \tag{3.15b}$$

where $n = \sqrt{1+\chi}$ is the refractive index of the linear and isotropic medium and $k_e^2 = \beta^2 - k_0^2 n^2$ acts as the eigenvalue. It is worth noting that full-vectorial characteristics of the electromagnetic field kept in Eq.(3.15) as long as each electric field component is included into the formulation, any anisotropic effect that involves different electric field components can be addressed by means of the perturbation terms in the polarization vector as presented in Eq.(3.14b). Using Dirac's notation, Eq. (3.15) can be written as:

$$\nabla_\perp^2 \left|e_{\alpha_j}\right\rangle = \left(\beta_j^2 - k_0^2 n^2\right) \left|e_{\alpha_j}\right\rangle, \tag{3.16}$$

where $|e_{\alpha i}\rangle$ are the normalized kets that represent the modal spatial distribution for each electric field component ($\alpha = x, y, z$) projected on the coordinate system. These normalized kets can be calculated from solutions to Eq.(3.15b) after imposing the corresponding boundary conditions associated to the waveguide characteristics, which leads to a set of functions $\{\mathbf{E_i}\left(\vec{\mathbf{r}}_\perp\right)\}$ that are able to propagate throughout the waveguide.

At this point, we can make use of a Hamiltonian formulation of the Helmholtz equation (in Eq.(3.16)) to describe some interactions and relationships that holds for the transversal fields in terms of those eventual transverse perturbation, as well as some other direct relationship that holds for the coupling factor integral expression. Once the basis of eigenkets $\left\{\left|e_{\alpha_j}\right\rangle\right\}$ is constructed by orthonormal and non-degenerated eigenfunctions that solve Eq.(3.16), first-order stationary perturbation theory allows to compute associated correction terms for the eigenvalue (propagation parameter) and eigenket (mode distortion) through the expressions [9]:

$$\tilde{\beta}^2 = \beta_0^2 + \langle e_{\alpha 0}|\hat{\mathbf{W}}_\mathbf{t}|e_{\alpha 0}\rangle \tag{3.17a}$$

$$|\tilde{e}_\alpha\rangle = |e_{\alpha 0}\rangle + \sum_{j=1, j\neq 0}^{\infty} \frac{\langle e_{\alpha j}|\hat{\mathbf{W}}_\mathbf{t}|e_{\alpha 0}\rangle}{\beta_0^2 - \beta_j^2} |e_{\alpha j}\rangle, \tag{3.17b}$$

where $\tilde{\beta}$ and $|\tilde{e}_\alpha\rangle$ are the propagation constant and mode field distribution after perturbation, respectively. Modified propagation constant can be calculated from

Eq.(3.17a) using the simplification:

$$\tilde{\beta} = \beta_0 \sqrt{1 + \frac{\Delta\beta^2}{\beta_0^2}} \approx \beta_0 + \frac{\Delta\beta^2}{2\beta_0}, \tag{3.18}$$

where $\Delta\beta^2 = \langle e_{\alpha 0}|\hat{\mathbf{W}}_{\mathbf{t}}|e_{\alpha 0}\rangle$. Here, it was assumed that $\Delta\beta^2 << \beta_0^2$. It is worth noting that perturbation operator $\hat{\mathbf{W}}_{\mathbf{t}}$ can include any inhomogeneity, linear anisotropy, and nonlinear effects, depending on which terms are included in Eq. (3.14b).

As discussed before, main advantage of the proposed formulation in this part of the thesis is to write the perturbation expressions in terms of the electric field components only. In order to accomplish this, we make use of the TEM wave properties to normalize eigenkets in terms of optical power using the relation of intensity of the electric field , where $|\vec{S}_z| = |\vec{E}_t|^2/2\eta$, with η the impedance of the medium. Based on this, we can write:

$$|\vec{S}_z| = \frac{|E_{xi}(x,y)|^2 + |E_{yi}(x,y)|^2}{2\eta} \tag{3.19}$$

$$\tag{3.20}$$

where medium impedance η is given by $\eta = \eta_0/n$. As it can be seen from Eq.(3.20), power written in terms of the electric field components can be decomposed as the sum of squares of the electric field components.

$$2P_{tz} = \frac{n}{2\eta_0} \iint \left(|\vec{E}_x(x,y)|^2 + |\vec{E}_y(x,y)|^2 \right) d\vec{A} \tag{3.21}$$

In the current formulation components of the electric field are treated independently leading to different normalization factor for each component in associated to the corresponding ket. However, power carried for each component can be used in the normalization factor such as the projection of the kets in the Cartesian coordinate system is given by:

$$\langle \vec{r}|e_{\alpha i}\rangle = \frac{E_{\alpha i}(x,y)}{\sqrt{\frac{1}{2\eta}\iint |E_{\alpha i}(x,y)|^2\, dxdy}} = \frac{E_{\alpha i}(x,y)}{\sqrt{\frac{n}{2\eta_0} A_{mi}}}, \tag{3.22}$$

where A_{mi} can be defined as the modal area for its respective component. Based on this definition orthogonality relationship for the current formulation will be given by:

$$\langle e_{\alpha i}|e_{\alpha j}\rangle = 2\eta\delta_{ij}. \tag{3.23}$$

It should be stressed that this formulation does not have same value of normalization as in the CMT. Therefore, any result obtained by these relationships in terms of possible affections of the perturbation to the transverse modal distributions should be calculated back to their initial values for being included in the CMT. Perturbed mode can be written back to coordinate space by:

$$\langle \vec{r} | \tilde{e}_{\alpha} \rangle = \langle \vec{r} | e_{\alpha 0} \rangle + \sum_{j=1, j \neq 0}^{\infty} \frac{\langle e_{\alpha j} | \hat{\mathbf{W}}_{\mathbf{t}} | e_{\alpha 0} \rangle}{\beta_0^2 - \beta_j^2} \langle \vec{r} | e_{\alpha j} \rangle , \tag{3.24a}$$

$$\tilde{E}_{\alpha 0}(x, y) = E_{\alpha 0}(x, y) + \sum_{j=1, j \neq 0}^{\infty} \frac{\langle e_{\alpha j} | \hat{\mathbf{W}}_{\mathbf{t}} | e_{\alpha 0} \rangle}{\beta_0^2 - \beta_j^2} \sqrt{\frac{A_{m0}}{A_{mj}}} E_{\alpha j}(x, y), \tag{3.24b}$$

Finally, perturbed transverse field will be given by:

$$\tilde{\mathbf{E}}_{1t} = \tilde{E}_{x0}(x, y) + \tilde{E}_{y0}(x, y). \tag{3.25a}$$

This result allows to write:

$$\hat{\tilde{e}}_{\nu t}(x, y) = \frac{\tilde{\mathbf{E}}_{1t}}{\sqrt{2 P_{tz}}} \tag{3.26a}$$

Leading to modified coupling coefficient for the transversal field defined by:

$$\tilde{K}_{\nu\mu}^{t} = \omega \iint \hat{\tilde{e}}_{t\mu}^{*}(x, y) \Delta\varepsilon_t \hat{\tilde{e}}_{\nu t}(x, y) dA. \tag{3.27}$$

In contrast to typical CMT, this formulation includes the possibility for modifying the coupling coefficient when tangential fields interact each other due to an external perturbation. Additionally, as it is stated in the perturbation theory, eigenfunctions are able to form a basis that allows to span the space of solutions, if completeness and orthogonality are satisfied [9]. These two latter conditions are the main difficulties in applying the perturbation theory to Eq.(3.16) with the aim of calculating the transverse mode distortions. However, in some scenarios a reduced set of elements taken from the set of solutions can be enough to describe the perturbed scenario. In practice, few-mode fibers are highly suitable for this type of analysis inasmuch as only some propagating modes can be excited and orthogonality relationships hold for all the components of the electric field. **Appendix B** presents a discussion of orthogonality between the spatial distribution of transverse modes and their consequences in the validity of the current formulation.

3.2.1 Numerical Experiments

This section presents a set of numerical experiments to show the accuracy of the HFHE method in the calculation of modal propagation parameters under the presence of external perturbations. Inhomogeneity and anisotropies of refractive-index profiles can be designed to enhance the inter-modal interaction, which can exploit the induced distortion on the mode field profile in the design, for instance, of spatial-multiplexing processes and all-optical switching. By means of the present formulation, the external perturbations can be conveniently engineered such as each component of the electric field in the propagating mode is affected selectively. The application of the current formulation is very suitable in few-mode fibers where the amount of supported propagating modes constitutes an orthogonal basis for each of the electric field components. Different types of analysis were performed in order to illustrate how the perturbations can be included into the analysis and the accuracies are also discussed. **Appendix B** presents additional simulations cases that can be of interest to the reader.

3.2.1.1 Linear Inhomogeneities

This section considers a step-index few-mode fiber with the following parameters: $n_{\text{core}} = 1.46$, $n_{\text{clad}} = 1.3$ and radius $\rho = 1.5[\mu\text{m}]$; the wavelength was set to be $\lambda = 1600[\text{nm}]$ in order to allow only one propagating mode for each family. In this case the set of solutions for the unperturbed Helmholtz equation is composed by orthogonal functions with propagating modes: $\{TE_{01}, TM_{01}, HE_{11}, EH_{11}, HE_{21}\}$. Perturbation consisted in the inclusion of spatial inhomogeneities for the linear refractive index in both the core and the cladding region, such us the perturbation strength, $\Delta n = |2n(r,\theta)\Delta\chi(r,\theta)|$, was imposed from the unperturbed case $\Delta n = 0$, to refractive index changes about $\Delta n \approx 10^{-2}$. This term can be included in Eq. (3.14b), where only the first two terms are considered. The presence of inhomogeneities in the spatial distribution of the permittivity makes to appear a polarization charge density at the interfaces between the inhomogeneous regions. It is worth noting that the first term of the operator in Eq.(3.14b) represents the polarization charge that can be found by $\rho_p = -\varepsilon_0 \frac{\nabla\varepsilon}{\varepsilon} \cdot \mathbf{E}$. In the case under study, the azimuthal change of susceptibility $\Delta\chi(\theta)$ will impose a surface charge density at each azimuthal interface $\theta = \theta_0'$. Using cylindrical coordinates polarization charge density at each azimuthal interface can be written by:

$$\rho_p(r', \theta', z') = \frac{\varepsilon_0}{r'} \left(\frac{\varepsilon_1 - \varepsilon_2}{\varepsilon_2} \right) E_{1\theta j}(r', \theta'_0, z') \delta(\theta - \theta'_0), \tag{3.28}$$

where subscript $1, 2$ defines both regions at the interface in which the azimuthal component of the electric field is directed from 1 to 2. Subscript j relates the mode function for the corresponding propagating mode. As it is stated in Eq.(3.28), the magnitude of the perturbation depends on the relative change of permittivity due to the inhomogeneity. For the refractive index contrasts under consideration, induced polarization charge at the interfaces can be neglected, thus the perturbation operator can be given by a simple expression $\hat{\mathbf{W}}_{\mathbf{t}} = \mu_0 \varepsilon_0 \omega^2 \Delta\chi^{(1)}(x, y)$, which is a spatial-dependent perturbation.

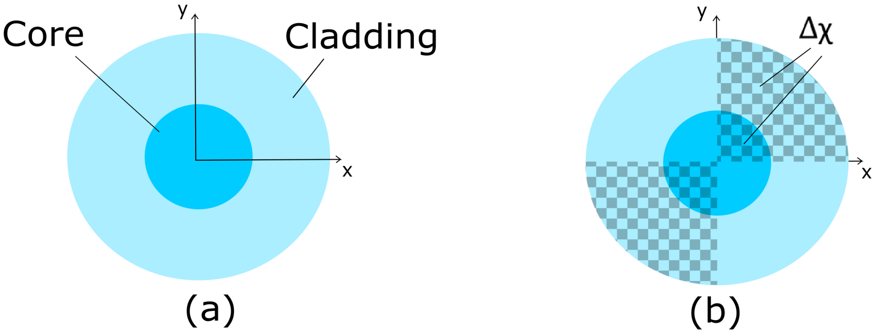

Figure 3.1: Spatial-dependent linear inhomogeneity and orthogonal propagating modes: (a) Unperturbed fiber; (b) perturbed fiber with azimuthal changes $\Delta\chi(\theta)$ of periodicity $\pi/2$

In order to compare the accuracy of the proposed approach in the prediction of the effects due to the inhomogeneities $\Delta\chi(x, y)$, the results obtained with the HFHE formulation were compared with those obtained from the vector FEM approach. Comparisons were performed for both the effective refractive index and the distortion in the electric-field distribution that undergoes each mode. It is worth noting that the simulations with the FEM are performed assuming that fiber does not suffer any perturbation, i.e., inhomogeneities are included as initial conditions of the problem, so it is not rigorously speaking an induced distortion by a perturbation, but an initial distribution of refractive index. This is an important advantage of the HFHE method because it can describe the transition from an initial spatial distribution of the guided mode into a distorted one due to the presence of an external perturbation, which can be used as an strategy for modal division multiplexing [4].

Figure 3.1 shows the spatial dependence of the perturbative terms. Once the perturbation is included, both the effective refractive index and the change in the field

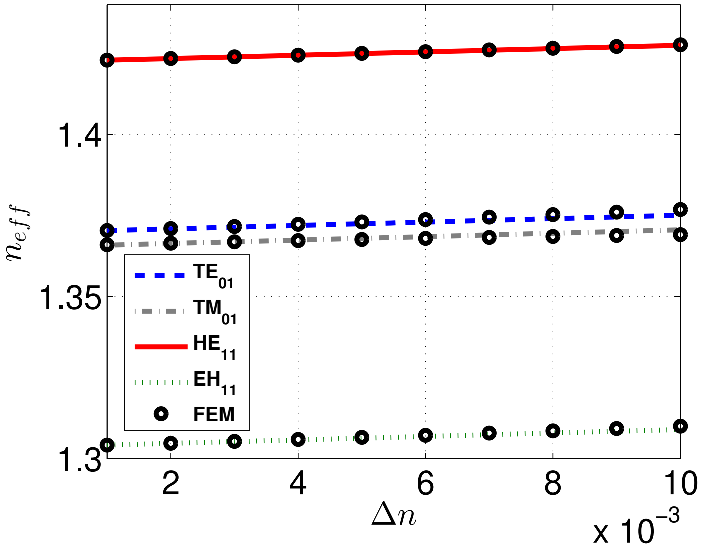

Figure 3.2: Effective refractive index of the perturbed optical fiber in Fig.3.1 (b) for the four propagation modes versus Δn obtained by our HFHE formulation (lines) and calculated by the vector FEM (dots).

distribution for each propagating mode are calculated as a function of the perturbation magnitude. Fig. 3.2 presents the dependence of the effective refractive index for each propagating mode as a function of the perturbation strength. From this figure, we can see that our results are in good agreement with the vector FEM solutions. We found a maximum absolute error about 0.1% between them at the strongest perturbation. Sources of the mismatch can come from neglecting the induced polarization charges due to the imposed inhomogeneities in the polarization vector. An additional comparison was performed on the calculation of the E_x field profiles of the guided modes due to the presence of the inhomogeneity. In Ref. [44] correction terms were applied only to propagation constants. However, by using HFHE formulation and through the perturbation method described before, spatial-distribution correction can also be well estimated after the perturbation, as it is presented in Fig. 3.3.

It must be noted that transverse modes are most affected because they do not present symmetry respect to the spatial inhomogeneity, increasing the magnitude of the coupling coefficient between modes in Eq. (3.17b). When these field distributions are compared with the unperturbed ones, the effect of the perturbation is to rotate the mode in a clockwise direction in which the rotation angle depends on the perturbation magnitude, and it is directly related with the coupling coefficient between TE and TM modes. In practice, this effect can be exploited by doping the fiber in specific

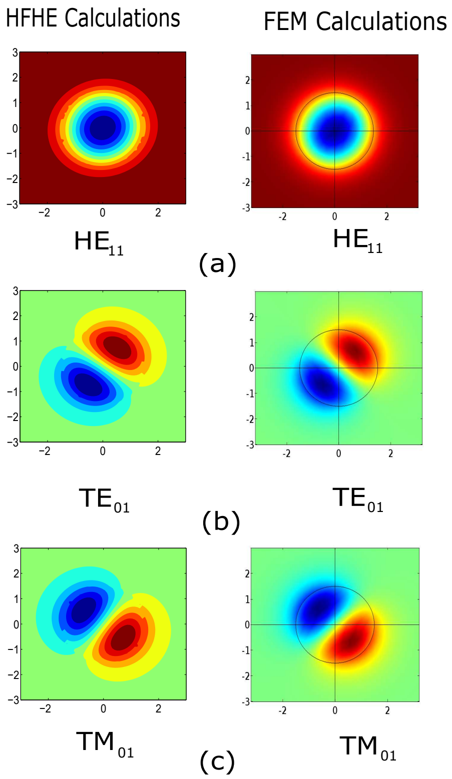

Figure 3.3: Mode field distributions (E_x-component) of the perturbed optical fiber in Fig. 3.1(b). (a) HE_{11} , (b) TE_{01} , (c) TM_{01}. When these field distributions are compared with the unperturbed ones in Fig. 3.1(c), the effect of the perturbation is to rotate the mode distribution in a clockwise direction.

regions where inhomogeneities can be controlled externally allowing mode conversion processes.

3.3 Fiber Bragg Gratings

A Fiber Bragg Grating (FBGs) is a particular case of an external perturbations along the propagation path. FBGs are changes on the refractive index of the core of the fiber that are intentionally induced along the propagation path in optical fibers in order to couple propagating modes. These changes are typically modeled assuming a perturbation of the effective refractive index given by [13]:

$$\delta n_{\text{eff}}(z) = \bar{\delta n}_{\text{eff}}(z) \left[1 + v \cos\left(\frac{2\pi}{\Lambda} z + \phi(z) \right) \right] . \tag{3.29}$$

As it was presented in the section above, the existence of a perturbation can couple co-propagating and contra-propagating modes. This section makes the analysis of Fiber Bragg Gratings (FBGs) based on the CMT and the notation followed in [13]. More details about the analysis of the effects of perturbations due to FBGs is presented in **Appendix C**.

The interaction between a propagating mode and a counter-propagating mode due to the existence of the longitudinal perturbation allows to find a reflection coefficient given by:

$$\rho(\kappa, \hat{\sigma}, L) = \frac{-j\kappa}{\sqrt{\kappa^2 - \hat{\sigma}^2}\coth(L\sqrt{\kappa^2 - \hat{\sigma}^2}) + j\hat{\sigma}}. \tag{3.30}$$

where parameter $\hat{\sigma}$ and κ are given by:

$$\hat{\sigma} = \delta + \sigma_{\nu\mu}(z) - \frac{1}{2}\frac{d\phi(z)}{dz} \tag{3.31}$$

$$\kappa = \kappa_{\nu\mu}(z) \tag{3.32}$$

detuning parameter δ is given by: $\delta = \beta_o - \frac{\pi}{\Lambda}$ and $\sigma_{\nu\mu}(z)$ is determined by:

$$\sigma_{\nu\mu}(z) = \omega n_{co}\overline{\delta n}_{co}(z) \iint \hat{e}^*_{t\mu}(x, y)\hat{e}_{\nu t}(x, y) dA \tag{3.33}$$

$$\kappa_{\nu\mu}(z) = \frac{v}{2}\sigma_{\nu\mu}(z). \tag{3.34}$$

In order to validate that the numerical implementation in this thesis is in agreement with previous results in literature, Figure 3.4 compares the reflected spectrum of an experimental FBG (taken from [13]) and its theoretical prediction assuming $L =$ 1[mm], $v = 1$, $\overline{\delta n}_{co} = 8 \times 10^{-4}$, $n_{co} = 1.45$. This latter is assumed because it is not given in the paper. As it can be seen from Fig. 3.4 implemented numerical in this thesis, reproduces main characteristics and magnitude of the reflected spectra of the experimental results presented in Ref. [13].

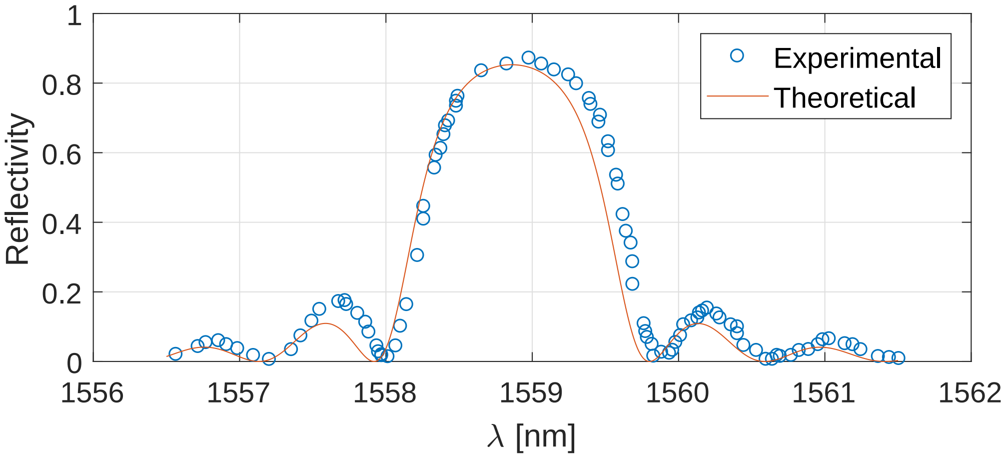

Figure 3.4: Comparison of the reflected spectrum of an experimental FBG (taken from [13]) and its theoretical prediction.

3.3.1 Non-Uniform Gratings

In practice uniform gratings are not always desired because they present several side lobes. Therefore, different types of apodizations are imposed to the grating. Dealing with non-uniform gratings requires the solution of the transfer matrix with z-dependent coupling coefficients, which normally requires the usage of numerical methods. Typically, a piecewise linear approximation is used for solving Eq.(C.12), such as each section is solved as a constant coefficients section. Based on this method, we are able to calculate the reflected spectrum from z-dependent gratings. Figures 3.5(a) and 3.5(b) present the comparison of our numerical implementation with those results presented in Ref. [13], for a grating that follows a Gaussian-apodized function given by:

$$\bar{\delta} n_{\mathrm{eff}}(z) = \bar{\delta} n_{co} e^{\left(\frac{-4\ln 2(z-L/2)^2}{\mathrm{FWHM}^2}\right)}, \tag{3.35}$$

where FWHM is the full-width-at-half-maximum of the grating profile. As it can be seen from Figs.(3.5(a,b)), numerical method impletemed in this thesis for modeling nonuniform gratings is in agreement with the results previously published in Ref.[13].

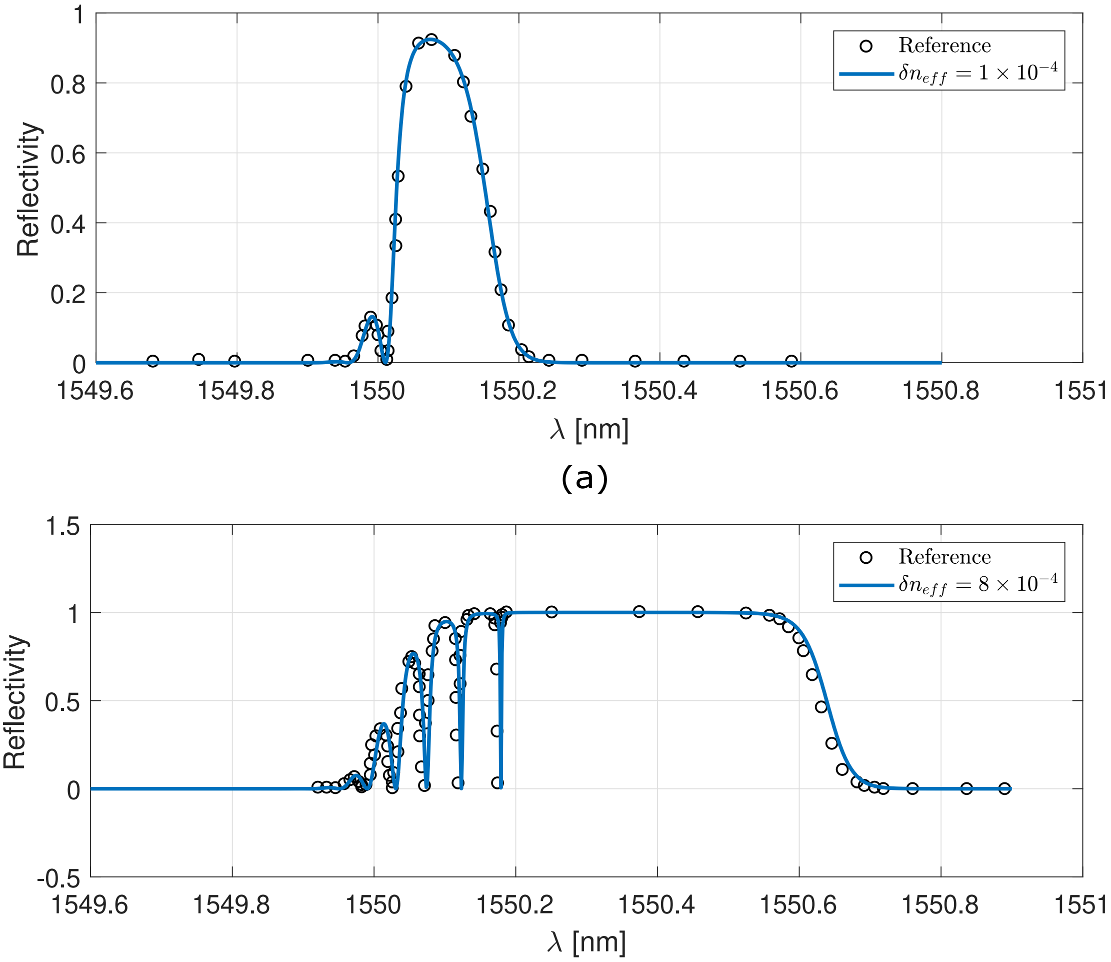

(a)

(b)

Figure 3.5: (a)Comparison with the reference results presented in [13]. Gaussian-apodized function, $L = 3$[cm], $v = 1$, $\bar{\delta n}_{co} = 1 \times 10^{-4}$, $n_{co} = 1.45$,FWHM= 1[cm].(b)Gaussian-apodized function, $L = 3$[cm], $v = 1$, $\bar{\delta n}_{co} = 8 \times 10^{-4}$, $n_{co} = 1.45$,FWHM= 1[cm].

3.3.2 Chirped Gratings

For those applications were the FBG is non-uniformly modulated in length, analysis of chirped gratings is of extremely high importance because this is the predominant scenario in many sensors based on this effect. Depending on the applied force and its distribution along the grating length is the reflected spectrum behavior. In Ref.[13], it is proposed an expression for writing the phase term of the grating $\phi(z)$, such as the term in the coupling coefficient associated to the chirped grating can be written by:

$$\frac{1}{2}\frac{d\phi}{dz} = \frac{-4\pi n_{\text{eff}} z}{\lambda_D^2}\frac{d\lambda_D}{dz}, \tag{3.36}$$

where λ_D is the equivalent wavelength associated with the grating pitch Λ by:

$$\lambda_D = 2n_{\text{eff}}\Lambda. \tag{3.37}$$

3.3.2.1 Linear Chirp

One of the simplest chirping is that composed of a linear increment of the grating along the FBG length. In order to include a linear chirping in the grating function description, we can write the pitch length dependence along z given by the expression:

$$\Lambda(z) = \Lambda_o \pm \gamma_p z, \tag{3.38}$$

where γ_p is a proportional constant. Therefore, we can write for the frequency:

$$\omega_g(z) = \frac{2\pi}{\Lambda(z)} = \frac{2\pi}{\Lambda_o \pm \gamma_p z}. \tag{3.39}$$

By using a Taylor series expansion and taking the first order only, we can write:

$$\omega_g(z) = \frac{2\pi}{\Lambda_o + \gamma_p z} \approxeq \frac{2\pi}{\Lambda_o} - \frac{2\pi}{\Lambda_o^2}\gamma_p z \tag{3.40}$$

$$\omega_g(z) = \frac{2\pi}{\Lambda_o - \gamma_p z} \approxeq \frac{2\pi}{\Lambda_o} + \frac{2\pi}{\Lambda_o^2}\gamma_p z \tag{3.41}$$

Based on this expression, we can write in general:

$$\omega_g(z) = k_p z \mp \frac{2\pi}{\Lambda_o} \tag{3.42}$$

$$\delta n_{\text{AC}}(z) = \cos\left(\frac{2\pi}{\Lambda_o} z \mp k_p z^2\right), \tag{3.43}$$

where k_p is a proportional quantity that relates the initial and final pitch in the chirp by:

$$k_p = \frac{2\pi}{\Lambda_o^2}\gamma_p. \tag{3.44}$$

If the last grating pitch is written in terms of the initial pitch frequency by a factor α_p, we can find the proportionality factor k_p by:

$$k_p = \frac{2\pi}{\Lambda_o L}(\alpha_p - 1) \tag{3.45}$$

this allows us to write:

$$\omega_g(z) = \frac{2\pi}{\Lambda_o L}(\alpha_p - 1)z + \frac{2\pi}{\Lambda_o} \tag{3.46}$$

$$\delta n_{\mathrm{AC}}(z) = \cos\left(\frac{2\pi}{\Lambda_o}z + \frac{2\pi}{\Lambda_o L}(\alpha_p - 1)z^2\right). \tag{3.47}$$

In order to include this expression in the previous results, we have:

$$\phi(z) = \frac{2\pi}{\Lambda_o L}(\alpha_p - 1)z^2 \tag{3.48}$$

$$\frac{1}{2}\frac{d\phi}{dz} = \frac{2\pi}{\Lambda_o L}(\alpha_p - 1)z \tag{3.49}$$

Figure 3.6 presents the effect on the reflected spectrum when a linear chirp is considered along the FBG. As it can be seen from the figure, the effect of a chirped grating relay on both: central wavelength and spectrum broadening. However, the reflectivity is highly attenuated when longer chirp periods are considered. This effect

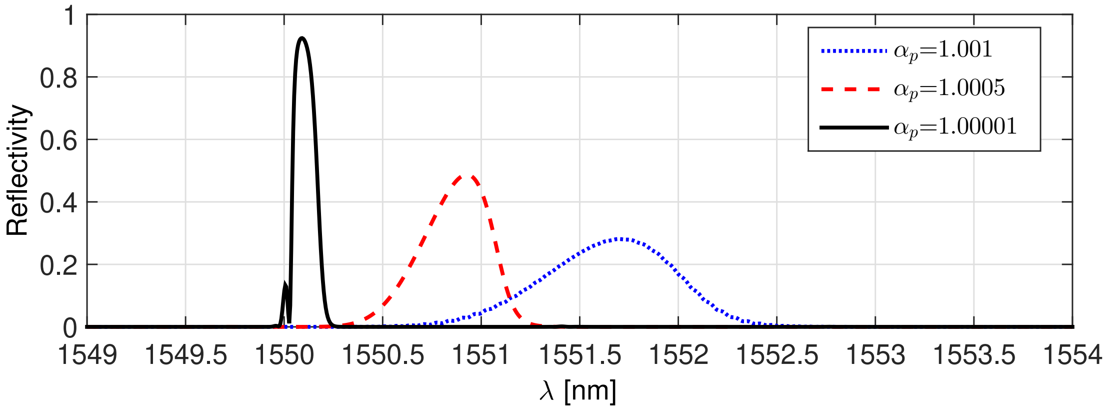

Figure 3.6: Comparison with the reference results presented in [13]. Gaussian-apodized function with different linear chirps, $L = 3cm$, $v = 1$, $\delta n_{co} = 1 \times 10^{-4}$, $n_{co} = 1.45$,FWHM$= 1cm$.

is directly related with the interference processs that holds for light in the grating, such as the matching condition for the phase between optical paths along the FBG is not longer satisfied, leading to a change in the peak reflection and the selectivity of the reflected spectrum (bandwidth).

3.3.2.2 Symmetric Linear Chirp

We can also have chirped gratings that vary along both directions of the FBG. For this case let's consider first a symmetric linear variation that begins at the middle of the FBG length. In this particular situation k_p can be written by:

$$k_p = \begin{cases} \frac{4\pi}{\Lambda_o L}(\alpha_p - 1) & 0 < z < L/2 \\ \frac{-4\pi}{\Lambda_o L}(\alpha_p - 1) & L/2 \leq z \leq L. \end{cases} \tag{3.50}$$

Therefore, the grating function can be written by:

$$\omega_g(z) = k_p = \begin{cases} \frac{4\pi(\alpha_p-1)}{\Lambda_o L} z + \frac{2\pi}{\Lambda_o} & 0 < z < L/2 \\ \frac{4\pi(1-\alpha_p)}{\Lambda_o L}(z - L) + \frac{2\pi}{\Lambda_o} & L/2 \leq z \leq L. \end{cases}, \tag{3.51}$$

in order to include this expression in the previous results, we have to find the argument of the cosine function. Therefore, we can write for $\cos(\omega_g(z)z) = \cos((2\pi/\Lambda_o)z + \phi(z))$, where we have for the phase:

$$\phi(z) = \begin{cases} \frac{4\pi(\alpha_p-1)}{\Lambda_o L} z^2 & 0 < z < L/2 \\ \frac{4\pi(1-\alpha_p)}{\Lambda_o L}(z^2 - Lz) & L/2 \leq z \leq L. \end{cases}, \tag{3.52}$$

calculating the derivatives respect to z, we have:

$$\frac{1}{2}\frac{d\phi}{dz} = \begin{cases} \frac{4\pi(\alpha_p-1)}{\Lambda_o L} z & 0 < z < L/2 \\ \frac{2\pi(1-\alpha_p)}{\Lambda_o L}(2z - L) & L/2 \leq z \leq L. \end{cases} \tag{3.53}$$

Following figure presents the effect of different values of α_p in the reflection spectrum.

It should be noticed the dramatic effect upon the reflection spectrum shape when a symmetric linear chirping is imposed to the FBG. In contrast to the reflection decaying spectra presented in Fig.3.6, resultant spectra due to symmetric linear chirp, present a two sided lobes in the reflection spectrum that separates each other as the coefficient factor α_p decreases. This effect can be understood as a splitting of the FBG into two different ones.

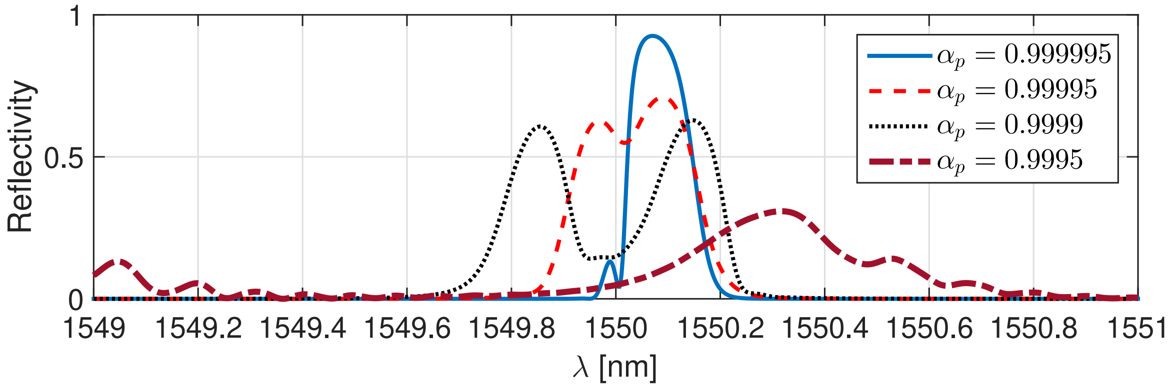

Figure 3.7: Comparison of different reflected spectrum results of Gaussian-apodized function with different linear symmetric chirps, $L = 3cm$, $v = 1$, $\bar{\delta n}_{co} = 1 \times 10^{-4}$, $n_{co} = 1.45$,FWHM$= 1cm$.

3.3.2.3 Asymmetric Linear Chirp

The same analysis can be performed over a linear chirp, but in this case we can consider an asymmetric chirp function, i.e. the inflection point is not located at the center of the FBG. For this case let's assume the inflection point is located at some point $z = L/m$, being m a real number such as: $0 < m < 1$. In this situation k_p can be written by:

$$k_p = \begin{cases} \frac{2m\pi}{\Lambda_o L}(\alpha_p - 1) & 0 < z < L/m \\ \frac{2m\pi}{\Lambda_o L}(1 - \alpha_p) & L/m \leq z \leq L. \end{cases} \tag{3.54}$$

Therefore, the grating function can be written by:

$$\omega_g(z) = k_p = \begin{cases} \frac{2m\pi(\alpha_p - 1)}{\Lambda_o L} z + \frac{2\pi}{\Lambda_o} & 0 < z < L/m \\ \frac{2m\pi(1-\alpha_p)}{\Lambda_o L(m-1)}(z - L) + \frac{2\pi}{\Lambda_o} & L/m \leq z \leq L. \end{cases}, \tag{3.55}$$

Using the same analysis for the phase function, $\cos(\omega_g(z)z) = \cos((2\pi/\Lambda_o)z + \phi(z))$, we can write for the phase:

$$\phi(z) = \begin{cases} \frac{2m\pi(\alpha_p - 1)}{\Lambda_o L} z^2 & 0 < z < L/2 \\ \frac{2m\pi(1-\alpha_p)}{\Lambda_o L(m-1)}(z^2 - Lz) & L/2 \leq z \leq L. \end{cases}, \tag{3.56}$$

calculating the derivatives respect to z, we have:

$$\frac{1}{2}\frac{d\phi}{dz} = \begin{cases} \frac{2m\pi(\alpha_p - 1)}{\Lambda_o L} z & 0 < z < L/2 \\ \frac{m\pi(1-\alpha_p)}{\Lambda_o L(m-1)}(2z - L) & L/2 \leq z \leq L. \end{cases} \tag{3.57}$$

Figure 3.8 presents the behavior of the reflectivity when different values for α_p are considered. It should be noticed that when α_p is smaller than the unity the spectrum is modified to the right of the central frequency. The ripples that appear in the spectra can be explained by the tunning condition that achieves the wavelength and phase of the incident light wave with the abrupt change caused by the slopes of the chirping function.

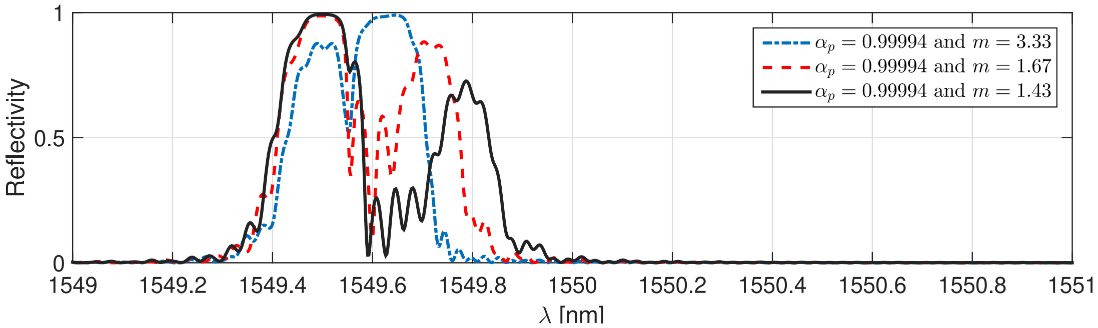

Figure 3.8: Comparison of different reflected spectrum results of Gaussian-apodized function with different linear symmetric chirps, $\lambda_D = 1549.5$ [nm], $L = 3cm$, $v = 1$, $\bar{\delta n}_{co} = 1 \times 10^{-4}$, $n_{co} = 1.45$,FWHM= $3cm$.

An different behavior is obtained in the reflected spectra when instead of a tension ($\alpha_p < 1$), we exert a compression ($\alpha_p > 1$) somewhere along the FBG. Figure 3.9 presents the results of the calculated spectrum when the asymmetric chirp occurs at different points along the FBG. In this particular case, smaller lobes appear in the left side of the peak wavelength. Same ripples in the reflected spectrum are also present as in the previous case.

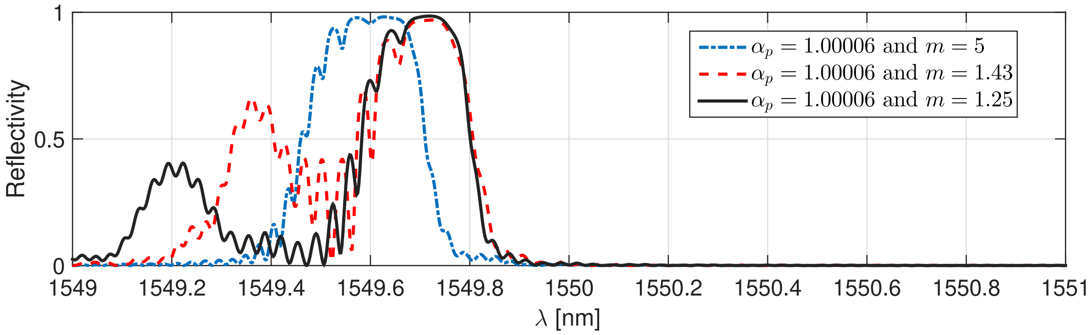

Figure 3.9: Comparison of different reflected spectrum results of Gaussian-apodized function with different linear symmetric chirps, $\lambda_D = 1549.5$ [nm],$L = 3cm$, $v = 1$, $\bar{\delta n}_{co} = 1 \times 10^{-4}$, $n_{co} = 1.45$,FWHM= $3cm$.

As it has been presented in this subsection, chirped FBGs exhibit different spectral shapes when different functions of grating distribution are considered. in contrast to the uniform deformation of the FBG where only a shifting of the central wavelength is expected, chirped FBGs exhibit important deformations on thee reflected spectrum that can be used for improving the sensing strategies based on FBGs. It is worth noting that sensitivity to the parameters is also an important issue in the spectrum shape, achieving multiple reflection spectra patterns and reflection peaks when coefficients of the chirping function are slightly changed.Therefore, one expects that chirped FBGs can easily set up as a good strategy for sensing mechanical strains and shape deformations.

3.4 Concluding Remarks

This chapter described main theoretical aspects of propagating modes in optical fibers. Orthogonality and completeness of guided electromagnetic fields in optical fibers were discussed and analyzed through well known analytical solutions for propagating modes. Coupled Mode Theory (CMT) basis was described and main results were derived (see **Appendix A** for details). Since CMT does not account explicitly for corrections to the propagation constant and spatial distribution of propagating modes for each component of the electric field when they are under a transverse external perturbation, a formulation of the Helmholtz equation in terms of eigenfunctions of an eigenvalue equation (considering Laplacian operator as a Hamiltonian operator) allowed to determine spatial distortion of propagating modes by using the first order perturbation theory. Numerical experiments showed the feasibility for using developed framework to successfully calculate spatial distortions due to transverse perturbations (see **Appendix B** for details). Therefore, a theoretical connection between spatially disturbed modes and coupled mode theory framework was achieved, so one could expand the arbitrary field $\mathbf{E}_{1t}$ in the transverse perturbed modal basis ($\hat{\tilde{e}}_{t\nu}(x,y)$) by:

$$\mathbf{E}_{1t}(x,y,z) = \sum_{\nu} \left(a_\nu(z) + b_\nu(z)\right) \hat{\tilde{e}}_{t\nu}(x,y) \tag{3.58}$$

where both effects can be considered. Amplitude coefficients can be then determined by solving the corresponding linear system that results in the CMT by:

$$a'_\mu(z) + j\tilde{\beta}_\mu a_\mu(z) = -j \sum_{\nu} \left[a_\nu(z)\left(\tilde{K}^t_{\nu\mu} + K^z_{\nu\mu}\right) + b_\nu(z)\left(\tilde{K}^t_{\nu\mu} - K^z_{\nu\mu}\right)\right] \tag{3.59}$$

$$b'_\mu(z) - j\tilde{\beta}_\mu b_\mu(z) = j \sum_{\nu} \left[a_\nu(z)\left(\tilde{K}^t_{\nu\mu} - K^z_{\nu\mu}\right) + b_\nu(z)\left(\tilde{K}^t_{\nu\mu} + K^z_{\nu\mu}\right)\right] \tag{3.60}$$

Finally, Fiber Bragg gratings were addressed as one of the most used optical devices for modulating light characteristics based on longitudinal perturbations upon a uniform grating (see **Appendix C** for details). Chirping effects were analyzed when longitudinal perturbation presents a phase chirp. Changes in the spectrum shape, as well as peak wavelength were observed in the reflection spectra. Since magnetostrictive and piezoelectric materials create a mechanical deformation that can be transferred to an FBG with some particular characteristics such as the particular sensitivity on the spectrum properties could be used as the strategy for modulating light and infer the external field magnitudes.

Chapter 4

Magnetization and Magnetostriction

Magnetic induction, $\vec{B}$, is the response of a medium due to the presence of a magnetic field $\vec{H}$. These two quantities can be related by the general expression:

$$\vec{B} = \mu_0 \left(\vec{H} + \vec{M} \right) \tag{4.1}$$

where μ_0 is the magnetic permeability of vacuum and $\vec{M}$ is the magnetization vector. This latter accounts for the properties of the material and describes of the magnetization process inside the material [6, 22]. When dealing with finite lengths of the magnetic material, magnetization makes a demagnetization field to appear, thus a correction of the total magnetizing or internal magnetic field should be done by:

$$\vec{H} = \vec{H}_{\mathrm{ext}} + \vec{H}_{\mathrm{dmg}} \tag{4.2}$$

where $\vec{H}_{\mathrm{dmg}}$ is the corresponding magnetic field due to the magnetization spatial distribution, therefore the geometry dependence of this field can be used to engineer some desired internal magnetic field distributions. Most traditional description of magnetization is based on a macroscopic interpretation of atomic interactions. This approach defines the existence of "magnetic moments" that are related to the population of electrons along the atom orbitals and their spin moments. Therefore, a magnetic material can be imaged as a collection of magnetic moments subdivided into regions, called magnetic domains, where the internal energy rules the alignment of the magnetic moments. On the other hand, the dependence of magnetic moment on the electronic charge cloud distribution in the atom, suggests that under the action of an external magnetic field the dimensions of this spatial distribution should be modified in a certain preferred direction, inducing displacements upon the neighboring ions, establishing a natural connection between magnetic properties and mechanical strain in the material. These relations determine the magneto-elastic properties of the material [33]. The averaged effect over a volume large enough to include many domains allows to describe the macroscopic behavior of magnetic and magnetostrictive materials [6]. Since this thesis deals with macroscopic magnetic effects, this magnetization description was chosen in this thesis as a valid framework for models and experiments. This chapter discusses the characteristics of the magnetization of materials and validates the implementation of the numerical models comparing their results to those presented previously in literature.

4.1 Demagnetization Field

This section will discuss the effects of the geometry over the magnetization and also the advantages of using different shapes of the sensors for taking advantage of certain type of internal magnetic field distributions. **Appendix D** presents a more general description for calculating the demagnetization field for a given magnetization inside an arbitrary shaped magnetic body as well as some comparisons against Finite Element Method predictions. Following description is known as the scalar approach and can be used to find the demagnetization field in case of a current free source media $\vec{J} = 0$. In this particular case we can write for the demagnetization field $\nabla \times \vec{H}_{\mathrm{dmg}} = 0$, which allows to propose a magnetic scalar potential such as $\vec{H}_{\mathrm{dmg}}(\vec{r}) = -\nabla\phi_m(\vec{r})$. In linear media one have $\nabla \cdot \vec{B}_{\mathrm{dmg}}(\vec{r}) = \mu_0 \nabla \cdot \left(\vec{H}_{\mathrm{dmg}}(\vec{r}) + \vec{M}(\vec{r})\right) = 0$. Combining both expressions and taking the divergence of the magnetic field, following expression can be written for the magnetic scalar potential:

$$\nabla^2 \phi_m(\vec{r}) = \nabla \cdot \vec{M}(\vec{r}), \tag{4.3}$$

where the divergence of the magnetization acts as a "magnetic source" in the volume domain, $\rho_m = -\nabla \cdot \vec{M}(\vec{r'})$ of the scalar potential, such as $\nabla^2\phi_m(\vec{r}) = -\rho_m$. This equation resembles the Poisson's equation, which in a free boundary space can be solved by using the divergence theorem and the Green's function in free space, this procedure leads to [19]:

$$\phi_m(\vec{r}) = -\frac{1}{4\pi} \iiint_{v'} \frac{\nabla' \cdot \vec{M}(\vec{r'})}{|\vec{r} - \vec{r'}|} d^3r' + \frac{1}{4\pi} \iint \frac{\vec{a}_n \cdot \vec{M}(\vec{r'})}{|\vec{r} - \vec{r'}|} ds', \tag{4.4}$$

In the particular case of a constant magnetization we have $\nabla' \cdot \vec{M}(\vec{r'}) = 0$. Therefore, second term of the integral in Eq.(4.4) contributes to the scalar potential $\phi_m(\vec{r})$.

Finally, magnetic field can be found by taking the gradient over the scalar magnetic potential function:

$$\vec{H}_{\text{dmg}}(\vec{r}) = -\nabla\phi_m(\vec{r}). \tag{4.5}$$

This method allows to calculate the demagnetization field for a given magnetization distribution and stresses the dependence of geometry upon the internal distribution of the total internal magnetic field and the resultant magnetization. In most cases the demagnetization field can be written as a function of a constant magnetization (M_o) and a geometrical factor function $G_f(\vec{r})$, i.e. $\vec{H}_{\text{dmg}}(\vec{r}) = -M_o G_f(\vec{r})$, such as the total internal magnetic field can be calculated by summing up the demagnetization field and the external field.

$$H_{\text{int}} = H_{\text{ext}} - M_o G_f(\vec{r}). \tag{4.6}$$

It should be noticed that the negative sign is included in the demagnetization field magnitude since it opposes to the external field. In the linear case, magnetization can be written in terms of the internal field by $M_0 = \chi_m H_{\text{int}}$. Therefore, we can write:

$$H_{\text{int}} = H_{\text{ext}} - \chi_m H_{\text{int}} G_f(\vec{r}), \tag{4.7}$$

which allows to solve for the internal field by:

$$H_{\text{int}} = \frac{H_{\text{ext}}}{1 + \chi_m G_f(\vec{r})}. \tag{4.8}$$

Once the internal field is calculated we can recalculate for the magnetization by:

$$M = \chi_m H_{\text{int}}. \tag{4.9}$$

This procedure can be used to find the internal distribution of magnetization for a finite length magnetic body immersed in an external magnetic field. **Appendix D** presents some examples of the current approximation and discusses its accuracy comparing against Finite Element Method.

Magnetization not only depends on geometry aspects of the magnetic body. There is also a well known non-linear behavior of magnetized bodies that should be addressed in the analysis of magnetization process. Next section presents the non-linear dependence of the magnetization in terms of the internal magnetic field.

4.2 Jiles-Atherton model

This section presents the main assumptions and considerations of the Jiles-Artherton model (J-A Model) for modeling the ferromagnetic hysteresis. This model was proposed initially in Ref. [20] and has been widely used in scientific community because of its simplicity and capabilities for fitting experimental results. J-A model uses the modified Langevin function for describing the internal effective field and its consequence in magnetization, and includes some corrections due to energy losses and hysteresis. Modified Langevin function of magnetization, M, considers the interaction of a system of magnetic moments under the action of a magnetizing magnetic field with the external field[24]. The equation that describes anhysteretic magnetization can be written by:

$$M_{\mathrm{an}} = M_s \left[\coth\left(\frac{H_{\mathrm{int}} + \alpha M_{\mathrm{an}}}{a} \right) - \frac{a}{H_{\mathrm{int}} + \alpha M_{\mathrm{an}}} \right] \tag{4.10}$$

where M_s is the saturation magnetization, H_{int} corresponds to the magnetizing field and a is a parameter that controls the slope of the magnetization before reaching saturation. This expression allows to describe the magnetization process in terms of the external magnetic field as a reversible process, i.e. during the magnetization domains earn potential energy from the external field, once the magnetic field stops, magnetic domains return to their initial state. Anhysteretic curve is achieved experimentally by applying a DC field H_{dc} superimposed by a decaying AC field H_{ac}. The oscillation of the magnetic field around a determined bias, H_{dc}, converges to a magnetization, $M(H_{dc})$, in the anhysteretic curve. It should be noticed that Eq.(4.10) for describing the anhysteretic modeling of the magnetization, configures a transcendental equation where the variable M is on both sides of the equation and can not be solved directly. A simple procedure to solve the anhysteretic equation consists into assign some values to a known variable X defined in a certain domain (e.g. $X \in [-10 \times 10^{-3}, 10 \times 10^{-3}]$), such as M can be calculated by direct evaluation. After M_{an} is found assuming values for X, magnetizing field H_{int} can be found by $H_{\mathrm{int}} = X - \alpha M_{\mathrm{an}}$. In order to validate this method, a comparison with reported experimental results was performed. Fig.4.1 presents the comparison of the anhysteretic curve modeled in Eq.(4.10) respect to experimental results presented in Ref. [25]. Parameters used for the calculation were $M_s = 1.6 \times 10^6$, $a = 1100$ and $\alpha = 1.6 \times 10^{-3}$. As it can be seen from the figure, the computed result follows the experimental data taken from [25].

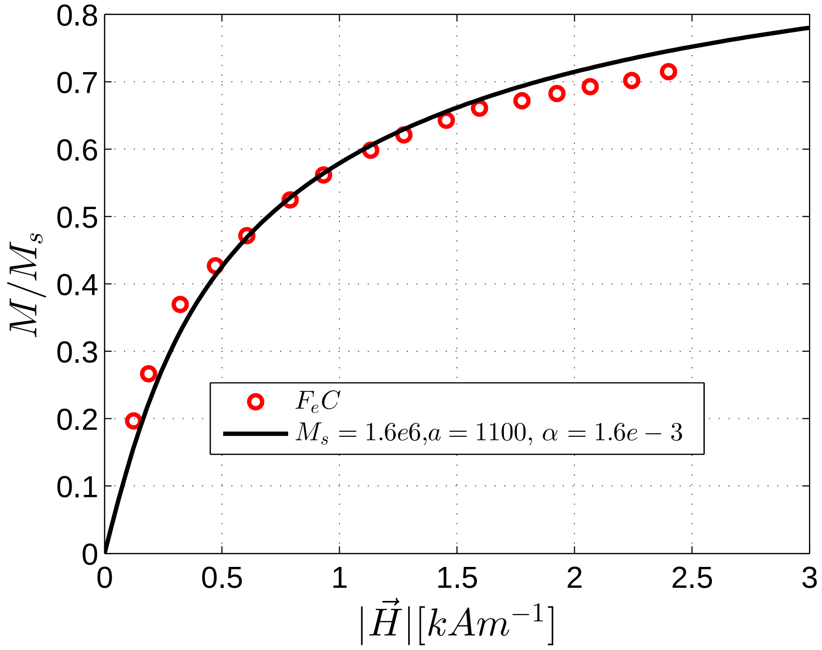

Figure 4.1: Magnetization in terms of the external magnetic field. circles: experimental, solid line: theoretical.Parameters used for the calculation were $M_s = 1.6 \times 10^6$, $a = 1100$ and $\alpha = 1.6 \times 10^{-3}$

4.2.1 Hysteresis in magnetization

Anhysteretic modeling presented in section before models reversible magnetization process. However, hysteretic behavior is observed in ferromagnetic materials when material is under different magnetic field loops, exhibiting different paths in magnetization [6]. When hysteretic curves want to be modeled, a frictional force should be considered in the work done by the external magnetic field. J-A model is one of the most widely used model to describe scalar (1D) ferromagnetic hysteresis, and it is based on the idea that magnetic domains alignment is impeded by the existence of an amount of energy density that pines the domain and restrict its formation [20]. Therefore, observed magnetization will differ from the anhysteretic one, due to the existence of this pinning energy when changing the direction of the magnetic field. The argument used in the J-A model establishes that this pinning energy is proportional to the volume stretched due to the wall motion during magnetization, thus a relation between the pinning energy density and magnetization can be established through the equation:

$$\frac{dE_{\text{loss}}}{dM} = k, \tag{4.11}$$

where k is a constant factor and E_{loss} is the energy due to this pinning. The proposed picture suggests that during magnetization (wall motion), there will be an amount of energy that is required to overcome the pinning energy. This amount of energy can be calculated by:

$$E_{\text{loss}} = \int dE_{\text{loss}} = \int k dM. \tag{4.12}$$

Since this energy losses is related to the opposition to the external magnetic field action, a factor δ is included to take into account the direction of the magnetic field, i.e. $\delta = +1$ if $dM/dH_{\text{int}} > 0$ and $\delta = -1$ if $dM/dH_{\text{int}} < 0$, this factor guarantees that energy due to pinning energy density will always act as a lossy force:

$$E_{\text{loss}} = \int \delta k dM. \tag{4.13}$$

Finally, total energy, E_t, associated to the magnetization process inside the material can be written by:

$$E_t = \int M dB_e = \int M_s \left[\coth\left(\frac{H + \alpha M}{a}\right) - \frac{a}{H + \alpha M}\right] dB_e, \tag{4.14}$$

where the effective induction field, B_e is given by $B_e = \mu_0 \left(H_{\text{int}} + \alpha M\right)$. Energy balance can be calculated over the total energy, such as it includes the losses due to the pinning energy and the magnetizing energy. Therefore, balance equation can be written by:

$$\int M dB_e + \int \delta k dM = \int M_s \left[\coth\left(\frac{H_{\text{int}} + \alpha M}{a}\right) - \frac{a}{H_{\text{int}} + \alpha M}\right] dB_e. \tag{4.15}$$

which can be written in terms of a differential equation by taking the derivative respect to dB_e:

$$\delta k \frac{dM}{dB_e} = M_s \left[\coth\left(\frac{B_e}{\mu_0 a}\right) - \frac{\mu_0 a}{B_e}\right] - M, \tag{4.16}$$

A more convenient expression is to write Eq.(4.16) as differential equation of the magnetizing field H_f instead of B_e. For accomplish this, we can proceed as follows:

$$M_{\text{an}} = M_s \left[\coth\left(\frac{B_e}{\mu_0 a}\right) - \frac{\mu_0 a}{B_e}\right] \tag{4.17}$$

$$\delta k \frac{dM}{dB_e} = M_{\text{an}} - M, \tag{4.18}$$

writing the derivative respect to H_{int}, we can write:

$$\frac{dM}{dB_e} = \frac{dM}{dH_{\text{int}}}\frac{dH_{\text{int}}}{dB_e}. \tag{4.19}$$

Since, $B_e = \mu_0 \left(H_{\text{int}} + \alpha M\right)$, we can find an expression for H_{int} and take the derivative respect to B_e. Finally, it can be obtained a differential equation in terms of the magnetizing field by:

$$\delta k \frac{dM}{dH_{\text{int}}}\left[\frac{1}{\mu_0} - \alpha\left(\frac{M_{\text{an}} - M}{\delta k}\right)\right] = M_{\text{an}} - M \tag{4.20}$$

Rearranging some terms, it can be obtained:

$$\frac{dM}{dH_{\text{int}}} = \frac{1}{\delta k/\mu_0 - \alpha\left(M_{\text{an}} - M\right)}\left(M_{\text{an}} - M\right). \tag{4.21}$$

There is an additional effect that can be included in the energy losses formulation. As it was suggested in Ref. [25], domain walls can simply bend instead of actually moving the domain boundaries. This interpretation allows the description of a reversible magnetization that recovers its previous magnitude when the magnetic field is removed. The main difference between this picture and the initially proposed, is that now magnetization can be changed without necessity of wall displacement and energy state can be restored after removing the external magnetic field. Under the assumption that wall bending corresponds to a circle curvature, reversible magnetization can be expressed in terms of the bending curvature (c) and the anhysteretic magnetization, M_{an}, by [25]:

$$M_{\text{rev}} = c\left(M_{\text{an}} - M\right), \tag{4.22}$$

where c is a constant that can be found experimentally from the susceptibilities in the anhysteretic magnetization curve[25]. As a consequence of including the possibility of wall domain bending as a reversible magnetization, total magnetization can be expressed as the sum of a irreversible component, described by the factor k, and a reversible component M_{rev}, such as:

$$M = M_{\text{irrev}} + M_{\text{rev}} \tag{4.23}$$

$$M = M_{\text{irrev}} + c\left(M_{\text{an}} - M\right) \tag{4.24}$$

$$M = \left(\frac{1}{1+c}\right) M_{\text{irrev}} + \left(\frac{c}{1+c}\right) M_{\text{an}} \tag{4.25}$$

Equation (4.25) is simply the sum between the solution of the irreversible magnetization given in Eq.(4.21) and the anhysteretic magnetization in Eq.(4.10). Therefore, differential equation for the total magnetization M in terms of the magnetizing field, will be given by:

$$\frac{dM}{dH_{\text{int}}} = \frac{1}{\delta k/\mu_0 - \alpha\left(M_{\text{an}} - M\right)}\left(M_{\text{an}} - M\right) + \left(\frac{c}{1+c}\right)\frac{dM_{\text{an}}}{dH_{\text{int}}}. \tag{4.26}$$

In order to validate the correct numerical implementation of this magnetization model, Figure 4.2(a) shows the comparison between experimental data and our computational calculations for an initial magnetization curve presented in Ref.[25]. As it can be seen from Fig. 4.2(a), the numerical implementation for the magnetization, including energy losses associated to reversible and irreversible process, reproduces the result of the experimental data presented in Ref.[25]. Figure 4.2(b) shows the prediction of magnetization for the initial magnetization curve and the ahysteretic curve. As it can be seen from Fig. 4.2(b), factor k can reproduce satisfactory the hysteretic curve.

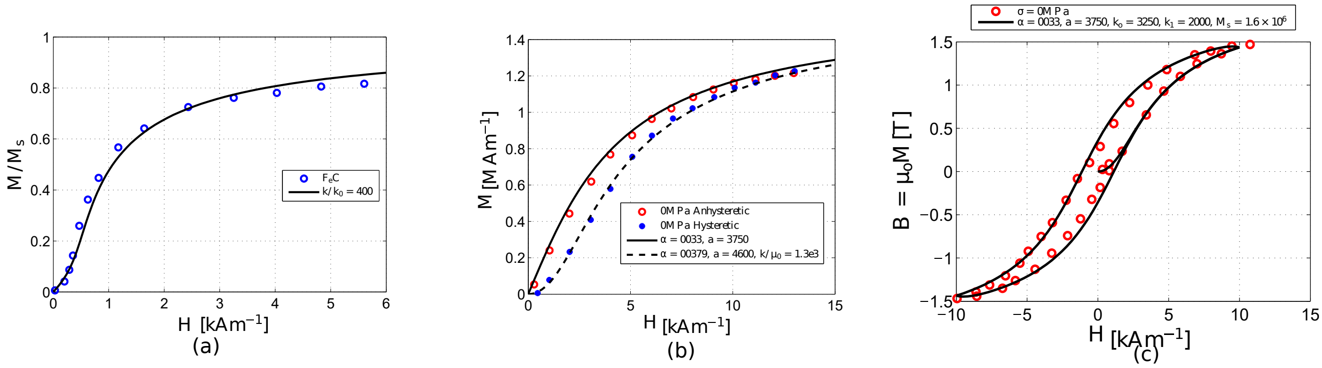

(a) (b) (c)

Figure 4.2: Magnetization curves (a) comparison between experimental data and theoretical initial magnetization presented in Ref.[25]. Used parameters were $M_s = 1.6 \times 10^6 [A/m]$, $k = 400$, $\alpha = 1.6 \times 10^{-3}$, $c = 0.2$. (b) Magnetization Curves for 0MPa Stress (circles: experimental data [24], solid line: anhysteretic curve, dashed line: hysteretic curve). (c) Hysteresis curve with no stress ($\sigma = 0MPa$), (circles: experimental data [24], solid line: theoretical). Parameters used: $\alpha = 0.033$, $a = 3750$A/m, $k_0 = 3250$, $k_1 = 2000$, $M_s = 1.6 \times 10^6$A/m, $H_{\max}$ =1500A/m.

An additional comparison took place considering a whole loop in the magnetic field leading to a hysteresis loops in the magnetization. In this case, lossy factor k can be defined as a field-dependent parameter $k(H)$. As it is discussed in [24], this functional dependence should be determined from the experimental data. Reproduced results used the following expression for this particular case:

$$k(H) = k_0 \left[1 + \frac{k_1}{k_0} \exp\left(-\frac{H_{\max}}{1500}\right)\right] \left\{1 - \left(\frac{M_{\max}}{M_s}\right)^2 \left[1 - \left(\frac{H}{H_{\max}}\right)^2\right]\right\}, \tag{4.27}$$

Fig. 4.2(c) shows the results obtained by the numerical computation implemented in this thesis and those results presented in [25]. As it can be seen from 4.2(c) there is an excellent agreement between them. It should be noticed that the implemented numerical calculations, reproduces correctly the initial magnetization curve, as well as the major hysteresis loop.

4.2.2 Effects of mechanical stress on magnetization

Experimental evidence have shown that magnetization curves can be affected by applying external stress upon the ferromagnetic material. This behavior is known as the magneto-mechanical effect and accounts for the changes in magnetization of a magnetic material due to the application of mechanical stresses. Inclusion of stress in magnetization can be done by an additional energy term due to the external mechanical action such as an equivalent magnetic field caused by the external stress can be included in the Langevin function argument [21]. This additional term comes from considering the energy associated to the strain and stress in the volume control,

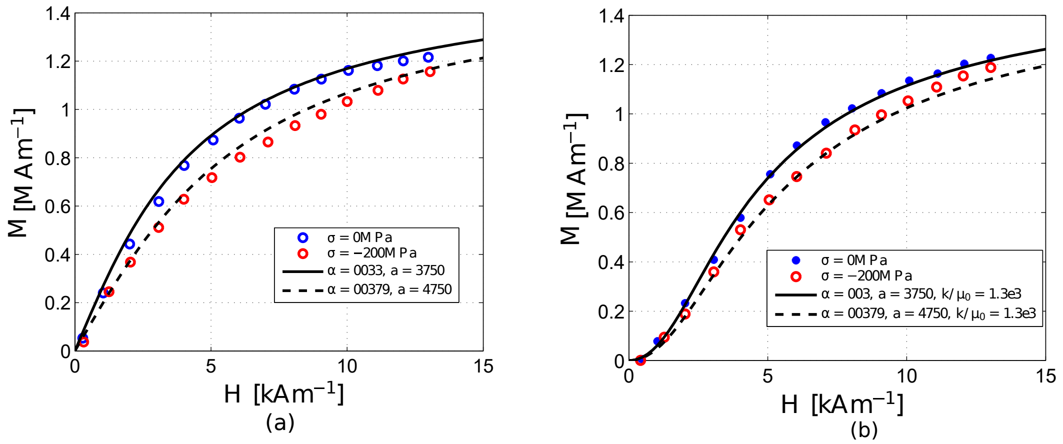

Figure 4.3: (a)Anhysteretic Magnetization Curve, (circles: experimental data [24], solid line: reproduced anhysteretic curve, dashed line: reproduced hysteretic curve). (b) Hysteretic Magnetization Curve, (circles: experimental data [24], solid line: anhysteretic curve, dashed line: hysteretic curve)

where the energy density per unit volume can be written by [21]:

$$E = \mu_0 HM + \frac{\mu_0}{2}\alpha M^2 + \frac{3}{2}\sigma\epsilon + TS, \tag{4.28}$$

being T the temperature, S the entropy, σ and ϵ the mechanical stress and strain respectively. Under the assumption of iso-entropic change, total change in energy can be associated to the action of an effective magnetizing field, H_{eff}, such as:

$$H_{\text{eff}} = \frac{1}{\mu_0}\frac{dE}{dM} \tag{4.29}$$

taking the corresponding derivative,

$$H_{\text{eff}} = H + \alpha M + \frac{3\sigma}{2\mu_0}\frac{d\epsilon}{dM}, \tag{4.30}$$

where ϵ is a function that depends on stress and magnetization given by:

$$\epsilon(\sigma, M) = \gamma_1(\sigma)M^2 + \gamma_2(\sigma)M^4 \tag{4.31}$$

$$\epsilon(\sigma, M) = (\gamma_{11} + \sigma\gamma_{12})M^2 + (\gamma_{21} + \sigma\gamma_{22})M^4 \tag{4.32}$$

$$\frac{d\epsilon(\sigma, M)}{dM} = 2(\gamma_{11} + \sigma\gamma_{12})M + 4(\gamma_{21} + \sigma\gamma_{22})M^3. \tag{4.33}$$

Through this additional term, modified Langevin function that accounts for the stress dependence in the anhysteretic magnetization can be written by:

$$M = M_s\left[\coth\left(\frac{H + \alpha M + \frac{3\sigma}{2\mu_0}\left(\frac{d\lambda}{dM}\right)}{a}\right) - \frac{a}{H + \alpha M + \frac{3\sigma}{2\mu_0}\left(\frac{d\lambda}{dM}\right)}\right] \tag{4.34}$$

Stress term can be numerically seen as an equivalent change in parameter a of the previous , and allowing a more accurate description of the anhysteretic curves under different stresses [24, 21]. Figure 4.3(a-b) has been obtained by using this additional term in the modified Langevin function. Fig.4.3(a) presents the anhysteretic magnetization curve for a specimen when it is at no stress condition and under compression stress. Inclusion of losses in the stress-dependent effective field can be done by using the same mathematical framework shown in sections before. Expression in Eq. (4.16) allows to find the magnetization magnitude taking into account the change on magnetization due to magnetic domain stretching described by a factor k (which has a physical interpretation in terms of losses as presented by Jiles and Artherton [20]), and effective induction field B_e should include the stress dependence term. Experimental data shown in Fig.4.3(b) were taken from [24]. Using the irreversible modeling, those experimental results were reproduced with a set of parameters k, α and a. In this particular case, a different set of parameters were used leaving α and k unchanged for both cases, but finding the best fit for a. Figures Fig.(4.4(a)) and Fig.(4.4(b)) present some parameters that are able to reproduce the experimental data of the anhysteretic behavior of the magnetization under different conditions of stress. Parameters used for describing the dependence of the magnetostriction coefficient $\epsilon(\sigma, M)$ were: $\gamma_{11} = 2 \times 10^{-18}$, $\gamma_{12} = 0.5 \times 10^{-26}$, $\gamma_{21} = 1 \times 10^{-30}$, $\gamma_{22} = -1 \times 10^{-39}$.

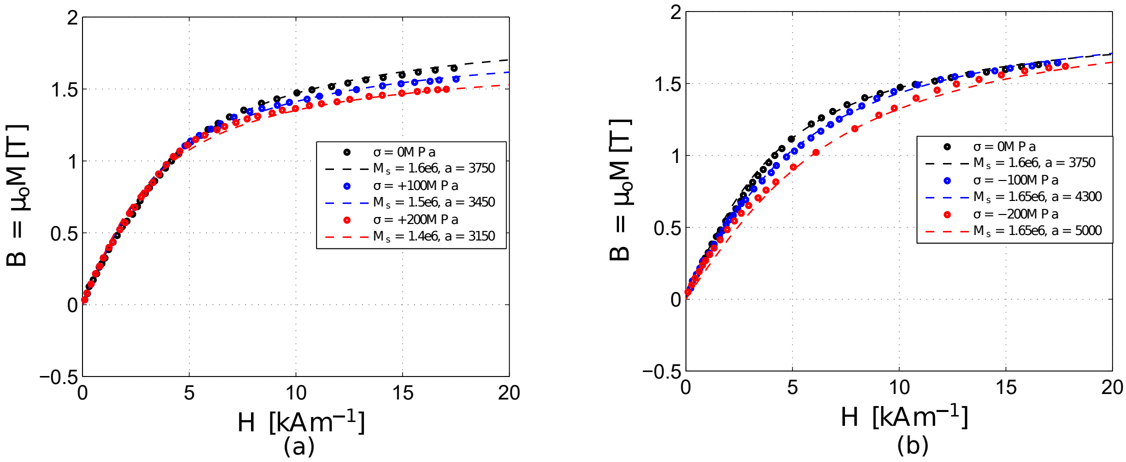

(a) (b)

Figure 4.4: (a) Anhysteretic Magnetization Curve, (circles: experimental data [24], dashed line: anhysteretic model with best fit parameters). (b) Anhysteretic Magnetization Curve, (circles: experimental data [24], dashed line: anhysteretic model with best fit parameters

4.2.2.1 Irreversible magnetization due to stress

As it was mentioned before, magnetization can be seen as the sum of two different effects: reversible and irreversible, where irreversible component will take into account the losses and reversible term is related to the flexibility of the magnetic wall domain [25, 21], based on this idea and the evident dependence of magnetization on stress, Jiles [21] proposed a stress-dependence rate of the irreversible magnetization based on a similar "law of approach" between the anisotropic and irreversible magnetization:

$$\frac{dM_{\text{irrev}}}{dW} = \frac{1}{\xi}\left(M_{\text{an}} - M_{\text{irrev}}\right), \tag{4.35}$$

where ξ is a constant coefficient and $W = \sigma^2/(2E)$ is the energy per unit volume supplied to the material due to the external stress σ with E the elasticity modulus.

$$M = M_{\text{irrev}} + M_{\text{rev}} \tag{4.36}$$

$$\frac{dM}{dW} = \frac{dM_{\text{irrev}}}{dW} + \frac{dM_{\text{rev}}}{dW} \tag{4.37}$$

$$\frac{dM}{dW} = \frac{1}{\xi}\left(M_{\text{an}} - M_{\text{irrev}}\right) + \frac{dM_{\text{rev}}}{dW} \tag{4.38}$$

taking into account the relationship proposed before for the reversible component

$$M_{\text{rev}} = c\left(M_{\text{an}} - M_{\text{irrev}}\right) \tag{4.39}$$

$$\frac{dM_{\text{rev}}}{dW} = c\left(\frac{dM_{\text{an}}}{dW} - \frac{dM_{\text{irrev}}}{dW}\right) \tag{4.40}$$

$$\frac{dM_{\text{rev}}}{dW} = c\frac{dM_{\text{an}}}{dW} - \frac{c}{\xi}\left(M_{\text{an}} - M_{\text{irrev}}\right), \tag{4.41}$$

total magnetization can be then written by:

$$\frac{dM}{dW} = \frac{1-c}{\xi}\left(M_{\text{an}} - M_{\text{irrev}}\right) + c\frac{dM_{\text{an}}}{dW}, \tag{4.42}$$

since $dW = (\sigma/E)\, d\sigma$, it can be written in terms of the stress as follows:

$$\frac{dM}{d\sigma} = \frac{\sigma\left(1-c\right)}{E\xi}\left(M_{\text{an}} - M_{\text{irrev}}\right) + c\frac{dM_{\text{an}}}{d\sigma}, \tag{4.43}$$

where irreversible magnetization is the solution to the following differential equation for the magnetic fields:

$$\frac{dM_{\text{irrev}}}{dH} = \frac{1}{\delta k/\mu_0 - \alpha\left(M_{\text{an}} - M_{\text{irrev}}\right)}\left(M_{\text{an}} - M_{\text{irrev}}\right) \tag{4.44}$$

$$M_{\text{an}} = M_s\left[\coth\left(\frac{H + \alpha M_{\text{an}} + \frac{3\sigma}{2\mu_0}\left(\frac{d\lambda}{dM}\right)}{a}\right) - \frac{a}{H + \alpha M_{\text{an}} + \frac{3\sigma}{2\mu_0}\left(\frac{d\lambda}{dM_{\text{an}}}\right)}\right] \tag{4.45}$$

4.2.2.2 Effects of stress on hysteresis loops

Major hysteresis loops exhibits also a dependence on stress. Reference [24] presents experimental results for steel samples under tension and compression stress and several magnetization loops. Figure 4.5(a) shows the magnetization loop for a tension stress test, when specimen is under $\sigma = +200$[MPa]. Fig. 4.5(b) presents same specimen but under compression ($\sigma = -200$[MPa]). Fig.4.5(c) summarizes both effects upon magnetization. As it can be seen in Fig.4.5(c), tension stress presents changes

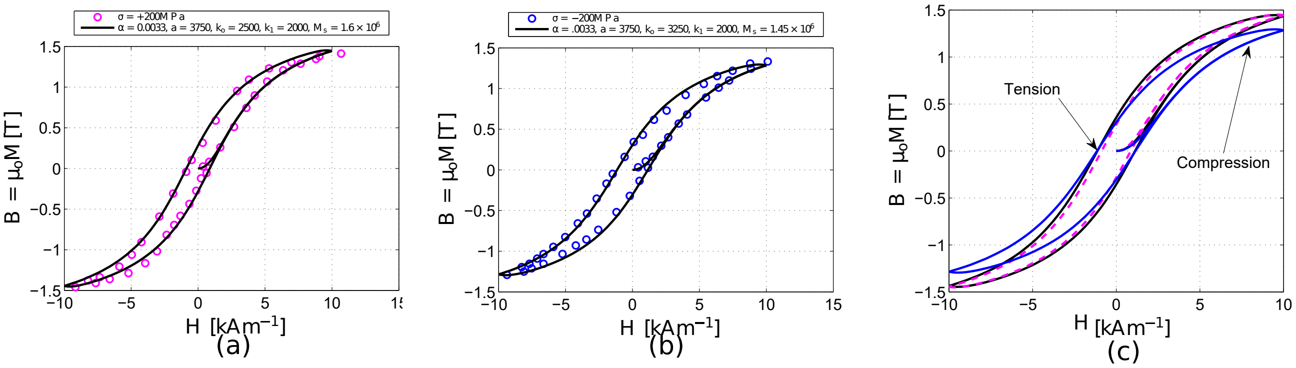

Figure 4.5: (a) Magnetization Curve Tension Stress ($\sigma = +200$[MPa]), (circles: experimental data [24], solid line: Theoretical). (b) Magnetization curve under compression stress ($\sigma = -200$[MPa]), (circles: experimental data [24], solid line: Theoretical). (c) Comparison between model predictions for different stress conditions showing the effects on the magnetization curve due to the stress nature.

in the loop area mostly when compared with the no stress case. On the other hand, compression effects presents a considerable reduction of the maximum magnetization reached at the same magnetic field leaving the loop area almost unchanged.

At this point main aspects of magnetization in finite length bodies have been addressed. Geometric and nonlinear effects have been discussed and experimental results were able to be reproduced and compared against exiting literature. Next section considers the magnetostriction effect described by the magnetization magnitude.

4.2.3 Magnetostriction

This section is based mainly in the description given in Ref. [22] and presents a simplified and basic perspective of magnetostriction of isotropic materials based on the modeling of domain alignments to certain direction of interest. Ferromagnetic materials exhibit a spontaneous strain for each domain due to the existence of spontaneous magnetization. Therefore, it is expected that the whole material body suffers a total deformation because of the individual deformations of the domains. With the aim of describing this issue, let's consider a set of domains (magnetic moments pointing in a certain direction in a defined volume) to have a given magnetization and maximum spontaneous strain e. Strain of the domain will vary from the direction of spontaneous magnetization M_s by the expression:

$$e(\theta) = e\cos^2\theta \tag{4.46}$$

Thus, strain of a certain domain could be maximum and some other will not present strain deformation.

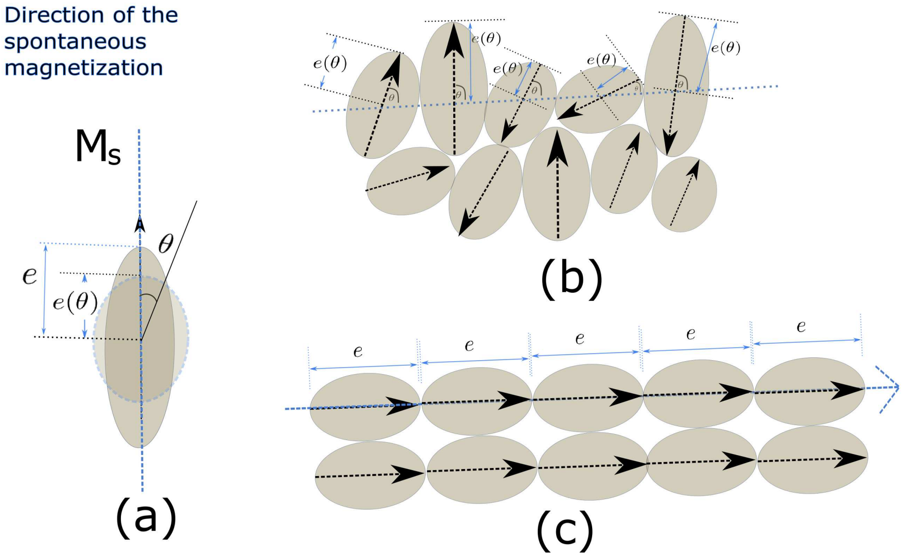

Figure 4.6: Description of the magnetostriction of an isotropic material. (a) direction of the spontaneous strain in a domain.(b) Several domains isotropically distributed. (c) Domains aligned to the external magnetic field direction.

Figure 4.6 (a) depicts this variation for one particular domain. Fig. 4.6 (b) shows a schematic of a set of randomly magnetized domains, i.e. magnetization direction does not depend on the crystallographic properties of the material and can be pointing to any direction, and its associated spontaneous strain can vary in magnitude given by ($e(\theta) = e\cos^2\theta$) where θ is also a random angle for each domain. An averaged deformation for several angles θ can be calculated by:

$$\epsilon_0 = \int_{-\pi/2}^{\pi/2} e\cos^2\theta \sin\theta d\theta \tag{4.47}$$

$$\epsilon_0 = \frac{e}{3} \tag{4.48}$$

This means that in average the whole body with randomly oriented spontaneous magnetizations as shown in Fig.4.6 (b) will be strained about $\epsilon_0 = e/3$. In Fig. 4.6 (c) we have assumed that all the domains have the same direction for their spontaneous magnetization and have the maximum allowed strain e. Considering that the body goes from a randomly distributed spontaneous magnetizations per domain to a determined magnetization direction for each of the domains with maximum strain e, we can calculate for the total strain in that direction, also called the saturation strain ϵ_s:

$$\epsilon_s = e - \epsilon_0 = \frac{2e}{3}. \tag{4.49}$$

Once we know in terms of the maximum strain per domain e, the saturation strain and the averaged strain for a randomly distributed domains, we can write an expression for an isotropic magnetic body regarding a certain direction. Let's assume we have an applied magnetic field H_{ext} pointing to a predefined direction that makes the magnetization to point along the same direction. Therefore, we can write an expression for the strain of each domain regarding the angle α of the domain with the external field. Therefore, we can simply write:

$$\epsilon(\alpha) = \frac{3}{2}\epsilon_s \left(\cos^2\alpha - \frac{1}{3}\right). \tag{4.50}$$

It should be noticed that we are still considering that the angle α between the field direction and the strain for each domain is assumed to be randomly distributed regarding the spontaneous magnetization vector M_s direction. In this description ϵ_s is considered as a constant and previously known value.

4.2.4 Magnetostriciton of Terfenol-D

Terfenol-D is a very well known material that possesses giant magnetostrictive properties. Monolithic Terfenol-D has been widely used in mechanical actuator applications because of its considerably large strain when it is under external magnetic fields.

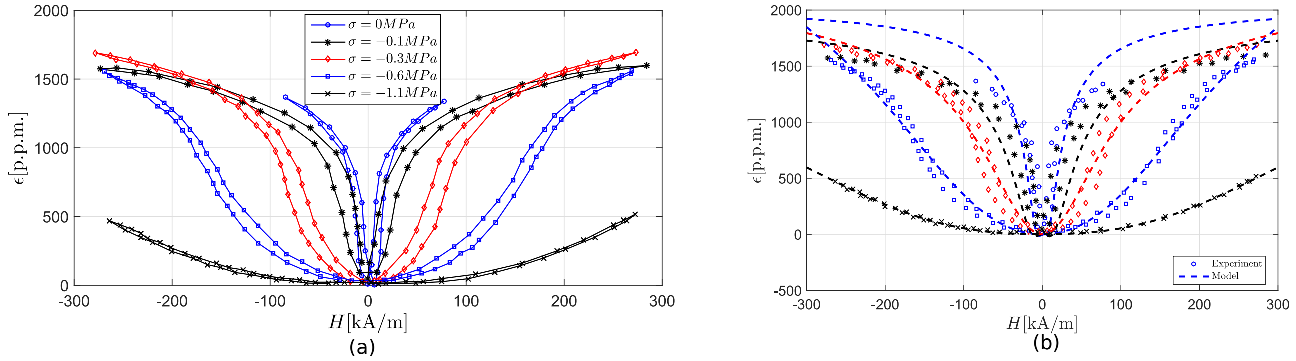

(a) (b)

Figure 4.7: (a) Strain ϵ for a monolithic Terfenol-D sample [10]. (b) Theoretical comparison with experimental results of magneto-strain λ for a monolithic Terfenol-D rod under different compression stresses (Dashed Lines: Theoretical, Dotted: Experiment [10]).

Monolithic Terfenol-D is normally manufactured in rod-shapes, being one of the most used geometries in industry and research applications. This section presents the validation of the previous models for reproducing experimental magnetostriction curves of Terfenol-D bars. Figure 4.7(a) presents some experimental results of compression tests performed upon monolithic Terfenol-D sample, which was exposed to a magnetic field directed along its axis. Mechanical strain of the bar was measured when compressed at different stresses magnitudes [10]. As it can be seen from the results, both the area of the hysteresis loop, as well as the shape/slope of the response, depend on the applied compression load. As it was discussed in the section before, an equivalent magnetic field caused by the external stress can be considered in the Langevin function argument such as the effective field that shapes the magnetization curve can be associated to an external stress magnitude. Therefore, magnetostriction ϵ[p.p.m] will be also a function that depends on stress, and it is expressed in general by the expression:

$$\epsilon(\sigma, M) = \gamma_1(\sigma)M^2 + \gamma_2(\sigma)M^4 \tag{4.51}$$

Although some functional dependence is required for the equivalent field in terms of stresses, it is more convenient to find its dependence in terms of parameter a_σ in a normalized Langevin function, such that the each stress condition can be fitted by using normalized experimental strain data:

$$\hat{\epsilon} = \left[\coth\left(\frac{H_{\text{ext}}}{a_\sigma}\right) - \frac{a_\sigma}{H_{\text{ext}}}\right]^2 + \hat{k}_n \left[\coth\left(\frac{H_{\text{ext}}}{a_\sigma}\right) - \frac{a_\sigma}{H_{\text{ext}}}\right]^4, \tag{4.52}$$

where $\hat{k}_n$ is also a fitting parameter to take into account high order terms of the magnetization. It is worth noting that through this method only H_{ext} is required during the fitting process and should not be confused with the effective field discussed in Ref.[21]. However, the effects of this latter are all included through the fitting parameter a_σ. Once a_σ is found for each particular case of stress that allows to obtain an expression for in terms of the stress, i.e. $a_\sigma(\sigma)$, the effective magnetic field due to stress can be written by:

$$\frac{H_{\text{ext}} + \alpha M + H_\sigma}{a_0} = \frac{H_{\text{ext}}}{a_\sigma(\sigma)} \tag{4.53}$$

where a_0 is the parameter that fits the curve when no stress is imposed to the magnetostrictive sample. By using this procedure and by means a non-linear fitting algorithm, functional form for a_σ in terms of the stress experimental data presented in Figure 4.7(a) can be obtained for each of the stress condition through a linear relation for the stress parameter $a_\sigma = \kappa\sigma + a_0$. Once the characteristics of the function that better fits the parameter a_σ is determined, coefficients of the magnetostriction curve can be found by fitting Eq.(4.51). Figure 4.8 presents the behavior of the fitting parameter for the normalized Langevin function when different compression stress

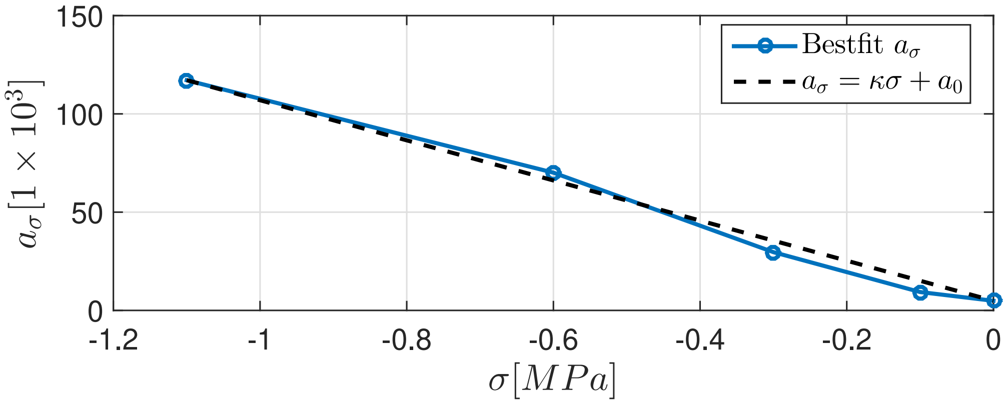

Figure 4.8: Bestfit for a_σ parameter. Linear fitting to describe the dependence of this parameter in terms of stress magnitude

magnitudes are considered. Afterwards, fitting function can be directly applied to Eq.(4.51) to obtain the magnetostriction magnitude. By using the models described and implemented above, and by using a fitting algorithm, functional form of magnetostriction can be reproduced in terms of the experimental stress data presented in Figure 4.7(a). Figure 4.7(b) presents the theoretical prediction contrasted to the experimental data. Typical magnetostriction coefficient associated to the second power of the magnetostriction curve can be found from the fitted coefficient $\gamma_1(\sigma)$ by the expression:

$$\epsilon_{s1}(\sigma) = \frac{M_s^2 \gamma_1(\sigma)}{1.5} \tag{4.54}$$

Figure 4.9 presents the behavior of the estimated magnetostriction coefficient associated to thw second power of the samples evaluated in Ref.[10]. As it can be seen from the figure, estimated magnetostriction coefficient presents a clear decrement when sample is under high magnitudes of compression. However, there is a region in the initial compression range where this effective magnetostriction coefficient increases respect to the no-stress condition. This effect can be understood from the idea that magnetostriction domains in compression are closer each other, thus when the external magnetic field forces the alignment in a determined direction there is a better transfer of mechanical strain between each domain. However, when the compression is high enough the magnetic domain is so mechanically restricted that internal energy is increased in magnetization instead of liberating strain. These results show that stress dependence of magnetostrictive materials could lead to important diminishing of the magnetostrictive effect and more complicated relationships are involved in their related physics that are certainly beyond the current thesis scope.

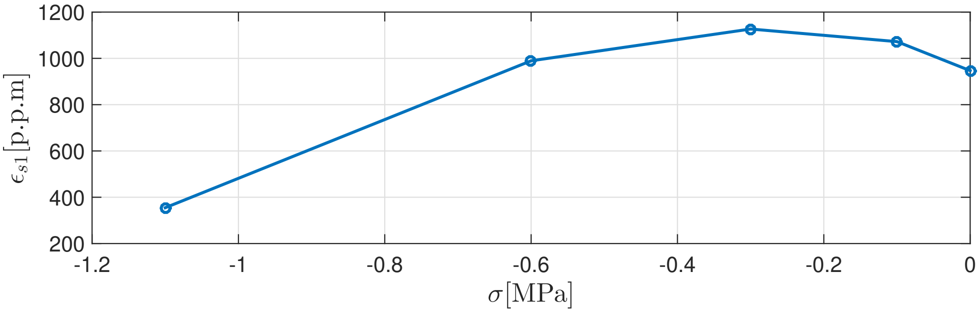

Figure 4.9: Estimation of the magnetostriction coefficient associated to the second power of magnetization for the sample presented in Ref.[10]

4.3 Concluding Remarks

As it was presented in this chapter, magnetization and magnetostrictive models that were implemented numerically by the author are able to reproduce experimental results presented in previous publications and experiments. Main characteristics of magnetization, such as anhysteretic behavior, hysteresis and mechanical stress-dependence, can be reproduced by the implemented models. As it was presented in the chapter, demagnetization field appears as a consequence of the finite lengths of the magnetic body. This field depends on the geometry and its able to change the spatial distribution of magnetic field inside the magnetic body, and consequently its magnetization. Based on this result, some magnetostrictive features of the magnetized body can be engineered to exhibit desired strains along specific regions of the body where the FBG (described in **chapter 3**) can be placed. As it is presented in this chapter, experimental magnetostrictive curves can be reproduced by the implemented models for magnetization and magnetostriction, which validates its usage in the coming sections.

Chapter 5

Magnetostrictive Composites

This section presents a proposal to model the magnetic behavior of a Terfenol-D composite. In the sections above the magnetic material has been considered as a continuous material. However, practical implementations of magnetostrictive composites use an epoxy matrix as a binder for the magnetic particles, where these latter can be selected in size and distribution inside the composite. This section proposes a numerical approach to analyze in a more realistic manner the behavior of magnetostrictive composites and shows some insights about the expected behavior of the magnetostriction based on the particle size and its distribution in the composite. Consider a continuous magnetic body as that shown in figure 5.1(a) and same geometric aspect body made of a magnetostrictive composite as shown in figure 5.1(b). Magnetostrictive composite is modeled by a set of finite number of discrete nonmagnetic cells with a magnetic cuboid inside that can partially or totally fill the cell volume. Magnetostrictive cuboid can be associated to a region of the space with volume ΔV_i defined by the prime coordinates, where the cuboid volume is determined in the intervals: $x'_1 \leq x'_i \leq x'_2$, $y'_1 \leq y'_i \leq y'_2$, $z'_1 \leq z'_i \leq z'_2$. Each cuboid can be assigned with a particular geometric apect ratio inside the nonmagnetic cell as those shown in figure 5.1(c), allowing the modeling of different magnetostrictive powder-particle sizes and orientations. Magnetostrictive material for each cell is determined by a magnetization vector ($\vec{M}_i(\vec{r'_i})$) located at the centroid of the cell, $\vec{r_i}'$. Magnetic vector potential at some observation point $\vec{r}$ due to the ith-cuboid can be calculated by:

$$\Delta\vec{A}_i(\vec{r}) = \frac{\mu_0}{4\pi}\frac{\vec{M}_i(\vec{r'_i}) \times \left(\vec{r} - \vec{r'_i}\right)}{|\vec{r} - \vec{r'_i}|^3}\Delta V_i \tag{5.1}$$

Taking into account that the region where holds the magnetization is very small compared to the microscopical distances that we are considering, we can write for the

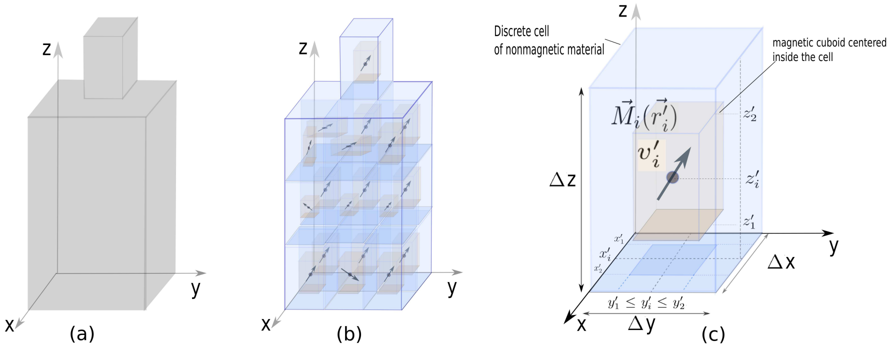

Figure 5.1: Engineered shape of Magnetostrictive device (a) Monolithic representation (b) Proposal of the magnetostrictive composite model (c) single cuboid in a discrete cell of non-magnetic material.

vector potential:

$$\vec{A}_i(\vec{r}) = \frac{\mu_0}{4\pi} \iiint_{v_i'} \frac{\vec{M}_i(\vec{r_i'}) \times \left(\vec{r} - \vec{r_i'}\right)}{|\vec{r} - \vec{r_i'}|^3} dv_i' \tag{5.2}$$

since the vector potential will depend on the volumetric distributions of the magnetization, we should define a particle geometry for dealing with this vector potential.

5.1 Cuboid small magnetic bodies

This subsection will define the magnetic vector potential for a small (still macroscopic) magnetic particle when its shape is considered as a cuboid with a constant magnetization vector $\vec{M}_i(\vec{r_i'}) = m_{xi}\hat{i}_x + m_{yi}\hat{i}_y + m_{zi}\hat{i}_z$. Applying the expression for the vector potential we can write for each component:

$$\vec{A}_{xi}(\vec{r}) = \frac{\mu_0}{4\pi} \iiint_{\Delta v_i'} \frac{m_{yi}\,(z - z') - m_{zi}\,(y - y')}{[(x - x')^2 + (y - y')^2 + (z - z')^2]^{(3/2)}} dx'dy'dz' \tag{5.3}$$

$$\vec{A}_{yi}(\vec{r}) = \frac{\mu_0}{4\pi} \iiint_{\Delta v_i'} \frac{m_{zi}\,(x - x') - m_{xi}\,(z - z')}{[(x - x')^2 + (y - y')^2 + (z - z')^2]^{(3/2)}} dx'dy'dz' \tag{5.4}$$

$$\vec{A}_{zi}(\vec{r}) = \frac{\mu_0}{4\pi} \iiint_{\Delta v_i'} \frac{m_{xi}\,(y - y') - m_{yi}\,(x - x')}{[(x - x')^2 + (y - y')^2 + (z - z')^2]^{(3/2)}} dx'dy'dz' \tag{5.5}$$

Based on these equations, we should find a solution for the integrals:

$$F_x(x, y, z) = \iiint_{\Delta v_i'} \frac{(x - x')}{[(x - x')^2 + (y - y')^2 + (z - z')^2]^{(3/2)}} dx'dy'dz' \tag{5.6}$$

$$F_y(x, y, z) = \iiint_{\Delta v_i'} \frac{(y - y')}{[(x - x')^2 + (y - y')^2 + (z - z')^2]^{(3/2)}} dx'dy'dz' \tag{5.7}$$

$$F_z(x, y, z) = \iiint_{\Delta v_i'} \frac{(z - z')}{[(x - x')^2 + (y - y')^2 + (z - z')^2]^{(3/2)}} dx'dy'dz' \tag{5.8}$$

Since the functional form of the integral is the same one for each variable we can find a solution for one of those, and extend the result to the rest of the variables. In order to accomplish this aim, let's first consider the integral:

$$F_1(a,z) = \int_{\Delta z'} \frac{(z-z')}{[a^2+(z-z')^2]^{(3/2)}} dz' \tag{5.9}$$

let be $u = (z-z')$, then $du = -dz'$, we can write:

$$F(a,u) = -\int_{\Delta u} \frac{u}{[a^2+u^2]^{\frac{3}{2}}} du \tag{5.10}$$

this integral can be solved analytically by:

$$F(a,u) = -\left(-\frac{1}{\sqrt{a^2+u^2}} \bigg|_{\Delta u} \right) \tag{5.11}$$

going back to the z' variable:

$$F(a,z') = \frac{1}{\sqrt{a^2+(z-z')^2}} \bigg|_{\Delta z'} \tag{5.12}$$

now we can write the triple integral respect to z' as:

$$F(x,y,z) = \int_{\Delta x'} \int_{\Delta y'} \left[\int_{\Delta z'} \frac{(z-z')}{[(x-x')^2+(y-y')^2+(z-z')^2]^{(3/2)}} dz' \right] dy'dx' \tag{5.13}$$

using the result for the integral obtained before we can write:

$$F(x,y,z) = \int_{\Delta x'} \int_{\Delta y'} \left[\frac{1}{\sqrt{(x-x')^2+(y-y')^2+(z-z')^2}} \bigg|_{\Delta z'} \right] dy'dx' \tag{5.14}$$

in order to solve this integral respect to y' we should find a solution for the integral:

$$F_2(y,a) = \int_{\Delta y'} \frac{1}{[(y-y')^2+a^2]^{\frac{1}{2}}} dy' \tag{5.15}$$

let be $u = y - y'$, then $du = -dy'$, then we can write:

$$F_2(u,a) = -\int_{\Delta u} \frac{1}{[u^2+a^2]^{\frac{1}{2}}} du' \tag{5.16}$$

we can solve this integral analytically by:

$$F_2(u,a) = -\ln\left[u+\sqrt{u^2+a^2}\right] \bigg|_{\Delta u} \tag{5.17}$$

retrieving back to the y' variable:

$$F_2(y',a) = -\ln\left[(y-y') + \sqrt{(y-y')^2 + a^2}\right]\Bigg|_{\Delta y'} \tag{5.18}$$

writing the integral again:

$$F(x,y,z) = \int_{\Delta x'}\left[\int_{\Delta y'}\left(\frac{1}{\sqrt{(x-x')^2+(y-y')^2+(z-z')^2}}\Bigg|_{\Delta z'}\right)dy'\right]dx' \tag{5.19}$$

using the result found for y'

$$F(x,y,z) = \int_{\Delta x'}\left[-\ln\left[(y-y') + \sqrt{(x-x')^2+(y-y')^2+(z-z')^2}\right]\Bigg|_{\Delta z'}\Bigg|_{\Delta y'}\right]dx' \tag{5.20}$$

for solving the last integral respect to x' we should find a solution for the integral:

$$F_3(x,a) = \int_{\Delta x'}\ln\left[a + \sqrt{(x-x')^2 + a^2 + b^2}\right]dx' \tag{5.21}$$

let be $u = (x-x')$, then $du = -dx'$. Therefore, we can write:

$$F_3(u,a) = -\int_{\Delta u'}\ln\left[a + \sqrt{u^2+a^2+b^2}\right]du \tag{5.22}$$

This integral can be solved analytically by:

$$\begin{aligned} F_3(u,a) = -\Bigg[& u\ln\left[\sqrt{u^2+a^2+b^2}+a\right] + a\ln\left[\sqrt{u^2+a^2+b^2}+u\right] \\ & -b\arctan\left(\frac{au}{b\sqrt{u^2+a^2+b^2}}\right) + b\arctan\left(\frac{u}{b}\right) - u\Bigg]\Bigg|_{\Delta u} \end{aligned} \tag{5.23}$$

going back to the x' variable:

$$\begin{aligned} F_3(x,a) = -\Bigg[& (x-x')\ln\left[\sqrt{(x-x')^2+a^2+b^2}+a\right] + \\ & a\ln\left[\sqrt{(x-x')^2+a^2+b^2}+(x-x')\right] \\ -b\arctan & \left(\frac{a(x-x')}{b\sqrt{(x-x')^2+a^2+b^2}}\right) + b\arctan\left(\frac{(x-x')}{b}\right) - (x-x')\Bigg]\Bigg|_{\Delta x'} \end{aligned} \tag{5.24}$$

writing the desired integral again:

$$F(x,y,z) = \int_{\Delta x'}\left[-\ln\left[(y-y') + \sqrt{(x-x')^2+(y-y')^2+(z-z')^2}\right]\Bigg|_{\Delta z'}\Bigg|_{\Delta y'}\right]dx' \tag{5.25}$$

replacing the integral for the corresponding result found for x' we have:

$$
\begin{aligned}
F(x,y,z) = \Bigg[&(x-x')\ln\left[\sqrt{(x-x')^2+(y-y')^2+(z-z')^2}+(y-y')\right]+\\
&(y-y')\ln\left[\sqrt{(x-x')^2+(y-y')^2+(z-z')^2}+(x-x')\right]\\
&-(z-z')\arctan\left(\frac{(y-y')(x-x')}{(z-z')\sqrt{(x-x')^2+(y-y')^2+(z-z')^2}}\right)+\\
&(z-z')\arctan\left(\frac{(x-x')}{(z-z')}\right)-(x-x')\Bigg]\Bigg|_{\Delta z'}\Bigg|_{\Delta y'}\Bigg|_{\Delta x'}
\end{aligned}
\tag{5.26}
$$

This solution can be extended to the other variables. For doing this, let's define:

$$
F_\Gamma(\Gamma,\gamma,\eta) = \iiint_{\Delta v_i'} \frac{\Gamma}{[\eta^2+\gamma^2+\Gamma^2]^{(3/2)}}dv' \tag{5.27}
$$

based on the results obtained before, we can write for the integral:

$$
\begin{aligned}
F_\Gamma(\Gamma,\gamma,\eta) = \Bigg[&\eta\ln\left[\sqrt{\eta^2+\gamma^2+\Gamma^2}+\gamma\right]+\\
&\gamma\ln\left[\sqrt{\eta^2+\gamma^2+\Gamma^2}+\eta\right]\\
&-\Gamma\arctan\left(\frac{\gamma\eta}{\Gamma\sqrt{\eta^2+\gamma^2+\Gamma^2}}\right)+\\
&\Gamma\arctan\left(\frac{\eta}{\Gamma}\right)-\eta\Bigg]\Bigg|_{\Delta v'}
\end{aligned}
\tag{5.28}
$$

Finally, the evaluation of the function at the cuboid will give us the value of the integral by:

$$
\begin{aligned}
F_\Gamma(\Gamma,\gamma,\eta)\Big|_{\Delta v'} &= [F_\Gamma(\Gamma_2,\gamma_2,\eta_2)-F_\Gamma(\Gamma_1,\gamma_2,\eta_2)]-[F_\Gamma(\Gamma_2,\gamma_1,\eta_2)-F_\Gamma(\Gamma_1,\gamma_1,\eta_2)]\\
&-[F_\Gamma(\Gamma_2,\gamma_2,\eta_1)-F_\Gamma(\Gamma_1,\gamma_2,\eta_1)]+[F_\Gamma(\Gamma_2,\gamma_1,\eta_1)-F_\Gamma(\Gamma_1,\gamma_1,\eta_1)],
\end{aligned}
\tag{5.29}
$$

where the arguments for the function $F_\Gamma(\Gamma,\gamma,\eta)$

$$
\Gamma_i = \begin{cases} (x-x_i') & i=1,2\\ (y-y_i') & i=1,2\\ (z-z_i') & i=1,2, \end{cases} \tag{5.30}
$$

for γ

$$
\gamma_i = \begin{cases} (y-y_i') & i=1,2\\ (z-z_i') & i=1,2\\ (x-x_i') & i=1,2 \end{cases} \tag{5.31}
$$

for η

$$\eta_i = \begin{cases} (z - z'_i) & i = 1, 2 \\ (x - x'_i) & i = 1, 2 \\ (y - y'_i) & i = 1, 2 \end{cases} \tag{5.32}$$

where the cuboid is defined in the region: $x'_1 \leq x' \leq x'_2$, $y'_1 \leq y' \leq y'_2$, $z'_1 \leq z' \leq z'_2$.

In the case of several magnetized bodies we can calculate the total vector potential, associated to the demagnetization field, by summing up all the contributions of the existing N magnetic bodies:

$$\vec{A}_{\text{dmg}}(\vec{r}) = \frac{\mu_0}{4\pi} \sum_i^N \iiint_{v'_i} \frac{\vec{M}_i(\vec{r'_i}) \times \left(\vec{r} - \vec{r'_i}\right)}{|\vec{r} - \vec{r'_i}|^3} dv'_i \tag{5.33}$$

where the integration for each magnetic body can be done by using the analytical solution found before. Once the vector potential is known, the magnetic flux density of the demagnetization field $\vec{B}_{\text{dmg}}(\vec{r})$ can be calculated taking the curl of the vector magnetic potential $\vec{B}_{\text{dmg}}(\vec{r}) = \nabla \times \vec{A}_{\text{dmg}}(\vec{r})$.

5.2 Determination of the induced magnetization

Magnetostrictive particles are magnetized by the application of an external field. this magnetization process depends on geometrical and mechanical factors, thus its distribution inside the whole composite is not known a priori. Therefore, we should calculate the magnetization $\vec{M}$ that will be induced by that external magnetic field and the current energy state of the magnetic body. If we assume that the induced magnetization $\vec{M}$ to be found can be written in terms of the magnetic field by:

$$\vec{M} = \left[\chi_m(|\vec{H}|, \sigma)\right] \vec{H} \tag{5.34}$$

where χ_m is the magnetic susceptibility. This quantity is typically considered as a function of the magnetic field only. However, as it was widely discussed in chapter 4, magnetic susceptibility can be considered in general as a function of several physical quantities, in particular the magnitude of the magnetic field intensity ($|\vec{H}|$) and the mechanical stress (σ). By using this fact, we could eventually include the external effects of the stress upon the magnetization. Considering the same discretization for the magnetization in small magnetic bodies, we will have for the magnetization:

$$\vec{M}_i = \left[\chi_m(|\vec{H}_i|, \sigma_i)\right] \vec{H}_i \tag{5.35}$$

Magnetic field intensity in this case can be decomposed by the sum of an external known field $\vec{H}_{\text{ext}}$ and the field due to the induced magnetization $\vec{H}_{\text{dmg}}$:

$$\vec{H} = \vec{H}_{\text{ext}} + \vec{H}_{\text{dmg}} \tag{5.36}$$

we have shown that the demagnetization field can be found if $\vec{M}(\vec{r})$ is known everywhere in the body by using the vector potential by:

$$\vec{A}_{\text{dmg}}(\vec{r}) = \frac{\mu_0}{4\pi} \sum_{j}^{N} \iiint_{v'_j} \frac{\vec{M}_j(\vec{r'_j}) \times \left(\vec{r} - \vec{r'_j}\right)}{|\vec{r} - \vec{r'_j}|^3} dv'_j \tag{5.37}$$

$$\vec{B}_{\text{dmg}}(\vec{r}) = \nabla \times \vec{A}_{\text{dmg}}(\vec{r}) \tag{5.38}$$

the magnetic flux density $\vec{B}_{\text{dmg}}(\vec{r})$ found by the application of the curl operation upon the vector potential should satisfy:

$$\vec{B}_{\text{dmg}}(\vec{r}) = \mu_0 \left(\vec{H}_{\text{dmg}}(\vec{r}) + \vec{M}(\vec{r})\right) \tag{5.39}$$

$$\vec{H}_{\text{dmg}}(\vec{r}) = \frac{\vec{B}_{\text{dmg}}(\vec{r})}{\mu_0} - \vec{M}(\vec{r}) \tag{5.40}$$

writing the demagnetization field explicitly in one of the cells that contains magnetic body:

$$\vec{H}_{\text{dmg}}(\vec{r_i}) = \frac{1}{4\pi} \nabla \times \left(\sum_{j}^{N} \iiint_{v'_j} \frac{\vec{M}_j(\vec{r'_j}) \times \left(\vec{r_i} - \vec{r'_j}\right)}{|\vec{r_i} - \vec{r'_j}|^3} dv'_i \right) - \vec{M}_i(\vec{r_i}) \tag{5.41}$$

where magnetization magnitude for each body $\vec{M}_j(\vec{r'_j})$ is still unknown. Taking into account that for each magnetic body it should be satisfied:

$$\vec{H}(\vec{r_i}) = \vec{H}_{\text{ext}}(\vec{r_i}) + \vec{H}_{\text{dmg}}(\vec{r_i}) \tag{5.42}$$

and considering also that magnetization can be related with the magnetic field intensity by:

$$\vec{M}_i(\vec{r_i}) = \left[\chi_m(|\vec{H}_i(\vec{r_i})|, \sigma(\vec{r_i}))\right] \vec{H}_i(\vec{r_i}) \tag{5.43}$$

where $|\vec{H}_i(\vec{r_i})|$ and $\sigma(\vec{r_i})$ are the magnetic field intensity and stress tensor at the magnetic body located at $\vec{r_i}$, we can write the equation for the magnetic field intensity as:

$$\frac{\vec{M}_i(\vec{r_i})}{\left[\chi_m(|\vec{H}_i(\vec{r_i})|, \sigma(\vec{r_i}))\right]} = \vec{H}_{\text{ext}}(\vec{r_i}) + \vec{H}_{\text{dmg}}(\vec{r_i}) \tag{5.44}$$

For linear materials and no mechanical stress conditions, we can simplify to:

$$\frac{\vec{M}_i(\vec{r_i})}{\chi_m} = \vec{H}_{\text{ext}}(\vec{r_i}) + \vec{H}_{\text{dmg}}(\vec{r_i}) \tag{5.45}$$

Therefore, magnetization $\vec{M}_i(\vec{r_i})$ will be the vector that satisfy the equation:

$$\frac{\vec{M}_i(\vec{r_i})}{\chi_m} - \vec{H}_{\text{dmg}}(\vec{r_i}) = \vec{H}_{\text{ext}}(\vec{r_i}) \tag{5.46}$$

that can be written explicitly in terms of the magnetization vector by:

$$\frac{\vec{M}_i(\vec{r_i})}{\chi_m} - \left[\frac{1}{4\pi}\nabla\times\left(\sum_{j}^{N}\iiint_{v'_j}\frac{\vec{M}_j(\vec{r'_j})\times\left(\vec{r_i}-\vec{r'_j}\right)}{|\vec{r_i}-\vec{r'_j}|^3}dv'_j\right) - \vec{M}_i(\vec{r_i})\right] = \vec{H}_{\text{ext}}(\vec{r_i}) \tag{5.47}$$

Rearranging some terms we have:

$$\vec{M}_i(\vec{r_i})\left(\frac{1+\chi_m}{\chi_m}\right) - \left[\frac{1}{4\pi}\nabla\times\left(\sum_{j}^{N}\iiint_{v'_j}\frac{\vec{M}_j(\vec{r'_j})\times\left(\vec{r_i}-\vec{r'_j}\right)}{|\vec{r_i}-\vec{r'_j}|^3}dv'_j\right)\right] = \vec{H}_{\text{ext}}(\vec{r_i}) \tag{5.48}$$

Using the function found before for the calculation of the triple integral $F_\Gamma(\Gamma,\gamma,\eta)$, we can write for the triple integral over one cuboid:

$$\vec{G}_j(\vec{M}_j,\vec{r_i}) = \iiint_{v'_j}\frac{\vec{M}_j(\vec{r'_j})\times\left(\vec{r_i}-\vec{r'_j}\right)}{|\vec{r_i}-\vec{r'_j}|^3}dv'_j \tag{5.49}$$

$$G_{xj}(m_{xj},m_{yj},m_{zj},\vec{r_i}) = m_{yj}F_{\Gamma_Z}(\Gamma,\gamma,\eta) - m_{zj}F_{\Gamma_Y}(\Gamma,\gamma,\eta) \tag{5.50}$$

$$G_{yj}(m_{xj},m_{yj},m_{zj},\vec{r_i}) = m_{zj}F_{\Gamma_X}(\Gamma,\gamma,\eta) - m_{xj}F_{\Gamma_Z}(\Gamma,\gamma,\eta) \tag{5.51}$$

$$G_{zj}(m_{xj},m_{yj},m_{zj},\vec{r_i}) = m_{xj}F_{\Gamma_Y}(\Gamma,\gamma,\eta) - m_{yj}F_{\Gamma_X}(\Gamma,\gamma,\eta) \tag{5.52}$$

Defining a new vector $\vec{R}_j(\vec{M}_j,\vec{r_i})$ by taking the curl over the resulting vector $\vec{R}_j(\vec{M}_j,\vec{r_i}) = \nabla\times\vec{G}_j(\vec{M}_j,\vec{r_i})$

$$R_{xj}(m_{xj},m_{yj},m_{zj},\vec{r_i}) = \partial_y G_{zj} - \partial_z G_{yj} \tag{5.53}$$

$$R_{yj}(m_{xj},m_{yj},m_{zj},\vec{r_i}) = \partial_z G_{xj} - \partial_x G_{zj} \tag{5.54}$$

$$R_{zj}(m_{xj},m_{yj},m_{zj},\vec{r_i}) = \partial_x G_{yj} - \partial_y G_{xj} \tag{5.55}$$

we can re-write the expressions above to have:

$$m_{xi}\left(\frac{1+\chi_m}{\chi_m}\right)-\frac{1}{4\pi}\sum_j^N R_{xj}=H_{x_{\text{ext}}}(\vec{r_i}) \tag{5.56}$$

$$m_{yi}\left(\frac{1+\chi_m}{\chi_m}\right)-\frac{1}{4\pi}\sum_j^N R_{yj}=H_{y_{\text{ext}}}(\vec{r_i}) \tag{5.57}$$

$$m_{zi}\left(\frac{1+\chi_m}{\chi_m}\right)-\frac{1}{4\pi}\sum_j^N R_{zj}=H_{z_{\text{ext}}}(\vec{r_i}) \tag{5.58}$$

partial derivatives ∂_x, ∂_y and ∂_z will act over the corresponding functions $F_\Gamma(\Gamma,\gamma,\eta)$ and the magnetization magnitudes can be taken out of the operation. Therefore, we can write:

$$\left(\frac{1+\chi_m}{\chi_m}\right)m_{xi}-\frac{1}{4\pi}\sum_j^N\left(\partial_y G_{zj}-\partial_z G_{yj}\right)=H_{x_{\text{ext}}}(\vec{r_i}) \tag{5.59}$$

$$\left(\frac{1+\chi_m}{\chi_m}\right)m_{yi}-\frac{1}{4\pi}\sum_j^N\left(\partial_z G_{xj}-\partial_x G_{zj}\right)=H_{y_{\text{ext}}}(\vec{r_i}) \tag{5.60}$$

$$\left(\frac{1+\chi_m}{\chi_m}\right)m_{zi}-\frac{1}{4\pi}\sum_j^N\left(\partial_x G_{yj}-\partial_y G_{xj}\right)=H_{z_{\text{ext}}}(\vec{r_i}) \tag{5.61}$$

replacing for the explicit dependences on the magnetization components.
Let's consider first for the x-component of the magnetization:

$$\begin{split}\left(\frac{1+\chi_m}{\chi_m}\right)m_{xi}-\frac{1}{4\pi}\sum_j^N\Big(&\partial_y\left(m_{xj}F_{\Gamma_Y}-m_{yj}F_{\Gamma_X}\right)\\ &-\partial_z\left(m_{zj}F_{\Gamma_X}-m_{xj}F_{\Gamma_Z}\right)\Big)=H_{x_{\text{ext}}}(\vec{r_i})\end{split} \tag{5.62}$$

gathering similar terms we can write:

$$\begin{split}\sum_j^N\Bigg(\left[\frac{4\pi(1+\chi_m)}{\chi_m}\delta_{ij}-\left(\partial_y F_{\Gamma_Y}+\partial_z F_{\Gamma_Z}\right)\right]m_{xj}+\left(\partial_y F_{\Gamma_X}\right)m_{yj}&\\ +\left(\partial_z F_{\Gamma_X}\right)m_{zj}\Bigg)&=4\pi H_{x_{\text{ext}}}(\vec{r_i})\end{split} \tag{5.63}$$

Now, let's consider for the y-component of the magnetization:

$$\left(\frac{1+\chi_m}{\chi_m}\right)m_{yi}-\frac{1}{4\pi}\sum_j^N\left(\partial_z G_{xj}-\partial_x G_{zj}\right)=H_{y_{\text{ext}}}(\vec{r_i}) \tag{5.64}$$

replacing the corresponding functions:

$$\begin{aligned}\left(\frac{1+\chi_m}{\chi_m}\right) m_{yi} - \frac{1}{4\pi}\sum_{j}^{N}\Big(&\partial_z\left(m_{yj}F_{\Gamma_Z} - m_{zj}F_{\Gamma_Y}\right)\\ &-\partial_x\left(m_{xj}F_{\Gamma_Y} - m_{yj}F_{\Gamma_X}\right)\Big) = H_{y_{\text{ext}}}(\vec{r_i})\end{aligned} \tag{5.65}$$

As we did before, let's gather similar terms:

$$\begin{aligned}\sum_{j}^{N}\Bigg(m_{xj}\partial_x F_{\Gamma_Y} + \left[\frac{4\pi(1+\chi_m)}{\chi_m}\delta_{ij} - \left(\partial_z F_{\Gamma_Z} + \partial_x F_{\Gamma_X}\right)\right] m_{yj}&\\ +m_{zj}\partial_z F_{\Gamma_Y}\Bigg) = 4\pi H_{y_{\text{ext}}}(\vec{r_i})&\end{aligned} \tag{5.66}$$

Now, let's consider for the z-component of the magnetization:

$$\left(\frac{1+\chi_m}{\chi_m}\right) m_{zi} - \frac{1}{4\pi}\sum_{j}^{N}\left(\partial_x G_{yj} - \partial_y G_{xj}\right) = H_{z_{\text{ext}}}(\vec{r_i}) \tag{5.67}$$

replacing by the corresponding functions:

$$\begin{aligned}\left(\frac{1+\chi_m}{\chi_m}\right) m_{zi} - \frac{1}{4\pi}\sum_{j}^{N}\Big(&\partial_x\left(m_{zj}F_{\Gamma_X} - m_{xj}F_{\Gamma_Z}\right)\\ &-\partial_y\left(m_{yj}F_{\Gamma_Z} - m_{zj}F_{\Gamma_Y}\right)\Big) = H_{z_{\text{ext}}}(\vec{r_i})\end{aligned} \tag{5.68}$$

Gathering similar terms and simplifying the expression following the same procedure done before over x and y components:

$$\begin{aligned}&\sum_{j}^{N}\Bigg(m_{xj}\partial_x F_{\Gamma_Z} + m_{yj}\partial_y F_{\Gamma_Z}\\ \left[\frac{4\pi(1+\chi_m)}{\chi_m}\delta_{ij} - \left(\partial_x F_{\Gamma_X} + \partial_y F_{\Gamma_Y}\right)\right] m_{zj}&\Bigg) = 4\pi H_{z_{\text{ext}}}(\vec{r_i})\end{aligned} \tag{5.69}$$

Retrieving the results obtained for each component:

$$\begin{aligned}\sum_{j}^{N}\Bigg(\left[\frac{4\pi(1+\chi_m)}{\chi_m}\delta_{ij}-\left(\partial_y F_{\Gamma_Y}+\partial_z F_{\Gamma_Z}\right)\right]m_{xj}+\left(\partial_y F_{\Gamma_X}\right)m_{yj}\\ +\left(\partial_z F_{\Gamma_X}\right)m_{zj}\Bigg)=4\pi H_{x_{\text{ext}}}(\vec{r_i})\end{aligned}\tag{5.70}$$

$$\begin{aligned}\sum_{j}^{N}\Bigg(\left(\partial_x F_{\Gamma_Y}\right)m_{xj}+\left[\frac{4\pi(1+\chi_m)}{\chi_m}\delta_{ij}-\left(\partial_z F_{\Gamma_Z}+\partial_x F_{\Gamma_X}\right)\right]m_{yj}\\ +\left(\partial_z F_{\Gamma_Y}\right)m_{zj}\Bigg)=4\pi H_{y_{\text{ext}}}(\vec{r_i})\end{aligned}\tag{5.71}$$

$$\begin{aligned}\sum_{j}^{N}\Bigg(\left(\partial_x F_{\Gamma_Z}\right)m_{xj}+\left(\partial_y F_{\Gamma_Z}\right)m_{yj}\\ \left[\frac{4\pi(1+\chi_m)}{\chi_m}\delta_{ij}-\left(\partial_x F_{\Gamma_X}+\partial_y F_{\Gamma_Y}\right)\right]m_{zj}\Bigg)=4\pi H_{z_{\text{ext}}}(\vec{r_i})\end{aligned}\tag{5.72}$$

Finally, performing the sum over the elements, we can obtain a matrix system for each of the components. As an example for x-component the matrix is given by:

$$\begin{bmatrix} L^x_{11} & L^y_{11} & L^z_{11} & L^x_{12} & L^y_{12} & L^z_{12} & .. & .. & L^x_{1N} & L^y_{1N} & L^z_{1N} \\ L^x_{21} & L^y_{21} & L^z_{21} & L^x_{22} & L^y_{22} & L^z_{22} & .. & .. & L^x_{2N} & L^y_{2N} & L^z_{2N} \\ L^x_{31} & L^y_{31} & L^z_{31} & L^x_{32} & L^y_{32} & L^z_{32} & .. & .. & L^x_{3N} & L^y_{3N} & L^z_{3N} \\ L^x_{41} & L^y_{41} & L^z_{41} & L^x_{42} & L^y_{42} & L^z_{42} & .. & .. & L^x_{4N} & L^y_{4N} & L^z_{4N} \\ \vdots & \vdots & \vdots & \vdots & \vdots & \vdots & .. & .. & \vdots & \vdots & \vdots \\ L^x_{N1} & L^y_{N1} & L^z_{N1} & L^x_{N2} & L^y_{N2} & L^z_{N2} & .. & .. & L^x_{NN} & L^y_{NN} & L^z_{NN} \end{bmatrix}\begin{bmatrix} m_{x1} \\ m_{y1} \\ m_{z1} \\ m_{x2} \\ m_{y2} \\ m_{z2} \\ . \\ . \\ . \\ m_{xN} \\ m_{yN} \\ m_{zN} \end{bmatrix}=4\pi\begin{bmatrix} H_{x1} \\ H_{x2} \\ H_{x3} \\ H_{x4} \\ . \\ . \\ . \\ H_{xN} \end{bmatrix}\tag{5.73}$$

where L^x_{ij}, L^y_{ij}, L^z_{ij} are the respective terms associated to the derivatives for each component.

5.2.1 Single Cube Case: $M_z = M_0$,$M_x = 0$,$M_y = 0$

This section will consider the case when the magnetization is imposed along a particular axis. In this case, we will consider the same scenario used in section 4.1 where the magnetization is assumed to have a constant value pointing along the external field. Since for this case there is only one component of the magnetization, the linear system for the magnetization components can be solved easily. In order to show how the formulation above calculates the demagnetization field and the magnetization itself along the cube axis, let's consider a single cuboid in the formulation presented before. In this case, we will consider that this single cube will have dimensions: L=2 × 2 × 2[cm^3], magnetic susceptibility $\chi_m = 9$, and is exposed to an uniform external field of $\vec{H}_{\text{ext}} = H_0\hat{i}_z$ with $H_0 = 1[A/m]$. Since in this particular case we are imposing transversal magnetization components to be zero, we can simplify the expression above to have:

$$\sum_{j}^{N=1}\Big((\partial_z F_{\Gamma_X})\, m_{zj}\Big) = 4\pi H_{x_{\text{ext}}}(\vec{r_i}) \tag{5.74}$$

$$\sum_{j}^{N=1}\Big((\partial_z F_{\Gamma_Y})\, m_{zj}\Big) = 4\pi H_{y_{\text{ext}}}(\vec{r_i}) \tag{5.75}$$

$$\sum_{j}^{N=1}\left(\left[\frac{4\pi(1+\chi_m)}{\chi_m}\delta_{ij} - (\partial_x F_{\Gamma_X} + \partial_y F_{\Gamma_Y})\right] m_{zj}\right) = 4\pi H_{z_{\text{ext}}}(\vec{r_i}) \tag{5.76}$$

For this case, first two equations lead to trivial solution, which means that $\partial_z F_{\Gamma_X} = 0$,$\partial_z F_{\Gamma_Y} = 0$. Since there is only one cube we should write:

$$\left[\frac{4\pi(1+\chi_m)}{\chi_m} - (\partial_x F_{\Gamma_X} + \partial_y F_{\Gamma_Y})\right] m_z = 4\pi H_0 \tag{5.77}$$

where magnetization m_z can be found everywhere in the magnetic body by simply evaluating the expression at any desired point:

$$m_z = \frac{4\pi H_0}{\left[\frac{4\pi(1+\chi_m)}{\chi_m} - (\partial_x F_{\Gamma_X} + \partial_y F_{\Gamma_Y})\right]} \tag{5.78}$$

Magnetic field along the axis can be calculated by: $\vec{H}_{z\text{int}} = \chi_m m_z \hat{i}_z$, then:

$$H_{z\text{int}} = \frac{4\pi\chi_m H_0}{\left[\frac{4\pi(1+\chi_m)}{\chi_m} - (\partial_x F_{\Gamma_X} + \partial_y F_{\Gamma_Y})\right]} \tag{5.79}$$

Finally, the demagnetization field can be calculated by $\vec{H}_{\text{dmg}} = \vec{H}_{z\text{int}} - H_0\hat{i}_z$. Figure 5.2 presents the comparison between the approach considered by the formulation above and the result obtained by using a COMSOL.

It should be noticed that the main difference between both results is due to the neglected transversal magnetization components, which are considered in the FEM simulation.

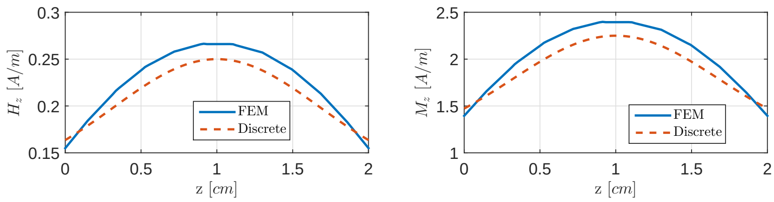

Figure 5.2: Comparison of the internal magnetic field and the magnetization for a single cube of side $L = 2[\mathrm{cm}]$ between the proposed discrete formulation and FEM.

5.2.2 Discretized cube case: $M_z = M_0$,$M_x = 0$,$M_y = 0$

In order to check the prediction performance when several cubes are considered to shape the magnetic body by using only the magnetization component that points in the same direction of the magnetic field, let's consider same single magnetic permeable cube, with relative permeability $\mu_r = 10$, side length of 2 $[cm]$, exposed to an external field give by $\vec{H}_{\text{ext}} = H_0\hat{i}_z$, with $H_0 = 1[A/m]$. In this case, we keep considering that magnetization is pointing in the same direction as the external field, but in this case we will have several cubes that will form the magnetic body under analysis. Figure 5.3 presents the idea behind discretization of the magnetic body into small magnetic cuboids.

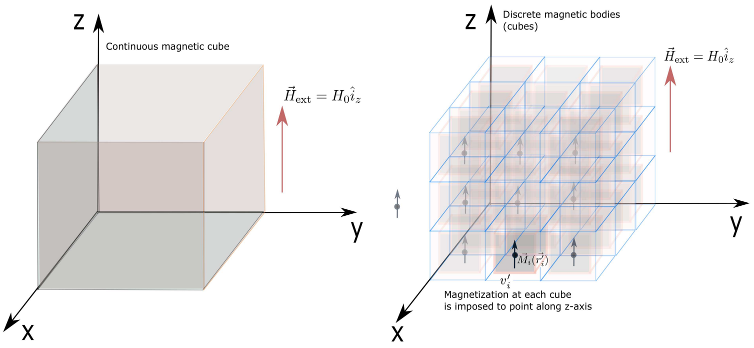

Figure 5.3: Ferromagnetic cube under the action of an external magnetic field, total magnetic body in a composite is modeled by several magnetic cubes.

Based on this fact we can write for the i-th magnetic cube:

$$\sum_{j}^{N=1} \left(\left(\partial_z F_{\Gamma_X} \right) m_{zj} \right) = 4\pi H_{x_{\text{ext}}}(\vec{r_i}) \tag{5.80}$$

$$\sum_{j}^{N=1} \left(\left(\partial_z F_{\Gamma_Y} \right) m_{zj} \right) = 4\pi H_{y_{\text{ext}}}(\vec{r_i}) \tag{5.81}$$

$$\sum_{j}^{N=1} \left(\left[\frac{4\pi(1+\chi_m)}{\chi_m}\delta_{ij} - \left(\partial_x F_{\Gamma_X} + \partial_y F_{\Gamma_Y} \right) \right] m_{zj} \right) = 4\pi H_{z_{\text{ext}}}(\vec{r_i}) \tag{5.82}$$

It is also worth noting that the external field is assumed to be uniform in the whole magnetic body. Therefore, magnetization magnitude for each cube can be calculated by solving the linear system above.

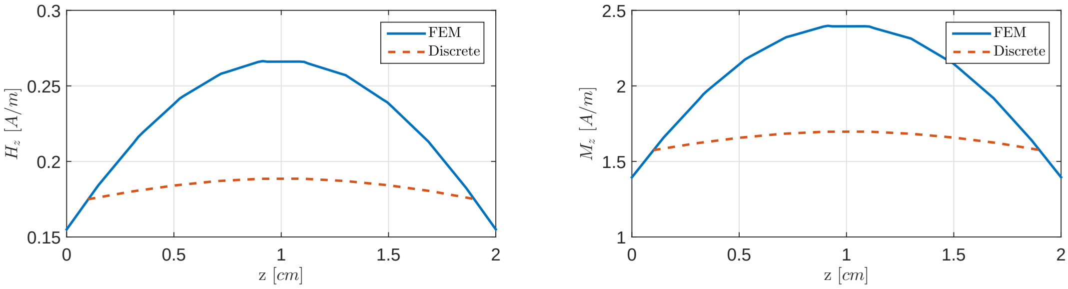

Figure 5.4: Ferromagnetic cube of dimensions $2 \times 2 \times 2[\mathrm{cm}^3]$ modeled by the composition of 1000 small cubes with magnetization along z-axis under the action of an external magnetic field.

As a result for this approximation the assumption of a constant magnetization component along z-axis results in an underestimation of the internal field and the magnetization. This result shows that by assuming only one component of the magnetization, the demagnetization field for each of the cube or cuboids is not completely taken into account. The accuracy on the demagnetization field calculation is very important in the estimation of the total energy associated to the magnetization of the magnetic grain. This also will determine the magnetostriction effect along certain direction of interest because it will affect the current elongation of a particle given its orientation when magnetic anisotropy is included.

5.2.3 Discretized cube case: full vectorial magnetization

This subsection will consider the three components for the magnetization to be calculated when the set of cubes are under the action of an uniform external magnetic field. In this case, the linear system to be solved is defined by the full set of equations

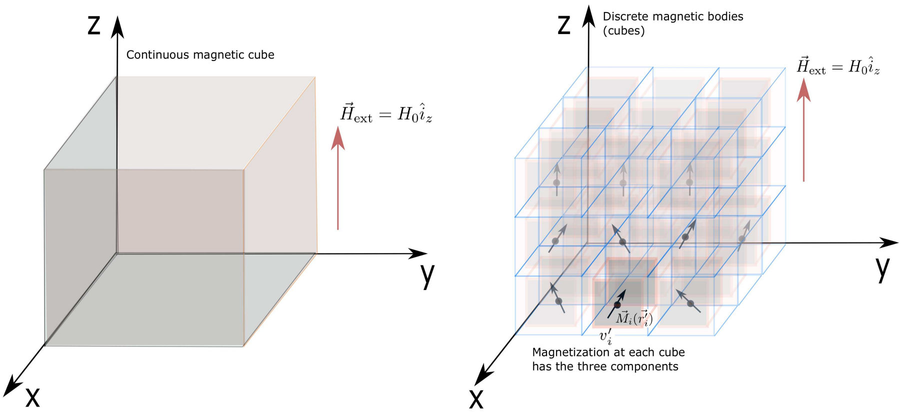

Figure 5.5: Ferromagnetic cube under the action of an external magnetic field, total magnetic body in the composite is modeled by several magnetic cubes with full vectorial magnetization.

derived before:

$$\sum_j^N \left(\left[\frac{4\pi(1+\chi_m)}{\chi_m}\delta_{ij} - \left(\partial_y F_{\Gamma_Y} + \partial_z F_{\Gamma_Z}\right) \right] m_{xj} + \left(\partial_y F_{\Gamma_X}\right) m_{yj} \right.$$
$$\left. + \left(\partial_z F_{\Gamma_X}\right) m_{zj} \right) = 4\pi H_{x\text{ext}}(\vec{r_i}) \tag{5.83}$$

$$\sum_j^N \left(\left(\partial_x F_{\Gamma_Y}\right) m_{xj} + \left[\frac{4\pi(1+\chi_m)}{\chi_m}\delta_{ij} - \left(\partial_z F_{\Gamma_Z} + \partial_x F_{\Gamma_X}\right) \right] m_{yj} \right.$$
$$\left. + \left(\partial_z F_{\Gamma_Y}\right) m_{zj} \right) = 4\pi H_{y\text{ext}}(\vec{r_i}) \tag{5.84}$$

$$\sum_j^N \left(\left(\partial_x F_{\Gamma_Z}\right) m_{xj} + \left(\partial_y F_{\Gamma_Z}\right) m_{yj} \right.$$
$$\left. \left[\frac{4\pi(1+\chi_m)}{\chi_m}\delta_{ij} - \left(\partial_x F_{\Gamma_X} + \partial_y F_{\Gamma_Y}\right) \right] m_{zj} \right) = 4\pi H_{z\text{ext}}(\vec{r_i}) \tag{5.85}$$

where magnetization components for each cube should be found that solves the linear system. In contrast to typical approximations of one component of magnetization, a more accurate estimation of the demagnetization factor for each grain can be performed by the set of the equations above. Figure 5.6 presents the comparison for the axial magnetic field and magnetization when the total cube is discretized by using 125 small cubes. In order to show the convergence of the proposed scheme when more cubes are considered, same scenario is run with 1000 small cubes to conform the whole cube under analysis. Results for this latter case are presented in Figure 5.7.

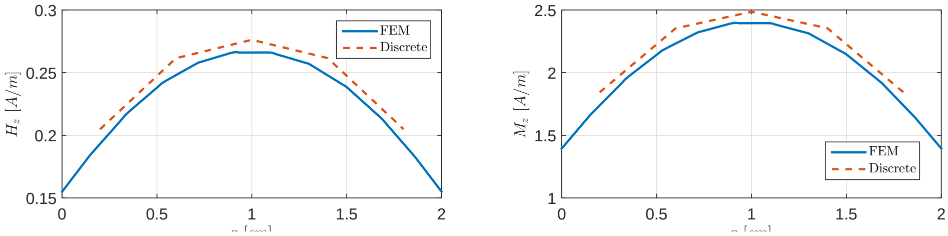

Figure 5.6: Ferromagnetic cube of dimensions $2 \times 2 \times 2[\text{cm}^3]$ modeled by the composition of 125 small cubes with full vectorial magnetization under the action of an external magnetic field.

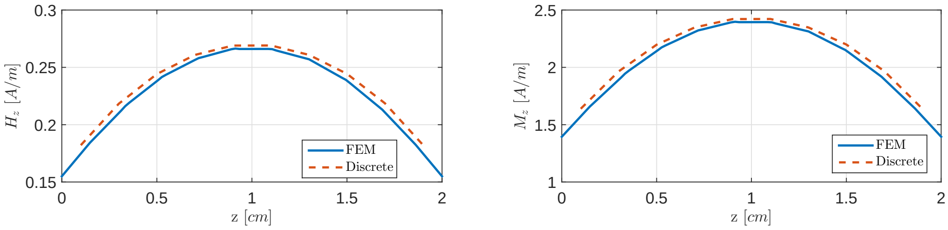

Figure 5.7: Ferromagnetic cube of dimensions $2 \times 2 \times 2[\text{cm}^3]$ modeled by the composition of 1000 small cubes with full vectorial magnetization under the action of an external magnetic field.

5.2.4 Inclusion of non-linear magnetization

Once the magnetic field flux density is calculated in the domain of interest, we can implement an iterative method for finding the actual magnetization state [39, 7]. This method refreshes the magnetization state $\vec{M}^{k+1}$ based on a previous estimation of the magnetization $\vec{M}^k$ and the non-linear interaction with the external magnetic field. To illustrate the iterative method, suppose a guessed initial state of magnetization $\vec{M}^k_{\text{dmg}}(\vec{r})$ for each magnetic body in the analysis, this magnetization allows to calculated the demagnetization field $\vec{H}^k_{\text{dmg}}(\vec{r})$ by a certain type of function that will depend on the geometry and number of cuboids in the simulation. Therefore, we can write:

$$\vec{H}^k_{\text{dmg}}(\vec{r}) = f(\vec{M}^k_{\text{dmg}}(\vec{r})) \tag{5.86}$$

we have for the total magnetic field inside the domain:

$$\vec{H}^k_{\text{T}} = \vec{H}_{\text{ext}} + \vec{H}^k_{\text{dmg}} \tag{5.87}$$

Let's suppose we have an non-linear dependence between the magnetization and the magnetizing field determined by constitutive relation $\chi(\vec{H}^k_{\text{T}})$, such as:

$$\vec{M}^{k+1}_c = \left[\chi(\vec{H}^k_{\text{T}})\right] \vec{H}^k_{\text{T}} \tag{5.88}$$

Finally, an updating equation to the magnetization state $\vec{M}^k$ can be written by:

$$\vec{M}^{k+1} = \vec{M}^k + \beta\left(\vec{M}_c^{k+1} - \vec{M}^k\right) \tag{5.89}$$

Once the new state for the magnetization is found, the iteration process begins again with the calculation of the associated demagnetization field $\vec{H}_{\text{dmg}}^{k+1}$ to the new state of magnetization $\vec{M}^{k+1}$. In our proposed approach we can guess the initial magnetization $\vec{M}_i^k(\vec{r_i})$ for all the cuboids that conform the body shape, this can be achieved by solving the linear system described in section above where the magnetization at the i-th cuboid should satisfy:

$$\frac{\vec{M}_i^k(\vec{r_i})}{\chi_m} - \left[\frac{1}{4\pi}\nabla\times\left(\sum_j^N \iiint_{v_j'} \frac{\vec{M}_j^k(\vec{r_j'})\times\left(\vec{r_i}-\vec{r_j'}\right)}{|\vec{r_i}-\vec{r_j'}|^3}dv_j'\right) - \vec{M}_i^k(\vec{r_i})\right] = \vec{H}_{\text{ext}}(\vec{r_i}) \tag{5.90}$$

Once $\vec{M}_i^k(\vec{r_i})$ is known for each cuboid, we can calculate the associated demagnetization vector by:

$$\vec{H}_{\text{dmg}}^k(\vec{r_i}) = \frac{1}{4\pi}\nabla\times\left(\sum_j^N \iiint_{v_j'} \frac{\vec{M}_j^k(\vec{r_j'})\times\left(\vec{r_i}-\vec{r_j'}\right)}{|\vec{r_i}-\vec{r_j'}|^3}dv_j'\right) - \vec{M}_i^k(\vec{r_i}) \tag{5.91}$$

It is worth noting that the demagnetization field can be calculated if the magnetization is given for all of the cuboids in the simulation. Then, total internal field at the center of the cuboid can be calculated by:

$$\vec{H}_{\text{T}}^k(\vec{r_i}) = \vec{H}_{\text{ext}}(\vec{r_i}) + \vec{H}_{\text{dmg}}^k(\vec{r_i}) \tag{5.92}$$

At this point we can calculate the non-linear magnetization based on the current magnetizing field $\vec{H}_{\text{T}}^k(\vec{r_i})$

$$\vec{M}_c^{k+1}(\vec{r_i}) = f(\vec{H}_{\text{T}}^k(\vec{r_i})) \tag{5.93}$$

One of the functions that can be used at this point is the Langevin function for the anhysteretic curve of magnetization, such as we can calculate for each component of the magnetization:

$$M_{x_c}^{k+1}(\vec{r_i}) = M_s\left(\coth\left[\frac{H_{x_{\text{T}}}^k(\vec{r_i})}{a_o}\right] - \frac{a_o}{H_{x_{\text{T}}}^k(\vec{r_i})}\right) \tag{5.94}$$

$$M_{y_c}^{k+1}(\vec{r_i}) = M_s\left(\coth\left[\frac{H_{y_{\text{T}}}^k(\vec{r_i})}{a_o}\right] - \frac{a_o}{H_{y_{\text{T}}}^k(\vec{r_i})}\right) \tag{5.95}$$

$$M_{z_c}^{k+1}(\vec{r_i}) = M_s\left(\coth\left[\frac{H_{z_{\text{T}}}^k(\vec{r_i})}{a_o}\right] - \frac{a_o}{H_{z_{\text{T}}}^k(\vec{r_i})}\right) \tag{5.96}$$

Where M_s is the saturation magnetization and a_o is a parameter that controls the curve shape. Finally, an updating equation to the magnetization state for the i-th cuboid, $\vec{M}^{k+1}(\vec{r}_i)$, can be written by:

$$\vec{M}^{k+1}(\vec{r}_i) = \vec{M}^{k}(\vec{r}_i) + \beta\left(\vec{M}_c^{k+1}(\vec{r}_i) - \vec{M}^{k}(\vec{r}_i)\right) \tag{5.97}$$

A relative error between magnetizations iterations can be defined, such as the global convergence of the iterative process can be monitored. This error was defined in our case by the expression:

$$\text{error} = \frac{1}{N}\sqrt{\sum_j^N \left(M_{x_j}^{k+1} - M_{x_j}^{k}\right)^2 + \sum_j^N \left(M_{y_j}^{k+1} - M_{y_j}^{k}\right)^2 + \sum_j^N \left(M_{z_j}^{k+1} - M_{z_j}^{k}\right)^2} \tag{5.98}$$

By using this definition of error we can stop the iterative process at certain minimum error and control the convergence to that minimum of the whole algorithm.

5.2.5 Inclusion of the Jiles-Artherton hysteresis model in the analysis of magnetostrictive composites

Based on the proposed method for the analysis of magnetostrictive composites by using a set of discrete cuboids that shape the geometry of the composite body, we were able to include the non-linear an-hysteretic behavior of the magnetization by using the well known Jiles-Artherton model [20, 25]. This section discusses the inclusion of hysteresis to the current model by considering the same two arguments about reversible and irreversible magnetization. Total work done by the magnetic field on a per-unit volume element can be calculated by:

$$E_t = \int \vec{H} \cdot d\vec{B}, \tag{5.99}$$

where $\vec{B} = \mu_0(\vec{H} + \vec{M})$, where we can write for the total energy done by the external magnetic field:

$$E_t = \frac{1}{\mu_0}\int \vec{B} \cdot d\vec{B} - \int \vec{M} \cdot d\vec{B}, \tag{5.100}$$

where $\int \vec{M} \cdot d\vec{B}$ is the work done over the magnetized body. In our case, total magnetizing field in the i-th cuboid is given by:

$$\vec{H}(\vec{r}_i) = \vec{H}_{\text{ext}}(\vec{r}_i) + \vec{H}_{\text{dmg}}(\vec{r}_i), \tag{5.101}$$

It is worth noting that $\vec{H}_{\text{dmg}}(\vec{r}_i)$ is a function of the magnetization and also depends on the geometry of the current i-th cuboid and the rest of the cuboids in the simulation. This field is given explicitly by:

$$\vec{H}^k_{\text{dmg}}(\vec{r}_i) = \frac{1}{4\pi}\nabla \times \left(\sum_j^N \iiint_{v'_j} \frac{\vec{M}^k_j(\vec{r}'_j) \times \left(\vec{r}_i - \vec{r}'_j\right)}{|\vec{r}_i - \vec{r}'_j|^3} dv'_j \right) - \vec{M}^k_i(\vec{r}_i) \tag{5.102}$$

Jiles-Atherton method proposes to simplify the interaction between dipoles by a simple factor of the magnetization such as the magnetizing field can be written by:

$$\vec{H}(\vec{r}_i) = \vec{H}_{\text{ext}}(\vec{r}_i) + \alpha_i \vec{M}(\vec{r}_i), \tag{5.103}$$

where α_i takes into account the demagnetization field that is dependent on the magnetization. In our formulation this factor can be calculated for each component of the demagnetization field and the corresponding magnetization component by:

$$\alpha_{x_i} = \frac{H_{x\text{dmg}}(\vec{r}_i)}{M_x(\vec{r}_i)} \tag{5.104}$$

If there is no hysteresis, magnetization can be written as a function of this effective field at the i-th cuboid:

$$M_{\text{anhy}}(\vec{r}_i) = M_s \left(\coth\left[\frac{H_{\text{ext}}(\vec{r}_i) + H_{\text{dmg}}(\vec{r}_i)}{a_o} \right] - \frac{a_o}{H_{\text{ext}}(\vec{r}_i) + H_{\text{dmg}}(\vec{r}_i)} \right) \tag{5.105}$$

Or in the same formulation as proposed by Jiles-Atherton we can write:

$$M_{\text{anhy}}(\vec{r}_i) = M_s \left(\coth\left[\frac{H_{\text{ext}}(\vec{r}_i) + \alpha_i M(\vec{r}_i)}{a_o} \right] - \frac{a_o}{H_{\text{ext}}(\vec{r}_i) + \alpha_i M(\vec{r}_i)} \right) \tag{5.106}$$

Therefore, the work done on the magnetic cuboid can be calculated by using the anhysteretic function for the magnetization:

$$\int M(\vec{r}_i) \cdot dB(\vec{r}_i) = \int M_{\text{anhy}}(\vec{r}_i) \cdot dB(\vec{r}_i), \tag{5.107}$$

However, the argument used by Jiles-Artherton establishes that there is an additional energy that must be supplied to overcome pinning sites in a volume when occurring the magnetization. This energy will be proportional through a constant factor k to the change in magnetization and it can be written by:

$$E_{\text{loss}} = \int k dM(\vec{r}_i), \tag{5.108}$$

since this energy losses is related to the opposition to the external magnetic field action, a factor δ is included to take into account the direction of the magnetic field regarding the current magnetization, i.e. $\delta = +1$ if $dM/dH > 0$ and $\delta = -1$ if $dM/dH < 0$, this factor guarantees that energy due to pinning energy density will always act as a lossy force:

$$E_{\text{loss}} = \int \delta k dM(\vec{r}_i), \tag{5.109}$$

Therefore, total energy on the sample should be the ammount of energy to magnetize the anhysteretic behavior minus the energy lost in overcoming pinning sites

$$\int M(\vec{r}_i) \cdot dB(\vec{r}_i) = \int M_{\text{anhy}}(\vec{r}_i) \cdot dB(\vec{r}_i) - \int \delta k dM(\vec{r}_i), \tag{5.110}$$

which can be written in terms of a differential equation taking the derivative respect to $dB(\vec{r}_i)$:

$$\delta k \frac{dM(\vec{r}_i)}{dB(\vec{r}_i)} = M_{\text{anhy}}(\vec{r}_i) - M(\vec{r}_i), \tag{5.111}$$

However, it is more convenient to write this expression as differential equation of $H_{\text{ext}}(\vec{r}_i)$ instead of $B(\vec{r}_i)$. For accomplish this, we can proceed as follows:

$$\frac{dM(\vec{r}_i)}{dB(\vec{r}_i)} = \frac{dM(\vec{r}_i)}{dH_{\text{ext}}(\vec{r}_i)} \frac{dH_{\text{ext}}(\vec{r}_i)}{dB(\vec{r}_i)}, \tag{5.112}$$

Now, magnetic flux density associated to this definition of the effective field $\vec{H}_{\text{e}}(\vec{r}_i) = \vec{H}_{\text{ext}}(\vec{r}_i) + \alpha_i \vec{M}(\vec{r}_i)$ in the i-th cuboid is given by:

$$\vec{B}_e(\vec{r}_i) = \mu_0 \vec{H}_{\text{e}}(\vec{r}_i) \tag{5.113}$$

$$B_x(\vec{r}_i) = \mu_0 \left(H_{x_{\text{ext}}}(\vec{r}_i) + \alpha_{x_i} M_x(\vec{r}_i)\right) \tag{5.114}$$

$$B_y(\vec{r}_i) = \mu_0 \left(H_{y_{\text{ext}}}(\vec{r}_i) + \alpha_{y_i} M_y(\vec{r}_i)\right) \tag{5.115}$$

$$B_z(\vec{r}_i) = \mu_0 \left(H_{z_{\text{ext}}}(\vec{r}_i) + \alpha_{z_i} M_z(\vec{r}_i)\right), \tag{5.116}$$

In the following we will find an expression for a general component $H_{\text{ext}}(\vec{r}_i)$ and take the derivative respect to $B(\vec{r}_i)$, then we obtain:

$$H_{\text{ext}}(\vec{r}_i) = \frac{B(\vec{r}_i)}{\mu_0} - \alpha_i M(\vec{r}_i) \tag{5.117}$$

$$\frac{dH_{\text{ext}}(\vec{r}_i)}{dB(\vec{r}_i)} = \frac{1}{\mu_0} - \alpha_i \frac{dM(\vec{r}_i)}{dB(\vec{r}_i)} \tag{5.118}$$

where expression $dM(\vec{r}_i)/dB(\vec{r}_i)$ can be replaced by:

$$\frac{dH_{\text{ext}}(\vec{r}_i)}{dB(\vec{r}_i)} = \frac{1}{\mu_0} - \frac{\alpha_i}{\delta k}\left(M_{\text{anhy}}(\vec{r}_i) - M(\vec{r}_i)\right) \tag{5.119}$$

By using the expression found above in the rule chain of derivatives, we can write an expression for dM/dB :

$$\frac{dM(\vec{r}_i)}{dB(\vec{r}_i)} = \frac{dM(\vec{r}_i)}{dH_{\text{ext}}(\vec{r}_i)}\frac{dH_{\text{ext}}(\vec{r}_i)}{dB(\vec{r}_i)} \tag{5.120}$$

$$\frac{dM(\vec{r}_i)}{dB(\vec{r}_i)} = \frac{dM(\vec{r}_i)}{dH_{\text{ext}}(\vec{r}_i)}\left[\frac{1}{\mu_0} - \frac{\alpha_i}{\delta k}\left(M_{\text{ani}}(\vec{r}_i) - M(\vec{r}_i)\right)\right], \tag{5.121}$$

replacing in the original expression we can write:

$$\frac{1}{\delta k}\left(M_{\text{anhy}}(\vec{r}_i) - M(\vec{r}_i)\right) = \frac{dM(\vec{r}_i)}{dH_{\text{t}}(\vec{r}_i)}\left[\frac{1}{\mu_0} - \frac{\alpha_i}{\delta k}\left(M_{\text{anhy}}(\vec{r}_i) - M(\vec{r}_i)\right)\right] \tag{5.122}$$

Rearranging some terms it can be obtained:

$$\frac{dM(\vec{r}_i)}{dH_{\text{t}}(\vec{r}_i)} = \frac{\left(M_{\text{anhy}}(\vec{r}_i) - M(\vec{r}_i)\right)}{\delta k/\mu_0 - \alpha_i\left(M_{\text{anhy}}(\vec{r}_i) - M(\vec{r}_i)\right)}. \tag{5.123}$$

As it was suggested in [25], domain walls can simply bend due to magnetic field more that overcome the pinning energy sites. This will result in reversible magnetization when the magnetic field is removed. Jiles-Atherton model proposes that magnetization is the sum of reversible and irreversible processes such that for the i-th cuboid we can write:

$$M(\vec{r}_i) = M_{\text{irr}}(\vec{r}_i) + M_{\text{rev}}(\vec{r}_i) \tag{5.124}$$

where a first approximation to the reversible magnetization can be written in terms of the anhysteretic magnetization by:

$$M_{\text{rev}}(\vec{r}_i) = c\left(M_{\text{anhy}}(\vec{r}_i) - M(\vec{r}_i)\right) \tag{5.125}$$

where c is a constant that can be found experimentally from the susceptibilities in the anhysteretic and normal magnetization curve[25]. As a consequence of including the possibility of wall domain bending as a reversible magnetization, total magnetization can be expressed as the sum of two magnetization components, such as:

$$M(\vec{r}_i) = \left(\frac{1}{1+c}\right)M_{\text{irr}}(\vec{r}_i) + \left(\frac{c}{1+c}\right)M_{\text{anhy}}(\vec{r}_i) \tag{5.126}$$

where $M_{\text{irr}}(\vec{r}_i)$ is the solution to the differential equation:

$$\frac{dM_{\text{irr}}(\vec{r}_i)}{dH_{\text{t}}(\vec{r}_i)} = \frac{\left(M_{\text{anhy}}(\vec{r}_i) - M_{\text{irr}}(\vec{r}_i)\right)}{\delta k/\mu_0 - \alpha_i\left(M_{\text{anhy}}(\vec{r}_i) - M_{\text{irr}}(\vec{r}_i)\right)}. \tag{5.127}$$

5.2.6 Quasi-static hysteresis model in the analysis of magnetostrictive composites

At this point we can calculate the hysteretic behavior of a quasi-static time dependent external field by:

$$\vec{H}_{\text{ext}}(\vec{r}_i, t_n) = \vec{H}_0 f(t_n) \tag{5.128}$$

where t_n corresponds to a discrete time step. With this magnitude of external magnetic field we can solve an internal loop with index k for calculating the anhysteretic magnetization (which was shown to converge as in the previous section) and the irreversible magnetization regarding the total magnetizing field. Let's consider an internal loop that is triggered each time the external field changes, this loop will calculate the anhysteretic magnetization from an initial guess of magnetization $\vec{M}_i^k(\vec{r_i})$ for all the cuboids that conform the body shape, this can be achieved by solving the linear system described in section above where the magnetization at the i-th cuboid should satisfy:

$$\frac{\vec{M}_i^k(\vec{r_i})}{\chi_m} - \left[\frac{1}{4\pi}\nabla \times \left(\sum_j^N \iiint_{v_j'} \frac{\vec{M}_j^k(\vec{r_j'}) \times \left(\vec{r_i} - \vec{r_j'}\right)}{|\vec{r_i} - \vec{r_j'}|^3} dv_j'\right) - \vec{M}_i^k(\vec{r_i})\right] = \vec{H}_0 f(t_n) \tag{5.129}$$

Once $\vec{M}_i^k(\vec{r_i})$ is known for each cuboid, we can calculate the associated demagnetization vector by:

$$\vec{H}_{\text{dmg}}^k(\vec{r_i}) = \frac{1}{4\pi}\nabla \times \left(\sum_j^N \iiint_{v_j'} \frac{\vec{M}_j^k(\vec{r_j'}) \times \left(\vec{r_i} - \vec{r_j'}\right)}{|\vec{r_i} - \vec{r_j'}|^3} dv_j'\right) - \vec{M}_i^k(\vec{r_i}) \tag{5.130}$$

Therefore, total internal magnetizing field at the center of the cuboid can be calculated by:

$$\vec{H}_{\text{T}}^k(\vec{r}_i, t_n) = \vec{H}_{\text{ext}}(\vec{r}_i, t_n) + \vec{H}_{\text{dmg}}^k(\vec{r}_i, t_n) \tag{5.131}$$

At this point we can calculate for the non-linear magnetization at iteration $k+1$ based on the magnetizing field in the iteration k, $\vec{H}_{\text{T}}^k(\vec{r}_i, t_n)$

$$\vec{M}_{\text{anhy}}^{k+1}(\vec{r}_i, t_n) = M_s \left(\coth\left[\frac{\vec{H}_{\text{T}}^k(\vec{r}_i, t_n)}{a_o}\right] - \frac{a_o}{\vec{H}_{\text{T}}^k(\vec{r}_i, t_n)}\right) \tag{5.132}$$

Where M_s is the saturation magnetization and a_o is a parameter that controls the curve shape. Finally, an updating equation to the magnetization state at the iteration step $k+1$ for the i-th cuboid, $\vec{M}^{k+1}(\vec{r}_i)$, can be written by:

$$\vec{M}^{k+1}(\vec{r}_i, t_n) = \vec{M}^{k}(\vec{r}_i, t_n) + \beta\left(\vec{M}^{k+1}_{\text{anhy}}(\vec{r}_i, t_n) - \vec{M}^{k}(\vec{r}_i, t_n)\right) \tag{5.133}$$

Once the relative error between magnetizations iterations converges to the desired one we can find the anhysteretic magnetization for the last iteration k_f in the the internal loop, we will have $\vec{M}^{k_f}_{\text{anhy}}(\vec{r}_i, t_n) = \vec{M}^{k_f}(\vec{r}_i, t_n)$.

Finally, we can write an updating equation in time for the irreversible component of magnetization by:

$$\begin{gathered} M_{\text{irr}}(\vec{r}_i, t_{n+1}) = M_{\text{irr}}(\vec{r}_i, t_n) + \\ \frac{\left(M^{k_f}_{\text{anhy}}(\vec{r}_i, t_n) - M_{\text{irr}}(\vec{r}_i, t_n)\right)}{\delta k/\mu_0 - \left(M^{k_f}_{\text{anhy}}(\vec{r}_i, t_n) - M_{\text{irr}}(\vec{r}_i, t_n)\right)} \left(H_{\text{ext}}(\vec{r}_i, t_{n+1}) - H_{\text{ext}}(\vec{r}_i, t_n)\right). \end{gathered} \tag{5.134}$$

with this magnetization and recalculating for the anhysteretic magnetization for $\vec{H}_{\text{ext}}(\vec{r}_i, t_{n+1})+$, $M^{k_f}_{\text{anhy}}(\vec{r}_i, t_{n+1})$ we can solve for:

$$M(\vec{r}_i, t_{n+1}) = \left(\frac{1}{1+c}\right) M_{\text{irr}}(\vec{r}_i, t_{n+1}) + \left(\frac{c}{1+c}\right) M^{k_f}_{\text{anhy}}(\vec{r}_i, t_{n+1}) \tag{5.135}$$

5.3 Magnetostriction of composites

Once the magnetization magnitude is known for each cuboid inside the composite. Magnetostriction curves can be calculated by using the expressions discussed in **chapter 4**. Expression that will be used for calculating the magnetostriction of each cuboid will consider the saturation magnetization M_s and the magnetostriction coefficient ϵ_s as known and constant values. These two values will be assumed to be known based on the fact that each cuboid is considered made of monolithic Terfenol-D. Therefore, its magnetostrictive coefficients and magnetic characteristics remain unchanged. Equation that calculated the magneto-strain for each cuboid can be given by:

$$\epsilon_i\left(M(\vec{r}_i)\right) = \frac{3}{2}\epsilon_s\left[\frac{M^2(\vec{r}_i)}{M_s^2}\right] \tag{5.136}$$

It is important to notice that strictly speaking, each cuboid will be under some stress distribution due to the epoxy curing. Indeed, after the interaction of the magnetostrictive particulate material with the external magnetic field, the individual strain of each particle could induce complicated stress distributions upon the epoxy matrix, and correspondingly, to the neighboring magnetostrictive particles. Although this effect could lead to very complicated relationships between mechanical strain resultant from the external field and the internal changes on the effective field due to the associated stress energy, this particular effect will be disregarded for the current formulation based on the fact that experiments (as those reproduced in **section 4.2.4**) show that high compressive stress should be applied to monolithic Terfenol-D material to affect in a representative manner the characteristics of magnetostriction coefficients. Additionally, in the current formulation model is aimed to include and describe the magnetic properties only, such as the resultant behavior of the particulate system can be understood in terms of the magnetic interactions of the cuboids.

5.3.1 Case of Study: Cylinder

This subsection presents the analysis of the proposed model when it is applied to one of the mostly used shape in Terfenol-D actuators, a cylindrical shape. Fig. 5.8 presents the comparison of the composite modeling against the magnetization obtained by COMSOL through the Finite Element Method. Simulation consisted on a cylinder of 1[cm] in radius and 3[cm] in length. In the FEM case, cylinder is modeled as a continuous magnetic body. In contrast, for the composite modeling a discretization in cuboids was implemented for the simulation with ΔX=1.3[mm], ΔY=1.3[mm] and ΔZ=1.9[mm].

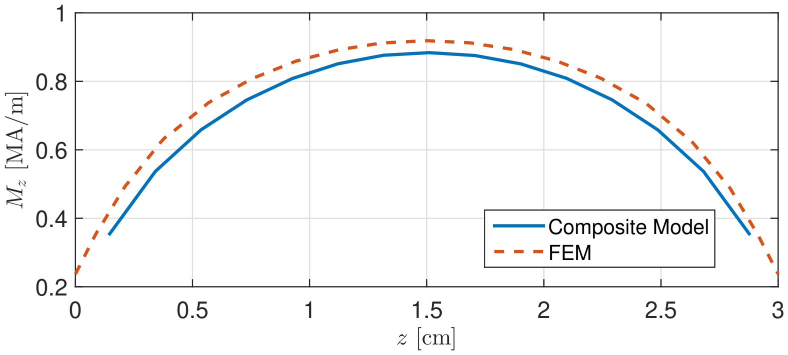

Figure 5.8: Magnetization z-component magnitude alonsg the cylinder axis. Comparison against FEM results (dashed line) against magnetization obtained through the composite modeling strategy (cuboids filled 100%).

As it can be seen from Fig. 5.8, there is a mismatch between both results. A relative error about 3.8% is calculated in the maximum of the magnetization. This mismatch can be caused by the discretization process of the cylindrical shape, which is performed through cuboids that could lead to a lack of geometrical representation when dealing with non rectangular shapes. Fig. 5.9 presents the discrete model of the cylinder whe it is represented through cuboids.

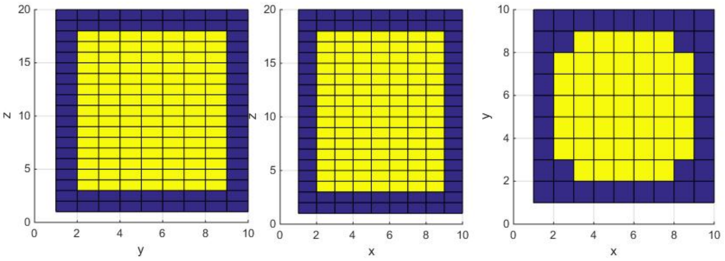

Figure 5.9: Discrete representation of the magnetic body as a set of finite cuboids (ΔX=1.3[mm], ΔY=1.3[mm] and ΔZ=1.9[mm]).

As it can be seen from Fig. 5.9 there is an evident lack of representation in geometry for the circular pattern since it should be represented by using the cuboid unit cells. This issue can be one of the source errors in the simulation. One of the advantages that presents current modeling strategy is the possibility of controlling the size of each cuboid in the composite.

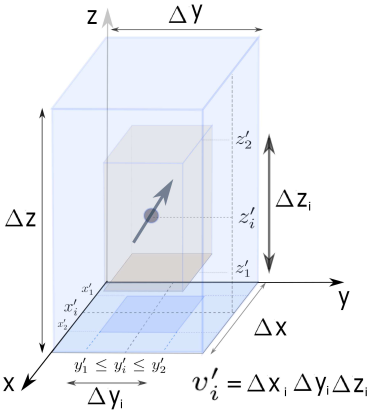

Figure 5.10: Definition of the size fraction of the magnetic cuboid $v'_i = \Delta X_i \Delta Y_i \Delta Z_i$

Figure 5.11 presents the calculation of the total strain achieved by different percentages of filling of magnetic material inside the cuboid unit cell. As it can be seen from Fig. 5.11 is that the effects of changing the volume fraction of the magnetostrictive material in the cuboid unit cell has effect in both: the total mechanical strain that can be obtained from the specimen and its magnetic properties, saturation and magnetostriction curve. These two effects have been observed in several experiments and theoretical predictions [12, 11]. An interesting prediction of the current model

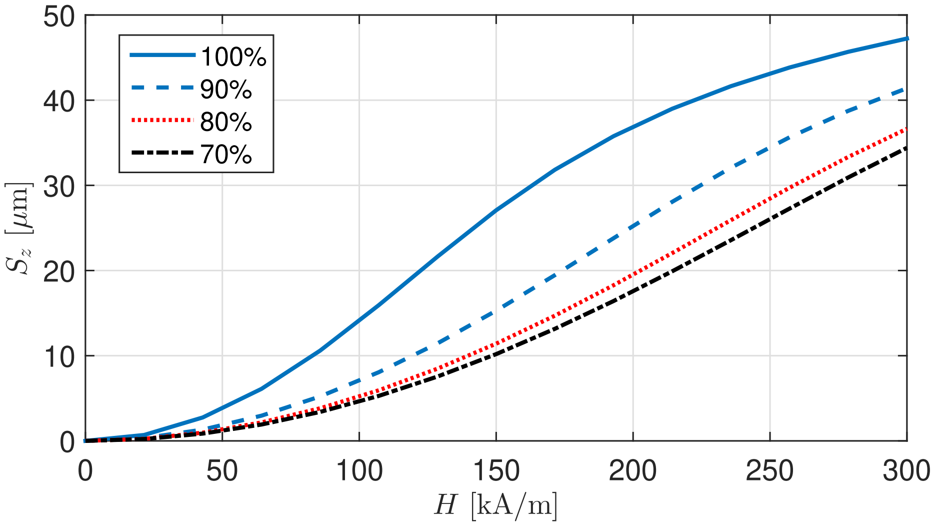

Figure 5.11: Discrete representation of the magnetic body as a set of finite cuboids (ΔX=1.3[mm], ΔY=1.3[mm] and ΔZ=1.9[mm]. Different size fractions.)

occurs when lower size fractions are considered in the analysis. Figure 5.12 presents the expected results when volume fraction smaller than 80% are considered. As it can be seen from the figure, higher mechanical strains are predicted for volumen fractions of 30% than those obtained by 80%. It is worth noting that in the formulation there have not been included any mechanical strain interaction between the epoxy matrix and the magnetostrictive inclusion. However, it is important to note that magnetic effects associated to the interaction between each of the magnetic bodies that composes the total volume have an effect in the total performance of the composite. This effect was observed experimentally in Ref. [11] where lower fractions of volume exhibited higher longitudinal magnetostriction. Although the explanation given in Ref. [11] included some stress transferred to the epoxy, current formulation gives an additional source of explanation of this phenomena based in magnetic effects only. An additional analysis that can be made by using the proposed formulation for analyzing the shape of the particle.

In the results of Fig.5.13 smaller unit cells were considered. Although, lower volume per unit cell is considered, total volume remain constant, such as more particulate material composes the total composite body, reaching even more magnetization that bigger particles in the 90% filling case. This theoretical result can explain some of the experimental results obtained for different particle concentration and sizes where a suitable optimization based on these two variables have been evidenced.

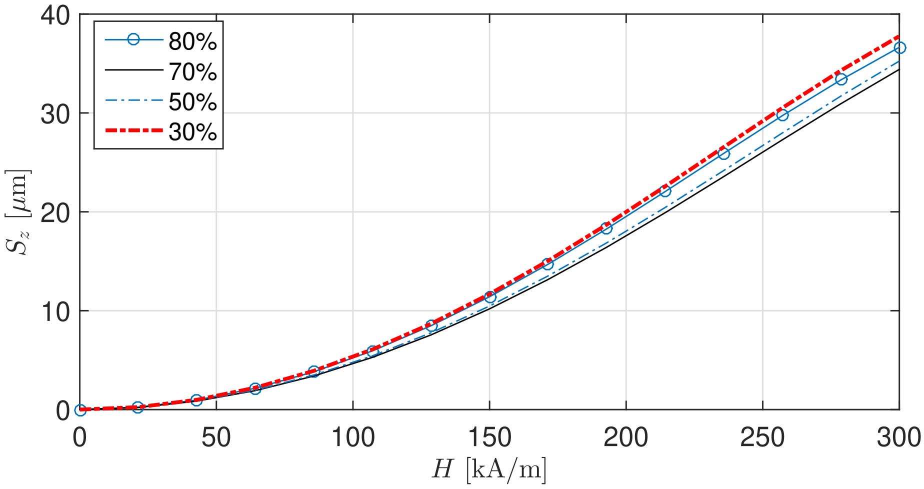

Figure 5.12: Discrete representation of the magnetic body as a set of finite cuboids (ΔX=1.3[mm], ΔY=1.3[mm] and ΔZ=1.9[mm]). Smaller size fractions of magnetostrictive composites.

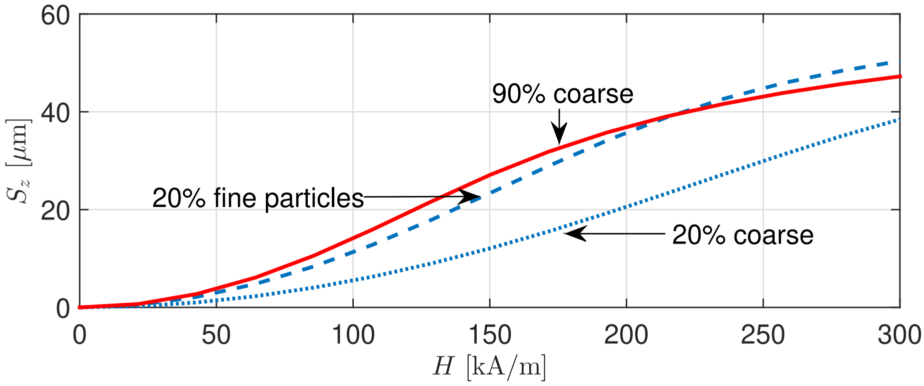

Figure 5.13: Discrete representation of the magnetic body as a set of finite cuboids (Coarse dimensions: ΔX=1.3[mm], ΔY=1.3[mm] and ΔZ=1.9[mm]) and (Fine dimensions: ΔX=625[μm], ΔY=625[μm] and ΔZ=1.3[mm]). Smaller size fractions of magnetostrictive composites.

5.4 Concluding Remarks

This chapter proposed a numerical model for describing magnetostrictive composites. Closed solution for vector magnetic potential was found for a single magnetic cuboid to represent the monolithic magnetostrictive particle. Afterwards, magnetization was calculated by writing a set of linear equations that involved full vectorial magnetization field and numerical methods were applied to solve the resultant system of equations. Proposed method allows flexible description of powder particle size and geometric aspect ratios. Several effects due to particulate geometry could be modeled through the proposed framework and compared against monolithic prediction. Additional characteristics of ferromagnetic materials such as hysteresis and nonlinearities were successfully included in the model.

Good agreement was found when comparing results from monolithic bodies simulated by FEM and those modeled through cuboids fully filled of magnetic material. The flexibility of defining specific sizes for each cuboid in the current model can be used to predict the influence that each particle geometry has upon the behavior of the whole body regarding its magnetization and consequently magnetostriction.

Chapter 6

Piezoelectricity

This section present most of the well known approaches for modeling piezoelectricity in materials. As it was discussed above, any type of external mechanical interaction that results in body deformation can be included in the strain equation as an additive term. Piezoelectric materials can be expressed by:

$$\xi_i = S^E_{ij}\sigma_j + d^P_{ij}E_j + \alpha\Delta T \tag{6.1}$$

where S^E_{ij} corresponds to the compliance matrix. This matrix is a characteristic of the material and is superscripted by E to denote that relates the compliance of the material at constant electric field E. Coefficients d^P_{ij} correspond to the coupling factors between strain and electric field in a piezoelectric material and, $\alpha\Delta T$ includes the effects of thermal expansion. Compliance matrix can be written explicitly by:

$$S^E = \frac{1}{\mathcal{Y}}\begin{bmatrix} 1 & -\nu & -\nu & 0 & 0 & 0 \\ -\nu & 1 & -\nu & 0 & 0 & 0 \\ -\nu & -\nu & 1 & 0 & 0 & 0 \\ 0 & 0 & 2(1+\nu) & 0 & 0 \\ 0 & 0 & 0 & 2(1+\nu) & 0 \\ 0 & 0 & 0 & 0 & 2(1+\nu) \end{bmatrix} \tag{6.2}$$

In principle piezoelectric can be created by the application of an external strong electric field over certain materials that induces some anisotropy on the electric charge distribution. This procedure is known as poling and allows the description of the crystal by means of an axial system, where the axis that points in the poling direction becomes the principal axis. Once the axis system is defined, the behavior of the piezoelectric material can be described by the coefficients d^P_{ij} to totally define th constitutive relations of the piezoelectric under study. Figure 6.1 presents the definition of the principal axes on the material anisotropy.

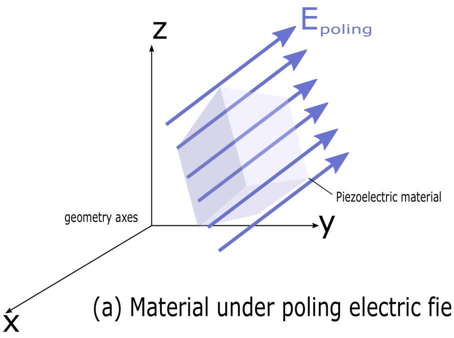

(a) Material under poling electric field

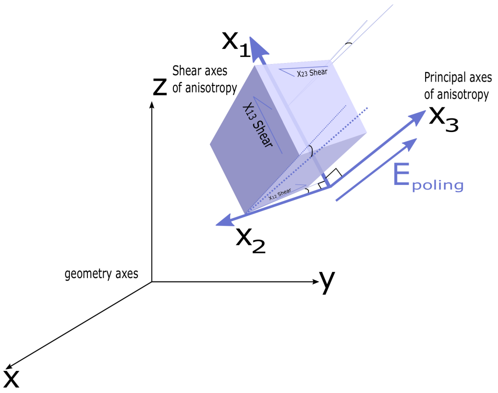

(b) Principal axes of anisotropy

Figure 6.1: (a) Material under poling electric field (b) Principal axes of anisotropy. X_3 points in the poling electric field direction. Shear axes can be also taken into account for describing the full strain deformation

As it is shown in Figure 6.1, prinicipal axis x_3 points in the poling direction. Shear deformations can be also taken into account by including the corresponding coefficients. A typical matrix of piezoelectric coefficients is given by:

$$d_{ij}^{P} = \begin{bmatrix} 0 & 0 & d_{31} \\ 0 & 0 & d_{32} \\ 0 & 0 & d_{33} \\ 0 & d_{24} & 0 \\ d_{15} & 0 & 0 \\ 0 & 0 & 0 \end{bmatrix} \tag{6.3}$$

Therefore, coefficients d_{3j} characterizes the strain along the j axis due to an electric field E_3 along the X_3 axis. Coefficient d_{24} determines the strain in the plane $2-3$ due to an electric field pointing along X_2 and d_{15} determines the strain in the plane $3-1$ due to an electric field pointing along X_1.

6.1 Piezoelectric composite bimorph actuator

A piezoelectric bimorph is a composite bilayer actuator that is characterized for having two piezoelectric layers and a metal shim in between them. As it is presented in **Appendix E**, the existence of a bending moment throughout the beam causes a deflection along the longitudinal dimension. This subsection derives the deflection expression for a bimorph actuator based on the same analysis provided before and including the electrostrictive effect upon the piezoelectric layers. Figure 6.2 presents a bimorph actuator with two piezoelectric layers with t_p in thickness. Those piezoelectric layers are bonded by a thin metallic shim of t_m in thickness. The width of the actuator is w and its length is L.

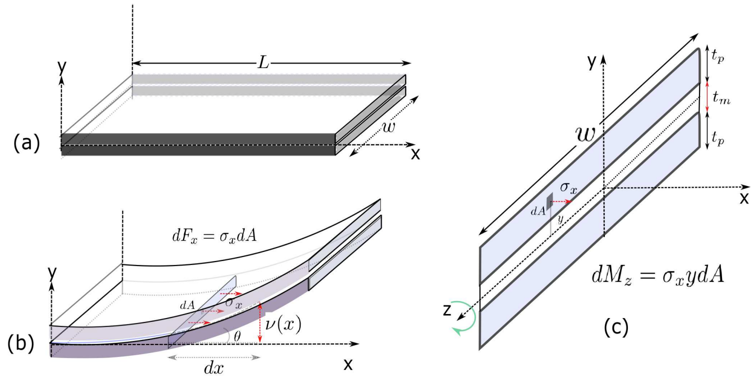

Figure 6.2: (a) Piezoelectric bimorph (b) deflection curve of cantilever bimorph (c) Cross section detail of the longitudinal stress

As it was discussed in the section above, the deflection curve can be found from the bending moment distribution along the beam. In the case of a symmetric bimorph the neutral axis still crosses the centroid of the transverse section.Therefore, same expressions can be found for the deflection curve as in the homogeneous case discussed before defining and effective curvature κ_{eff}, such as we can write:

$$\xi_x = \kappa_{\text{eff}} y, \tag{6.4}$$

Where ξ_x will be the strain profile, that should be found based on the neutral axis location. In a symmetric bimorph, such as this one we are dealing with, the neutral axis location will coincides with the centroid of the cross section. Following the same analysis as before, the defection curve can be found once the curvature is known by integrating the expression:

$$\frac{d^2\nu(x)}{dx^2} = \kappa_{\text{eff}} \tag{6.5}$$

We can follow the same procedure for finding κ_{eff} from the bending moment. However, in this case we have two layers that make each stress component to have different values based on the region and will be determined by the poling direction and voltage excitation upon the piezoelectric layers. Figure 6.3 presents the adopted polarization (material axes described by X_1,X_2,X_3) for a given piezoelectric material.

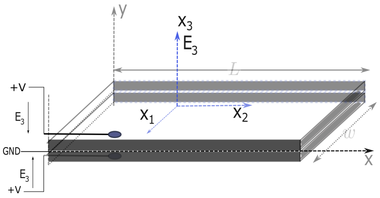

Figure 6.3: Piezoelectric bimorph polarization depending on the voltage excitation

We can write the longitudinal stress over the cross section as follows:

$$\sigma_x(y(x),z) = \begin{cases} \mathcal{Y}_p\xi_x - d_{31}\mathcal{Y}_p E_3 & -t_p - t_m/2 < y < -t_m/2 \\ \mathcal{Y}_m\xi_x & -t_m/2 < y < t_m/2 \\ \mathcal{Y}_p\xi_x + d_{31}\mathcal{Y}_p E_3 & t_m/2 < y < t_p + t_m/2 \end{cases} \tag{6.6}$$

where $\mathcal{Y}_m$ and $\mathcal{Y}_p$ are the Young's module of the metal shim and the piezoelectric layer respectively. It should be noticed that there is an additional term in the stress function for the piezoelectric regions. This term corresponds to the electrostriction caused by the electric field upon the piezoelectric material. Negative or positive sign will depend on the polarization of the layer respect to the electric field, which is determined by the electrodes arrangement in the bimorph and the poling direction for the piezoelectric layer. For this case, superior layer is under an anti-parallel electric field respect to the poling direction and lower layer is excited along the poling direction (See Figure 6.3 for details). Total moment at the cross section can be calculated by:

$$M_{\text{piezo}} = \iint \sigma_x(y(x),z) y dy dz \tag{6.7}$$

Therefore, we can write an integral for each corresponding region:

$$M_{\text{piezo}} = \int_{-t_p-t_m/2}^{-t_m/2} \left(\mathcal{Y}_p\xi_x - d_{31}\mathcal{Y}_p E_3\right) wydy + \int_{-t_m/2}^{t_m/2} \left(\mathcal{Y}_m\xi_x\right) wydy + \int_{t_m/2}^{t_p+t_m/2} \left(\mathcal{Y}_p\xi_x + d_{31}\mathcal{Y}_p E_3\right) wydy \tag{6.8}$$

we replace the expression for the strain into the integrals to obtain:

$$M_{\text{piezo}} = \int_{-t_p - t_m/2}^{-t_m/2} \left(\mathcal{Y}_p \left(-\kappa_{\text{eff}} y\right) - d_{31}\mathcal{Y}_p E_3\right) wydy + \\ \int_{-t_m/2}^{t_m/2} \left(\mathcal{Y}_m \left(-\kappa_{\text{eff}} y\right)\right) wydy + \int_{t_m/2}^{t_p + t_m/2} \left(\mathcal{Y}_p \left(-\kappa_{\text{eff}} y\right) + d_{31}\mathcal{Y}_p E_3\right) wydy \quad (6.9)$$

Rearranging terms in the integrals:

$$M_{\text{piezo}} = \int_{-t_p - t_m/2}^{-t_m/2} \left(-\kappa_{\text{eff}}\mathcal{Y}_p w y^2 - d_{31}\mathcal{Y}_p E_3 w y\right) dy + \\ \int_{-t_m/2}^{t_m/2} -w\mathcal{Y}_m \kappa_{\text{eff}} y^2 dy + \int_{t_m/2}^{t_p + t_m/2} \left(-\kappa_{\text{eff}}\mathcal{Y}_p w y^2 + d_{31}\mathcal{Y}_p E_3 w y\right) dy \quad (6.10)$$

integration can be performed directly to obtain:

$$M_{\text{piezo}} = \left[-\kappa_{\text{eff}}\mathcal{Y}_p w \frac{y^3}{3} - d_{31}\mathcal{Y}_p E_3 w \frac{y^2}{2}\right]\Bigg|_{-t_p - t_m/2}^{-t_m/2} + \\ \left[-w\mathcal{Y}_m \kappa_{\text{eff}} \frac{y^3}{3}\right]\Bigg|_{-t_m/2}^{t_m/2} + \left[-\kappa_{\text{eff}}\mathcal{Y}_p w \frac{y^3}{3} + d_{31}\mathcal{Y}_p E_3 w \frac{y^2}{2}\right]\Bigg|_{t_m/2}^{t_p + t_m/2} \quad (6.11)$$

simplifying the expression, we have:

$$M_{\text{piezo}} = -\mathcal{Y}_p \kappa_{\text{eff}} w \left(\frac{t_m^2 t_p}{2} + t_m t_p^2 + \frac{2t_p^3}{3}\right) - \mathcal{Y}_m \kappa_{\text{eff}} w \frac{t_m^3}{12} - \mathcal{Y}_p w d_{31} E_3 \left(t_m t_p + t_p^2\right) \quad (6.12)$$

Now, a free body analysis over the cantilever bimorph should be done in order to write the static equilibrium equations. Figure 6.4 presents the free body diagram for the case under study. As it can be seen, there is an initial force over the cantilever bimorph that corresponds to its own weight. Therefore, there is a total reaction moment $M_{zR}(0)$ on the fixed point due to the weight, as well as a total vertical force

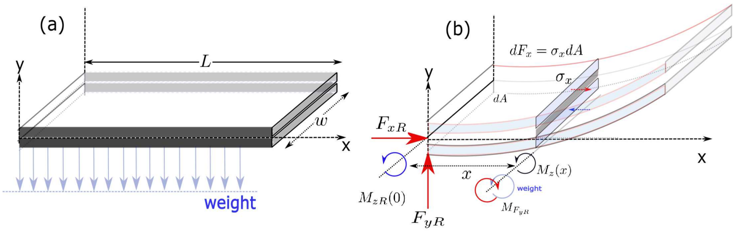

Figure 6.4: (a) Distributed weight force (b) free-body diagram with the current forces over the piezoelectric bimorph cantilever

directed upwards F_{yR} to compensate the weight of the whole actuator. Additionally, since in the piezoelectric bimorph there is an additional term in the stress function due to the driving electric field $\sigma_{xE} = \pm d_{31}\mathcal{Y}_p E_3$, we have to express force equilibrium along the longitudinal axes,

$$F_{xR}(0) - w\int_{-t_m/2-t_p}^{t_m/2+t_p} \sigma_x(y)dy = 0, \tag{6.13}$$

integration can be done using the piecewise stress function to have:

$$\begin{aligned} F_{xR}(0) - w\int_{-t_m/2-t_p}^{-t_m/2} &\left(\mathcal{Y}_p\kappa_{\text{eff}}y - d_{31}\mathcal{Y}_p E_3\right)dy \\ &- w\int_{-t_m/2}^{t_m/2} \mathcal{Y}_m\kappa_{\text{eff}}y dy \\ &- w\int_{t_m/2}^{t_m/2+t_p} \left(\mathcal{Y}_p\kappa_{\text{eff}}y + d_{31}\mathcal{Y}_p E_3\right)dy = 0, \end{aligned} \tag{6.14}$$

since the bimorph is symmetric, the neutral axis crosses the centroid of cross-section. This makes the integrals in the extensional force equilibrium to cancel out, implying $F_{xR}(0) = 0$.

On the other hand, for the calculation of the bending moment equilibrium, we can assume that the total weight is W_g and it is distributed uniformly along the beam, we will have that the sum of the bending moments at some point x of the deflection curve is given by:

$$M_{zR}(0) - M_{F_{yR}} + M_{\text{piezo}}(x) + \int_o^x \frac{W_g}{L} x dx = 0, \tag{6.15}$$

Weight moments are not considered, leading to:

$$M_{\text{piezo}}(x) = 0, \tag{6.16}$$

which allows us to calculate the curvature by[50]:

$$\kappa_{\text{eff}} = \frac{12\mathcal{Y}_p d_{31}E_3\left(t_m t_p + t_p^2\right)}{2\mathcal{Y}_p\left(3t_m^2 t_p + 6t_m t_p^2 + 4t_p^3\right) + \mathcal{Y}_m t_m^3} \tag{6.17}$$

The sign of the curvature will be dependent on the convention assumed for the bending moments and also the deflection direction. Since the curvature results being independent of the x coordinate, and $\nu(0) = 0$ and $\nu'(0) = 0$. The deflection curve can be calculated simply by:

$$\nu(x) = \kappa_{\text{eff}} \frac{x^2}{2} \tag{6.18}$$

In order to validate the modeling presented before, a bimorph bender with dimensions $w = 7.8$[mm], $L = 28$[mm], $t_m = 0.1$ and $t_p = 0.35$[mm] was simulated by using Finite Element Method FEM. Metal shim was assumed to be made of aluminum with a Young module given by $\mathcal{Y}_m = 70 \times 10^9$[Pa]. The poling direction of the piezoelectric was assumed to points in the y-direction of the coordinate system (see Fig. 6.3). Mechanical properties of the piezoelectric layers were considered based on typical ceramic characteristics. In the analysis a Young module $\mathcal{Y}_p = 60.6 \times 10^9$[Pa] was assumed for the piezoelectric layer with a piezoelectric coefficient $d_{31} = 650 \times 10^{-12}$[m/V]. This piezoelectric coefficient was taken from the maximum tip displacement that commercial piezoelectric bimorph achieve under maximum external field when it is operated by exciting both piezoelectric layers as shown in Fig. 6.3. In practical implementations of bimorph actuators, dielectric constant of the piezoelectric decreases the effective electric field produced by the charge density on the bimorph surface.

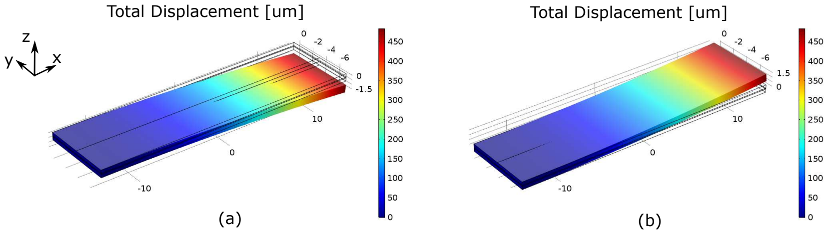

Figure 6.5: (a) Total downward displacement. (b) Total upward displacement.

Figure 6.5 presents the total mechanical displacement that exhibits the bimorph when 150V are applied upon the piezoelectric layers. As it can be seen from Fig. 6.5 both sides deflection can be obtained depending on the resultant electric field direction across the layer. Figure 6.6 presents the deflection curve calculated by the analytical approach when an electric field about $E_3 = 428.6$[kV/m] is applied across the piezoelectric layers. As it can be seen from Figure 6.6, there is an underestimation in the analytical solution respect to the FEM result in the deflection strain along z. It is highly important to note, that analytical derivation assumes a constant electric field magnitude. However, in practice strain associated to the bending action modifies the electric displacement magnitude along the cross section. Therefore, electric field magnitude results in a continuous linear distribution along the cross section instead

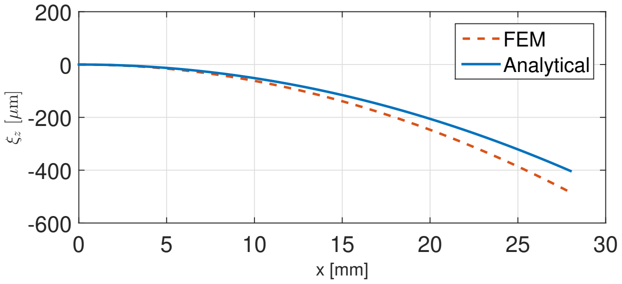

Figure 6.6: Calculation of the deformation for the bimorph under analysis via FEM and analytical procedure presented before. (a) downward deflection. (b) Upward deflection

of a constant value as assumed in the analytical approach. This situation is closer to practical implementations and causes the mismatch between analytical approach and the results obtained by FEM. Figure 6.7(a) presents the actual distribution of the electric field along the cross section, showing a spatial distribution with a maximum field about to ±750[kV/m] close to the bimorph external surfaces and decreases about to ±100[kV/m] on the metal shim surface (Fig.6.7(b)).

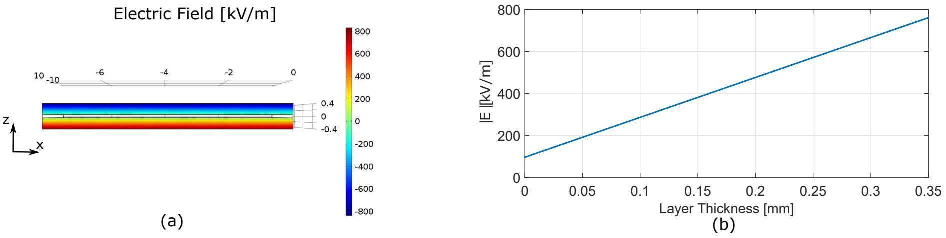

Figure 6.7: Actual electric field distribution across bimorph piezoelectric layers. (a) Spatial distribution of electric field(both layers) (b) Electric field norm across one piezoelectric layer

6.2 Effective field correction

As it is presented before, the distribution of the electric field along the cross section differs to the analytical assumption of a constant electric field. A rigorous solution should include the effects in the electric field due to the bending action upon the piezoelectric that modifies the electric field magnitude along the cross section. However, a simplified correction can be proposed to find an effective field magnitude such as total momentum upon the cross section is equivalent in both cases. Afterwards, this effective field can be plugged into the analytical approach as a constant magnitude to satisfy that total bending moment equations on the cross section is equivalent to that created by the linear distribution of the electric field. Total moment on a piezoelectric layer can be calculated by:

$$\int_{t_p} E_{\text{eff}} w y dy = \int_{t_p} E_3(y) w y dy, \tag{6.19}$$

spatial dependence of the electric field can be described by a linear relation based on the maximum and minimum electric field found at the plate surfaces:

$$E_3(y) = \frac{E_{\text{max}} - E_{\text{min}}}{t_p} y + E_{\text{min}}. \tag{6.20}$$

Plugging the expression into the momentum integrals one finds an effective field given by:

$$E_{\text{eff}} = \frac{2}{3} E_{\text{max}} + \frac{1}{3} E_{\text{min}}. \tag{6.21}$$

Considering this effective field for the current case, analytical approach can be recalculated by using $E_3 = 533.33[\text{kV/m}]$, which is around 1.24 times the initial electric field calculated under uniform distribution assumption. Figure 6.8 presents the deflection curve with the corrected field magnitude. As it can be seen from Fig. 6.8 effective field included in the analytical formulation increases the accuracy of the predicted deflection curve. This proposed method of effective field correction enables to use the analytical formulation for accounting spatial electric field distribution along the cross section of the bimorph actuator.

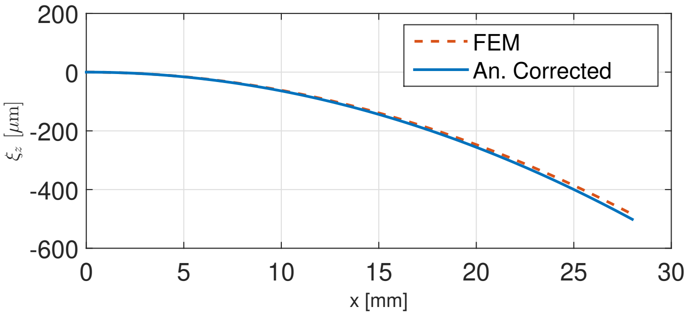

Figure 6.8: Comparison of deflection curve when corrected effective field is considered in the analytical formulation.

6.3 Concluding Remarks

This chapter presented the theoretical framework for piezoelectric bimorph actuator. Analytical description of this type of actuators was derived and compared to Finite

Element Method (FEM) results. Owing to the assumption of constant electric field in the analytical model, some differences along the deflection curve were found. However, the definition of an effective electric field in the analytical approach can be proposed to enable the use of the analytical description to fit the FEM calculations. Effective field correction is proposed as a consequence of the spatial distribution of the electric field inside the bimorph plates when strain modifies total electric displacement field. In order to provide a more accurate definition of the effective field, total bending moment was calculated for a linearly distributed electric field along the cross section such as a constant effective field results in the same amount of bending moment. As it was shown in this chapter effective field correction decreased the relative error at the tip displacement from 16.77% to 3.57%.

Chapter 7

Experimental Results

This chapter presents some of the experimental set-ups that were conducted to validate the theoretical framework developed in the previous chapters. Two main optical fiber-based magnetic and electric field sensors were implemented to propose a suitable arrangement for measuring electrical variables in high voltage power systems. Magnetic field was inferred by using magnetostriction as a sensing principle, and electric field by means of piezolectric bimorph/unimorph actuators.

Two main strategies for developing the aforementioned fiber-based sensors were tackled in the experimental set-ups. Supported on the theoretical background developed in **chapter 5** and the properties that geometry offers in controlling the distribution of the internal magnetic field, which in turns controls the strain generated by magnetostriction, magnetic field sensor was implemented through an embedded Fiber Bragg Grating (FBG) into Terfenol-D/Epoxy composite. Electric field sensor was achieved based on the discussed relationships in **chapter 6** through the implementation of a piezoelectric bimorph as an electric-field actuator. Experimental results were compared in both cases with the expected theoretical performance. Although good agreements were obtained between predicted and measured results in both sensors, some of the most important issues that could cause the mismatches are discussed by the author and addressed as future work plans. This chapter is organized as follows: First section deals with the magnetic field sensor implemented through a Terfenol-D/Epoxy composite. Initially some geometric aspects were considered in order to determine what kind of magnetic body geometry was more suitable to implement and offered more advantages regarding the internal field distribution. A closed solution for the internal magnetic field is obtained for frustum cone case based on the assumptions discussed in **chapter 4** for monolithic magnetostrictive bodies. Afterwards, proposed modeling strategy described in **chapter 5** is used for the particular shape of a frustum cone. Effects on the internal magnetic field due to the particle size and randomness distribution is analyzed. Comparison against FEM solutions is presented for each case. Nonlinearity of the magnetization was included by using the Langevin function in the J-A model. Error curves are presented for validating the convergence of the proposed method for this particular geometry. Main steps of the composite fabrication is presented. Theoretical broadening of the reflected spectrum is calculated by using the theoretical expected strains profiles upon the FBG. Finally, a set of comparison of the experimental implementations and theoretical predictions is performed.

Second section of the chapter presents the results of the implementation of a high voltage sensor by using the piezoelectric bimorph discussed in **chapter 6** and a FBG attached to it. Longitudinal strain is transferred to the FBG producing central wavelength shifting. Characterization of the sensor in single side operation of the bimorph is performed for compression and tension actuation. For allowing inference of the external voltage magnitude based on optical power measurements, a technique based on a reference FBG is used. Such as central wavelength modulation of the attached FBG to the bimorph can be filtered by the reference FBG, leading to spectrum change in the transmitted optical signal. Several frequencies were considered in the experimental, achieving good performance up to 1.0kHz.

7.1 Magnetostrictive frustum cone for magnetic field sensing

As it was discussed in sections before, fiber-based sensing principle of magnetic fields based on magnetostriction requires to transfer the induced strain from the magnetostrictive material to an optical device such as a FBG. As it as widely discussed in **chapter 3**, optical parameters of FBG can be changed by exerting strain along the grating, i.e. uniform and nonuniform strains can be exerted to the longitudinal perturbation of the FBG controlling its optical interference characteristics. Since the strain produced by magnetostriction is dependent on the magnetization, external magnetic field magnitude can be estimated from the characteristics of the optical reflection spectrum from the optical device [36]. If only end points of the FBG are anchored to the mechanical action, uniform induced strain will be transferred to the grating and uniform change in the effective pitch period will lead to a wavelength shift of the reflected central peak. However, if the FBG is embedded in the magnetostrictive material or composite, internal magnetic field distribution will govern the strain profile exerted to the FBG. Therefore, mechanical strain transferred to the optical device will be affected by the respective geometry of the magnetostrictive material (as presented in the demagnetization field effects discussed in **chapter 4**). Geometric dependence of the internal magnetization distribution, $\vec{M}(\vec{r})$, can be used to engineer different shapes of the magnetostrictive composites in order to turn an initially nonchirped FBG into a chirped one, allowing to sense the external field magnitude through optical power measurements.

7.1.1 Frustum cone with different side-slopes

An initial approach for the geometry consists in a variation of the cylinder discussed in **chapter 4**). In this case a frustum cone with different side wall geometries is considered. The selection of this particular shape of the sensor is based on its simplicity for being manufactured experimentally, as well as some material can be saved when compared with cylindrical shapes. As it has been discussed in the sections above, geometric shape of the magnetic body has an evident influence upon the distribution of the internal magnetic field. Frustum cone presents a very different distribution when compared with the cylindrical or spherical shape. This section is aimed to compute the effects of changing the side slope in a frustum cone to determine which side slope is more suitable to induced nonuniform strain upon the fiber. Consider a frustum cone shaped that has a bottom radius b_0 and an upper radius a_0, as shown in Fig.(7.1). In this particular case, radius at the side wall will be given in general by the function: $z' = a_p\,(b_0 - r)^n$, where a_p is a constant.

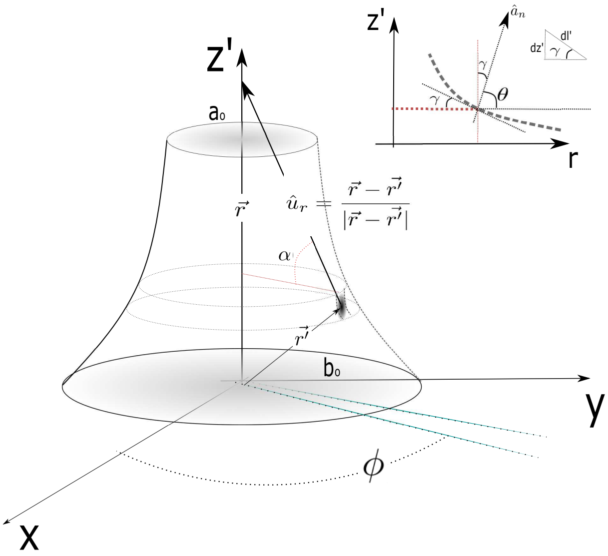

Figure 7.1: Uniformly magnetized frustum cone with parabolic side

Constant a_p of the parabolic function that describes the side wall can be written by:

$$a_p = \frac{L}{(b_0 - a_0)^n} \tag{7.1}$$

Function that describes the radius can be written by:

$$r(z') = b_0 - \sqrt[n]{\frac{z'}{a_p}}. \tag{7.2}$$

Normal vector to the body surface can be found by taking the gradient of the function $f(r, z') = z' - a_p(r - b_0)^n$ evaluated at the contour radius, for both even an odd exponents n. Taking the gradient and calculating the unitary vector at the surface in cylindrical coordinates, i.e. $\hat{n}' = \nabla f(r(z'), z')/|\nabla f(r(z'), z')|$, it can be obtained:

$$\hat{n}' = \frac{\left[a_p n \left(\frac{z'}{a_p}\right)^{\frac{n-1}{n}}\right] \hat{i}_r + \hat{i}_z}{\sqrt{1 + \left[a_p^2 n^2 \left(\frac{z'}{a_p}\right)^{\frac{2n-2}{n}}\right]}}. \tag{7.3}$$

It is worth noting that deriving the expression for the gradient one should be consistent of the concavity of the functions that describe the side contour of the magnetic body, such that the normal vector points out in the maximum decrement of the function. Assuming that the magnetic body is under a constant external magnetic field directed along the z-axis, $\vec{H} = H_0 \hat{i}_z$, one can assume as a first approach, a magnetization vector along the same direction, i.e. $\vec{M} = M_0 \hat{i}_z$ with M_0 being a constant. Therefore, the equivalent surface magnetic current, $\vec{K}_m = \left(M_0 \hat{i}_z\right) \times \vec{a}_n$, can be written by:

$$\vec{K}_m = M_0 \frac{\left[a_p n \left(\frac{z'}{a_p}\right)^{\frac{n-1}{n}}\right]}{\sqrt{1 + \left[a_p^2 n^2 \left(\frac{z'}{a_p}\right)^{\frac{2n-2}{n}}\right]}} \hat{i}_\varphi. \tag{7.4}$$

Finally, magnetic flux density along the z-axis can be calculated from the integral:

$$B_{\mathrm{mg}}(z) = \frac{\mu_0}{2} \int_0^L \frac{\left(\vec{K}_m \times \hat{u}_r\right)_{\hat{i}_z} r(z')}{\cos\theta \left[(z - z')^2 + r(z')^2\right]} dz', \tag{7.5}$$

Magnetic field flux density in Eq.(7.5) can be evaluated numerically by using well known integration methods [16]. Intensity of the demagnetization field can be found from the constitutive equation:

$$H_{\mathrm{mg}}(z) = \frac{B_{\mathrm{mg}}(z)}{\mu_0} - M_0. \tag{7.6}$$

Trapezoidal rule was used to calculate the magnetic field intensity for different side contours controlled by the parameter n in Eq.(7.2), and evaluate the effect of geometry in the field distribution along the z-axis. Since M_0 continues being unknown, we can assume a linear magnetization relationship with the internal field $H_{\text{int}}(z)$ given by:

$$M_0 = \chi_m H_{\text{int}}(z) \tag{7.7}$$

allowing to find a magnetization magnitude based on the internal field. Therefore, internal magnetic field can be calculated as the sum of the external field and the demagnetization field by:

$$H_{\text{int}}(z) = H_{\text{ext}}(z) + H_{\text{mg}}(z) \tag{7.8}$$

$$H_{\text{int}}(z) = H_{\text{ext}}(z) + \frac{B_{\text{mg}}(z)}{\mu_0} - \chi_m H_{\text{int}}(z). \tag{7.9}$$

Magnetic flux density is given by:

$$B_{\text{mg}}(z) = \frac{\mu_0 M_0}{2} \int_0^L \frac{\left(\vec{K}_m \times \hat{u}_r\right)_{\hat{\imath}_z} r(z')}{\cos\theta\left[(z-z')^2 + r(z')^2\right]} dz', \tag{7.10}$$

Therefore, we can write for the internal field:

$$H_{\text{int}}(z) = \frac{H_{\text{ext}}(z)}{1 + \chi_m \left[1 - \frac{1}{2}\int_0^L \frac{\left(\vec{K}_m \times \hat{u}_r\right)_{\hat{\imath}_z} r(z')}{\cos\theta[(z-z')^2 + r(z')^2]} dz'\right]}. \tag{7.11}$$

Fig. 7.2 presents the calculations of the internal magnetic field for truncated cones with top and bottom radii $a_0 = 0.2$[cm] and $b_0 = 0.5$[cm] respectively, a total length of $L = 1.85$[cm], and different paraboloid radius contours given by Eq.(7.2).
As it can be seen from Fig.7.2, magnetic field intensity along the axis presents different longitudinal profiles depending on the order of the parabolic side-contour showing that the geometry of the side contour has an important effect in the internal field distribution along the axis. Longitudinal distribution of the magnetic field for two cylinders with matched minor and major radii have been included as a reference. It should be highlighted that the most tilted profile is that obtained by the straight side contour ($n = 1$), while the effects of higher orders in the parabolic geometry tends to flat the profile as in the limit case of a cylinder. In **Appendix F** the analytical solution for the frustum under constant magnetization assumption is shown.

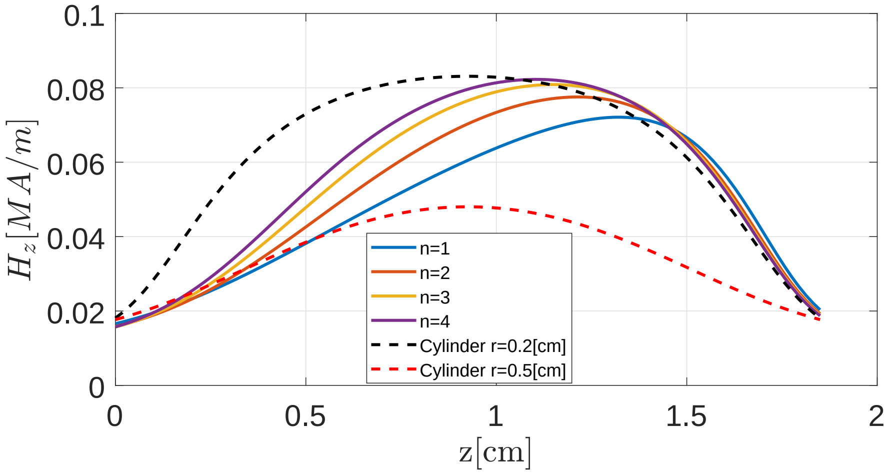

Figure 7.2: Internal magnetic field along the axis for different geometries due to the demagnetization field

7.1.2 Mechanical strain transfer to a coaxial FBG

This section An FBG was placed in a cylindrical hole along cone axis with about 330[μm] in diameter. Thus, epoxy was injected into the hole such that it bonded the FBG to the cone as it is shwon in Fig.(7.3).

When the magnetostrictive composite exhibits large enough magnetostriction properties, mechanical strains can be transfered to a nonchirped FBG placed coaxially to cone, as shown in Fig. (7.1), with the aim to modify the properties of the reflected and transmitted optical spectrum from the FBG. Expected internal distribution of the internal magnetic field will produce a nonuniform strain profile along the axis that can be transferred to the FBG period to induce a chirp [51, 26, 18, 41, 34]. As a result, magnetostriction effect can modify the parameters of the Bragg grating by changing the reflection spectrum characteristics of the FBG [26]. Therefore, the total period of the chirped grating can be written in general by:

$$\Lambda(H_{\text{int}}, z) = \Lambda_0 + \Delta\Lambda(H_{\text{int}}, z) \tag{7.12}$$

where the grating period dependence on the magnetic field can be seen as an effect over the central wavelength and an additional induced nonuniform strain due to the magnetostriction. Since temperature produces also an additional strain in the grating period, the total effect over this parameter can be estimated by [41, 36, 17]:

$$\begin{aligned} \Delta\Lambda(H_{\text{int}}, z) &= \Lambda_0\,(1 - P_{\text{eff}})\,\epsilon(M(H_{\text{int}}, z)) \\ &+ \Lambda_0\,((1 - P_{\text{eff}})(\alpha_M - \alpha_n) + \alpha_n + \zeta)\,\Delta T \end{aligned} \tag{7.13}$$

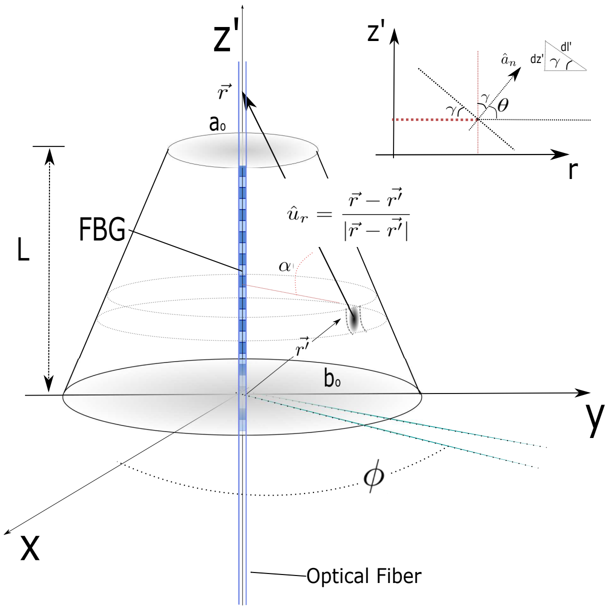

Figure 7.3: Magnetized frustum cone with an embedded coaxial nonchirped FBG

where n_{eff} is the effective refractive index of the fiber, and P_{eff} corresponds to the total strain-optic effect assumed to be dependent on the axial strain only [41, 34]. Thermal expansion can be taken into account by coefficients α_M and α_n that correspond to the thermal expansion coefficients for the magnetostrictive composite and the fiber, and ζ is the thermo-optic coefficient of the fiber. ΔT is the change of temperature that suffers the whole system during the measuring process. However, temperature effects on the chirp magnitude can be neglected [51, 26]. Temperature dependence was not considered in the scope of this thesis and it is left for future work. In order to avoid any drift due to possible temperature effects,. measurements took place in a relatively constant temperature environment. A central wavelength shifting is expected as an averaged effect of the total expansion occurred on the cone, leading to a net increase in the magnitude of the central wavelength in the reflected spectrum that can be directly correlated to the external magnetic field. On the other hand, nonuniform strain will drive the local induced strain $\epsilon(M(H_{\text{int}}, z))$ due to internal magnetization along the axis and will determine the shape of the reflected spectrum. Strain due to magnetostriction can be calculated by using the magnetization magnitude along the axis:

$$\epsilon\left(M(H_{\text{int}}, z)\right) = \frac{3}{2}\epsilon_s \left[\left(\frac{M^2(z)}{M_s^2}\right)\right] \tag{7.14}$$

where ϵ_s should be determined experimentally and $M(z)$ is the magnetization distribution along the axis for different external magnetic fields. In contrast to uniformly strained FBGs [36], steeped strain profiles transferred to FBGs will result in a chirped phase function for the Bragg grating period that turns out into a strong dependence of the reflected spectrum shape magnitude [13, 18]. These effects imply a dependence on the total optical power reflected back from the FBG, allowing the correlation of the optical power with the external field magnitude, which simplifies enormously the instrumentation and measurement devices required during the practical implementation. Once the FBG is bounded along the axis of the cone, the grating will be modulated in length by the magnetostriction effect, leading to a peak wavelength shifting and broadening of the reflected spectrum around the central wavelength. For calculating these effects, it was considered the same description for the effective refractive index in a FBG used in **Chapter 3** and Ref. [13], where the refractive index perturbation can be written by the expression:

$$\delta n_{\text{eff}}(z) = \bar{\delta n}_{\text{eff}}(z)\left[1 + v\cos\left(\frac{2\pi}{\Lambda_0}z + \phi(z)\right)\right], \tag{7.15}$$

being $\bar{\delta n}_{\text{eff}}$ an effective refractive index and v represents the fringe visibility. $\phi(z)$ is the phase shift defined by the chirp effect. Frequency of the grating is controlled by the argument of the cosine function, $\cos(\omega_g(z)z)$, that in general can be written as a function of z by $\omega_g(z) = 2\pi/\Lambda(z)$, such as for a uniform grating spacing should result in a constant grating frequency given by $\omega_0 = 2\pi/\Lambda_0$. Once the chirping period is determined for several magnetic fields, we can determine both: the spectrum shape of the light reflected back from the FBG and the total optical power associated to each magnetic field. Consider a conical frustum with top and bottom radii a_0=0.2[cm] and b_0=0.5[cm] respectively, total length of L=3[cm]. Magnetization was simulated by using the Langeving function to account for nonlinear behavior of magnetization with parameters $\alpha = 0$ and $a = 60084$. Magnetostriction coefficient for the theoretical calculation was assumed to be $\epsilon_s = 750$[ppm]. Figure 7.4 presents the behavior of the magnetostriction curve for the current theoretical analysis. It is worth noting that saturation of the magnetostriction curve is due to the nonlinear magnetization process modeled by the Langevin function as explained in **Chapter 4**. Figure 7.5 presents the theoretical strain distribution of the FBG period caused by the internal distribution of the magnetization for different magnetic fields. Two different behaviors can be theoretically obtained from the strain distribution imposed by the magnetostriction and the side of light incidence. Figure 7.6 presents the theoretical response when light incidents through the cone's top and basis. As it can be seen from both figures, depending on the direction of incident light, the spectrum response of the FBG exhibits different spectral properties. As ti can be seen from

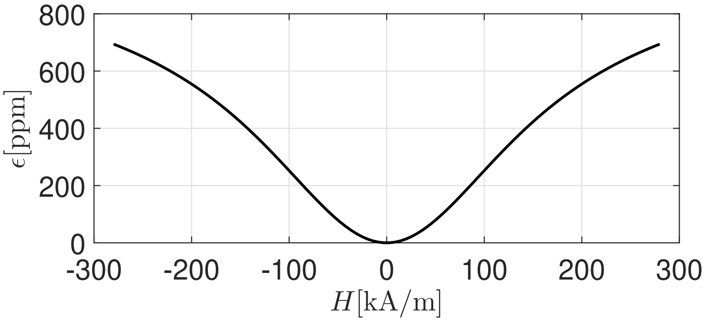

Figure 7.4: magnetostrictive curve for the theoretical analysis

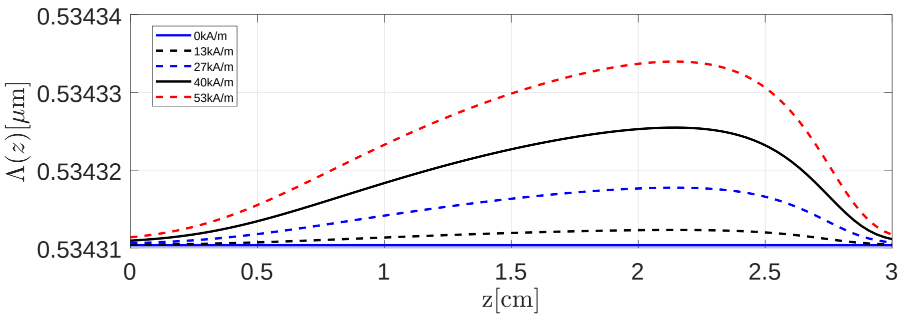

Figure 7.5: Theoretical strain distribution along the cone axis caused by the nonuniform magnetic field distribution inside the cone

Fig.7.6(a), incidence through the cone's top leads to broadening of the spectrum with small shifting in frequency for the peak wavelength. On the other hand, incidence thorough the cone basis presents some wavelength shifting for the peak wavelength as well as some broadening in the reflected spectrum for different magnetic fields. Since spectral broadening occurs in both cases, a dependence on the total optical power can be also obtained in both configurations. Figure 7.7 shows the theoretical optical power associated to each of the spectrum shapes when light incidents through basis and top.

As it can be seen from Fig. 7.7 normalized optical power increases in both scenarios reaching a saturation point. In the case of top incidence (Fig. 7.7(a)) behavior of the reflected is dominated by the high slope of the initial section of the transferred strain. Therefore, the wavelength shifting is minimal. In the other case, there is an appreciable shifting and spectrum broadening (Fig. 7.7(b)), this latter accounting as well for power increment. In this particular case, there is a slightly inflection point in the external magnetic field magnitude where the optical power folds to decrease. This effect is mainly because at some point of the transferred strain, the interference pattern that reflects one specific wavelength is lost due to the high deformation of

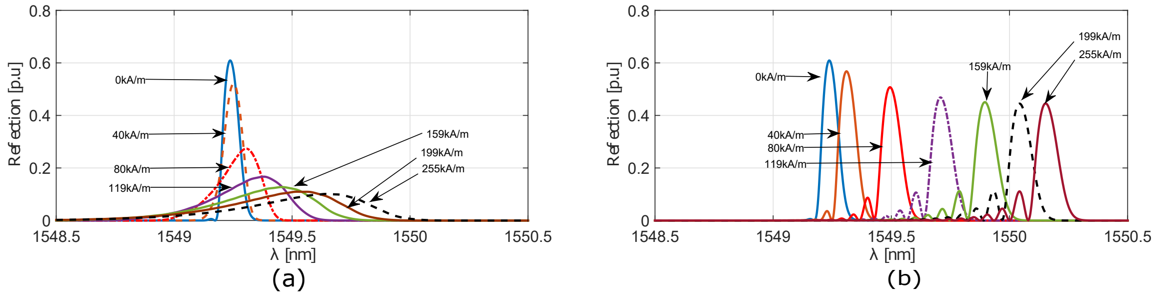

Figure 7.6: Theoretical reflected spectrum from the FBG under the strain distribution caused by the nonuniform magnetic field inside the conical frustum. (a) Incidence through the top. (b) Incidence through the basis.

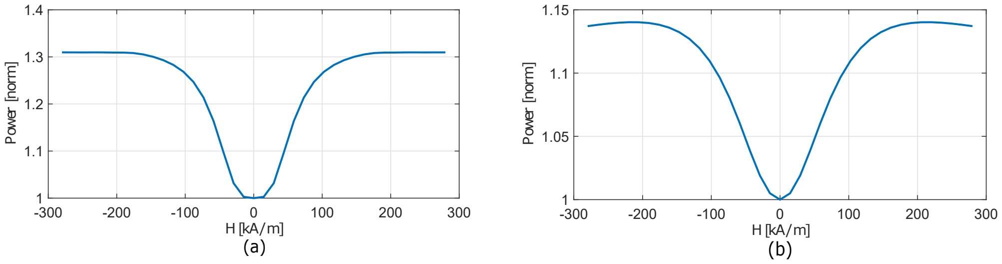

Figure 7.7: Theoretical optical power of the light reflected from the FBG under different magnetic field magnitudes. (a) Incidence through the top. (b) Incidence through the basis.

the initial section, appearing some ringing spectrum at the left side of the peak wavelength. It is important to note that this is the typical behavior of linear chirp discussed in **chapter 3**. In the following subsections, a set of practical implementation of a fiber magnetic sensor were done based on the theoretical framework presented before but using magnetostrictive composites instead of monolithic magnetostrictive materials.

7.1.3 Magnetostrictive composite fabrication

Monolithic implementations of magnetostrictive transducers presents some manufacturing disadvantages. Particularly, Terfenol-D is restricted to be manufactured in specific geometrical shapes. Additionally, Terfenol-D in its monolithic phase it is very brittle, which restricts its usage in some industrial applications. These drawbacks have motivated the use of magnetostrictive composites for developing new magnetic field sensors. This subsection describes the fabrication of magnetostrictive composites, where instead of monolithic Terfernol-D, an epoxy resin is used as a host matrix for Terfenol-D powder. One of the advantages of using epoxy resin is the capability of having several geometrical shapes, which represents a high flexibility in the proposition and fabrication of engineering composites. Figure 7.8 shows the process of the mold construction. Once the mold is fabricated, Terfenol-D powder and epoxy resin can be mixed to form the desired geometrical shape. Figure 7.9 depicts the fabrication process of a 3D-cone shape magnetostrictive composite.

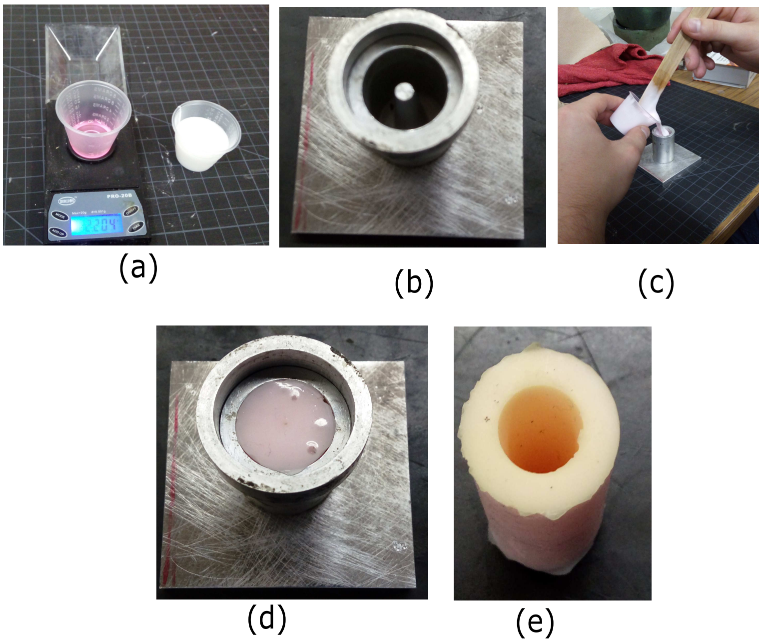

Figure 7.8: Negative cone-volume mold fabrication, (a) Mold resin, (b) Cavity for the mold fabrication, (c-d) filling the cavity with the mold, (e) Cone Mold, (e) mold with negative volume of the cone

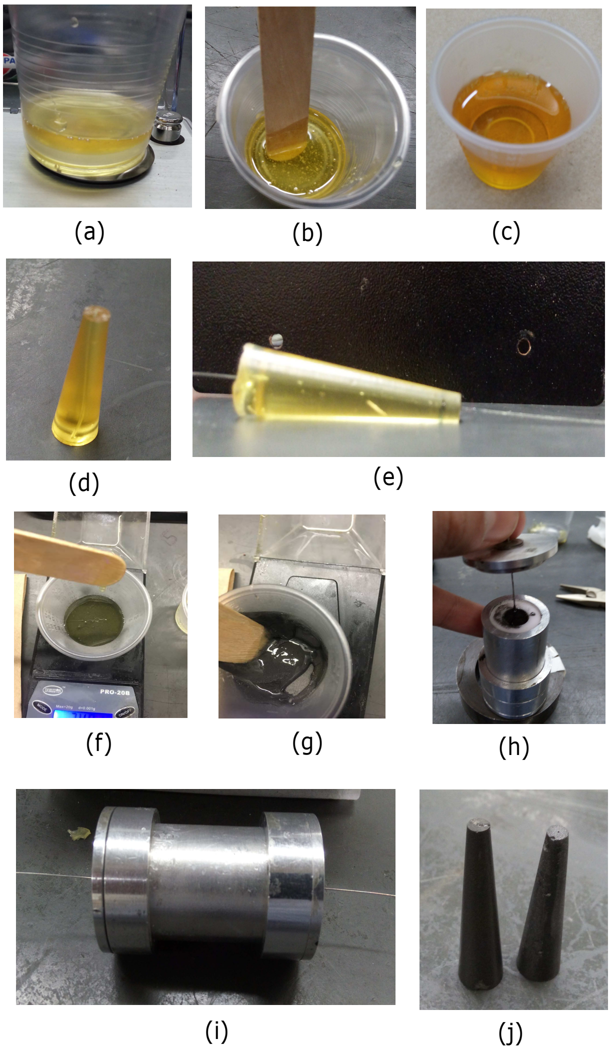

Figure 7.9: cone shape magnetostrictive Composite Fabrication, (a) Epoxy-Hardener Ratio Fabrication, (b) Air bubbles in Epoxy-Hardener Mix, (c) Epoxy-Hardener Mix after vacuum chamber (d) Epoxy Cone with coaxial cavity (e) Epoxy Cone with coaxial Fiber Optic (f) Epoxy-resin and Iron or Terfenol-D powder particles (g) Magnetostrictive Composite, (h) Magnetostrictive Composite in mold cavity with a piano-wire (i) Cavity with piano-wire (j) Cone-shaped Magnetostrictive Composite

Composite fabrication specification by mass					
Cone Ø	Terf.-D [gr]	Epoxy [gr]	Hard.[gr]	T-D mass in comp. [gr]	Ratio
1, Ø =330.2μm	8.989	5.200	2.345	6.19	54%
2, Ø =431.8μm	10.086	3.543	1.829	7.44	65%
3, Ø =330.2μm	10.939	3.621	1.888	7.58	67%

Table 7.1: Composite fabrication of frustum cones. Axial channel diameters: Cone 1, Ø =330.2μm. Cone 2, Ø =431.8μm. Cone 3, Ø =330.2μm. Terfenol-D mass used in the mixture, used mass Epoxy/Hardener, Terfenol-D mass in the cone, Ratio between Terfenol-D mass and total mass

A magnetostrictive cone-shaped composite was fabricated of Terfenorl-D powder with particle sizes between 200-300 [μ m]. The composite was made by using epoxy resin to mold a cone with 3[cm] in length and three different cases were considered in the fabrication. Total mass of this cone made of monolithic Terfenol-D can be calculated by:

$$m_T = \rho\frac{\pi}{3}L\left(b_o^2 + a_o^2 + a_o b_o\right) \tag{7.16}$$

Density of Terfenol-D is reported to be about 9200-9300 [kg/m^3], leading to a total monolithic mass around $m_T = 11.4$[gr]. Since the usage of epoxy and hardener during the fabrication process, density of the Terfenol-D particulate composite will depend on the mixture ratios. Fabrication process firstly mixes the epoxy/hardener slightly avoiding air bubbles inclusion. Afterwards, the epoxy/hardener mixture is put into a vacuum chamber to extract some of the air bubbles gained in the mixture during the mixing process. Finally, Terfenol-D particles are added to the mixture and slightly mixed. Once the composite mixture looks homogeneous, it is poured into the cone mold for curing. Depending on the amount of Terfenol-D powder added to the mixture, one can calculate the ratio of Terfenol-D in the composite and the corresponding total mass of magnetostrictive material used for fabricating the cone. Table 7.1 resumes the amount of epoxy-hardener and Terfenol-D powder during the fabrication process of the mixing.

As it shown in Table 7.1, different channel diameters were used for the experimental set-up. Cone 1 was the cone that used less amount of Terfenol-D with the smallest channel diameter gauge with the aim to validate is less material was able to generated the chirping process.

7.1.4 Magnetostrictive composite frustum cone

In the previous analysis of the mechanical strain transferred to the coaxially embedded FBG, the internal magnetic field distribution was assumed to be created by a monolithic magnetostrictive frustum cone. However, as it was discussed and presented in **chapter 5** some corrections in the formulation of the internal field distribution should be done for accounting particulate material effects. This section will analyze the case of a frustum cone by using the model developed in **chapter 5** for dealing with magnetic composites and depending on the magnetization distribution to calculate the associated magnetostriction. Figure 7.10 presents a schematic of a frustum cone made of magnetic particulate material modeled by cuboids. Figure 7.11 shows the actual aspect of a discretized cone by using the proposed model for dealing with magnetostrictive composites. Depending on the cuboid size the representation of the actual geometry will be enhanced. As it can be seen from Fig. 7.11 representation of circular shapes leads to some inaccuracies regarding geometry because of the rectangular system used for solving the vector potential equations in **Chapter 5**. However, it will be shown in this chapter that inaccuracies in the internal magnetic field calculation and consequently the magnetization, can be neglected in describing the main aspects of the magnetostrictive results. For the initial case, a frustum cone made of Terfenol-D/Epoxy with same geometric dimensions as in the monolithic case was considered. Radius at the bottom and the top $b_0 = 5$[mm], $a_0 = 2$[mm], respectively,

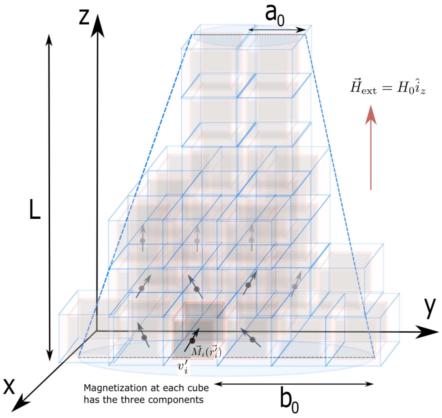

Figure 7.10: Schematic of the discretization of a frustum cone of radius at the bottom and the top b_0, a_0, respectively and length L.

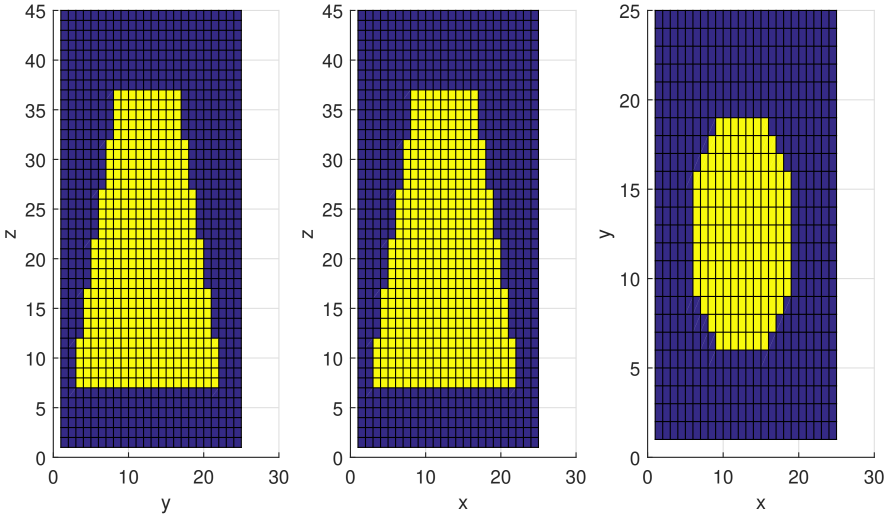

Figure 7.11: Actual discretization of the cone in cuboids by using the proposed discrete model to analyze magnetostrictive composites.

and length $L = 3$[cm]. Different discretization sizes were considered in the analysis. Typical cuboid dimension was about $v_i' = 0.83 \times 0.83 \times 2.25[\text{mm}^3]$. However, some simulations were performed with smaller particles (cuboid maximum length side about 250[μm]) to validate the results.Figure 7.12 presents the magnetization distribution (equi-potential lines) inside the composite when discrete particles are considered.

Figure 7.13 presents the comparison between Finite Element Method (FEM) calculations and the current approach for the magnetic field and magnetization along the axis for a frustum cone, when the magnetic material fills totally the discrete cell. As it can be seen from the figure, current proposal is able to reproduce main characteristics of the induced magnetization in the frustum cone. It is worth noting that differences can be due to the discretization process where geometrical representation through cuboids could lead to the discrepancies between both calculations.

One of the main advantages of the proposed composite model is that we can control the size of magnetic body for each cell, thus we can evaluate different scenarios associated to the size distribution of the magnetic bodies in the analysis of the magnetostrictive composite. Figure 7.14 presents the comparison of the magnetic field and magnetization along the axis for different volume fraction of the magnetic body inside the cell. Magnetization and magnetic field are evaluated at the center of each magnetic body. As it can be seen from Figure 7.14, the main effect of the magnetic particle size is to decrease the steepness of the magnetization distribution along the axis, reaching a flatter profile for the lowest volume fraction considered in the calcu-

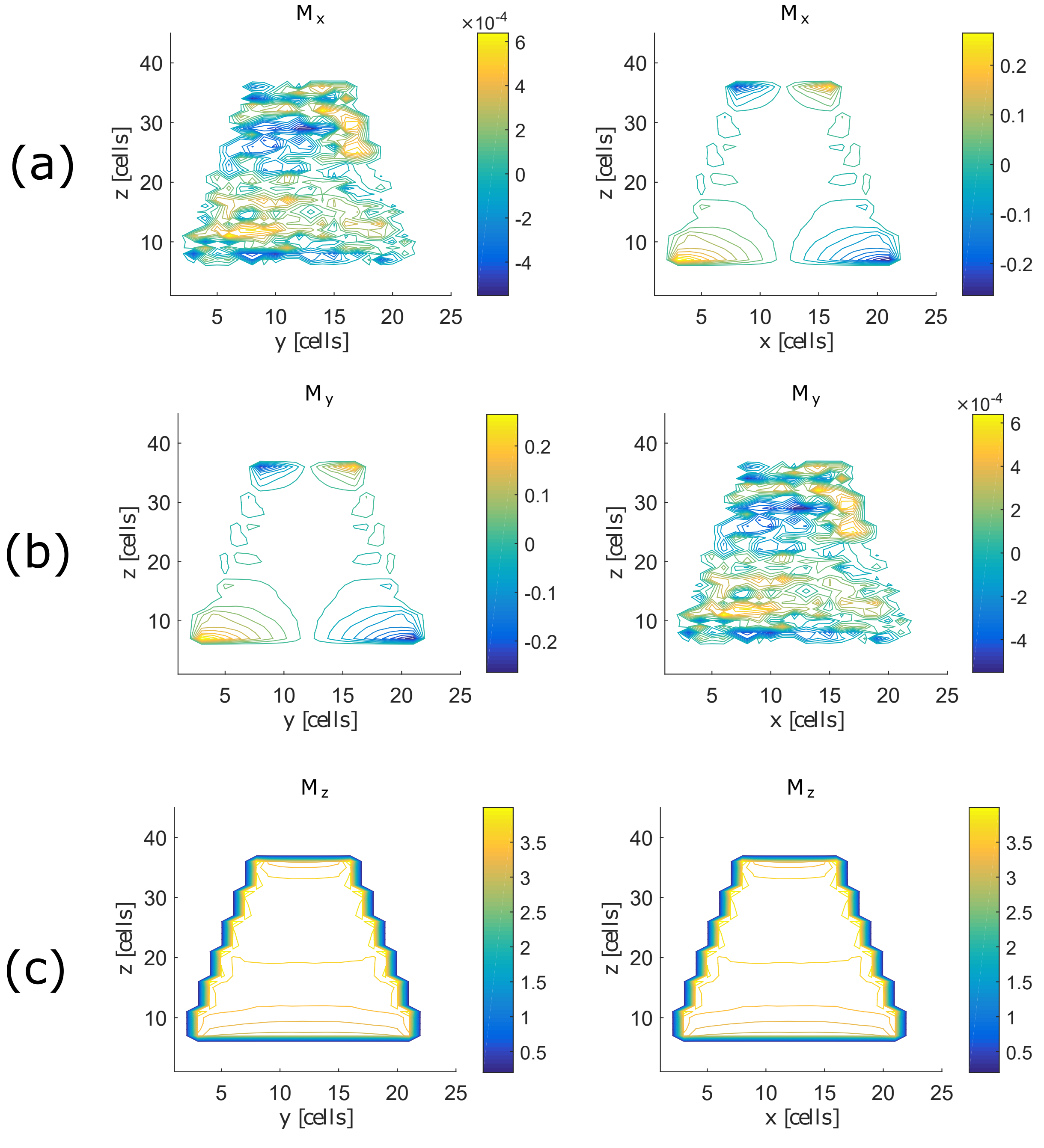

Figure 7.12: Internal distribution of magnetization by using the proposed composite model. Transverse cuts along axis of the frustum cone (a) x-component (b) y-component (c) z-component

lations. This result shows that the effect of the spatial distribution of the particles not necessarily changes the main aspect of internal field profile when compared to the solid analysis, but the size of the particles plays an important role in the steepness of the internal magnetization profile.

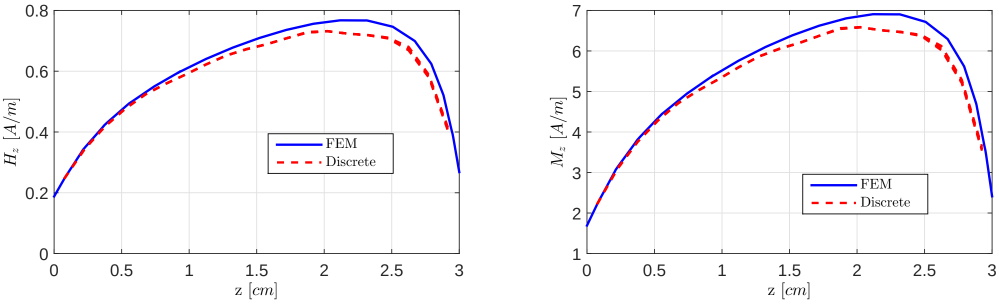

Figure 7.13: Calculated magnetic field and magnetization along the axis for a frustum cone of radius at the bottom and the top $b_0 = 5$[mm],$a_0 = 2$[mm], respectively and length $L = 3$[cm].(solid line: FEM, dashed line: current discrete approach).

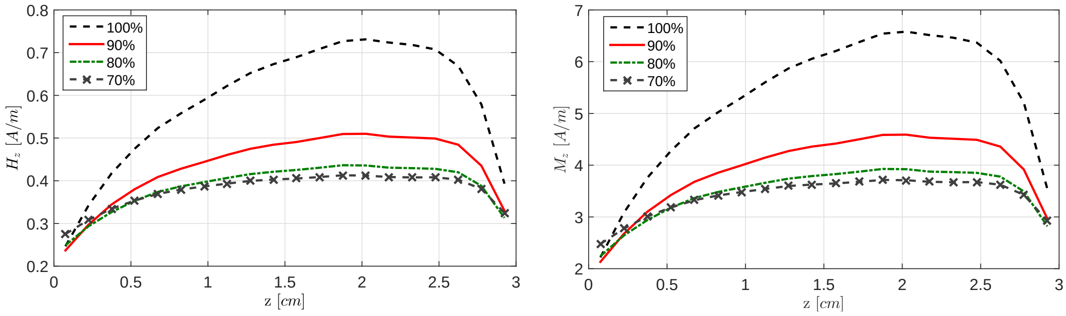

Figure 7.14: Calculated magnetic field and magnetization along the axis for a frustum cone for different volume fractions. (radius at the bottom and the top $b_0 = 5$[mm],$a_0 = 2$[mm], length $L = 3$[cm])

Since in the experimental process different particulate magnetostrictive material sizes are included in the same composite. An additional simulation was performed to calculate the response of the magnetization along the axis of the cone when different particles sizes are present in the magnetic body. In this case, a simulation assigning different dimensions to each of the cuboid was implemented, such as we can approximate the magnetization response due to non-uniform size particles. Since in the proposed formulation dimensions for each cuboid ΔX_i, ΔY_i, ΔZ_i can be specifically determined as an input, total magnetization effect pointing along the z-axis can be evaluated based on a random distribution of the particle sizes. Figure 7.15 present the behavior of the internal magnetic field and magnetization when two ranges of variation in size are considered. It is worth noting that the inclusion of random sizes in the particulate material leads to some ripples in the magnetic field magnitude as well as in magnetization along the axis. This effect is understood from the spaces between magnetic particles that leads to a some variations in coupled field magnitude between magnetic bodies in the composite. However, same effect happens to the steepness of

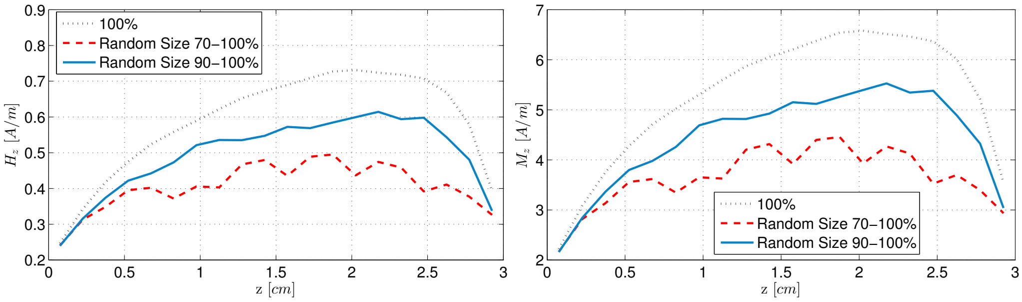

Figure 7.15: Calculated magnetic field and magnetization along the axis for a frustum cone for random sizes of the particles (being 100% of the volume a particle about $700\mu m$). (radius at the bottom and the top $b_0 = 5$[mm],$a_0 = 2$[mm], length $L = 3$[cm])

the magnetic field when decreasing the effective volume that fills the magnetostrictive material in the discrete cell as shown in Fig.7.14. There is an additional issue that should be taken into account for the analysis of the composite responses. In the previous analyses unit cell size was about two times (700[μm]) the actual particle size used in the experiment (300[μm]). Therefore, with the aim of checking for the influence of the unit cell size in the discretized model, a last simulation case was performed regarding the particle random size and the number of particles in the total volume. In this case a greater number of cells were used to model the magnetic body which means smaller unit cell size, thus smaller dimensions for the particulate material. Since randomness showed to have some ripple effect upon the internal field, this random sizes of the particles were also included in the simulation. Figure 7.16 presents the comparison of the internal magnetic field and associated magnetization when smaller particulate grains are considered. As it can be seen from Fig.7.16(a), there are some differences between the responses for random sizes between 90% to 100%. However, bigger sizes for the particles tracks the main characteristics of the internal field along the axis for the correspondent percent of particle size. Magnetization is also well represented by bigger particles. These results suggest that the parameter that controls the magnetization and internal field characteristics along the axis is mostly the volume fraction to the corresponding cell size instead of its actual size. Therefore, acceptable results can be obtained by using bigger unit cell sizes if the right volume fraction is taken into account.

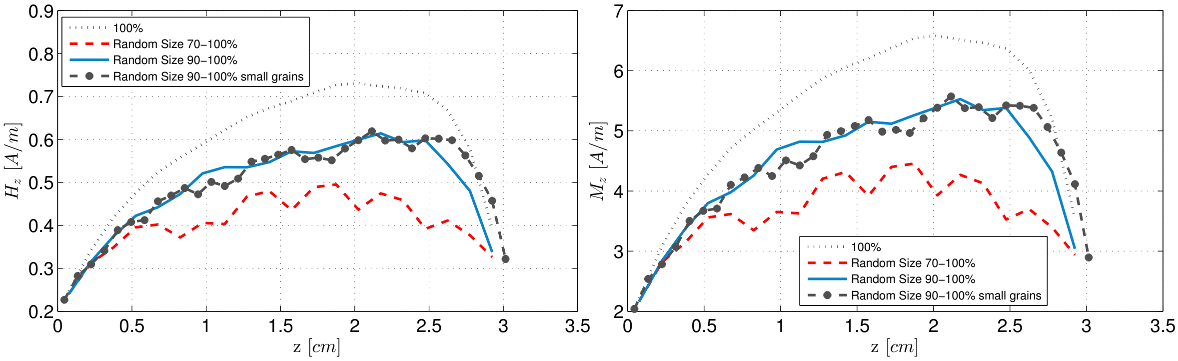

Figure 7.16: Calculated magnetic field and magnetization along the axis for a frustum cone for random sizes of the particles when smaller particles are included (being 100% of the volume a particle about $250\mu m$). (radius at the bottom and the top $b_0 = 5$[mm],$a_0 = 2$[mm], length $L = 3$[cm])

7.1.4.1 Anhysteretic model for the composite frustum cone

This section presents the implementation of the proposed approach over a frustum cone with the same dimensions of that presented before. Therefore, consider a frustum cone of radius at the bottom and the top $b_0 = 5$[mm], $a_0 = 2$[mm], respectively, and length $L = 3$[cm]. For the sake of simplicity analysis the anhysteretic behavior of the cone is modeled through the modified Langevin function presented by Jiles and Artherton [24]. In this case, we are going to assume that each component of the magnetization vector of each cuboid satisfy the equation:

$$M = M_s \left(\coth \left[\frac{H_{\text{ext}} + \alpha M}{a_o} \right] - \frac{a_o}{H_{\text{ext}} + \alpha M} \right) \tag{7.17}$$

In the initial proposition of the JA model, factor α represents the interaction between the magnetic dipoles and it is typically chosen to fit the experimental data. One of the advantages of the current formulation is that this parameter can be evaluated from the geometry of the composite through the demagnetization field. Therefore, modified Langevin function for the discretized model can be written by:

$$M = M_s \left(\coth \left[\frac{H_{\text{ext}} + H_{\text{dmg}}(M)}{a_o} \right] - \frac{a_o}{H_{\text{ext}} + H_{\text{dmg}}(M)} \right) \tag{7.18}$$

where all the components of the demagnetization field can be taken into account for the calculation. First simulation case will present the convergence of the iterative method when this non-linearity in the magnetization is included. Linear susceptibility can be calculated from the modified Langevin function by the expression:

$$\chi_0 = \frac{M_s}{3a_o}, \tag{7.19}$$

Let's consider a saturation magnetization of $M_s = 1.5$[MA/m] and $a_o = 55556$[A/m] such as the susceptibility in the linear region of the saturation function is about $\chi_0 \approxeq 9$. However, with the aim to validate the convergence of the method we will consider and initial susceptibility of $\chi_m = 4$ and $\chi_m = 40$ to guess an initial magnetization, thus the iterative process should converge in both cases to the magnetization defined by the modified Langevin function at the corresponding internal magnetic field. External field is considered along the z-axis by $\vec{H}_{\text{ext}} = H_0 \hat{i}_z$, with $H_0 = 10$[A/m]. Figure presents the results of the magnetization along the z-axis of the frustum cone when initial guesses of magnetization are far from the current magnetization defined by the modified Langevin function. Convergence error plots are also presented in Fig. 7.18(a) to show that in both situations the iterative algorithm finds the current solution for a maximum relative error of $\text{error}_{\max} = 1 \times 10^{-3}$. Next simulation considered different magnitudes of the external magnetic field when the magnetization for each cuboid is driven by a modified Langevin function defined by the parameters

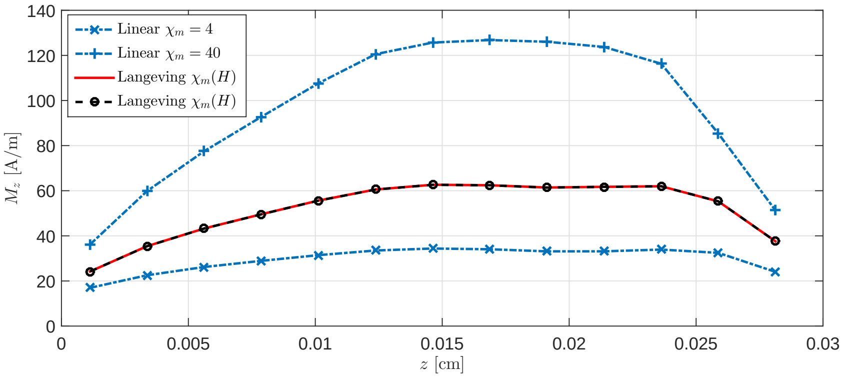

Figure 7.17: Magnetization along the z-axis of the frustum cone for two guessed initial magnetizations and convergence to the same magnetization profile defined by the modified Langevin function.

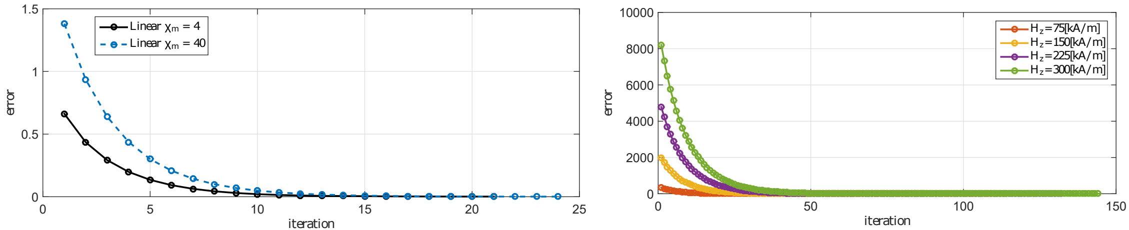

(a) (b)

Figure 7.18: (a)Error convergence for two initial susceptibilities to guess the initial magnetization inside the magnetic body. (b)Error convergence for different external magnetic fields along the z-axis.

$M_s = 1.5$[MA/m] and $a_o = 35556$[A/m]. Figure 7.18(b) presents the convergence plot when different external magnetic fields are considered. Maximum relative error for stopping the iterative process was set to $\text{error}_{\text{max}} = 1 \times 10^{-3}$. Magnetization inside the body was calculated for each of the external fields. Figure 7.19(a) presents the results of the z-component of the magnetization along the axis of the frustum cone. Finally, Fig 7.19(b) presents the magnetization against the external magnetic field for different points along the axis of the frustum cone.As it can be seen from the figure, those points located at the volumetric center of the cone reach the saturation easier than those points at the top and bottom. This is expected from the distribution of the magnetization magnitude.

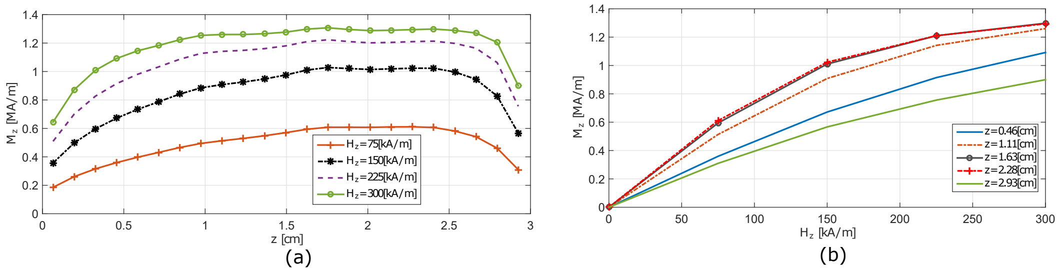

(a) (b)

Figure 7.19: z-component of magnetization along the axis for different external magnetic fields (a) Magnetization along the axis for different external magnetic fields. (b) magnetization for different heights along the axis of the frustum cone.

7.1.4.2 Effects of the particle shape in the anhysteretic behavior of the composite frustum cone

Taking advantage of the proposed formulation for modeling composites, random sizes and shapes of the magnetic material can be included in the simulation. As it was shown before, the presence of random particle sizes in the composite tends to decrease the total magnetization when compared with the solid case and includes some fluctuations of the magnetization magnitude along the longitudinal axis. Additionally, shape of the cuboid contributes with a demagnetization field that can be seen as an additional anisotropy due to the geometrical shape and the orientation regarding the external magnetic field. Next simulation considered two different types of magnetic cuboids in the composite. One of the cuboids had set to have a wider dimensions for the ΔX_i and ΔY_i, i.e. $\Delta X_i > \Delta Z_i$ and $\Delta Y_i > \Delta Z_i$. On the other hand, we considered cuboids where the longer dimension was along the z-axis, i.e. $\Delta Z_i > \Delta Y_i$ and $\Delta Z_i > \Delta X_i$. The idea behind this simulation is to compare the effects upon the magnetization when different demagnetization fields for a z-directed external field occurs in each cuboid. Figure 7.20 presents a comparison of the magnetization along the axis of a frustum cone of radius at the bottom and the top respectively of $b_0 = 5$[mm], $a_0 = 2$[mm], and length $L = 3$[cm]. For the first simulation case a grid of $\Delta x_i = \Delta y_i = 833 \mu m$ and $\Delta z_i = 780 \mu m$. For the second simulation $\Delta x_i = \Delta y_i = 416.67 \mu m$ and $\Delta z_i = 1.6mm$.

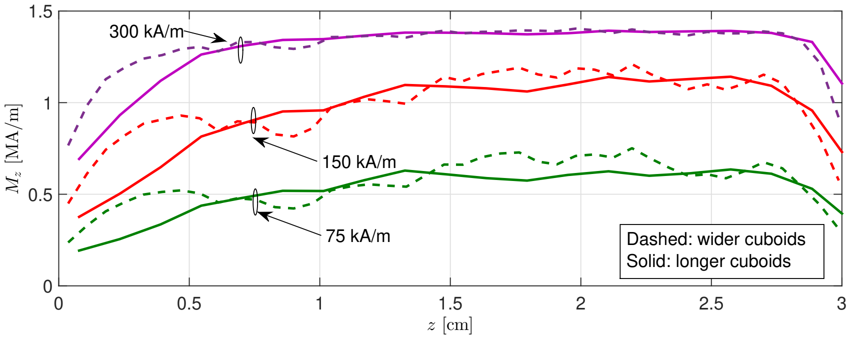

Figure 7.20: Nonlinear magnetization along the axis for two different shapes of grains. Dashed lines considers random size of cuboids with a maximum size of $\Delta x_i = \Delta y_i = 833 \mu m$ and $\Delta z_i = 780 \mu m$. Continuous line considers random size of cuboids with a maximum size of $\Delta x_i = \Delta y_i = 416.67 \mu m$ and $\Delta z_i = 1.6mm$.

Figure 7.20 suggests that the contribution of shape anisotropy in the case of wider cuboids induces important variations of the magnetization profile along the axis. In contrast, when longer particles are considered softer profiles of magnetization along the axis are obtained. This behavior is explained by the contribution of the demagnetization field due to the cuboid shape, which in the last case is smaller and the multi-cuboid interactions is the dominant effect over the magnetization of the whole body. Next simulation case shows the results of the quasi-static algorithm for different positions along the cone axis. Figure 7.21 presents the behavior of the anhysteretic magnetization for a modified Langevin with parameter $a_0 = 15556$[A/m] and $M_s = 1.5$[MA/m].

Hysteresis was also included by using the Jiles-Atherton proposal. Figure 7.22 presents the hysteresis curves for reversible and irreversible magnetizations at different heights of the cone, when $c = 0.2$ and $a_0 = 15556$[A/m]. Lossy factor was set to be $k/\mu_0 = 10e3$.

Figure 7.23 presents the anhysteretic and the hysteretic curve for the cuboid at $z = 2$[cm] of the axis of the cone. In this hysteretic consideration the reversible and irreversible magnetizations were considered. Parameters of the anhysteretic modified Langevin function were $a_0 = 15556$[A/m] and $M_s = 1.5$[MA/m]. Different lossy factors were consider to check the typical increment on the internal area of the hysteresis

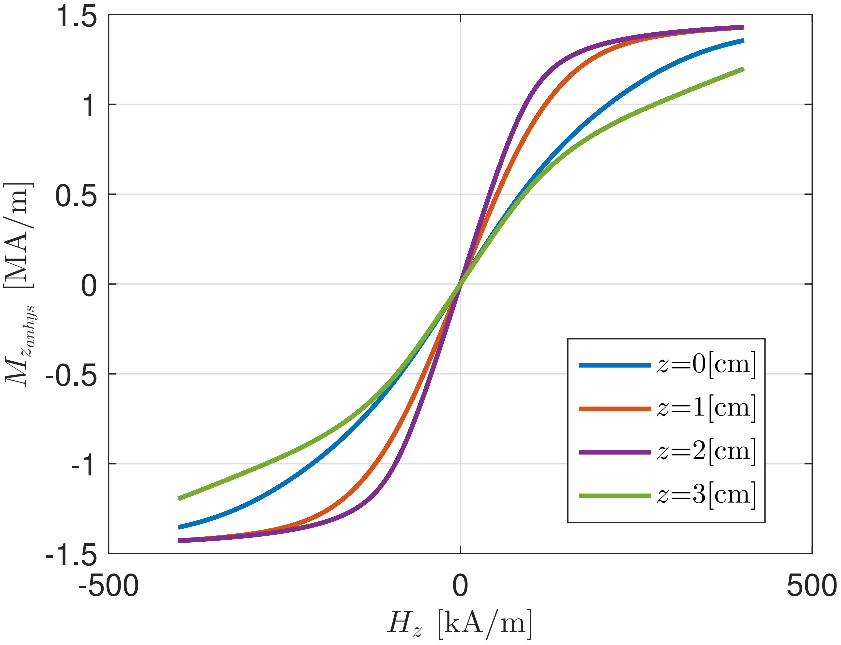

Figure 7.21: Anhysteretic curves at different heights of the cone.

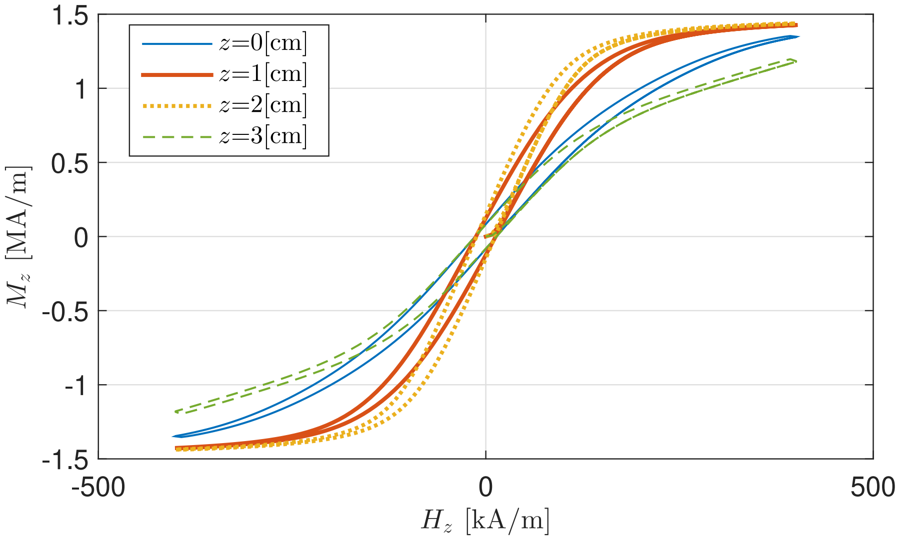

Figure 7.22: Hysteretic curves at different heights of the cone.

curve, these factors were $k/\mu_0 = 10e3$, $k/\mu_0 = 100e3$ and $k/\mu_0 = 1000e3$. All the simulations include a factor for accounting the reversible magnetization of $c = 0.2$.

An additional simulation was performed in order to check the effects of the particle size in the hysteresis behavior of the composite. Figure 7.24 presents the behavior of the hysteresis curves for the same discretization case. However, one of the simulation case includes a random size of the particle inside the discrete cell. As it can

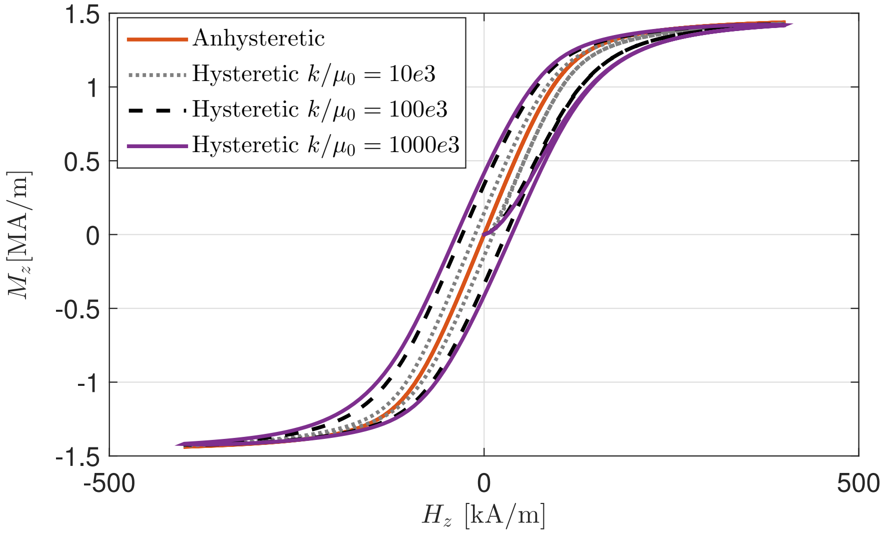

Figure 7.23: Anhysteretic and Hysteretic curve for one of the cuboids at $z = 2$[cm] of the cone axis.

be seen from the results, an important reduction of the loop area in the hysteretic behavior of the cone a different heights is noticed. In contrast, the saturation point is reached almost at the same magnetic field. As it was shown in the previous section, the effects of the particle size on the magnetization of each cuboid are of great importance. Therefore, Jiles-Atherthon model will be also driven by this dependence on the particle size.

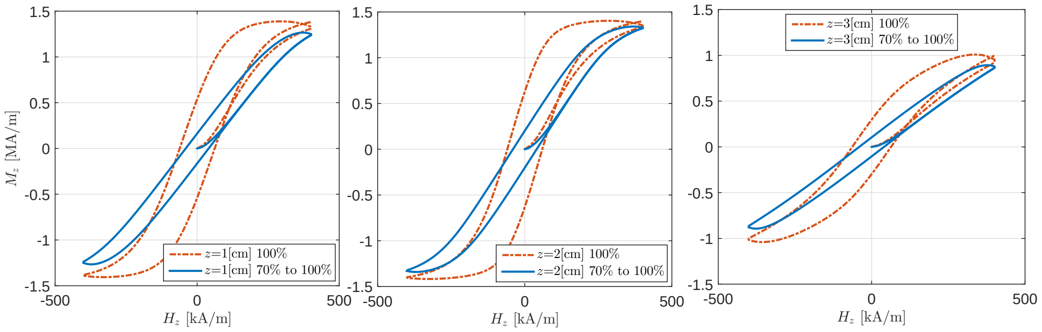

Figure 7.24: Hysteresis curves at different heights of the cone axis when random particles sizes are considered.

7.1.4.3 Comparison against the analytical approach

The assumption of linearity in the analytical approach becomes an important difference between the results obtained in the composite model and those results obtained by the analytical solution. Figure 7.25 shows the comparison for the magnetization along the axis between theoretical approach when magnetic susceptibility is considered a function of the magnetization and those results obtained by using the composite model presented in **Chapter 5**.

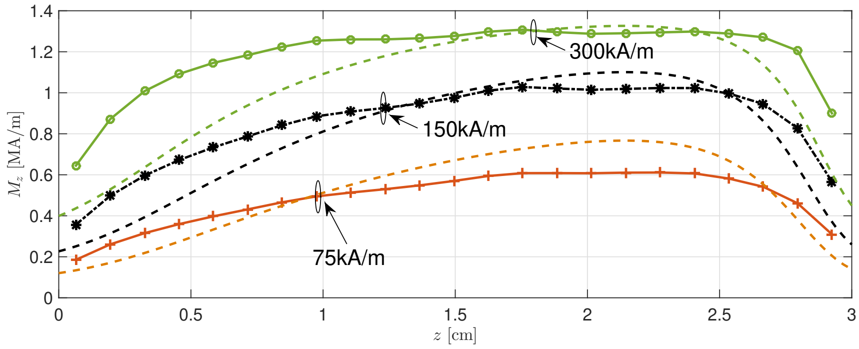

Figure 7.25: Comparison of the analytical approach against the results obtained by the proposed composite model assuming anhysteretic magnetization. Dashed lines: Analytical. Solid with markers: Composite model

As it can be seen from Fig. 7.25 analytical approach predicts relatively good the magnetization value in some range in the cone center. However, there is an underestimation in the first section of the cone length. This is because the model that has been assumed for the saturation of the cuboids in the composite case, where transverse components of magnetization contribute to saturate quickly along this top and bottom sections of the cone. As it will be shown in the following, this effect associated to the increment of the initial slope has important effects upon the behavior of the reflected spectrum and the broadening properties. In order to present these effects, same simulation scenario presented in **section 7.1.2** was simulated again, but in this case by using the composite model including anhysteretic magnetization process. Figure 7.26 presents the theoretical spectrum responses when light incidents through the top (Fig. 7.26(a)) and basis (Fig. 7.26(b)). An important difference with the results calculated by the analytical approach in **section 7.1.2** is that spectral broadening are very similar each other and present wider bandwidths. Based on the same argument of spectral broadening, there is a dependence on the optical power for both cases. Figure 7.27 presents the theoretical normalized optical power for both sides of light input. As it can be seen from Fig.7.27 same main tendency is obtained for the normalized power in both cases. There is a particular difference associated to the initial slope of the top incidence of light. Although maximum normalized power in sightly higher, sensitivity in the initial region is certainly larger as in the

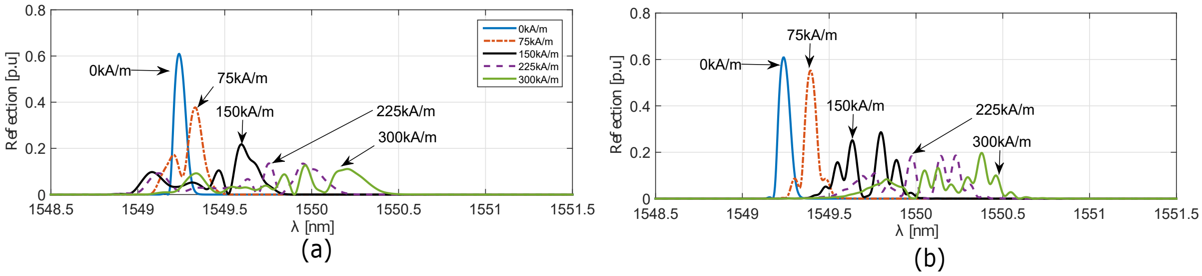

Figure 7.26: Theoretical reflected spectrum from the FBG under the strain distribution caused by the nonuniform magnetic field inside the conical frustum calculated using the composite model. (a) Incidence through the top. (b) Incidence through the basis.

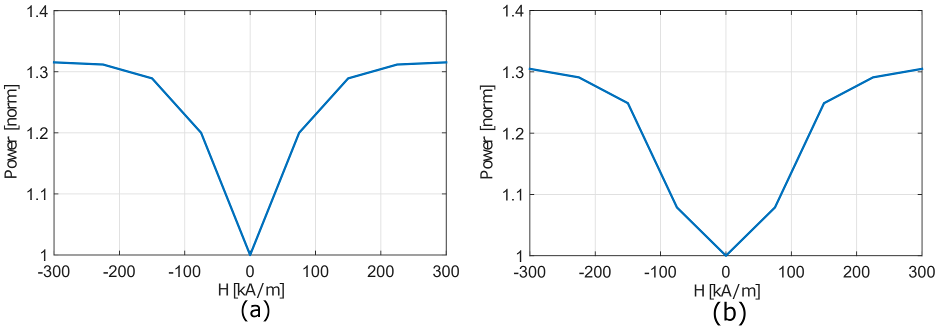

Figure 7.27: Theoretical normalized optical power. (a) Incidence through the top. (b) Incidence through the basis.

theoretical case analyzed by using the analytical approach. Another important result derived form the composite model is that both top and basis incidence of light leads to around 1.3 times the initial power due to broadening. This effect can be explained by the initial slope that will be transferred to the FBG when anhysteretic behavior is included. Following sections presents some of the experimental results that were acquired during the implementation of the magnetic field sensor.

7.1.4.4 Curing and FBG bonding process

Once the cone-shape composite is fabricated. A FBG is attached coaxial to the cone by using fiber bond epoxy. Before performing any measurement of the magnetostrictive behavior of a cone-shaped composite, it was required to leave the bond between the FBG and cone to cure completely. Since mechanical properties can be changed during this process, the FBG reflection spectrum was monitored during the whole curing time process. Fig. 7.28 presents the reflection Spectrum before and after FBG bonding process.

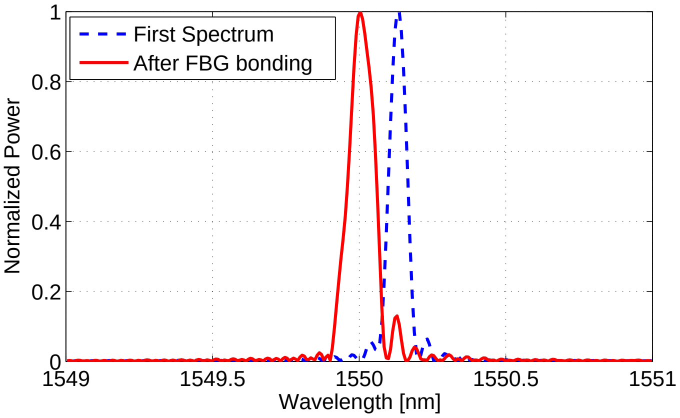

Figure 7.28: Reflection Spectrum before and after FBG bonding process

As it can be seen from Fig.(7.28) the bonding process between the FBG and the cone leads to a wavelength shift in the peak reflected wavelength, but also a modification in the total spectrum change. This curing process implies an initial non-uniform strain distribution along the FBG. prediction of this *pre-strain* in the FBG is a very difficult task because it involves several factors associated to the mechanical condition of the FBG inside the channel, different dynamics of curing process of the bonding epoxy, as well as non-uniformities of the amount of epoxy along the FBG. Control strategies of all these factors during the fabrication process are part of future improvements for the construction of this type of sensors and are proposed as future work. In the scope of this thesis, the analysis is performed upon some initial assumptions and it is focused on describing the main characteristics of the sensor for its suitable implementation in practice.

7.1.4.5 Experimental measurements

This subsection is aimed to show the experimental behavior of the sensor when it is exposed to the magnetic field. Experimental set-up consisted in introducing the cone-shaped composite into an external magnetic field produced by a set of Helmholtz coils that generates an uniform magnetic field along the cone axis. During measurements reflected spectra from the embedded FBG were done by using an Optical Spectrum Analyzer (OSA) during different magnetization cycles, as well as the use of a photodetector for measuring the optical power reflected back from the embedded FBG.Figure 7.29 shows the experimental set-up for measuring the external magnetic field. Fig 7.29(a) shows the magnetostrictive composite frustum cone place between two Helmholtz coils. Fig 7.29(b) presents a schematic of the optical circuit for measuring the reflected spectrum characteristics of the embedded FBG and Fig 7.29(c) presents the simplified optical circuit where the optical spectrum analyzer is replaced by a photo detector with a data acquisition system.

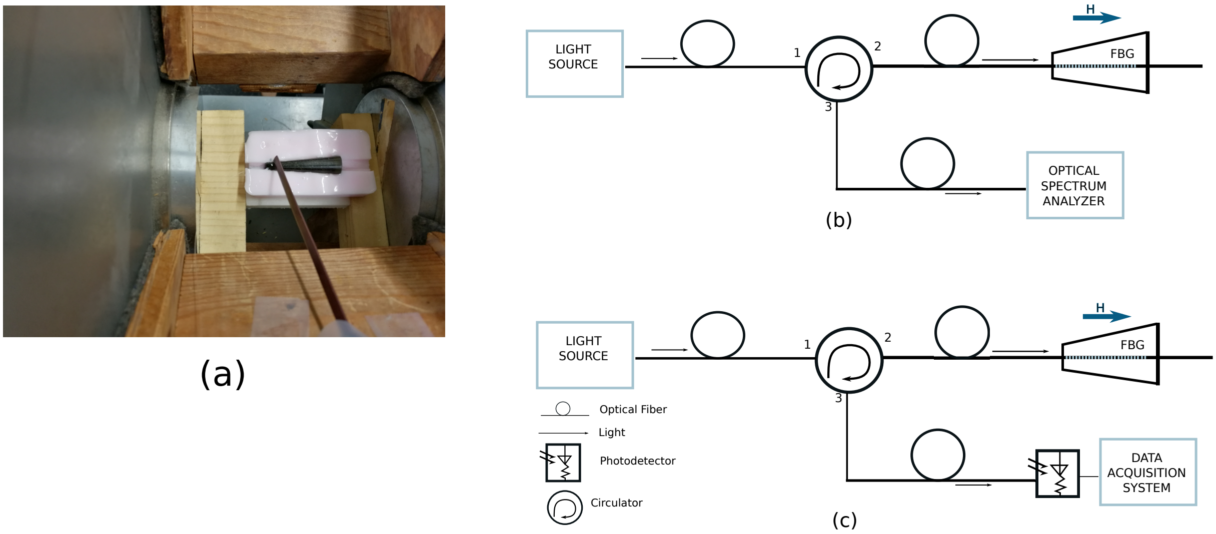

Figure 7.29: Experimental set-up (a) Magnetostrictive cone immersed in a uniform magnetic field generated by a pair of Helmholtz coils. (b)Schematic of the optical circuit for measuring the reflected spectrum. (c) Simplified optical circuit for measuring optical power.

In this set-up, magnetic field was measured using a calibrated probe, which was located close to one of the cone's end. Magnetic flux density measured by the probe was increased up to $B_m = 3000$[G] and decreased down to the minimum value. Afterwards, magnetic field was reversed and increased again up to the top and decreased gradually to zero. This test allows to determine hysteresis and saturation of the composite and the effects upon the embedded FBG.

7.1.4.6 Averaged magnetization method for characterization of the magnetostrictive composite

An averaged magnetization method can be used for describing the experimental shifting in central wavelength, such as reflected peak wavelength can be associated to an uniform period change due to tensile force at the ends of the cones, as it is depicted in Fig. 7.30. Based on the change of the reflected peak wavelength, one can approximate the magnetostriction coefficient of the composite by:

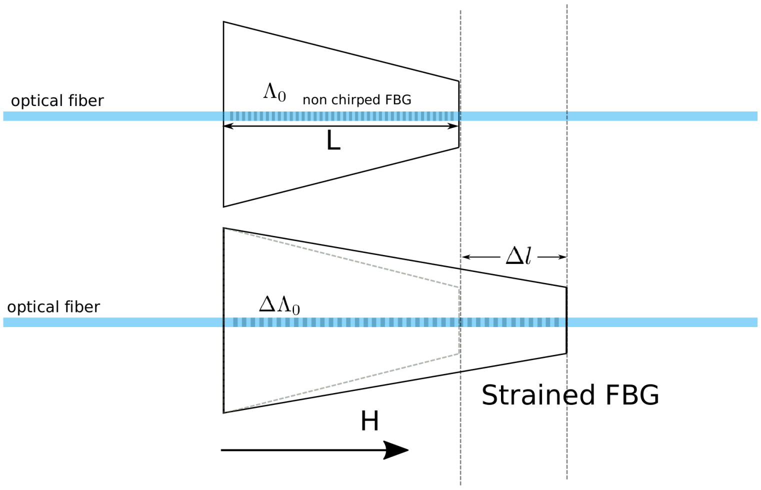

Figure 7.30: Transfer of uniform strain to the FBG along the axis of the cone

$$\xi = \frac{\Delta l}{L} = \frac{\Delta\Lambda_0}{\Lambda_0} = \frac{\Delta\lambda_c}{\lambda_c} \tag{7.20}$$

where ϵ corresponds to the elongation along the axis. Therefore, we can write for the strain due to magnetostriction:

$$\xi = \frac{\Delta\lambda_c}{\lambda_c} = \frac{3}{2}\epsilon_s\left[\frac{\bar{M}^2}{M_s^2}\right] \tag{7.21}$$

where ϵ_s represents the magnetostriction constant, M_s is the saturation magnetization and $\bar{M}$ is the magnetization of the cone. This latter can be described by using the Langevin function:

$$\bar{M} = M_s\left[\coth\left(\frac{H_{\text{int}} + \alpha\bar{M}}{a}\right) - \frac{a}{H_{\text{int}} + \alpha\bar{M}}\right], \tag{7.22}$$

where H_{int} is the internal magnetic field, α represents a coupling between the magnetic dipoles, a is a parameter that controls the shape of the function[20, 24, 23]. Figure

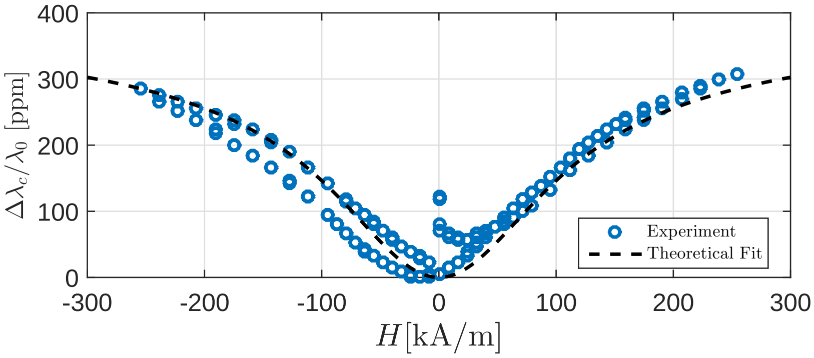

Figure 7.31: Magnetostrictive curve in terms of the normalized change in the central wavelength $\Delta\lambda_c(\bar{M})/\lambda_{c0}$ of the FBG versus the external magnetic field intensity.

7.31 presents the theoretical magnetostrictive curve based on modeling of the magnetization by the Langevin function with $a = 41852$ and $M_s = 1.6\times10^6$[A/m] and fitting to the experimental data for λ_c, $\bar{\lambda}_c(M)$. Its variation $\Delta\lambda_c(\bar{M}) = \bar{\lambda}_c(M) - \lambda_{c0}$ can be assumed to be proportional to the square of magnetization [33], i.e. $\Delta\bar{\lambda}_c(M) = \gamma_1\bar{M}^2$, where $\bar{M}^2$ is the mean square value of the magnetization, $\gamma_1 = 2.5982 \times 10^{-13}$ [nm m^2/A^2] is a fitting coefficient, and $\lambda_{c0} = 1549.4$[nm]. The normalized variation $\Delta\lambda_c(\bar{M})/\lambda_{c0}$ tracks the expected behavior of a magnetostrictive curve. With the average grating period is defined by $\bar{\Lambda}(M) = 0.5\bar{\lambda}_c(M)/n_{\text{eff}}$, magnetostrictive strain constant associated with the square of the magnetization can be estimated with γ_1 by expressing $\epsilon_{s1} = \gamma_1\lambda_{c0}^{-1}M_s^2/1.5$ which gives $\epsilon_{s1} \approx 272.41$[ppm]. Hence, the axial strain distribution can be obtained from $\epsilon(M(z)) = 1.5\epsilon_{s1}(M(z)/M_s)^2$ that enables the evaluation of the chirp function. Since the phase shift introduced by the chirp function will contain the information of the nonuniform strain distribution along the FBG and can be written as $\phi(z) = 2\pi z(\Lambda^{-1}(z) - \bar{\Lambda}^{-1})$. Its derivative relates to the frequency chirping and can be applied to the coupled mode theory for modeling the corresponding reflectance spectrum [13]. Figure 7.32 presents the comparison of the experimental spectrum and the theoretical prediction for different magnetic field magnitudes. As it can be seen from the figure, theoretical results capture most features in the experimental spectra, particularly their shapes, under various external magnetic field magnitudes. Experimental spectra have wider band than those from theory even at low field magnitudes. This effect can be attributed to the introduction of a prestrain, in addition to the magnetostrictive strain, from the curing of the epoxy for bonding the FBG into the channel. Such an effect in the fabrication process becomes the random factor for accurate matching the theory to experiments.

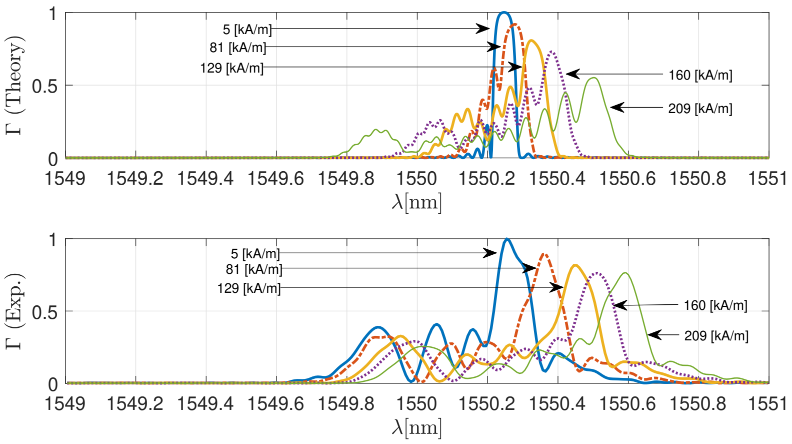

Figure 7.32: Comparison of theoretical (above) and experimental power reflectance spectrum Γ under various external magnetic field intensities.

An additional simulation was implemented for including the effects that the composite model can predict in the interaction with the embedded FBG. Figure 7.33 presents the comparison of the spectra for different external magnetic field magnitudes. As it can be seen from Fig.7.33 there is a lower influence upon the maximum reflected wavelength when compared to the previous case. However, there is still a clear chirping effect upon the FBG due to the internal distribution of the field. It should be noticed that in this last simulation case the total excursion of the maximum reflected peak follows much better the experimental case.

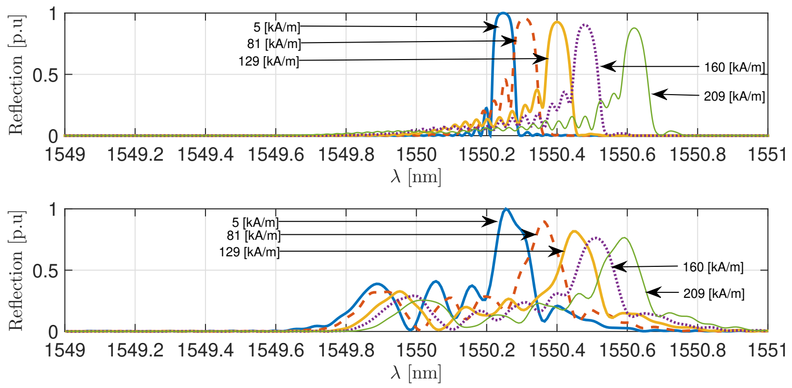

Figure 7.33: Comparison of theoretical response using the composite model for $M_s = 1.6 \times 10^6$, $a_{co} = 35556$, and particle size about 0.54% (above) and experimental power reflectance spectrum Γ under various external magnetic field intensities.

One of the most important advantages provided by this sensor over conventional magnetic field transducer based on magnetostriction is its ability to indicate the external magnetic field magnitude by a single optical power measurement with a photodetector. Figure 7.34 presents the experimental results of the total optical power normalized by its lowest value obtained from spectra recorded with a spectrum analyzer and direct power measurements with a photodetector. Both methods produce consistent results with maximum normalized power increasing with magnetic fields to about 1.02 times of the minimum power before diminishing under the external magnetic field around 155 [kA/m]. Although the total power reflectance initially rises with spectral widening caused by frequency chirping, this upward trend cannot be sustained when the shift of λ_c above a few times of the initial linewidth and the total power reflectance remains flat or even below its maximum.

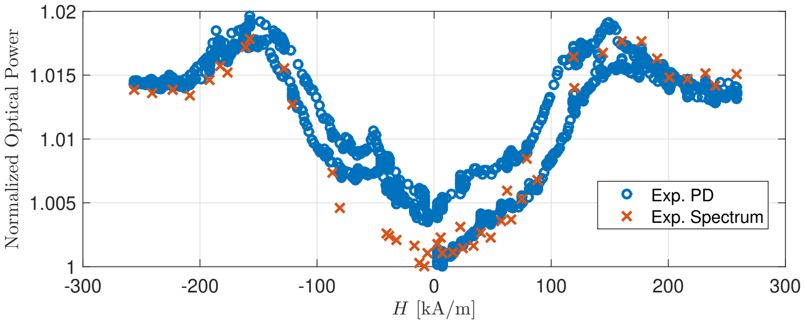

Figure 7.34: Normalized optical power of the reflected signal from the FBG as a function of the external magnetic field intensities. (circles: power measured by a photodetector, crosses: power calculated from experimental power spectra)

7.1.4.7 Slightly chirped reflected spectrum

As it was discussed in previous sections, there were fabricated three cones with different initial conditions. Both cones that used wider channel diameter presented more consistent reproduction of reflected wavelengths. Figure 7.35 presents the relative change in central wavelength as a function of the external magnetic field and a theoretical fitting based on the Langevin function using the same procedure of averaged magnetization discussed in section before.

As it has been done before, once the central wavelength is explained by the Langevin function we can reproduce the spectrum for different magnetic field magnitudes. Table 7.2 presents the fitted constants for describing the relative central wavelength change in terms of the external magnetic field.

An important result of this fitting process is that three cones presented very similar magnetostriction coefficients, even with different channel diameters and amount of

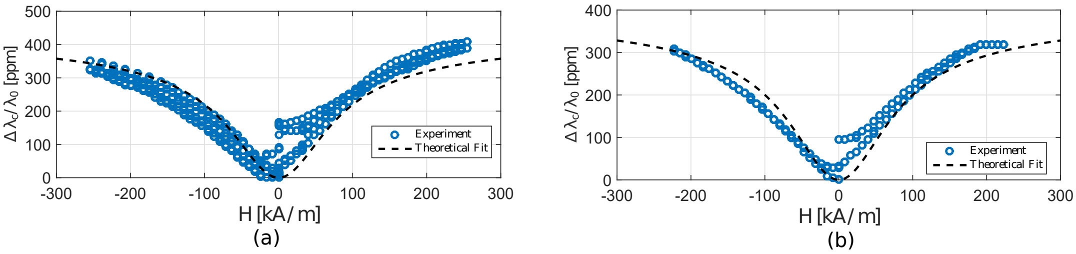

Figure 7.35: relative central wavelength of the reflected spectrum. (a) Cone 2 Ø =431.8μm (b) Cone 3 Ø =330.2μm

Fitting parameters in averaged magnetization		
Cone Ø	a [A/m]	ϵ_s [ppm]
1, Ø =330.2μm	41852	272.41
2, Ø =431.8μm	29624	293.45
3, Ø =330.2μm	29942	270.07

Table 7.2: Fitting parameters averaged magnetization: Cone 1, Ø =330.2μm. Cone 2, Ø =431.8μm. Cone 3, Ø =330.2μm. a-parameter in Langevin function, ϵ_s:approximated magnetostrictive coefficient.

Terfenol-D in each composite. Figure 7.36 presents the spectrum reproduction for different magnetic field magnitudes for cone 2 and cone 3. As it can be seen from Fig. 7.36(a)-(b) is that these two particular cones did not show important changes in the spectrum. However, Cone 2 presented a slightly broadening in the left side of the spectrum (Fig. 7.36(a)). Therefore, both cones were successfully modeled through central wavelength shifting. These results suggest that bonding process in this two particular cones was not that good as for cone 1 case, so the nonuniform strain created by the magnetization distribution along the axis is not fully transferred to the FBG, exhibiting the averaged effect exclusively that leads to a quasi-uniform strain deformation upon the FBG.

7.1.5 Time domain response analysis

This subsection presents the experimental and theoretical analysis of the frequency response for the magnetostrictive composite under a time dependent magnetic field. Frequency response was limited to low frequencies in the experimental set-up because the high inductive load of the electromagnet required high voltage amplifications for the input signal in order to get appreciable magnetic fields magnitudes. Therefore, only low frequencies up to 25Hz were able to be excited in the electromagnet to produce detectable fields by the implemented sensor. Due to the temporal response of

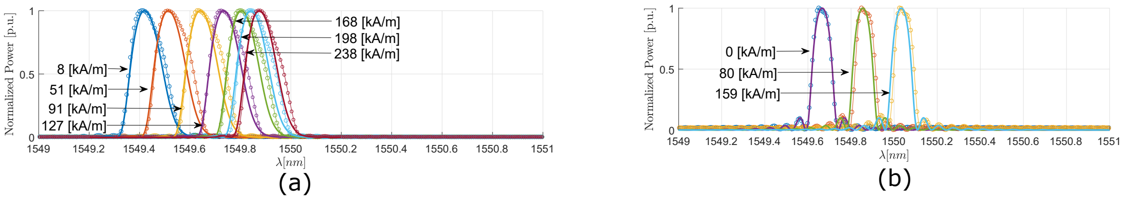

Figure 7.36: Spectrum Reproduction for different magnetic fields magnitudes (dots: experimental, lines: theoretical) (a) cone 2, Ø =330.2μm T-D ratio=65% (b) cone 3, Ø =330.2μm T-D ratio=67%.

typical optical spectrum analyzers, frequency analysis was performed through optical power measurements directly. Time domain responses of the magnetostrictive sensor were captured by a data acquisition system connected to a photo-detector. Load resistor for the photo-detector was carefully selected to guarantee sensitivity and meeting input requirements of the acquisition system. A load resistor of 10kΩ was used for acquiring the data. Figure 7.37 presents the temporal response of the optical power reflected back from the FBG under several magnetic fields magnitudes and frequencies. As it can be seen from the figures, low frequencies were able to generate higher magnetic field magnitudes. However, for higher frequencies maximum magnetic field magnitude decreased due to the incrementation of the associated impedance of the electromagnet, leading to a decrement in the current through the coil which turns into a lower magnetic field excitation.

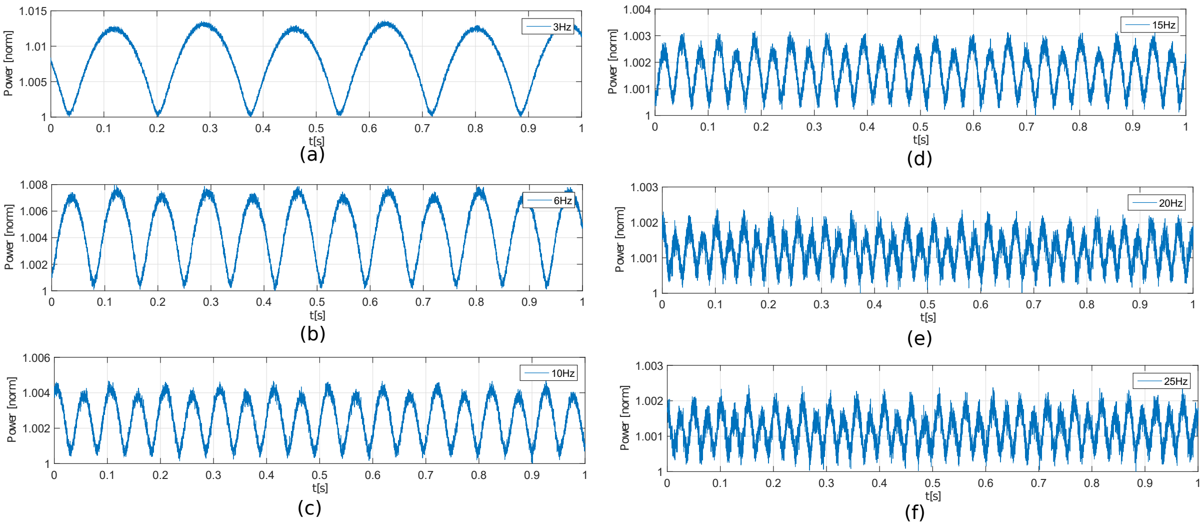

Figure 7.37: Optical power time-domain response under different magnetic field magnitudes and frequencies. (a) f = 3Hz. (b) f = 6Hz. (c) f = 10Hz. (d) f = 15Hz. (e) f = 20Hz. (f) f = 25Hz.

In order to analyze the response of the magnetostrictive sensor to frequency, a comparison of the experimental results against the expected result for DC excitation was performed. Figure 7.38 presents the external magnetic field magnitudes that were excited at different frequencies against the maximum ripple of normalized power, which can be also understood as the sensitivity of the sensor. Fig. 7.38 presents the comparison for different magnitudes when the magnetostrictive sensor was under a external magnetic field excitation at different frequencies. As it can be seen lower frequencies presented a higher deviation from the expected DC results. This figure suggests that there is an important change in sensitivity when the magnetostrictive sensor is under different frequencies. This can be due to some saturation-frequency dependence as well as mechanical response in the strain transfer to the FBG that should be validated in future works. In contrast, at lower fields experimental and expected results in the DC case are around the same region of change. Same behavior is presented for

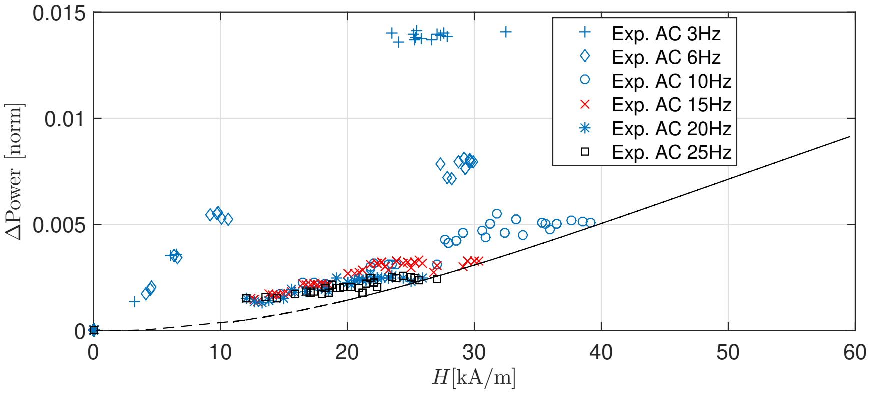

Figure 7.38: Comparison of the expected ripple in normalized optical power for different frequencies: 10Hz, 15Hz, 20Hz, 25Hz.

higher frequencies under 40kA/m in the external magnetic field. Although, there are some discrepancies when compared to the DC expected ripple, those frequencies are located around the same sensitivity in optical power. This frequency analysis shows that there could be some dependence on frequency of the saturation curve for the magnetostrictive composite and should be addressed in future works for improving the sensitivity of the magnetostrictive sensor to higher frequencies.

7.2 Piezoelectric Bimorph for Electric field Sensing

This section discusses the electric field sensing through piezoelectric materials. In this case the strategy for sensing the electric field is based on a bimorph actuator that transfers uniform strain to a couple of FBGs attached to each of its faces. Fibers were attached at one point at each end to induce uniform strain along the grating. Figure 7.39 depicts the two possibilities for the actuator operation.

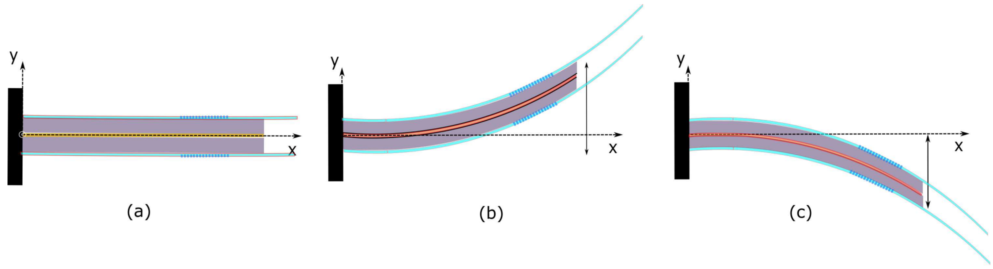

Figure 7.39: Experimental set-up for an electric field sensor based on a bimorph actuator. (a) bimorph in rest condition (b) positive bending (c) negative bending

Bimorph behavior will be determined by the relative orientation of the electric field across the layers regarding to the poling direction of each layer. An important difference of the current experimental implementation with the bimorph actuator in **chapter 6**, is that in this case active layers are poled in opposite directions as shown in Fig. 7.40(a), thus bending of the bimorph is achieved by single side excitation. This particular situation implies some changes in the results obtained in **chapter 6** and technically constitutes a unimorph operation. In contrast to the bimorph actuator, neutral axis in the unimorph does not coincide with the centroid of the cross section, this characteristic makes to appear a net extensional force, along the midplane, different from zero. Following the same analysis as in **chapter 6**, under only one side operation and assuming a constant electric field across the piezoelectric layer, longitudinal stress upon the cross section at a given point x can be written by:

$$\sigma_x(y(x), z) = \begin{cases} \mathcal{Y}_p\xi_x(x) - d_{31}\mathcal{Y}_pE_3 & -t_p - t_m/2 < y < -t_m/2 \\ \mathcal{Y}_m\xi_x(x) & -t_m/2 < y < t_m/2 \\ \mathcal{Y}_p\xi_x(x) & t_m/2 < y < t_p + t_m/2 \end{cases} \tag{7.23}$$

where $\mathcal{Y}_m$ and $\mathcal{Y}_p$ are the Young's module of the metal shim and the piezoelectric layer respectively. t_m and t_p represents the thickness of the metal and piezoelectric layers and w is the width of the cross section. Effective curvature for the single side operation is reduced to a half of the equation 6.17, thus it can be calculated by:

$$\kappa_{\text{eff}} = \frac{6\mathcal{Y}_p d_{31} E_3 \left(t_m t_p + t_p^2\right)}{2\mathcal{Y}_p \left(3t_m^2 t_p + 6t_m t_p^2 + 4t_p^3\right) + \mathcal{Y}_m t_m^3} \tag{7.24}$$

Therefore, deflection curve will be given by:

$$\nu(x) = \kappa_{\text{eff}} \frac{x^2}{2} \tag{7.25}$$

achieving a half of the maximum deflection. Figure 7.41 shows the calculated deflection curve obtained by COMSOL solving for the single side operation, and the results calculated by using the effective curvature in Eq. 7.24 and the correction to the electric field through the effective field proposed in **section 6.2**.

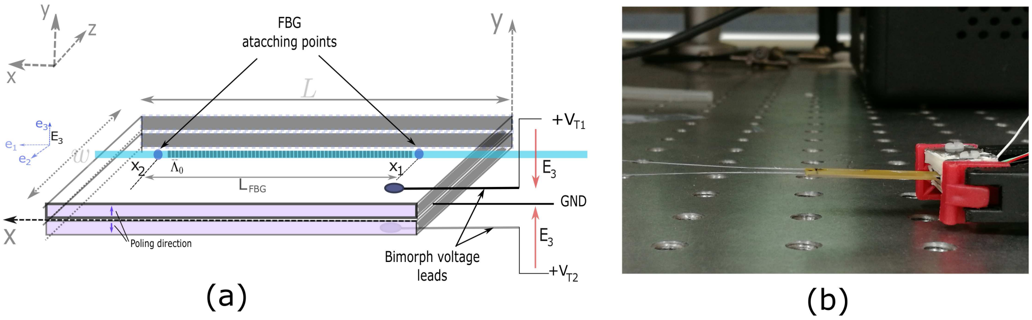

Figure 7.40: (a) Poling direction convention and FBG anchoring points(b) Experimental implementation of a piezoelectric bimorph with two FBGs attached to each piezo side

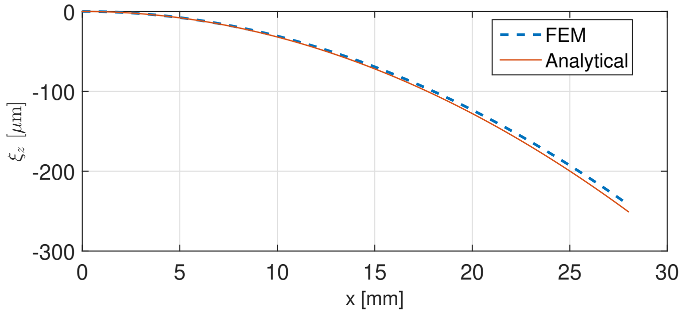

Figure 7.41: Comparison of deflection curve

In this particular set-up, fibers will be interacting with different longitudinal strains depending on which layer is excited and its particular polarity. An important difference of this operation compared to the bimorph operation in **Chapter 6** is that surfaces of the actuator will exhibit different longitudinal strain depending on its configuration. Figure 7.42 shows the possible configurations to operate the current bimorph. For sake of simplicity, Fig. 7.42 shows only one of the FBG attached to the outer surface of the lower layer. Configuration A excites upper layer to induce tension upon the FBG. Configuration B excites the bottom layer to induce compression upon the FBG.

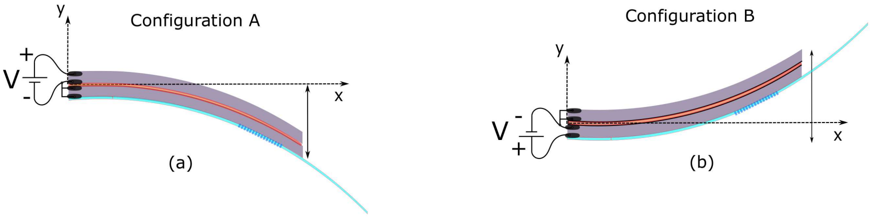

Figure 7.42: Experimental set-up for an electric field sensor based on a bimorph actuator. (a) bimorph in rest condition (b) positive bending (c) negative bending

The strains upon the FBG for each configuration, in contrast to the symmetry observed in the bimorph actuator of **Chapter 6**, will be different each other because the neutral axis won't match the midplane. This mismatch is explained by the fact that for configurations A and B, the inactive layer (that one not excited) acts as a passive material causing an asymmetric distribution of the longitudinal strains respect to the mid-plane, leading to different maximum strains at the surfaces of the layers for both configuration of operation. Figure 7.43 presents the calculated longitudinal strains upon the layers of the bimorph when it is excited in configuration A and B. As it can be seen from Fig. 7.43(a), configuration A presents higher longitudinal strains for the upper layer when it is excited in direct polarity respect to the poling direction. Tension upon the upper layer is almost three times greater than the lower face. Same effect happens in configuration B but for lower layer. Fig. 7.43(b) shows the longitudinal strains calculated for configuration B when applied voltage polarity is in the same direction of poling. As it can be seen in this figure, longitudinal strain upon the lower layer is almost three times grater than the upper layer.

In the practical implementation for the current transducer, two FBGs were attached to each of the surface layers in the bimorph. Different excitation configurations were used for the implementation to validate the theoretical results about the asymmetric longitudinal strain. Figure 7.44 presents the simulation results obtained by FEM when the longitudinal strain is calculated at the tip of the piezoelectric bimorph.

As it can be seen from Fig.7.44 the expected ration between the slopes in both conditions is m_C/m_T=2.85. This result suggests that at least for the range of analysis

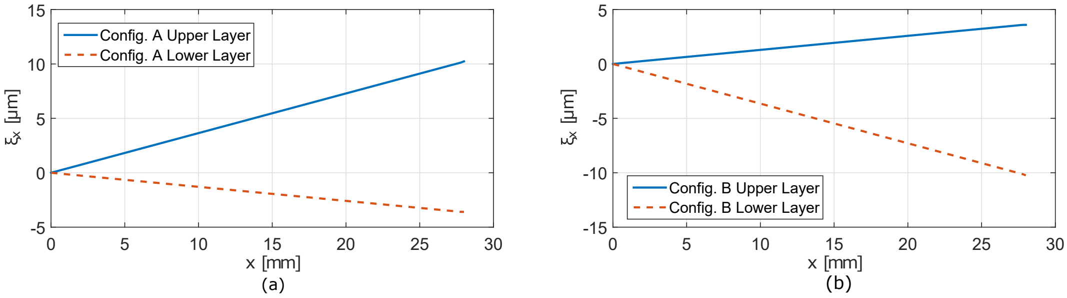

Figure 7.43: Longitudinal strains upon the actuator surface depending on which layer is excited. Theoretical sensitivity ratio between maximum strains operations m_C/m_T=2.85. (a) Configuration A: Upper layer is excited. (b) Configuration B: Bottom layer is excited.

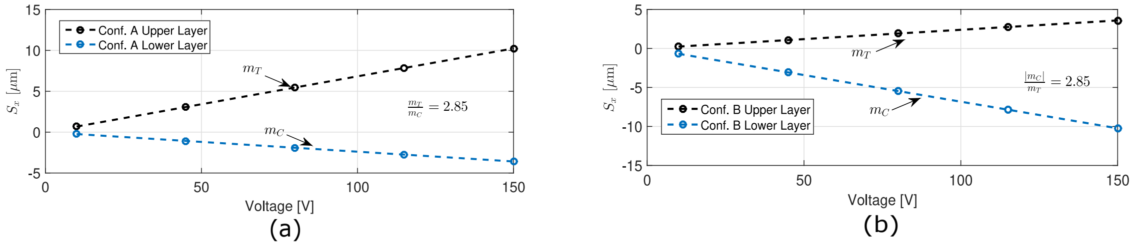

Figure 7.44: Longitudinal strains upon the actuator surface depending on which layer is excited as a function of the driving voltage. Theoretical sensitivity between maximum strains operations $|m_C|/m_T$=2.85 is validated. (a) Configuration A: Upper layer is excited. (b) Configuration B: Bottom layer is excited.

there is a linear relation between the longitudinal strain and the driving voltage magnitude. Since this ration is the same one for the strain along the bimorph, this linear relation applies for all the points along the bimorph length.

7.2.0.1 Case 1: Fiber on the lower face in Compression and Tension

This case was performed over the fiber located on the lower part of the bimorph. For the first condition the bimorph was polarized to have a negative bending, i.e. lower face experimented a compression and upper face experimented a tension. Since the fiber under test was bonded on the lower face, it suffered a compression for this initial condition. After that, the bimorph was opposite polarized to exert on this same fiber a tensional force. Figure 7.45(a) presents some of the measured reflected spectrum for different voltages that exerted a negative bending over the bimorph, acting as a compression strain upon the lower FBG. When the bimorph is polarized to have a positive bending, the lower FBG behaves under tension. Figure 7.45(b) presents some of the spectrum recorded for different magnitudes of voltage. As it can be seen from both figures, a slight change in the spectrum shape can be explained from the non-uniform strain distribution along the FBG. Figure 7.46 presents the behavior of the central wavelength when the lower FBG in the current experimental set-up is under tension and compression. As it was discussed in the theoretical background in the section above two different sensitivities can be obtained upon the FBG depending on the configuration and excitation of the piezoelectric layers. Fig. 7.46 presents the linear fits for two different operations of the bimorph that lead to tension and compression upon the lower FBG. Linear fits result in a slope of $m_T = 0.0025[\text{nm/V}]$ under tension action and a slope of $m_C = -0.0077[\text{nm/V}]$ under compression. These two sensitivities are in agreement with the theoretical expectation to be about three times each other in magnitude. Based on this results, spectra of the FBG can be modeled through . Figure 7.47 presents the spectral response of the FBG attached to the lower side of the bimorph when it is under tension and compression.

7.2.0.2 Case 2: Fiber on the upper face in Compression and Tension

Same measurements were performed upon the upper FBG in the experimental set-up. Figure 7.48 presents the experimental spectra obtained for the FBG attached to the upper piezoelectric layer for different voltages.

Figure 7.49 shows the experimental central reflected wavelength for the FBG attached to the upper layer in the bimorph when it is under different voltages. Additional linear fit lines are plotted to fit the experimental data. Slopes of the linear fits are shown for both cases: tension and compression. As it can be seen from this particular experiment, there is a deviation from the expected linear behavior when the upper FBG is in tension. This can be due to the bonding characteristics of the FBG to the piezoelectric layer surface. Bonding quality in FBG based sensors are one of the most difficult issues to guarantee in the fabrications process. Defects in bonding processes lead to undesirable behaviors and non-linear effects as occurred in this experimental case. Although, this nonlinearity is not explained by the current model, linear part of

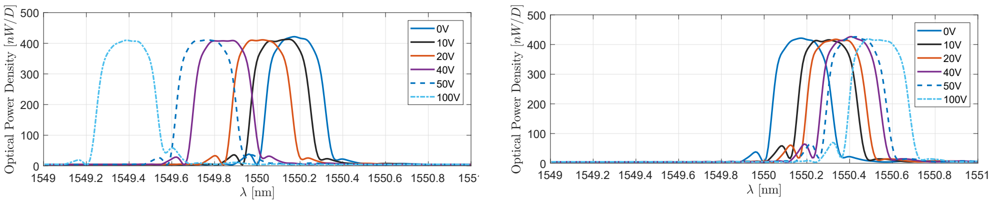

(a)

(b)

Figure 7.45: (a) Measured spectrum for the lower FBG in compression. (b) Measured spectrum for the lower FBG in tension.

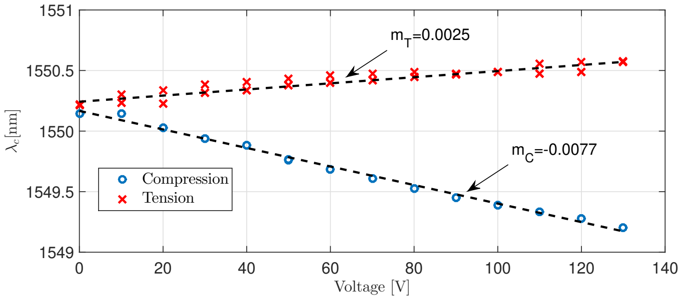

Figure 7.46: Measured spectrum for the lower FBG in tension and compression. Sensitivity in tension m_T=0.0025[nm/V]. Sensitivity in compression m_C=-0.0077[nm/V]. Sensitivity ratio $|m_C|/m_T$=3.08.

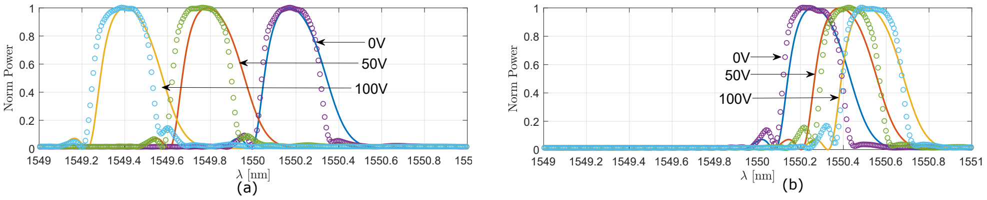

Figure 7.47: (a) Spectra for the lower FBG in compression (b) Spectra for the lower FBG in tension (dots: measured, solid: theoretical)

the reflected wavelength in tension presents the same sensitivity as that obtained for the FBG attached to the lower side of the bimorph. Indeed, sensitivity ratio between linear parts in tension and compression is about m_C/m_T=4.53 which is still close to the expected ratio.

7.2.1 AC voltage measurements with a bimorph actuator

This subsection presents the results that were obtained for the bimorph when it was under an alternate electric field. In this case, lower FBG was used to sense the deformation occurred in the bimorph when it is under electric field excitation. Two different strategies were used for sensing the mechanical deflection. Figure 7.50 depicts a schematic of the optical circuits used for each case. A first strategy considered to interrogate the central wavelength reflected back form the FBG when AC electric fields of different magnitudes and frequency were applied to the active layer (see Fig. 7.50(a)). Although this method allows to determine directly the effects of the extensional forces upon the FBG, it implies the usage of sophisticated equipments for interrogating the peak wavelength, as well as it frequency response is limited by the sampling frequency of these equipments, which are not able to follow rapid changes of the peak wavelengths. A second strategy was to include an additional FBG that

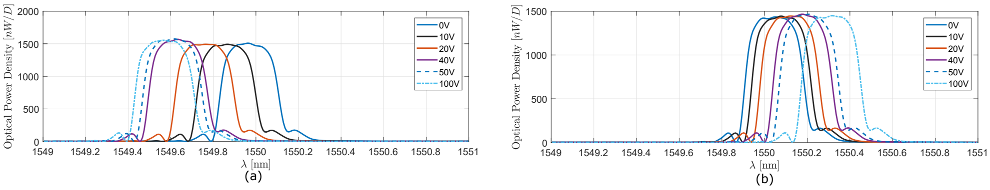

Figure 7.48: Power Reflected Spectrum for the experimental setup (a) Compression (b) Tension

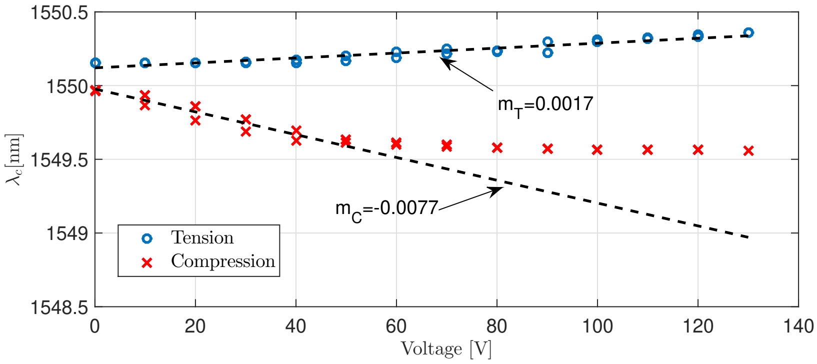

Figure 7.49: Central wavelength of the upper FBG in tension and compression. Sensitivity in tension m_T=0.0017[nm/V]. Sensitivity in compression m_C=-0.0077[nm/V]. Sensitivity ratio $|m_C|/m_T$=4.53.

worked as a filter of the reflected spectrum from the sensing FBG (that on under extensional force. See Fig. 7.50(b)). This technique is very well known in literature and allows to use a photo-detector instead of a wavelength interrogator. Since sensing FBGs were successfully modeled by uniform strain transfer in the section before, next subsections present the results obtained experimentally by means of these two measurement methods, as well as the comparison of the expected results by using the theoretical model.

7.2.1.1 Central wavelength shifting

This subsection shows the results for the behavior of the central wavelength reflected back from the FBG attached to the lower side of the bimorph by using the optical circuit presented in Fig.7.50(a). Measurements of the central reflected wavelength were done by using an optical wavelength interrogator manufactured by Micron Optics, model si425, with a wavelength range from 1520nm to 1570nm with a maximum resolution of 2pm for each channel. During the experiments, voltage and frequency were changed to analyze the behavior of the reflected central wavelength. Figure 7.51 shows the behavior of the central reflected wavelength for different voltage magnitudes

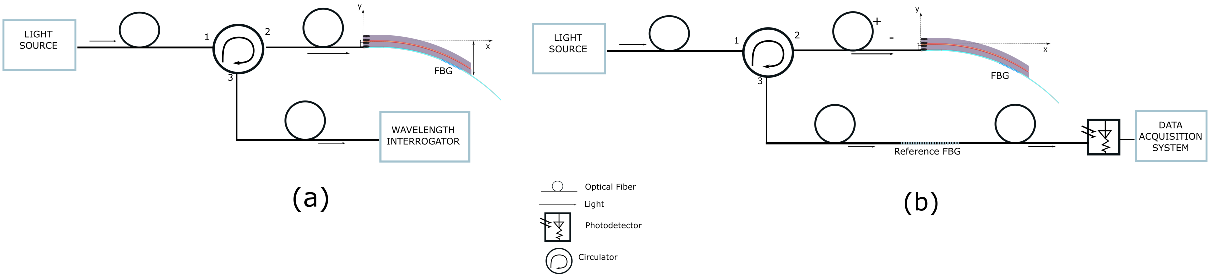

Figure 7.50: Optical circuits for inferring the external voltage. (a) Measuring through peak wavelength interrogator (b) Measuring through optical power by using a fixed FBG as a reference (fixed filter technique)

at 7Hz sinusoidal excitation, and Figure 7.52 presents the behavior of the reflected wavelength at 20V of excitation with different frequencies.

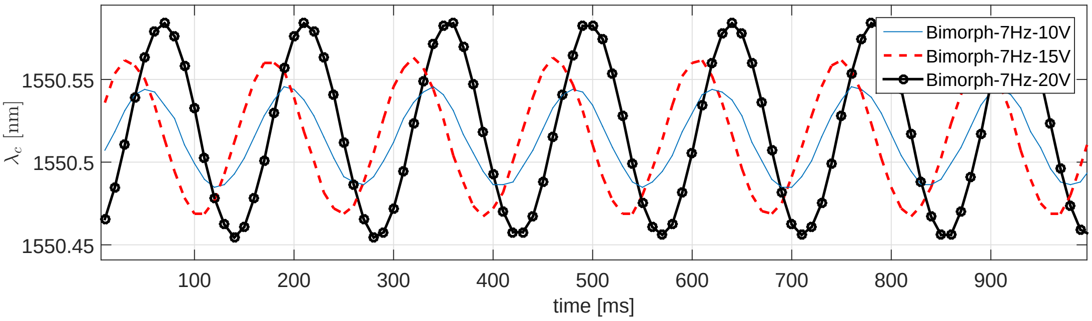

Figure 7.51: Central Reflected Wavelength for different voltage magnitudes at 7Hz sinusoidal excitation

As it can be seen from Figures 7.51 and 7.52, optical system responds correctly two both type of excitations. As it is expected the excursion magnitude of the reflected central wavelength accounts for the voltage magnitude. Figure 7.53 presents the peak-to-peak excursion of the central wavelength for different magnitudes of the driving voltage at different frequencies.

As it can be seen from Figure 7.53 frequency response of the bimorph presents a linear tendency in the analyzed range of frequency. It should be highlighted that optical interrogator used for the measurements does not present a high sweep frequency. Therefore, range of analysis is restricted up to 20Hz approximately. A set of different waveforms in the driving voltage were used to check the bimorph response. Figure 7.54 presents the behavior of the bimorph when the driving voltage was set to 5Hz in frequency and 10V in amplitude, under sawtooth, square and triangular waveform excitation.

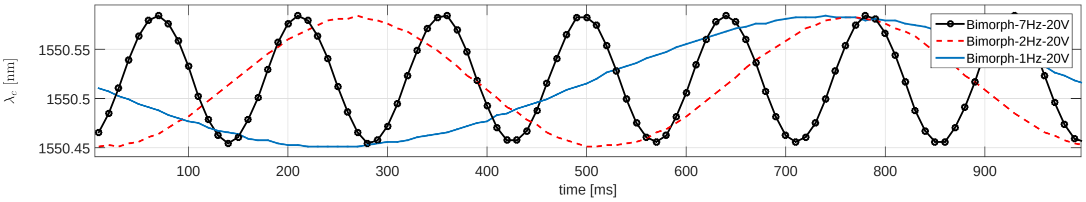

Figure 7.52: Central Reflected Wavelength for different frequencies at 20V magnitude of the excitation source

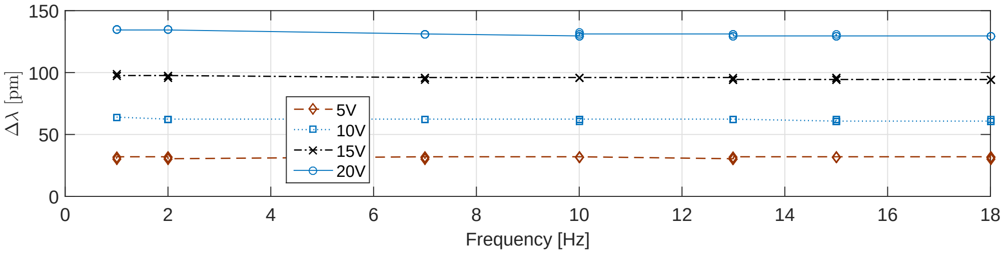

Figure 7.53: Excursion of the central wavelength reflected back from the FBG attached to the bimoprh, when it is under different voltage magnitudes and frequency values.

As it can be seen from Fig. 7.54, the optical response follows in the reflected wavelength the imposed waveform by the source. However, it should be noticed that the measurement device is limited in frequency response due to the sampling frequency of the wavelength interrogator. In order to overcome this limitation, an additional FBG can be used as a reference such as the interaction between this reference spectrum and the reflected spectrum from the FBG attached to the bimorph leads to a optical-power variable spectrum, which allows the measurement with a photodetector instead of wavelength interrogator. Next section presents the results of the bimorph when a reference FBG is used as a filter.

7.2.1.2 Optical power detection method by using a reference FBG

As it was discussed in the section before, the analysis of the electric field sensor is mostly restricted by the sampling characteristics of the optical interrogator. This issue can be overcome by using an additional FBG to act as a filter such as the frequency response of the cascade FBG arrangement allows to deduce the applied voltage by using an optical power detector. This measurement technique allows to characterize the electric field sensor in a wider range of frequency. Figure 7.55 presents the spectra of the FBG from the bimorph, the reflectance spectrum of the FBG that

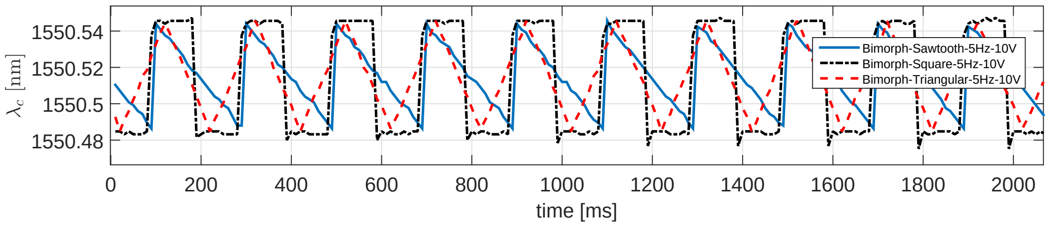

Figure 7.54: Reflected central wavelength under different signal waveforms of the driving voltage.

will serve as a filter and the resultant spectrum when the light reflected back from the sensing FBG (attached to the bimorph) and is transmitted through the reference filter. As it can be seen from Fig. 7.55(b) experimental transmitted spectrum can be successfully reproduced from the interaction between the reflected light from the sensing FBG and the transmittance characteristics of the filter. Main advantage of this method is that transmitted spectrum will present a variable optical power, thus the overlapping between transmission spectrum and reflected light from the sensing FBG can be measured by optical power measurements when the bimorph is under the electric field action.

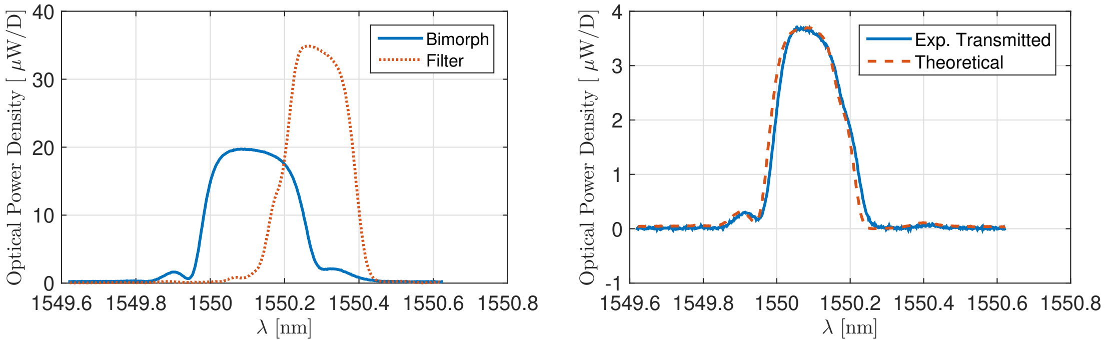

Figure 7.55: Reference FBG filter technique. (a) Reflectance spectrum of the FBG attached to the bimorph and the FBG used as a reference filter. (b) Experimental transmitted spectra and theoretical calculation under no excitation.

The particular configuration for using the transmitted spectrum through the reference FBG as measured variable is a slight variation of the common optical circuit that uses this technique. Typically, an additional optical circulator is used in the circuit to use the reflectance properties of the reference FBG instead of the transmittance characteristics. The strategy of using the transmittance properties saves one optical element, but it has to be very well tuned for achieving some region of linear operation. Figure 7.56(a) presents the theoretical spectra transmitted to the

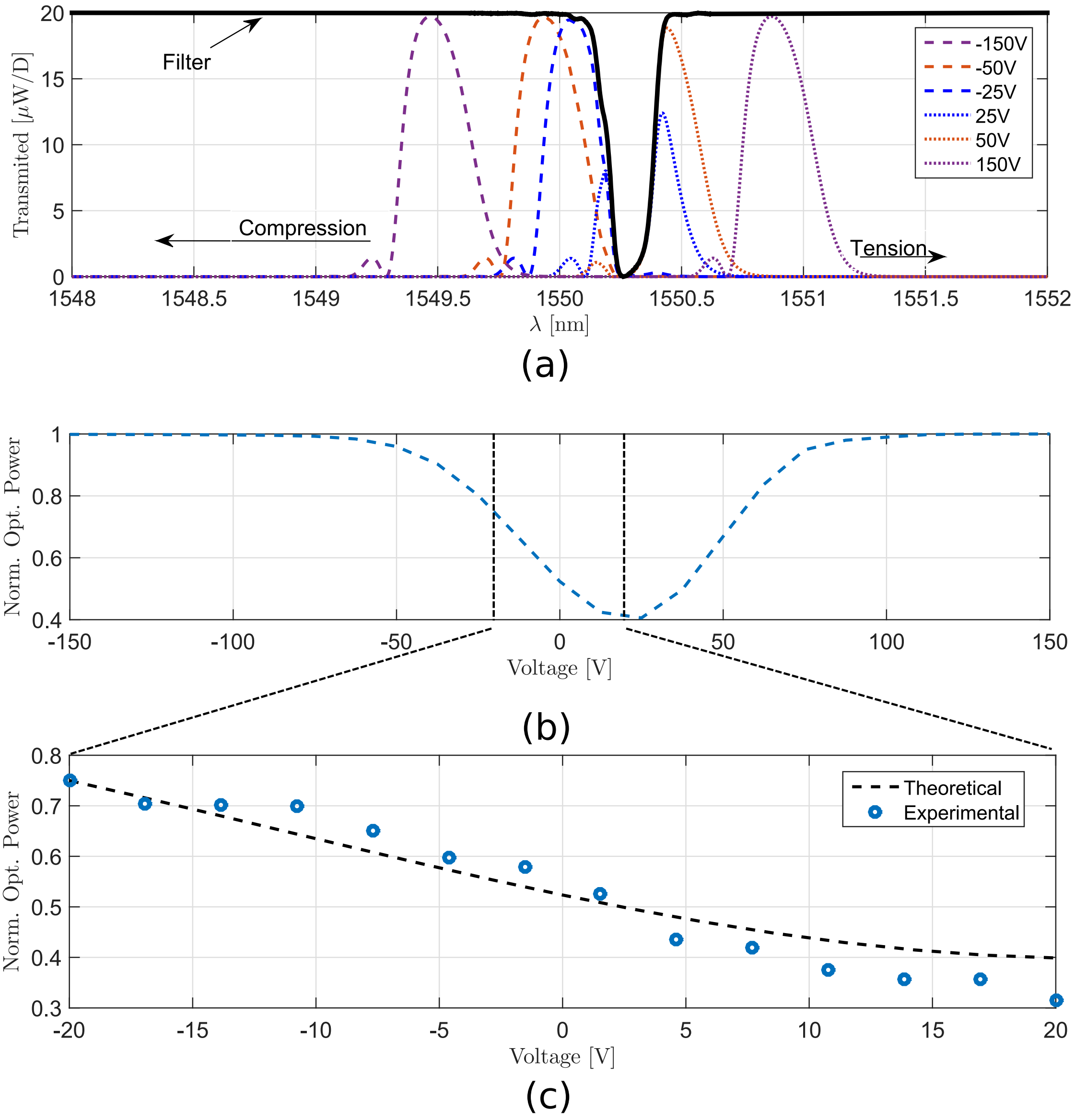

(a)

(b)

(c)

Figure 7.56: (a)Theoretical calculation of the transmitted spectra (b) Normalized optical power for the transmitted spectra. (c) Theoretical and experimental comparison of the optical power in the interval of interest.

photodetector in the implemented optical circuit. It should be noticed that in AC excitation, compression and tension can be achieved upon the FBG exciting the same piezoelectric layer. On the other hand, total optical power was calculated from the resultant spectrum for different values of the excitation voltage and normalized to the maximum power as shown in Fig. 7.56(b). As it can be observed from this figure, there are two saturation regions for driving voltages where total normalized power of the transmitted spectrum remains constant. This effect occurs because the sensing FBG lies far from the reference FBG rejection wavelength interval. An additional characteristic of this implementation is that symmetry of the total transmitted power is about 20V. Therefore, an approximated range in driving voltages can be determined for having almost linear output in optical power. This range can be proposed to be between -20V and 20V. Figure 7.56(c) presents the experimental results of the total normalized optical power for positive and negative voltages, and the expected results by using the theoretical response of the transmittance. As it can be seen from Fig.7.56(c), experimental data is followed by the theoretical expectations in the range of interest. In order to analyze the frequency response of the current sensor, resultant optical signal was connected to a photo-detector manufactured by Thorlabs, reference DET08CFC/M-InGaAs, with a responsitivity about 0.9[A/W] at 1550nm. Output of photodetector was connected to an oscilloscope with input impedance of 1[MΩ], while the input voltage was set to a constant amplitude to 10V peak and changed in frequency. Figure 7.57 presents the optical power measured in the time domain at the photo-detector for different frequency excitations. Optical power waveforms are

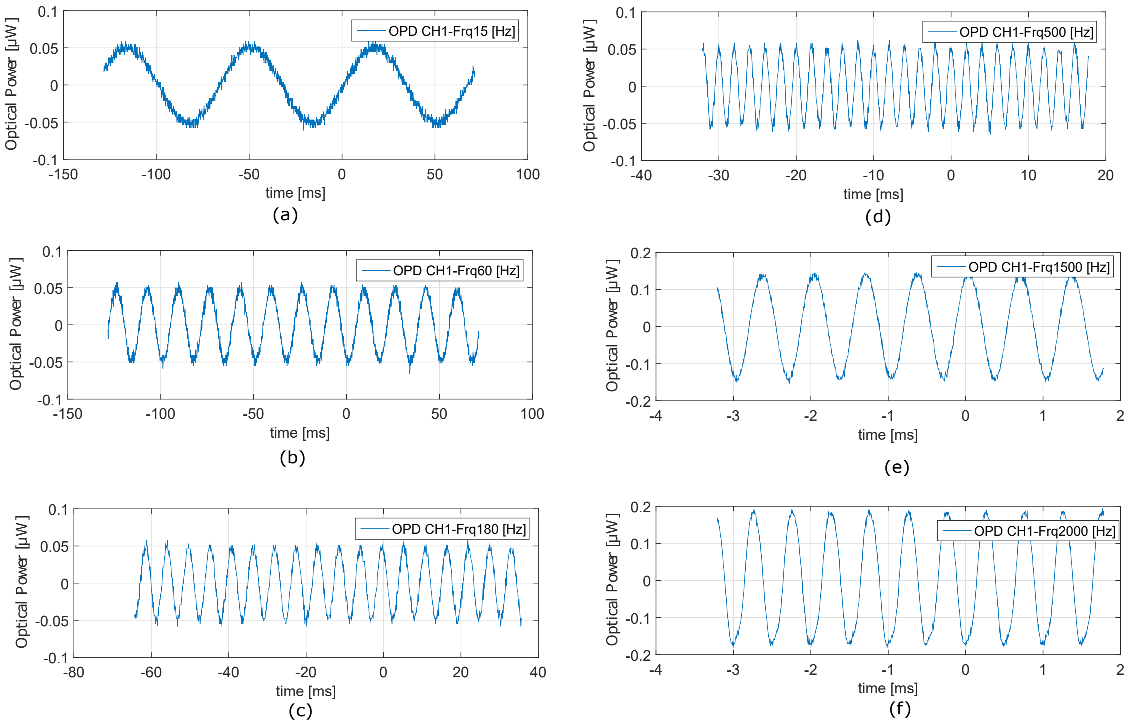

Figure 7.57: Time domain response in optical power for several frequencies. (a) 15Hz.(b) 60Hz. (c) 180Hz. (d) 500Hz. (e) 1500Hz. (f) 2000Hz.

shown unbiased for the sake of simplicity. It is worth noting that there is a clear increase in the amplitude measured at the photo-detector when driving frequency goes higher. Figure 7.58 shows the frequency response of the optical power amplitude for

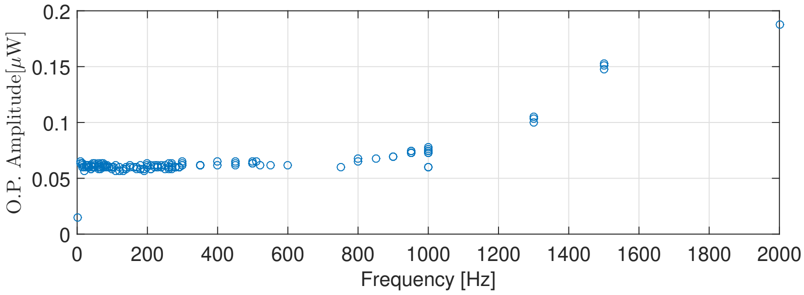

Figure 7.58: Frequency response in optical power measured at the photodetector for constant input voltage amplitude (20Vpp)

several frequencies. As it can be seen from Fig.7.58 there is an increase in the optical power amplitude when frequency goes beyond 800Hz approximately. This increment in the amplitude can occur due to the poor mechanical response of the bimorph for those frequencies, such as the attached FBG is not properly strained at these frequencies, leading to an averaged bending condition that is far from the deflection region that allows the modulation of the optical power and transmits higher optical power. Resonant frequency for the current bimorph was specified to be around 370Hz where a slight increase was also detected in the optical power. Linear behavior in frequency is well determined below 280Hz approximately, which allows the use of this sensor for low frequency or steady state applications.

7.2.1.3 High voltage power line measurements

Once the performance of the bimorph as an optical transducer of external voltage has been reviewed in previous section, this section presents the experimental results when the bimorph sensor is used for sensing high voltage at industrial frequency (60Hz). As it was discussed in the previous sections, deflection curve of the piezoelectric bimorph depends on the volatge upon the active layer. Figure 7.59 presents a schematic of the implemented set-up for measuring high voltages by using the sensor described in section before, where capacitive characteristics of the piezoelectric bimorph are used in a capacitive divisor for estimating a external high voltage. As it is shown in the schematic set-up in Fig.7.59, high voltage magnitude will be divided between the capacitance of the bimorph C_b and the external capacitance C_a by the expression:

$$V_b = \frac{C_a}{C_a + C_b} V_{\text{ext}} \tag{7.26}$$

Capacitance of the bimorph is around $C_b = 550$[nF] for each layer. Capacitance C_a was implemented through a series capacitive divisor available at the laboratory,

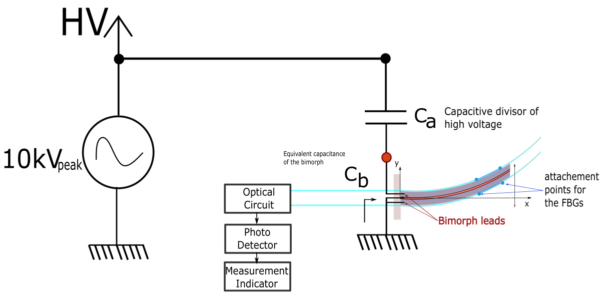

Figure 7.59: Schematic of the experimental set-up for measuring high voltage systems

to obtained an equivalent capacitance about $C_a = 4.53[\text{nF}]$ to obtain a reduction ratio about 122.4 times of the external voltage. This strategy of using a capacitive divisor is widely used in high voltage measurements because large impedances can be obtained by using relatively small capacitances. Figure 7.60 shows the actual implementation of the experimental set-up. In this experimental setup, a variac was

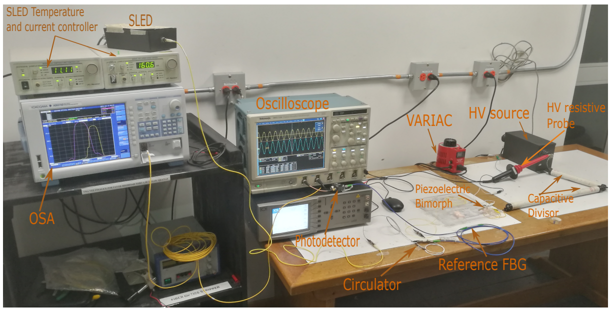

Figure 7.60: Experimental set-up for measuring high voltages

use to control the high voltage magnitude generated by a transformer that acted as a high voltage source. A capacitive divisor was placed between the high voltage side and one of the bimorph ends. Magnitude of the voltage source was increased gradually and optical signals measured at the photo detector by an oscilloscope were saved for each step. Voltage was increased up to 5kV when clear distortions in the optical signal were observed. Figure 7.61 presents the time domain response for different voltage magnitudes. As it can be seen from Fig.7.61 amplitude measured in the optical signal depends on the magnitude of the external voltage. As it was expected from the characterization of the bimorph as voltage sensor, voltages upon the active piezoelectric layer greater than 20Vp will lead to some distortions in the corresponding signal for the optical power. This effect is explained in the non-linear behavior that optical power of the transmitted spectrum presents respect to voltage input. Indeed, saturation present in Fig.7.61(f) occurs in the lower region of the

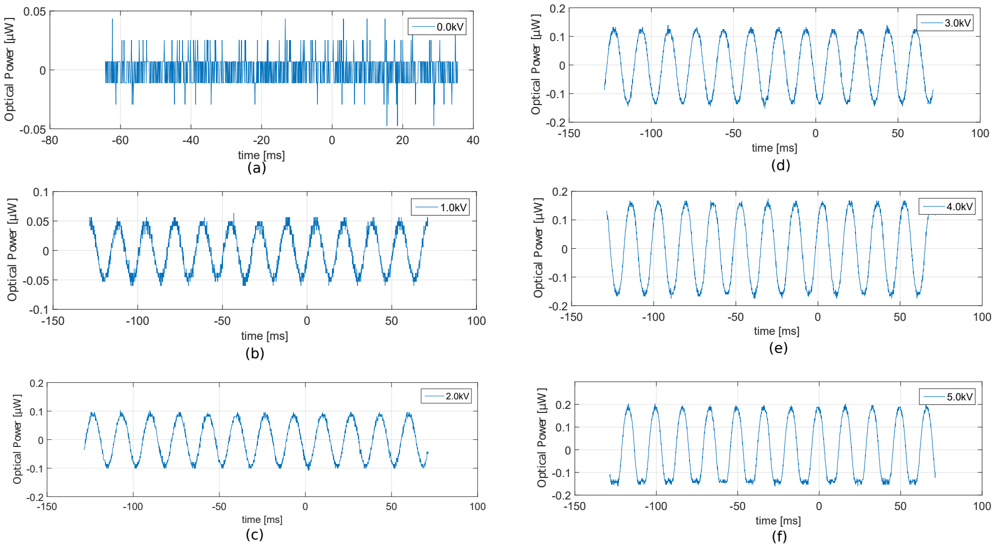

Figure 7.61: Time domain responses for different external voltage magnitudes. (a)0[kV]. (b)1[kV]. (c)2[kV]. (d)3[kV]. (e)4[kV]. (f)5[kV].

optical power as predicted in the theoretical model presented in Fig.7.56(b). Figure 7.62 present the experimental results and the linear fit for the optical power amplitude and the external field amplitude. As it can be seen from Fig.7.62 a linear fit between

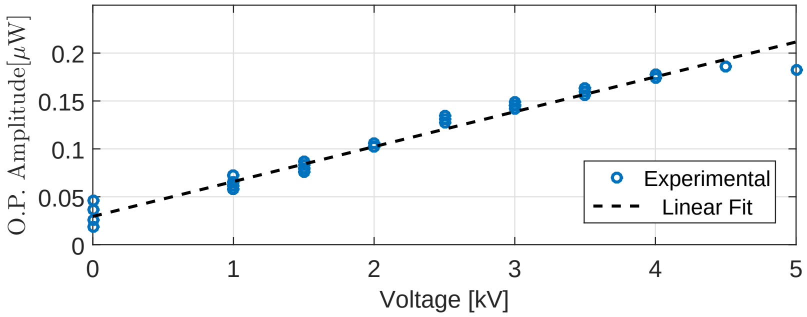

Figure 7.62: Experimental behavior of the optical signal amplitude for different external voltage

external voltage and optical power amplitude can be used for estimating the external voltage for voltages up to 4kV. A total sensitivity of 0.03867[μW/kV] was achieved for the current capacitive divisor. It should be noticed that depending on the capacitive divisor hogher voltages can be measured such as the voltage upon the bimporh active layer lies between the linear region presented presented in Fig.7.56(b).

Chapter 8

Conclusions and future work

This thesis dealt with the proposal, analytical background and practical implementation of two fiber optic based sensors for measuring electrical variables in high voltage systems. Particularly, this dissertation addressed the measurement of magnetic field and voltage by using Fiber Bragg grating as optical device to modulate light and infer external variable magnitudes. Most of the models implemented in this thesis were compared against previous literature reports as well as commercial finite element simulation software to validate their accuracy. A comparison between experimental data obtained and theoretical expectations have been presented as thoroughly as possible in order to explain the phenomena involved in the physical interactions of the sensors. As they were presented along the document, three main conclusions should be highlighted from the obtained results: first, the formulation of interaction characteristics of optical fibers by extending the coupled mode theory with a Hamiltonian formulation of the Helmholtz's equation to account for transverse perturbations. Numerical simulations showed the feasibility of using the developed framework to successfully calculate spatial distortions from transverse perturbations. As future work, Fiber Bragg gratings in few-modes fibers could be analyzed by using the developed framework to combine the interference properties of the longitudinal grating with the spatial distortions that the propagating modes suffer under transverse perturbations. This combination could lead to the development of optical devices that can control conversion between modes (spatial characteristics due to transverse perturbations) and frequency selectivity in the reflected spectrum (longitudinal perturbations).

Second, the proposition of a numerical method for predicting the magnetic characteristics of magnetostrictive powder/epoxy composites with arbitrary shapes. A closed solution for vector magnetic potential was found for a single magnetic cuboid to represent the monolithic magnetostrictive particle immersed into an epoxy matrix.

Afterwards, the magnetization was calculated by a set of linear equations that involved full vectorial magnetization field. The advantage of the proposed method is that it allows for a flexible description of powder particle size and geometric aspect ratios. When this method was applied to the frustum cone geometry, internal distribution of the magnetization in the linear and non-linear regime showed to lead to important differences from the expected results if a monolithic material is assumed. Experimental results were successfully reproduced through the proposed model. A future scenario of analysis considers different size fractions along the height of the frustum cone. Figure 8.1 presents the profile of the magnetic field and the magnetization when different density distributions of magnetic bodies are considered. In this simulation case, different particles sizes were considered, where the smallest one is assumed to have a 70% of size fraction and the biggest one is simulated through a 100% of size fraction. Linear distribution of these particles were considered from top to bottom in two cases: big particles at the bottom and small particles at the top. Conversely, bigger particles at the top and smaller at the bottom. As it can be seen from Figure 8.1 the distribution of bigger particles at the top keeps the non-uniform profile of the magnetization. On the contrary, when bigger particles are located at the bottom a flatter profile is obtained. These characteristics are very important to account in order to save magnetostrictive material.

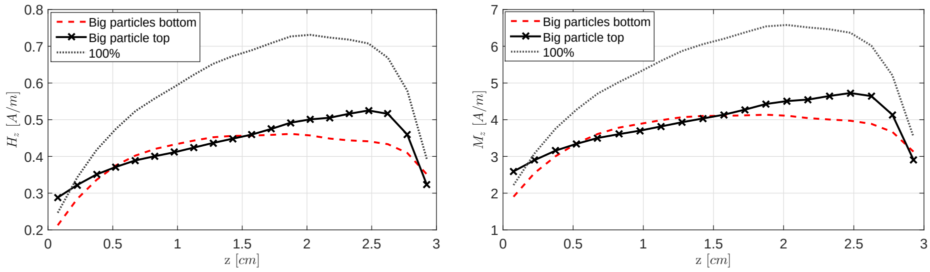

Figure 8.1: Calculated magnetic field and magnetization along the axis for a frustum cone for linear particles size distribution. (Cone radius at the bottom and the top $b_0 = 5[mm]$,$a_0 = 2[mm]$, length $L = 3[cm]$)

Finally, the design and implementation of two fiber-based sensors for sensing electric variables, magnetic field and voltage magnitudes, was presented. The magnitudes of the external fields were as similar as possible to those from high voltage systems. Some limitations were found in frequency characterization but good performance was evidenced for low frequency applications. Proposed sensors were implemented in practice and the results were contrasted to the theoretically expected behavior, leading to very good agreements. The magnetic field sensor was based on a uniform FBG embedded coaxially into a magnetostrictive composite that turned into chirped FBG when non-uniform strain due to the internal distribution of the magnetization is exerted along the grating. Experimental results for this sensor showed that the curing process induces several effects in the FBG spectrum, since some pre-strain distributions are exerted to the FBG due to the drying process of the epoxy that bonds the FBG coaxially to the cone. As future work, a method to ensure manufacturing consistency is required for improving the magnetostrictive transducer with the aim to reduce initial pre-strain and increase the accuracy.

On the other hand, voltage sensing with a piezoelectric bimorph presented very good agreement with the theoretical predictions. In the theoretical description of the bimorph operation, the definition of an effective electric field in the analytical approach was proposed to correct the maximum strain as a consequence of the spatial distribution of the electric field inside the bimorph plates when strain modifies total electric displacement field. This effective field was calculated for a linearly distributed electric field along the cross section such as it creates the same amount of bending moment. Relative error at the tip displacement was improved from 16.77% to 3.57% in the analytical calculation when compared to a finite element method solution. Two different strategies were used for sensing the mechanical deflection and the associate external voltage magnitude upon the piezoelectric layer. A first strategy considered to interrogate the central wavelength reflected back form the sensing FBG that required the usage of a wavelength interrogator, and a second strategy by using an additional FBG to act as a filter such as the frequency response of the cascade FBG arrangement allows to deduce the applied voltage by using an optical power detector. These two detection methods were implemented for different external voltage magnitudes and frequencies. Very good agreements were achieved between theoretical and experimental results, and a linear transduction function was achieved for the external high voltage inputs and the optical power amplitude measurements. Temperature dependency was not considered in the current scope of this thesis since measurements of the addressed interactions took place in a relatively constant place. However, for practical implementations of these type of sensors a rigorous temperature analysis must be performed in order to propose effective temperature correction strategies or proper thermal insulation.

Appendix A

Propagating modes in Optical Fibers

The analysis of a fiber optic as a waveguide amounts to finding the solutions of the Maxwell's equations subjected to the boundary conditions imposed by the waveguide. A typical approach for finding these solutions is the decomposition into tangential (also called transverse) and longitudinal components of the electromagnetic field. This decomposition is very useful in the description of electromagnetic field in waveguides, where the **longitudinal** direction corresponds to the **propagating direction** and **tangential** components are those components that lye on the **waveguide cross-section**. Consider the Maxwell's equations for a source-free medium:

$$\nabla \times \mathbf{E} = -j\omega\mu\mathbf{H} \tag{A.1}$$

$$\nabla \times \mathbf{H} = j\omega\varepsilon\mathbf{E} \tag{A.2}$$

where $\mathbf{E}$ and $\mathbf{H}$ are complex vectors. Let's consider the following decomposition for the electric and magnetic field:

$$\mathbf{E} = \begin{bmatrix} E_x \\ E_y \\ 0 \end{bmatrix} + \begin{bmatrix} 0 \\ 0 \\ E_z \end{bmatrix} \tag{A.3}$$

$$\mathbf{E} = \mathbf{E}_t + \mathbf{E}_z \tag{A.4}$$

$$\mathbf{H} = \mathbf{H}_t + \mathbf{H}_z \tag{A.5}$$

applying this decomposition of the electric and magnetic field to the Maxwell's equations:

$$\nabla \times (\mathbf{E}_t + \mathbf{E}_z) = -j\omega\mu\,(\mathbf{H}_t + \mathbf{H}_z) \tag{A.6}$$

$$\nabla \times (\mathbf{H}_t + \mathbf{H}_z) = j\omega\varepsilon\,(\mathbf{E}_t + \mathbf{E}_z)\,, \tag{A.7}$$

In the following, main calculations for the electric field components will be shown. Same procedure can be followed for the magnetic field. Writing rotational operator explicitly and equating components in the equations, it leads to:

$$\frac{\partial E_y}{\partial x} - \frac{\partial E_x}{\partial y} = -j\omega\mu H_z \tag{A.8}$$

$$\frac{\partial}{\partial z}\begin{bmatrix} -E_y \\ E_x \end{bmatrix} + \nabla \times E_z = -j\omega\mu \begin{bmatrix} H_x \\ H_y \end{bmatrix}, \tag{A.9}$$

which can be more simplified by using the identity:

$$\hat{i}_z \times \mathbf{E}_t = \begin{vmatrix} \hat{i} & \hat{j} & \hat{z} \\ 0 & 0 & 1 \\ E_x & E_y & 0 \end{vmatrix} = \begin{bmatrix} -E_y \\ E_x \\ 0 \end{bmatrix} \tag{A.10}$$

$$\frac{\partial}{\partial z}\begin{bmatrix} -E_y \\ E_x \end{bmatrix} = \frac{\partial}{\partial z}\hat{i}_z \times \mathbf{E}_t = \hat{i}_z \times \frac{\partial \mathbf{E}_t}{\partial z}. \tag{A.11}$$

Therefore, Maxwell's equation can be written in terms of tangential and longitudinal components of the electromagnetic field by:

$$\frac{\partial E_y}{\partial x} - \frac{\partial E_x}{\partial y} = -j\omega\mu H_z \tag{A.12}$$

$$\hat{i}_z \times \frac{\partial \mathbf{E}_t}{\partial z} + \nabla \times E_z = -j\omega\mu \mathbf{H}_t \tag{A.13}$$

$$\frac{\partial H_y}{\partial x} - \frac{\partial H_x}{\partial y} = j\omega\varepsilon E_z \tag{A.14}$$

$$\hat{i}_z \times \frac{\partial \mathbf{H}_t}{\partial z} + \nabla \times H_z = j\omega\varepsilon \mathbf{E}_t \tag{A.15}$$

defining the transversal operator $\nabla_t = (\frac{\partial}{\partial x}, \frac{\partial}{\partial y}, 0)$, it can be shorted further by:

$$\nabla_t \times \mathbf{E}_t = -j\omega\mu H_z \tag{A.16}$$

$$\hat{i}_z \times \frac{\partial \mathbf{E}_t}{\partial z} + \nabla_t \times E_z = -j\omega\mu \mathbf{H}_t \tag{A.17}$$

$$\nabla_t \times \vec{H}_t = j\omega\varepsilon E_z \tag{A.18}$$

$$\hat{i}_z \times \frac{\partial \mathbf{H}_t}{\partial z} + \nabla_t \times H_z = j\omega\varepsilon \mathbf{E}_t. \tag{A.19}$$

It is worth noting that tangential and longitudinal components are related each other in the equations above. Therefore, finding the transversal distribution of the fields in the waveguide allows to find longitudinal components, and the electromagnetic field can be completely described.

A.0.1 Electromagnetic Power

Electromagnetic power is typically used as a normalization factor for the electromagnetic field modes in waveguides. Therefore, this subsection will show a very well known derivation of the optical power from the Poynting vector definition. Poynting vector is defined as: $\vec{\mathcal{S}} = \mathbf{E} \times \mathbf{H}$, and relates the electric and magnetic energy that an electromagnetic wave can carry on through propagation. In practice, optical power is a physical quantity measured by electro-optic devices, thus only real components of the electric and magnetic fields are detected. Based on this, we can write down:

$$\mathcal{S} = \Re\left\{\mathbf{E}e^{j\omega t}\right\} \times \Re\left\{\mathbf{H}e^{j\omega t}\right\} \tag{A.20}$$

$$\mathcal{S} = \frac{1}{2}\left(\mathbf{E}e^{j\omega t} + \mathbf{E}^{*}e^{-j\omega t}\right) \times \frac{1}{2}\left(\mathbf{H}e^{j\omega t} + \mathbf{H}^{*}e^{-j\omega t}\right) \tag{A.21}$$

$$\mathcal{S} = \frac{1}{4}\left(\mathbf{E} \times \mathbf{H}e^{j2\omega t} + \mathbf{E}^{*} \times \mathbf{H} + \mathbf{E} \times \mathbf{H}^{*} + \mathbf{E}^{*} \times \mathbf{H}^{*}e^{-j2\omega t}\right) \tag{A.22}$$

An important simplification disregards fast oscillations in time leading to:

$$< \mathcal{S} >= \frac{1}{4}\left(\mathbf{E}^{*} \times \mathbf{H} + \mathbf{E} \times \mathbf{H}^{*}\right) \tag{A.23}$$

Assuming a waveguide oriented through z-direction, averaged z-component of the Poynting vector is given by:

$$< \mathcal{S}_z >= \frac{1}{4}\left(\mathbf{E}_t^{*} \times \mathbf{H}_t + \mathbf{E}_t \times \mathbf{H}_t^{*}\right) \tag{A.24}$$

being $\mathbf{E}_t$ and $\mathbf{H}_t$ tangential components of the field. Based on this result it is more useful to define a new vector $\vec{S}_z$ that holds for the tangential field components given by:

$$\vec{S}_z = \mathbf{E}_t \times \mathbf{H}_t^{*}, \tag{A.25}$$

such as,

$$\Re\left\{\vec{S}_z\right\} = \frac{1}{2}\left(\vec{S}_z + \vec{S}_z^{*}\right). \tag{A.26}$$

This definition allows the calculation of the total power through the cross-section of the waveguide using the tangential components only, leading to the expression:

$$P_{tz} = \frac{1}{4}\iint\left(\mathbf{E}_t^{*} \times \mathbf{H}_t + \mathbf{E}_t \times \mathbf{H}_t^{*}\right) \cdot d\vec{A} \tag{A.27}$$

A.0.2 Orthogonality between transversal guided modes

The most well known procedure for showing the orthogonality relationship between two solutions of the Maxwell's equation, takes advantage of a vectorial identity closely related with the reciprocity theorem in electromagnetism. This latter relates the electric and magnetic field of a source and a receptor located at different positions, and establishes an equivalence between "electromagnetic" effects when source and receptor positions are switched [32]. A similar procedure is used in [28] resulting in a natural relationship with the Poynting's vector and power carried by each mode, establishing that each mode carriers its own power independently. Assume two solutions to the Maxwell's equation in a waveguide (it will be seen later the importance of being electromagnetic fields in a waveguide), i.e. $\mathbf{E}_1$,$\mathbf{H}_1$,$\mathbf{E}_2$ and $\mathbf{H}_2$ and their conjugated vectors $\mathbf{E}_1^*$,$\mathbf{H}_1^*$,$\mathbf{E}_2^*$ and $\mathbf{H}_2^*$. Since we are dealing with conjugated expression of the fields, Maxwell's equations including these conjugated vectors are given by:

$$\nabla \times \mathbf{E} = -j\omega\mu\mathbf{H} \tag{A.28}$$

$$\nabla \times \mathbf{H} = j\omega\mu\mathbf{E} \tag{A.29}$$

$$\nabla \times \mathbf{E}^* = j\omega\mu\mathbf{H}^* \tag{A.30}$$

$$\nabla \times \mathbf{H}^* = -j\omega\mu\mathbf{E}^*. \tag{A.31}$$

We will use the vector identity $\nabla\cdot(a\times b) = b(\nabla\times a) - a(\nabla\times b)$ over the fields $\mathbf{E}_1\times\mathbf{H}_2^*$ and $\mathbf{E}_2^*\times\mathbf{H}_1$, to obtain:

$$\nabla\cdot(\mathbf{E}_1\times\mathbf{H}_2^*) = j\omega\left(\varepsilon\mathbf{E}_1\mathbf{E}_2^* - \mu\mathbf{H}_1\mathbf{H}_2^*\right) \tag{A.32}$$

$$\nabla\cdot(\mathbf{E}_2^*\times\mathbf{H}_1) = -j\omega\left(\varepsilon\mathbf{E}_1\mathbf{E}_2^* - \mu\mathbf{H}_1\mathbf{H}_2^*\right) \tag{A.33}$$

summing both results, it can be obtained:

$$\nabla\cdot(\mathbf{E}_1\times\mathbf{H}_2^* + \mathbf{E}_2^*\times\mathbf{H}_1) = 0. \tag{A.34}$$

Since we are dealing with waveguides, ∇ operator can be separated into its transversal and longitudinal components as we did for the components before, $\nabla = \nabla_t + \nabla_z$, resulting in:

$$\nabla_t\cdot(\mathbf{E}_1\times\mathbf{H}_2^* + \mathbf{E}_2^*\times\mathbf{H}_1) + \nabla_z\cdot(\mathbf{E}_1\times\mathbf{H}_2^* + \mathbf{E}_2^*\times\mathbf{H}_1) = 0. \tag{A.35}$$

it should be noticed that the ∇_z operator will extract the z-component of the internal vectorial products. This implies the following expressions:

$$\nabla_z\cdot(\mathbf{E}_1\times\mathbf{H}_2^*) = \frac{\partial}{\partial z}\left(H_{2y}^*E_{1x} - H_{2x}^*E_{1y}\right), \tag{A.36}$$

$$\nabla_z\cdot(\mathbf{E}_2^*\times\mathbf{H}_1) = \frac{\partial}{\partial z}\left(E_{2x}^*H_{1y} - E_{2y}^*H_{1x}\right). \tag{A.37}$$

An important highlight should be done about the scalar nature of this term. Although it is written as a vectorial operation, the whole result should lead to a scalar value, thus it is required to include a dot product with the unitary vector $\hat{\imath}_z$. By using this artifact the expression for the longitudinal ∇_z operator can be written as:

$$\nabla_z \cdot (\mathbf{E}_1 \times \mathbf{H}_2^* + \mathbf{E}_2^* \times \mathbf{H}_1) = \frac{\partial}{\partial z}(\mathbf{E}_{1t} \times \mathbf{H}_{2t}^* + \mathbf{E}_{2t}^* \times \mathbf{H}_{1t}) \cdot \hat{\imath}_z. \tag{A.38}$$

The usefulness of this result is that it relates the tangential components of the electric and magnetic fields instead of dealing with the whole filed components. As it will be shown latter, this will lead to a set of properties that are satisfied by these tangential components. Using this result, we can write for Eq.(A.35):

$$\nabla_t \cdot (\mathbf{E}_1 \times \mathbf{H}_2^* + \mathbf{E}_2^* \times \mathbf{H}_1) + \frac{\partial}{\partial z}(\mathbf{E}_{1t} \times \mathbf{H}_{2t}^* + \mathbf{E}_{2t}^* \times \mathbf{H}_{1t}) \cdot \hat{\imath}_z = 0. \tag{A.39}$$

In case of longitudinal dependence of each component of the propagating modes, i.e. z-dependence in the form $e^{-j\beta_i z}$, being β_i the propagation constant for the i-mode, derivative regarding z leads to:

$$\nabla_t \cdot (\mathbf{E}_1 \times \mathbf{H}_2^* + \mathbf{E}_2^* \times \mathbf{H}_1) - j(\beta_1 - \beta_2)(\mathbf{E}_{1t} \times \mathbf{H}_{2t}^* + \mathbf{E}_{2t}^* \times \mathbf{H}_{1t}) \cdot \hat{\imath}_z = 0, \tag{A.40}$$

After integrating over the cross section, first term of the left side of the equation vanishes by using the Stokes theorem and integrating over an infinite curve far from the axis waveguide where all propagating fields are null. As it is mentioned in [28], this argument also applies for radiation modes focused on the oscillatory behavior of the radiation modes. It should be also noticed that $\hat{\imath}_z$ is parallel to $d\vec{A}$, thus $d\vec{A} = \hat{\imath}_z \cdot dA$, being $dA = dxdy$. This procedure leads to:

$$-j(\beta_1 - \beta_2) \iint (\mathbf{E}_{1t} \times \mathbf{H}_{2t}^* + \mathbf{E}_{2t}^* \times \mathbf{H}_{1t}) \cdot d\vec{A} = 0 \tag{A.41}$$

The analysis can be also performed when both fields are co-propagating in the negative direction of z-axis. For doing this, we should change the corresponding signs in the magnetic field (to satisfy the power flow direction that can be easily verified by using the “right-hand” rule, but it can be also shown by symmetry properties of the Maxwell’s equations [28]) as:

$$\mathbf{E}_{-\nu t}(x, y) = \mathbf{E}_{\nu t}(x, y) \tag{A.42}$$

$$\mathbf{H}_{-\nu t}(x, y) = -\mathbf{H}_{\nu t}(x, y) \tag{A.43}$$

$$\mathbf{E}_{-\mu t}(x, y) = \mathbf{E}_{\nu t}(x, y) \tag{A.44}$$

$$\mathbf{H}_{-\mu t}(x, y) = -\mathbf{H}_{\mu t}(x, y) \tag{A.45}$$

This procedure should also consider that z-dependence will be known given by $e^{j\beta_i z}$, being β_i the propagation constant for the i-mode, leading to:

$$-j(\beta_\nu - \beta_\mu) \iint (\mathbf{E}_{\nu t} \times \mathbf{H}^*_{\mu t} + \mathbf{E}^*_{\mu t} \times \mathbf{H}_{\nu t}) \cdot d\vec{A} = 0 \tag{A.46}$$

which is exactly the same result as for co-propagating forward modes. This means that the term of the equation $\iint (\mathbf{E}_{\nu t} \times \mathbf{H}^*_{\mu t} + \mathbf{E}^*_{\mu t} \times \mathbf{H}_{\nu t}) \cdot d\vec{A}$ should be zero for any case when $\beta_\nu \neq \beta_\mu$.

$$\iint (\mathbf{E}_{\nu t} \times \mathbf{H}^*_{\mu t} + \mathbf{E}^*_{\mu t} \times \mathbf{H}_{\nu t}) \cdot d\vec{A} = 0. \tag{A.47}$$

It is worth noting that when $\beta_\nu = \beta_\mu$ in expression (A.46) is trivially satisfied by the first factor. Then, we can calculate the non-zero value of the integral term, which will lead to the total power through the cross-section area as in Eq. (A.27):

$$\iint (\mathbf{E}_{\nu t} \times \mathbf{H}^*_{\nu t} + \mathbf{E}^*_{\nu t} \times \mathbf{H}_{\nu t}) \cdot d\vec{A} = 4P_{tz}. \tag{A.48}$$

A particular case occurs when the analysis of Eq.(A.39) is performed over two counter-propagating modes. For this case we have to change the tangential magnetic field only:

$$\mathbf{E}_{\nu t}(x, y) = \mathbf{E}_{\nu t}(x, y) \tag{A.49}$$

$$\mathbf{H}_{\nu t}(x, y) = \mathbf{H}_{\nu t}(x, y) \tag{A.50}$$

$$\mathbf{E}_{-\mu t}(x, y) = \mathbf{E}_{\mu t}(x, y) \tag{A.51}$$

$$\mathbf{H}_{-\mu t}(x, y) = -\mathbf{H}_{\mu t}(x, y) \tag{A.52}$$

leading to an expression given by:

$$-j(\beta_\nu + \beta_\mu) \iint (-\mathbf{E}_{\nu t} \times \mathbf{H}^*_{\mu t} + \mathbf{E}^*_{\mu t} \times \mathbf{H}_{\nu t}) \cdot d\vec{A} = 0. \tag{A.53}$$

this result shows that for two counter-propagating modes, the equation above is only satisfied when:

$$\iint (\mathbf{E}^*_{\mu t} \times \mathbf{H}_{\nu t} - \mathbf{E}_{\nu t} \times \mathbf{H}^*_{\mu t}) \cdot d\vec{A} = 0. \tag{A.54}$$

An additional expression can be derived by using the orthogonality relation previously found. Summing Eq.(A.47) and Eq.(A.54) we can find a simplified expression that should be also satisfied [28]:

$$\iint (\mathbf{E}_{\nu t} \times \mathbf{H}^*_{\mu t}) \cdot d\vec{A} = 0. \tag{A.55}$$

Moreover, if instead of summing the expressions we make a subtraction, we can obtain an additional relation that is also true for the analysis:

$$\iint (\mathbf{E}^*_{\mu t} \times \mathbf{H}_{\nu t}) \cdot d\vec{A} = 0. \tag{A.56}$$

These two last expressions (Eqs.(A.55) and (A.56)) are also orthogonality relationships that are very useful to connect the modal fields using plane wave relations of the field components and will play an important role in the analysis of the Helmholtz equation written in a Hamiltonian formulation, particularly in supporting the normalization for establishing the orthogonality relationships and the basis expansion. Additionally, orthogonality relations found in this subsection support the Coupled Mode Theory (CMT) and establishes the power-mode independence between transversal solutions of propagating modes in waveguides [28].

A.0.3 Normalization to optical power

A natural normalization factor for defining orthonormality relations uses the total optical power carried out by the mode. Normalization factor will be done in terms of power P, i.e $P = 2P_{zt}$ instead of P_{tz} which is followed in [28]. As it was shown in Eq.(A.27) total power through the cross-section of the waveguide can be written by:

$$P_{tz} = \frac{1}{4} \iint (\mathbf{E}^*_t \times \mathbf{H}_t + \mathbf{E}_t \times \mathbf{H}^*_t) \cdot d\vec{A}. \tag{A.57}$$

Since $\mathbf{E}_t \times \mathbf{H}^*_t$ becomes real in waveguides (which physically means propagated power through the waveguide), we define P as:

$$P = 2P_{tz} = \Re\left\{\iint \mathbf{E}_t \times \mathbf{H}^*_t \cdot d\vec{A}\right\} = \iint (\mathbf{E}_t \times \mathbf{H}^*_t) \cdot d\vec{A}. \tag{A.58}$$

It should be noticed that the normalization factor must be P, thus in our definition we will use $P = 2P_{tz}$. Based on this definition, the orthogonality relationship will be written by:

$$\hat{e}_{\nu t}(x, y) = \frac{\mathbf{E}_{1t}}{\sqrt{2P_{tz}}} = \frac{\mathbf{E}_{1t}}{\sqrt{\iint (\mathbf{E}_{1t} \times \mathbf{H}^*_{1t}) dA}} \tag{A.59}$$

$$\hat{h}_{\nu t}(x, y) = \frac{\mathbf{H}_{1t}}{\sqrt{2P_{tz}}} = \frac{\mathbf{H}_{1t}}{\sqrt{\iint (\mathbf{E}_{1t} \times \mathbf{H}^*_{1t}) dA}} \tag{A.60}$$

$$\iint (\hat{e}_{\nu t}(x, y) \times \hat{h}^*_{\nu t}(x, y)) dA = \delta_{\nu\mu} \tag{A.61}$$

Therefore, orthogonality relationship can be written by:

$$\iint (\hat{e}_{\nu t}(x,y) \times \hat{h}^{*}_{\nu t}(x,y))dA = \delta_{\nu\mu} \tag{A.62}$$

A.0.4 Modes of a Waveguide

A mode of a waveguide is defined as a field solution of the form:

$$\mathbf{E}(x,y,z) = \mathbf{E}_{\nu}(x,y)e^{-j\beta_{\nu}z} \tag{A.63}$$

$$\mathbf{H}(x,y,z) = \mathbf{H}_{\nu}(x,y)e^{-j\beta_{\nu}z} \tag{A.64}$$

where β_{ν} can be real or complex. In the first case leading to propagating modes and the the second one to evanescent modes. When this particular form of the fields (where the z-dependence is explicitly determined) are inserted into the Maxwell's equations, it leads to:

$$\nabla_t \times \mathbf{E}_{\nu t}(x,y) = -j\omega\mu H_{\nu z}(x,y) \tag{A.65a}$$

$$\nabla_t \times \mathbf{H}_{\nu t}(x,y) = j\omega\varepsilon E_{\nu z}(x,y) \tag{A.65b}$$

$$-j\beta_{\nu}\left(\hat{i}_z \times \mathbf{E}_{\nu t}(x,y)\right) + \nabla_t \times E_{\nu z}(x,y) = -j\omega\mu\mathbf{H}_{\nu t}(x,y) \tag{A.65c}$$

$$-j\beta_{\nu}\left(\hat{i}_z \times \mathbf{H}_{\nu t}(x,y)\right) + \nabla_t \times H_{\nu z}(x,y) = j\omega\varepsilon\mathbf{E}_{\nu t}(x,y) \tag{A.65d}$$

Solutions for guided modes should satisfy set of Eqs.(A.65). There are some properties of the solutions that are typically desired: completeness and orthogonality. These two are of great importance because allows the expansion of arbitrary solutions in terms of this modal field solutions. Next procedure (followed from [28]) shows how to find an expression for the orthogonality of propagating modes.

A.0.5 Modal Expansion

Orthogonality relations and completeness allow the determination of a set of modes that form a basis for expressing any arbitrary tangential field as a linear combination of modal tangential fields. However, completeness is not totally guaranteed for the Maxwell's equations associated to the boundary conditions even with the existence of an orthogonal basis [45, 44]. Anyway, a modal expansion can be proposed for an arbitrary tangential field in terms of forward and backward modes. If only forward modes are considered in the expansion:

$$\mathbf{E}_t(x,y) = \sum_{\nu} (a_\nu)\, \hat{e}_{\nu t}(x,y) \tag{A.66a}$$

$$\mathbf{H}_t(x,y) = \sum_{\nu} (a_\nu)\, \hat{h}_{\nu t}(x,y) \tag{A.66b}$$

where expansion coefficients can be found by:

$$\int \left(\mathbf{E}_t(x,y) \times \hat{h}^*_{\mu t}\right) dA = \sum_{\nu} (a_\nu) \int \left(\hat{e}_{\nu t} \times \hat{h}^*_{\mu t}\right) dA \tag{A.67}$$

$$a_\mu = 2 \int \left(\mathbf{E}_t(x,y) \times \hat{h}^*_{\mu t}(x,y)\right) dA \tag{A.68}$$

for the magnetic field coefficients we have:

$$\int \left(\hat{e}^*_{\mu t} \times \mathbf{H}_t(x,y)\right) dA = \sum_{\nu} (a_\nu) \int \left(\hat{e}^*_{\mu t} \times \hat{h}_{\nu t}\right) dA \tag{A.69}$$

$$a_\mu = 2 \int \left(\hat{e}^*_{\mu t}(x,y) \times \mathbf{H}_t(x,y)\right) dA \tag{A.70}$$

In case of forward and backward modes were considered into the expansion, we can write:

$$\mathbf{E}_t(x,y) = \sum_{\nu} a_\nu \hat{e}_{\nu t}(x,y) + \sum_{\nu} b_\nu \hat{e}_{-\nu t}(x,y) \tag{A.71}$$

$$\mathbf{H}_t(x,y) = \sum_{\nu} a_\nu \hat{h}_{\nu t}(x,y) + \sum_{\nu} b_\nu \hat{h}_{-\nu t}(x,y) \tag{A.72}$$

since for propagating modes, forward and backward fields are related by $\hat{e}_{-\nu t}(x,y) = \hat{e}_{\nu t}(x,y)$ and $\hat{h}_{-\nu t}(x,y) = -\hat{h}_{\nu t}(x,y)$, we can write:

$$\mathbf{E}_t(x,y) = \sum_{\nu} (a_\nu + b_\nu)\, \hat{e}_{\nu t}(x,y) \tag{A.73}$$

$$\mathbf{H}_t(x,y) = \sum_{\nu} (a_\nu - b_\nu)\, \hat{h}_{\nu t}(x,y) \tag{A.74}$$

as in the case before, we can find the coefficients of the expansion by using the orthogonality relation. Thus, we multiply each term by the corresponding field to find the same relation as in the orthonormality case:

$$\int \left(\mathbf{E}_t(x,y) \times \hat{h}^*_{\mu t}\right) dA = \sum_\nu (a_\nu + b_\nu) \int \left(\hat{e}_{\nu t} \times \hat{h}^*_{\mu t}\right) dA \tag{A.75}$$

$$\int \left(\hat{e}^*_{\mu t} \times \mathbf{H}_t(x,y)\right) dA = \sum_\nu (a_\nu - b_\nu) \int \left(\hat{e}^*_{\mu t} \times \hat{h}_{\nu t}\right) dA \tag{A.76}$$

Applying the orthogonal relationship found before, we can write:

$$2\int \left(\mathbf{E}_t(x,y) \times \hat{h}^*_{\mu t}\right) dA = (a_\mu + b_\mu) \tag{A.77}$$

$$2\int \left(\hat{e}^*_{\mu t} \times \mathbf{H}_t(x,y)\right) dA = (a_\mu - b_\mu) \tag{A.78}$$

where we can simply add and subtract both equations to obtain the corresponding expansion coefficients:

$$a_\mu = \int \left(\mathbf{E}_t(x,y) \times \hat{h}^*_{\mu t}(x,y) + \hat{e}^*_{\mu t}(x,y) \times \mathbf{H}_t(x,y)\right) dA \tag{A.79}$$

$$b_\mu = \int \left(\mathbf{E}_t(x,y) \times \hat{h}^*_{\mu t}(x,y) - \hat{e}^*_{\mu t}(x,y) \times \mathbf{H}_t(x,y)\right) dA. \tag{A.80}$$

An additional important result is the calculation of the averaged Poynting vector of the arbitrary field $\mathbf{E}_t$ and $\mathbf{H}_t$, in terms of the expansion coefficients:

$$<\mathcal{S}>= \frac{1}{4}\left(\mathbf{E}^*_t \times \mathbf{H}_t + \mathbf{E}_t \times \mathbf{H}^*_t\right) \tag{A.81}$$

$$<\mathcal{S}>= \frac{1}{2}\sum_\nu a^*_\nu a_\nu - b_\nu b^*_\nu \tag{A.82}$$

A.0.6 Polarization vector as a source of coupling

As it was presented in the previous sections, orthogonality relations were derived from Maxwell equations in free-source media. In presence of polarization sources, Maxwell equations can be written as:

$$\nabla \times (\nabla \times \mathbf{E}(\vec{r})) = \mu_0\omega^2\mathbf{D}(\vec{r}) \tag{A.83a}$$

$$\nabla \times \left(\frac{1}{\varepsilon(\vec{r})}\nabla \times \mathbf{H}(\vec{r})\right) = \mu_0\omega^2\mathbf{H}(\vec{r}) \tag{A.83b}$$

$$\nabla \cdot \mathbf{D}(\vec{r}) = 0 \tag{A.83c}$$

$$\nabla \cdot \mathbf{H}(\vec{r}) = 0, \tag{A.83d}$$

where time dependence is assumed to be $\exp(j\omega t)$. Vectors $\mathbf{E}(\vec{r})$ and $\mathbf{H}(\vec{r})$ are the electric and magnetic field vector. $\mathbf{D}(\vec{r})$ represents the electric displacement vector given by $\mathbf{D}(\vec{r}) = \varepsilon_0\mathbf{E}(\vec{r}) + \mathbf{P}(\vec{r})$, with $\varepsilon(\vec{r})$ electric permittivity of the media and ε_0 permittivity of vacuum. $\mathbf{P}(\vec{r})$ the polarization vector that includes linear and nonlinear responses given by: $\mathbf{P}(\vec{r}) = \mathbf{P}_L(\vec{r}) + \mathbf{P}_{NL}(\vec{r})$ [8]. Polarization vector $\mathbf{P}(\vec{r})$ is responsible for including linear and non-linear response of dielectrics. In the case of isotropic materials, the linear term of the polarization vector can be expressed through a scalar relation with the electric field, i.e. $\mathbf{P}_L(\vec{r}) = \varepsilon_0\chi\mathbf{E}(\vec{r})$, where χ is the first order electrical susceptibility of the material. However, when anisotropies are present, the polarization vector and the electric field vector must be related trough a tensorial relationship given by $\mathbf{P}_L(\vec{r}) = \varepsilon_0\hat{\chi}^{(1)}\mathbf{E}(\vec{r})$ [8, 43]. On the other hand, nonlinear response of the material implies to take into account a set of relatively more complex relations with the electric field [8]. In the majority of dielectrics, the nonlinear polarization vector can be written in terms of powers of the electric field as $\mathbf{P}_{NL}(\vec{r}) = P\left(\mathbf{E}^2\left(\vec{\mathbf{r}}\right), \mathbf{E}^3\left(\vec{\mathbf{r}}\right), ..., \hat{\chi}^{(2)}, \hat{\chi}^{(3)}, ...\right)$, where $\hat{\chi}^{(j)}$ corresponds to the high-order susceptibility tensors. Far from their natural resonances, this relation can be given by a sum of these terms: $\mathbf{P}_{NL}(\vec{r}) = \varepsilon_0\left(\hat{\chi}^{(2)}\mathbf{E}\left(\vec{\mathbf{r}}\right)\mathbf{E}\left(\vec{\mathbf{r}}\right) + \hat{\chi}^{(3)}\mathbf{E}\left(\vec{\mathbf{r}}\right)\mathbf{E}\left(\vec{\mathbf{r}}\right)\mathbf{E}\left(\vec{\mathbf{r}}\right) +, ...,\right)$ [8]. Perturbations in polarization vector is able to couple modes in the optical waveguide, such as propagating, radiation and evanescent modes can interact and interchange power between them.

A.0.7 Coupled Mode Theory

In this subsection, polarization vector will be treated as a perturbation source that allows the interactions between two modes. This interaction will be described by using the modal expansion and orthogonality properties found for the propagating modes in the preceding subsections. Let's consider two different fields, i.e. $\mathbf{E}_1$,$\mathbf{H}_1$,$\mathbf{E}_2$ and $\mathbf{H}_2$ and their conjugated vectors $\mathbf{E}_1^*$,$\mathbf{H}_1^*$,$\mathbf{E}_2^*$ and $\mathbf{H}_2^*$. As an assumption, consider that one of the EM fields ($\mathbf{E}_1$ and $\mathbf{H}_1$) satisfy a no source-free relationship. Maxwell's equations for these fields are given by:

$$\nabla \times \mathbf{E}_1 = -j\omega\mu\mathbf{H}_1 \tag{A.84a}$$

$$\nabla \times \mathbf{H}_1 = j\omega\varepsilon\mathbf{E}_1 + j\omega\mathbf{P}_1 \tag{A.84b}$$

$$\nabla \times \mathbf{E}_2 = -j\omega\mu\mathbf{H}_2 \tag{A.84c}$$

$$\nabla \times \mathbf{H}_2 = j\omega\varepsilon\mathbf{E}_2. \tag{A.84d}$$

Using the same Stokes theorem procedure used before and integrating over an infinite curve far from the axis waveguide, the left side of the equation will vanish, leading to:

$$\iint \frac{\partial}{\partial z}(\mathbf{E}_{1t} \times \mathbf{H}^*_{2t} + \mathbf{E}^*_{2t} \times \mathbf{H}_{1t})dA = -j\omega \iint \mathbf{E}^*_2 \cdot \mathbf{P}_1 \cdot d\vec{A}. \tag{A.85}$$

This result resembles the orthogonality relationship found before for source-free electromagnetic propagation. In this particular case, **one must consider a longitudinal dependence of each coefficient in the mode expansion. This z-dependence is made explicit to associate the interaction between modes along the propagation path due to a polarization source**. Let's consider $\mathbf{E}_{1t}$ and $\mathbf{H}_{1t}$ arbitrary tangential fields that are generated by a source of polarization $\mathbf{P}_1$, and let's take advantage of the current form of Eq.(A.85) to write them in terms of modal fields. By doing this, we can expand the arbitrary field $\mathbf{E}_{1t}$ and $\mathbf{H}_{1t}$ in the modal basis by:

$$\mathbf{E}_{1t}(x, y, z) = \sum_{\nu} \left(a_\nu(z) + b_\nu(z)\right) \hat{e}_{t\nu}(x, y) \tag{A.86}$$

$$\mathbf{H}_{1t}(x, y, z) = \sum_{\nu} \left(a_\nu(z) - b_\nu(z)\right) \hat{h}_{t\nu}(x, y). \tag{A.87}$$

where expansion coefficients are z-dependent given by: $a_\nu(z) = A_\nu(z)e^{-j\beta_\nu z}$ and $b_\nu(z) = B_\nu(z)e^{j\beta_\nu z}$. Two different types of z-dependence for the mode $\mathbf{E}_2$, $\mathbf{H}_2$ can be considered. In one case, it can be a forward propagating mode, with $\mathbf{E}_2 = \hat{e}_{t\mu}(x, y)e^{-j\beta_\mu z} + \hat{e}_{z\mu}(x, y)e^{-j\beta_\mu z}$, and in the other case, it can be a backward propagating mode $\mathbf{E}_2 = \hat{e}_{t\mu}(x, y)e^{j\beta_\mu z} - \hat{e}_{z\mu}(x, y)e^{j\beta_\mu z}$. In both cases, modal fields ($\hat{e}_\mu$ and $\hat{h}_\mu$) should satisfy the orthogonal relationships given by:

$$\int \left(\hat{e}_{t\nu} \times \hat{h}^*_{t\mu}\right) dA = \frac{\delta_{\nu\mu}}{2}, \tag{A.88}$$

$$\int \left(\hat{e}^*_{t\nu} \times \hat{h}_{t\mu}\right) dA = \frac{\delta_{\nu\mu}}{2}. \tag{A.89}$$

Assuming forward propagating modes, tangential components $\mathbf{E}_{2t}$ and $\mathbf{H}_{2t}$ are given by: $\mathbf{E}_{2t} = \hat{e}_{\mu t}(x, y)e^{-j\beta_\mu z}$ and $\mathbf{H}_{2t} = \hat{h}_{\mu t}(x, y)e^{-j\beta_\mu z}$. Plug in them into Eq.(A.85) and applying the orthogonality relationship leads to:

$$\frac{\partial}{\partial z}\left(a_\mu(z)e^{j\beta_\mu z}\right) = -j\omega \iint \left(\hat{e}^*_{t\mu}(x, y) + \hat{e}^*_{z\mu}(x, y)\right) e^{j\beta_\mu z} \cdot \mathbf{P}_1 \cdot d\vec{A} \tag{A.90}$$

$$a'_\mu(z) + j\beta_\mu a_\mu(z) = -j\omega \iint \left(\hat{e}^*_{t\mu}(x, y) + \hat{e}^*_{z\mu}(x, y)\right) \cdot \mathbf{P}_1 \cdot d\vec{A}. \tag{A.91}$$

Now, in case of backward propagating mode field, tangential fields $\mathbf{E}_{2t}$ and $\mathbf{H}_{2t}$ can be obtained by replacing $\hat{e}_{-\mu} = \hat{e}_{\mu}$ and $\hat{h}_{-\mu} = -\hat{h}_{\mu}$, which changes the expression to be:

$$\frac{\partial}{\partial z}\left(b_{\mu}(z)e^{-j\beta_{\mu}z}\right) = j\omega \iint \left(\hat{e}^{*}_{t\mu}(x,y) - \hat{e}^{*}_{z\mu}(x,y)\right) e^{-j\beta_{\mu}z} \cdot \mathbf{P}_1 \cdot d\vec{A} \tag{A.92}$$

$$b'_{\mu}(z) - j\beta_{\mu}b_{\mu}(z) = j\omega \iint \left(\hat{e}^{*}_{t\mu}(x,y) - \hat{e}^{*}_{z\mu}(x,y)\right) \cdot \mathbf{P}_1 \cdot d\vec{A}. \tag{A.93}$$

Finally, we can write for the expansion coefficients that accounts for forward and backward propagating modes:

$$a'_{\mu}(z) + j\beta_{\mu}a_{\mu}(z) = -j\omega \iint \left(\hat{e}^{*}_{t\mu}(x,y) + \hat{e}^{*}_{z\mu}(x,y)\right) \cdot \mathbf{P}_1 \cdot d\vec{A} \tag{A.94}$$

$$b'_{\mu}(z) - j\beta_{\mu}b_{\mu}(z) = j\omega \iint \left(\hat{e}^{*}_{t\mu}(x,y) - \hat{e}^{*}_{z\mu}(x,y)\right) \cdot \mathbf{P}_1 \cdot d\vec{A} \tag{A.95}$$

where $a'_{\mu}(z)$ and $b'_{\mu}(z)$ represent total derivatives regarding z of the coefficients. Polarization vector $\mathbf{P}_1$ can be written in terms of the electric field by:

$$\mathbf{P}_1 = \Delta\varepsilon\mathbf{E}_1, \tag{A.96}$$

As expressed in Eq.(A.96), longitudinal and tangential decomposition for the polarization vector will depend on the tensor nature of the term $\Delta\varepsilon$. In the particular case, we can write change of permittivity tensor by:

$$\Delta\varepsilon = \left[\begin{array}{cc} \Delta\varepsilon_t & 0 \\ 0 & \Delta\varepsilon_z \end{array}\right], \tag{A.97}$$

which allows to write polarization vector in the same fashion of longitudinal and transverse components by:

$$\mathbf{P}_1 = \Delta\varepsilon\mathbf{E}_1 \tag{A.98}$$

$$\mathbf{P}_1 = \Delta\varepsilon_t\mathbf{E}_{1t} + \Delta\varepsilon_z\mathbf{E}_{1z}, \tag{A.99}$$

replacing $\mathbf{E}_{1t}$ by its corresponding modal expansion, polarization vector can be written by:

$$\mathbf{P}_1 = \Delta\varepsilon_t\left(\sum_{\nu}\left(a_{\nu}(z) + b_{\nu}(z)\right)\hat{e}_{\nu t}(x,y)\right) + \Delta\varepsilon_z\mathbf{E}_{1z}. \tag{A.100}$$

From Maxwell's equation: $\nabla \times \mathbf{H}_1 = j\omega\varepsilon\mathbf{E}_1 + j\omega\mathbf{P}_1$, we can find for the z-component of the electric field:

$$\nabla \times \mathbf{H}_{1t} = j\omega\varepsilon\mathbf{E}_{1z} + j\omega\mathbf{P}_{1z} \tag{A.101}$$

$$\nabla \times \mathbf{H}_{1t} = j\omega\varepsilon\mathbf{E}_{1z} + j\omega\Delta\varepsilon_z\mathbf{E}_{1z} \tag{A.102}$$

$$\mathbf{E}_{1z} = \frac{1}{j\omega\left(\varepsilon + \Delta\varepsilon_z\right)}\nabla \times \mathbf{H}_{1t}, \tag{A.103}$$

where one can expand $\mathbf{H}_{1t}$ in terms of the basis elements,
i.e. $\mathbf{H}_{1t}(x,y,z) = \sum_\nu \left(a_\nu(z) - b_\nu(z)\right) \hat{h}_{\nu t}(x,y)$, leading to:

$$\mathbf{E}_{1z} = \frac{1}{j\omega\left(\varepsilon + \Delta\varepsilon_z\right)} \nabla \times \left(\sum_\nu \left(a_\nu(z) - b_\nu(z)\right) \hat{h}_{\nu t}(x,y) \right) \tag{A.104}$$

rotational operator acting upon the tangential magnetic field in the modal expansion can be replaced by: $\nabla \times \hat{h}_{\nu t}(x,y) = j\omega\varepsilon \hat{e}_{\nu z}(x,y)$, allowing to write:

$$\mathbf{E}_{1z} = \frac{j\omega\varepsilon}{j\omega\left(\varepsilon + \Delta\varepsilon_z\right)} \left(\sum_\nu \left(a_\nu(z) - b_\nu(z)\right) \hat{e}_{\nu z}(x,y) \right), \tag{A.105}$$

which can be plugged in Eq.(A.100) to obtain:

$$\begin{gathered} \mathbf{P}_1 = \Delta\varepsilon_t \left(\sum_\nu \left(a_\nu(z) + b_\nu(z)\right) \hat{e}_{\nu t}(x,y) \right) \\ + \frac{\Delta\varepsilon_z \varepsilon}{\left(\varepsilon + \Delta\varepsilon_z\right)} \left(\sum_\nu \left(a_\nu(z) - b_\nu(z)\right) \hat{e}_{\nu z}(x,y) \right). \end{gathered} \tag{A.106}$$

Once polarization vector is written in the modal expansion terms, we can plug this expression into Eq.(A.94), first for the forward coefficient:

$$a'_\mu(z) + j\beta_\mu a_\mu(z) = -j\omega \iint \left(\hat{e}^*_{t\mu}(x,y) + \hat{e}^*_{z\mu}(x,y) \right) \cdot \mathbf{P}_1 \cdot d\vec{A} \tag{A.107}$$

to obtain:

$$\begin{aligned} a'_\mu(z) + j\beta_\mu a_\mu(z) = -j\omega \iint \sum_\nu \left[\left(a_\nu(z) + b_\nu(z)\right) \hat{e}^*_{t\mu}(x,y) \Delta\varepsilon_t \hat{e}_{\nu t}(x,y) \right] dA \\ + - j\omega \iint \sum_\nu \left[\left(a_\nu(z) - b_\nu(z)\right) \hat{e}^*_{z\mu}(x,y) \frac{\Delta\varepsilon_z \varepsilon}{\left(\varepsilon + \Delta\varepsilon_z\right)} \hat{e}_{\nu z}(x,y) \right] dA \end{aligned} \tag{A.108}$$

and for the backward coefficient:

$$b'_\mu(z) - j\beta_\mu b_\mu(z) = j\omega \iint \left(\hat{e}^*_{t\mu}(x,y) - \hat{e}^*_{z\mu}(x,y) \right) \cdot \mathbf{P}_1 \cdot d\vec{A}, \tag{A.109}$$

which leads to:

$$\begin{aligned} b'_\mu(z) - j\beta_\mu b_\mu(z) = j\omega \iint \sum_\nu \left[\left(a_\nu(z) + b_\nu(z)\right) \hat{e}^*_{t\mu}(x,y) \Delta\varepsilon_t \hat{e}_{\nu t}(x,y) \right] dA \\ -j\omega \iint \sum_\nu \left[\left(a_\nu(z) - b_\nu(z)\right) \hat{e}^*_{z\mu}(x,y) \frac{\Delta\varepsilon_z \varepsilon}{\left(\varepsilon + \Delta\varepsilon_z\right)} \hat{e}_{\nu z}(x,y) \right] dA, \end{aligned} \tag{A.110}$$

we can define tangential and longitudinal coupling coefficients by:

$$K^t_{\nu\mu} = \omega \iint \hat{e}^*_{t\mu}(x,y)\Delta\varepsilon_t \hat{e}_{\nu t}(x,y)dA \tag{A.111a}$$

$$K^z_{\nu\mu} = \omega \iint \hat{e}^*_{z\mu}(x,y)\frac{\Delta\varepsilon_z\varepsilon}{(\varepsilon+\Delta\varepsilon_z)}\hat{e}_{\nu z}(x,y)dA \tag{A.111b}$$

then we are able to write for the forward and backward amplitudes:

$$a'_\mu(z) + j\beta_\mu a_\mu(z) = -j\sum_\nu \left[a_\nu(z)\left(K^t_{\nu\mu}+K^z_{\nu\mu}\right) + b_\nu(z)\left(K^t_{\nu\mu}-K^z_{\nu\mu}\right)\right] \tag{A.112}$$

$$b'_\mu(z) - j\beta_\mu b_\mu(z) = j\sum_\nu \left[a_\nu(z)\left(K^t_{\nu\mu}-K^z_{\nu\mu}\right) + b_\nu(z)\left(K^t_{\nu\mu}+K^z_{\nu\mu}\right)\right] \tag{A.113}$$

An additional step is followed in [28] to write an explicit set of expressions for the amplitude of the expansion coefficient instead of the coefficient itself. Then we can write:

$$a_\mu(z) = A_\mu(z)e^{-j\beta_\mu z} \tag{A.114}$$

$$b_\mu(z) = B_\mu(z)e^{j\beta_\mu z} \tag{A.115}$$

from this definition we can write:

$$A_\mu(z) = a_\mu(z)e^{j\beta_\mu z} \tag{A.116}$$

$$B_\mu(z) = b_\mu(z)e^{-j\beta_\mu z} \tag{A.117}$$

this expression has the advantage that taking the derivative of the coefficient respect to z, it will lead to:

$$A'_\mu(z) = \left(a'_\mu(z) + j\beta_\mu a_\mu(z)\right)e^{j\beta_\mu z} \tag{A.118}$$

$$B'_\mu(z) = \left(b'_\mu(z) - j\beta_\mu b_\mu(z)\right)e^{-j\beta_\mu z} \tag{A.119}$$

in order to apply this result we can multiply by their corresponding exponential dependence at each side of Eqs.(A.112 and A.113) to obtain:

$$A'_\mu(z) = -j\sum_\nu \left[a_\nu(z)\left(K^t_{\nu\mu}+K^z_{\nu\mu}\right) + b_\nu(z)\left(K^t_{\nu\mu}-K^z_{\nu\mu}\right)\right]e^{j\beta_\mu z} \tag{A.120}$$

$$B'_\mu(z) = j\sum_\nu \left[a_\nu(z)\left(K^t_{\nu\mu}-K^z_{\nu\mu}\right) + b_\nu(z)\left(K^t_{\nu\mu}+K^z_{\nu\mu}\right)\right]e^{-j\beta_\mu z}. \tag{A.121}$$

Using the same definition for the coefficients $a_\nu(z)$ and $b_\nu(z)$, we have:

$$a_\nu(z) = A_\nu(z)e^{-j\beta_\nu z} \tag{A.122}$$

$$b_\nu(z) = B_\nu(z)e^{j\beta_\nu z}, \tag{A.123}$$

which allows to write:

$$A'_\mu(z) = -j\sum_\nu \left[A_\nu(z)e^{-j\beta_\nu z}\left(K^t_{\nu\mu} + K^z_{\nu\mu}\right) + B_\nu(z)e^{j\beta_\nu z}\left(K^t_{\nu\mu} - K^z_{\nu\mu}\right)\right] e^{j\beta_\mu z} \tag{A.124}$$

$$B'_\mu(z) = j\sum_\nu \left[A_\nu(z)e^{-j\beta_\nu z}\left(K^t_{\nu\mu} - K^z_{\nu\mu}\right) + B_\nu(z)e^{j\beta_\nu z}\left(K^t_{\nu\mu} + K^z_{\nu\mu}\right)\right] e^{-j\beta_\mu z} \tag{A.125}$$

where we can make some simplifications to write:

$$\begin{aligned} A'_\mu(z) = -j\sum_\nu A_\nu(z)\left(K^t_{\nu\mu} + K^z_{\nu\mu}\right)e^{-j(\beta_\nu - \beta_\mu)z} + ... \\ -j\sum_\nu B_\nu(z)\left(K^t_{\nu\mu} - K^z_{\nu\mu}\right)e^{j(\beta_\nu + \beta_\mu)z} \end{aligned} \tag{A.126}$$

$$\begin{aligned} B'_\mu(z) = j\sum_\nu A_\nu(z)\left(K^t_{\nu\mu} - K^z_{\nu\mu}\right)e^{-j(\beta_\nu + \beta_\mu)z} + ... \\ j\sum_\nu B_\nu(z)\left(K^t_{\nu\mu} + K^z_{\nu\mu}\right)e^{j(\beta_\nu - \beta_\mu)z}. \end{aligned} \tag{A.127}$$

We have followed the procedure presented in [28] and showed in detail the derivation of the coupled mode equations Eq.(A.126) and Eq.(A.127). The problem to solve hereafter is to find the expressions for the evolution along z-direction for $A_\mu(z)$ and $B_\mu(z)$, based on the number of modes considered in the expansion.

A.0.7.1 Contra-directional Coupling Equations

In this case we will consider that only two modes are in interaction. A forward propagating mode with amplitude $a_\nu(z) = A_\nu(z)e^{-j\beta_\nu z}$ and a backward propagating mode with amplitude $b_\mu(z) = B_\mu(z)e^{j\beta_\mu z}$. Therefore, equations Eq.(A.126) and Eq.(A.127) are required to be used. Fortunately, they simplify to the interaction between forward and backward propagating modes:

$$A'_\nu(z) = -jA_\nu(z)\left(K^t_{\nu\nu} + K^z_{\nu\nu}\right) - jB_\mu(z)\left(K^t_{\nu\mu} - K^z_{\nu\mu}\right)e^{j(\beta_\nu + \beta_\mu)z} \tag{A.128}$$

$$B'_\mu(z) = jA_\nu(z)\left(K^t_{\nu\mu} - K^z_{\nu\mu}\right)e^{-j(\beta_\nu + \beta_\mu)z} + jB_\mu(z)\left(K^t_{\mu\mu} + K^z_{\mu\mu}\right) \tag{A.129}$$

which in general can be written in a matrix form given by:

$$\frac{d}{dz}\begin{bmatrix} A_\nu \\ B_\mu \end{bmatrix} = \begin{bmatrix} -j\left(K^t_{\nu\nu}+K^z_{\nu\nu}\right) & -j\left(K^t_{\nu\mu}-K^z_{\nu\mu}\right)e^{j(\beta_\nu+\beta_\mu)z} \\ j\left(K^t_{\nu\mu}-K^z_{\nu\mu}\right)e^{-j(\beta_\nu+\beta_\mu)z} & j\left(K^t_{\mu\mu}+K^z_{\mu\mu}\right) \end{bmatrix}\begin{bmatrix} A_\nu \\ B_\mu \end{bmatrix} \tag{A.130}$$

For optical fibers one can consider pure transverse modes or quasi-transverse modes, this latter is a commonly used approximation in optical fibers under the “weakly guide” assumption, i.e. refractive index contrast between core and cladding is small, normally around $\Delta \approx 0.001$. Based on this approximation we can write:

$$\frac{d}{dz}\begin{bmatrix} A_\nu \\ B_\mu \end{bmatrix} = \begin{bmatrix} -j\left(K^t_{\nu\nu}\right) & -j\left(K^t_{\nu\mu}\right)e^{j(\beta_\nu+\beta_\mu)z} \\ j\left(K^t_{\nu\mu}\right)e^{-j(\beta_\nu+\beta_\mu)z} & j\left(K^t_{\mu\mu}\right) \end{bmatrix}\begin{bmatrix} A_\nu \\ B_\mu \end{bmatrix} \tag{A.131}$$

We want to analyze the case where the forward and backward mode that are coupled by the perturbation have exactly the same propagation constant, i.e. $\beta_\nu = \beta_\mu = \beta_o$. We can also write $\kappa = K^t_{\nu\mu}$, $\delta = \beta_o + \kappa$, This implies to solve the characteristic polynomial of the matrix $\mathbb{M}$:

$$\lambda^2 - (\delta^2 - \kappa^2) = 0 \tag{A.132}$$

$$\lambda = \pm\sqrt{\delta^2 - \kappa^2}. \tag{A.133}$$

Once the roots of the characteristic polynomial are solved, matrix can be diagonalized through its eigenvalues and eigenvectors. Therefore, we can write the matrix as:

$$\begin{bmatrix} R(z) \\ S(z) \end{bmatrix} = \begin{bmatrix} \cosh(j\beta_s z) - \frac{\sqrt{\delta^2-\kappa^2}}{\delta}\sinh(j\beta_s z) & \frac{\kappa}{\delta}\sinh(j\beta_s z) \\ \frac{\kappa}{\delta}\sinh(j\beta_s z) & \cosh(j\beta_s z) + \frac{\sqrt{\delta^2-\kappa^2}}{\delta}\sinh(j\beta_s z) \end{bmatrix}\begin{bmatrix} R(0) \\ S(0) \end{bmatrix}. \tag{A.134}$$

In typical situations with this type of coupling, the input amplitude of the forwarding mode is set to be $R(0) = 1$ and the amplitude of the backward is set to be $S(L) = 0$, where L is the total length of interaction. Therefore, $R(L)$ and $S(0)$ become the incognito values. Then, we can be solved by [28]:

$$S(0) = \frac{-j\kappa}{\sqrt{\kappa^2-\delta^2}\coth(L\sqrt{\kappa^2-\delta^2}) + j\delta} \tag{A.135}$$

$$R(L) = \frac{\sqrt{\kappa^2-\delta^2}}{\sqrt{\kappa^2-\delta^2}\cosh(L\sqrt{\kappa^2-\delta^2}) + j\delta\sinh(L\sqrt{\kappa^2-\delta^2})} \tag{A.136}$$

where the reflection factor at the input can be written by:

$$\rho = \frac{S(0)}{R(0)} = S(0) \tag{A.137}$$

$$\rho = \frac{-j\kappa \sinh(L\sqrt{\kappa^2 - \delta^2})}{\sqrt{\kappa^2 - \delta^2}\cosh(L\sqrt{\kappa^2 - \delta^2}) + j\delta \sinh(L\sqrt{\kappa^2 - \delta^2})} \tag{A.138}$$

A.0.7.2 Co-directional Coupling Equations

In this case we will consider that only two modes are in interaction. A forward propagating mode with amplitude $a_\nu(z) = A_\nu(z)e^{-j\beta_\nu z}$ and a forward propagating mode with amplitude $a_\mu(z) = A_\mu(z)e^{-j\beta_\mu z}$. Therefore, equation Eq.(A.126) is the only one required because only forward modes are considered. Based on this we can write for the interaction between two forward propagating modes:

$$A'_\nu(z) = -jA_\nu(z)\left(K^t_{\nu\nu} + K^z_{\nu\nu}\right) - jA_\mu(z)\left(K^t_{\nu\mu} + K^z_{\nu\mu}\right)e^{-j(\beta_\mu - \beta_\nu)z} \tag{A.139}$$

$$A'_\mu(z) = -jA_\nu(z)\left(K^t_{\nu\mu} + K^z_{\nu\mu}\right)e^{-j(\beta_\nu - \beta_\mu)z} - jA_\mu(z)\left(K^t_{\mu\mu} + K^z_{\mu\mu}\right) \tag{A.140}$$

which can be written in a matrix form as:

$$\frac{d}{dz}\begin{bmatrix} A_\nu \\ A_\mu \end{bmatrix} = \begin{bmatrix} -j\left(K^t_{\nu\nu} + K^z_{\nu\nu}\right) & -j\left(K^t_{\nu\mu} + K^z_{\nu\mu}\right)e^{j(\beta_\nu - \beta_\mu)z} \\ -j\left(K^t_{\nu\mu} + K^z_{\nu\mu}\right)e^{-j(\beta_\nu - \beta_\mu)z} & -j\left(K^t_{\mu\mu} + K^z_{\mu\mu}\right) \end{bmatrix}\begin{bmatrix} A_\nu \\ A_\mu \end{bmatrix} \tag{A.141}$$

For optical fibers one can consider pure transverse modes or quasi-transverse modes, this latter is a commonly used approximation in optical fibers under the "weakly guide" assumption, i.e. refractive index contrast between core and cladding is small, normally around $\Delta \approx 0.001$. Based on this approximation we can write:

$$\frac{d}{dz}\begin{bmatrix} A_\nu \\ A_\mu \end{bmatrix} = \begin{bmatrix} -j\left(K^t_{\nu\nu}\right) & -j\left(K^t_{\nu\mu}\right)e^{j(\beta_\nu - \beta_\mu)z} \\ -j\left(K^t_{\nu\mu}\right)e^{-j(\beta_\nu - \beta_\mu)z} & -j\left(K^t_{\mu\mu}\right) \end{bmatrix}\begin{bmatrix} A_\nu \\ A_\mu \end{bmatrix} \tag{A.142}$$

We can also write $\kappa = K^t_{\nu\mu}$ and $2\delta = \beta_\nu - \beta_\mu$, to obtain:

$$A'_\nu = -j\kappa A_\nu - j\kappa A_\mu e^{j2\delta z} \tag{A.143}$$

$$A'_\mu = -j\kappa A_\nu e^{-j2\delta z} - j\kappa A_\mu \tag{A.144}$$

Solving the equation system as before, we can find for co-direction coupling, under boundary conditions given by $R(0) = 1$ and $S(0) = 0$, the expressions given by:

$$R(z) = \cos^2(\eta)e^{-j\beta_s z} + \sin^2(\eta)e^{-j\beta_m z} \tag{A.145}$$

$$S(z) = \cos(\eta)\sin(\eta)\left(e^{-j\beta_s z} - e^{-j\beta_m z}\right) \tag{A.146}$$

Appendix B

Orthogonality between fiber-optic transverse modes

Orthogonality condition must be tested between the set of solutions to Eq.(3.16). In the case of EH and HE families, it is easy to demonstrate orthogonality since their angular dependence leads to a null inner product independently of the radial functions [38]. However, when the orthogonality condition is tested between solutions of the same family, it will depend on Bessel's functions associated to the radial coordinate [38]:

$$\langle e_{li}|e_{lj}\rangle_{r<a} = \pi A_{li}A_{lj}\left[\int_0^a J_\nu(\frac{u_{li}}{a}r)J_\nu(\frac{u_{lj}}{a}r)rdr\right] \tag{B.1a}$$

$$\langle e_{li}|e_{lj}\rangle_{r>a} = \pi A_{li}A_{lj}\left[\int_a^\infty K_\nu(\frac{w_{li}}{a}r)K_\nu(\frac{w_{lj}}{a}r)rdr\right], \tag{B.1b}$$

where A_l, A_m are complex constants, a is the fiber core radius; u_{li},u_{lj},w_{li} and w_{lj} are different roots of the transcendental equation for the EH or HE hybrid mode [38]. A simple inspection over the integral in Eq. (B.1) shows that the inner product between two general modes vanishes only when u_{li} and u_{lj} are roots of the Bessel function $J_\nu(r)$ with $r \in [0,a]$, which is not the case for the step-index fibers, because u_{li} and u_{lj} are determined by the boundary conditions at the core-cladding interface and in general they do not coincide with a root of the Bessel function [5]. This fact shows that hermiticity of the Laplacian operator in step-index fiber waveguides underlies on the boundary conditions, which supports the discussion presented in Ref.[27] about the non-hermiticity of the operator that results from Eq.(3.11a) after multiplying from the left by $\hat{\mathbf{B}}^{-1}$. Since Laplacian operator in step-index fibers is non-hermitian, it is not possible to use the typical procedures for finding their corresponding correction terms to the eigenvalue and eigenstate [9]. Indeed, it is required more sophisticated expressions in the formulation of perturbative terms in order to deal with non-hermitian operators and propose an approached solution by using the whole set of non-orthogonal eigenstates [37]. Another possibility is to find a set of orthonormal functions through a systematic orthogonalization process such as Gramm-Schmidt [9], which allows to span each eigenstate $|e_{\alpha_i}\rangle$ as a linear combination of a new orthonormal set of functions $\{|v_{\alpha_i}\rangle\}$ that could be used as an orthogonal basis. This procedure works fine when degeneracy is present. However, in the case of non-degeneracy, this new-basis elements will not constitute eigenstates of the zero-th order Hamiltonian [37, 35].

A more practical approach is to select some elements from the set of solutions in order to form a convenient orthogonal reduced basis that guarantees the diagonal matrix representation of the Laplacian operator [9, 46]. This assumption can make sense physically in fiber optics since propagating modes constitute a finite basis and under a small external perturbation these modes will interact among each other instead of changing the mathematical nature of the solutions. The procedure for selecting solutions consists in testing the hermiticity of the operator between the functions of the set of solutions. By solving Eq. (3.16), it is found a finite number of functions $\left\{|e_{\alpha_j}\rangle\right\}$ with different eigenvalues, $k^2_{\alpha_j} = \beta^2_j - k^2_0 n^2$. We can write two different eigenvalue equations: $\nabla^2_\perp |e_{\alpha_i}\rangle = k^2_{\alpha_i} |e_{\alpha_i}\rangle, \nabla^2_\perp |e_{\alpha_j}\rangle = k^2_{\alpha_j} |e_{\alpha_j}\rangle$. Assuming that each ket $|e_{\alpha_i}\rangle$ has associated a corresponding bra $\langle e_{\alpha_i}|$, Hermitian condition of the Laplacian operator can be tested through:

$$\langle e_{\alpha_j}|\nabla^2_\perp|e_{\alpha_i}\rangle = \langle e_{\alpha_i}|\nabla^2_\perp|e_{\alpha_j}\rangle^* \tag{B.2a}$$

$$k^2_{\alpha_i} \langle e_{\alpha_j}|e_{\alpha_i}\rangle = (k^2_{\alpha_j})^* \langle e_{\alpha_j}|e_{\alpha_i}\rangle \, . \tag{B.2b}$$

Since the eigenvalues obtained in Eq. (3.16) are real valued, conjugation makes no effects in the test. When there is not degeneracy between propagating modes, $k^2_{\alpha_i} \neq k^2_{\alpha_j}$, Eqs. (B.2) are satisfied only by these spatial distributions that are strictly orthogonal each other. Whether the inner product between two non-degenerate solutions is different from zero, i.e. $\langle e_{\alpha_i}|e_{\alpha_j}\rangle \neq 0$, hermiticity test of the Laplacian operator upon these solutions will fail and they are not suitable functions to be used in the reduced basis. An important case to take into account appears when $\langle e_{\alpha_i}|e_{\alpha_j}\rangle = 0$, Eq. (B.2) is satisfied but eigenvalues could be degenerated, $k^2_{\alpha_i} = k^2_{\alpha_j}$, which implies to use a different formulation of perturbation theory [9]. Although this is not found in step-index fibers because of eigenvalues are different each other, this could happen under the weakly-guiding approximation [38], where degeneracy can be overcome grouping degenerated modes into a new set of propagating modes, known as Linearly Polarized (LP) modes, which can also be analyzed by using the same formulation.

Certainly, the accuracy of the result will depend on the number of modes that are included into the basis as well as the perturbation nature. It is shown in this thesis that perturbations involving spatial inhomogeneities, as well as some anisotropies and non-linearities, can be analyzed through this simplification leading to accurate results in the propagation parameters, as long as the optical fiber propagates few modes only. However, other type of perturbations that imposes strong changes over the number of propagating modes must be addressed by different approaches.

B.0.1 Additional set of numerical experiments

An additional set of numerical experiments were considered for testing the validity of the approximation by using the proposed formulation of the HFHE.

B.0.1.1 Linear Anisotropies

Linear anisotropies can be also included into the HFHE formulation, these can be considered in the second terms of Eq. (3.14b). In this case the perturbation term is an imposed anisotropy that additionally has a spatial variation in the refractive index. The same spatial dependence shown in Fig. 3.1(b) is used for the anisotropic perturbation, but in this case the perturbation term is defined as a diagonal tensor given by:

$$\hat{\mathbf{W}}_{\mathbf{t}} = \mu_0 \varepsilon_0 \omega^2 \begin{bmatrix} \Delta\chi^{(1)}(x,y) & 0 & 0 \\ 0 & -\Delta\chi^{(1)}(x,y) & 0 \\ 0 & 0 & \Delta\chi^{(1)}(x,y) \end{bmatrix} \tag{B.3}$$

This situation differs greatly from the previous case, since we must now include the effect of the perturbation on each component of the electric field in the propagating mode exploiting the full-vector characteristics of the formulation. A negative perturbation is included for the y-component in order to induce a linear uniaxial birefringence in the waveguide. Fig. B.1 presents the comparison between the full-vectorial calculation by the FEM and the HFHE for those propagating modes that are most affected.

As can be seen from Fig. B.1, the results obtained from the two schemes are in good agreement. In this instance a maximum mismatch about 0.6% was found between them. This case is of great importance in propagation analysis, because it allows the calculation of individual effects over the electric-field components of the propagating modes under a external perturbation. A significant difference between

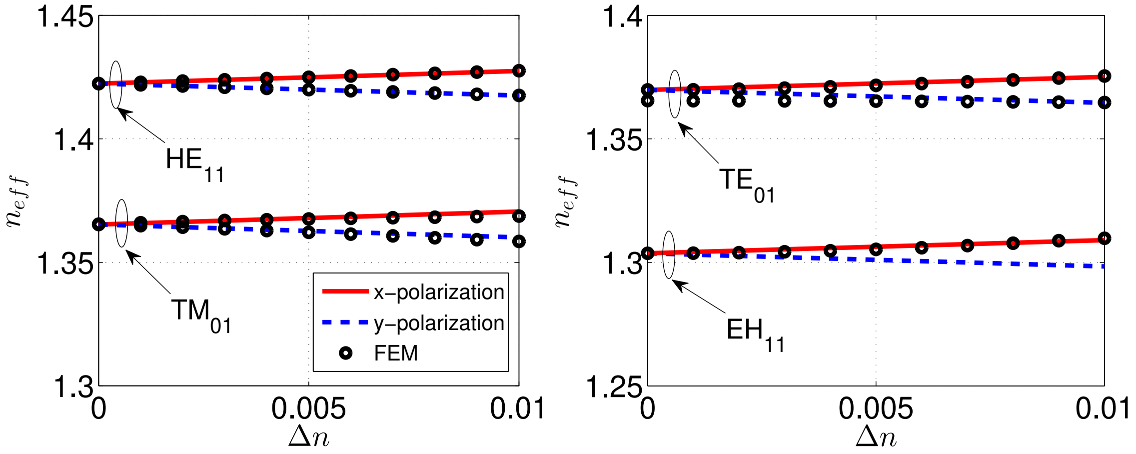

Figure B.1: Effective refractive index of the optical fiber with uniaxial birefringence having the same spatial dependence of Fig.3.1(b) versus Δn obtained by the HFHE formulation (lines) and calculated by the vector FEM (dots). Solid lines correspond to E_x component and dashed lines to E_y component.

both prediction occurs when calculating effective refractive index for the EH_{11} mode. As can be observed in Fig. B.1, the FEM method does not report birefringence for this mode and the predicted effective refractive index remains on the calculated values for the x-component in the HFHE method. This discrepancy could be related with the corresponding mode-profile for the hybrid EH_{11} mode and the spatial distribution of the imposed inhomogeneity. FEM solves the vectorial eigenvalue problem independently of the coordinate axis orientation and unperturbed mode distributions, whereas HFHE method starts from an analytical solution expressed in well-defined coordinate axes and calculates the effects of the perturbation upon the unperturbed mode distributions leading to correction terms for each electric field component as shown in Fig. B.1.

B.0.1.2 Kerr Nonlinearity

In silica optical fibers second order susceptibility term $\hat{\chi}^{(2)}$ is null due to the material symmetry [8]. However, $\hat{\chi}^{(3)}$ can cause several nonlinear effects, such as: four-waves mixing phenomena (FWM), third harmonic generation (THG), self-phase modulation (SPM), and cross-phase modulation (XPM). In practice, FWM and THG effects require phase-matching conditions that are typically of great difficulty to achieve in optical fibers [3], therefore Kerr effect is typically included through the refractive-index dependence on the electric field intensity, which is related with the SPM. This refractive index change is given by [3]:

$$\Delta n\left(\omega,|\mathbf{E}|\right)=\frac{3}{8n}\Re\big(\chi^{(3)}_{xxxx}\big)\,|\mathbf{E}|^2=\bar{n}_2\,|\mathbf{E}|^2\,, \tag{B.4}$$

where $\Re\Big(\chi^{(3)}_{xxxx}\Big)$ is the real part of the third-order susceptibility under the assumption of a constant state of polarization and $\bar{n}_2$ is known as the nonlinear index coefficient. In optical fiber analyses, it is very common to report the nonlinear Kerr parameter or simply the nonlinear refractive index, n_2, which is calculated by $n_2=2\bar{n}_2/\varepsilon_0 nc$ [3]. To calculate the induced change in susceptibility due to the Kerr-type nonlinearity, it is known that $\Delta\chi=2n\Delta n$, thus:

$$\Delta\chi=\frac{3}{4}\Re\big(\chi^{(3)}_{xxxx}\big)\,|\mathbf{E}|^2\,. \tag{B.5}$$

It has been shown in literature that scalar approach is not always accurate enough to correctly determine the effective refractive index associated with the nonlinear effect [42]. Therefore, a vectorial description of the Kerr-nonlinearity must be considered for an accurate description of its associated nonlinear effects. By means of a similar procedure, used in section B.0.1.1, a full vectorial relation can be included in the calculation of the effective nonlinear refractive index through a perturbation term given by

$$\hat{\mathbf{W}}_{\mathbf{t}}=\mu_0\varepsilon_0\omega^2\boldsymbol{\Delta}\chi(x,y), \tag{B.6}$$

where $\boldsymbol{\Delta}\chi(x,y)$ is a diagonal tensor that will affect each of the electric field components based on the material symmetry properties. For silica fibers the full vectorial effect of the polarization vector can be arranged through a second-rank diagonal tensor by following equations [49, 48]:

$$\Delta\chi(x,y)_{x,y}=\frac{3}{4}\Re\big(\chi^{(3)}_{xxxx}\big)\left(|E_x|^2+|E_y|^2+\frac{1}{3}|E_z|^2\right) \tag{B.7a}$$

$$\Delta\chi(x,y)_{z}=\frac{3}{4}\Re\big(\chi^{(3)}_{xxxx}\big)\left(\frac{1}{3}\left(|E_x|^2+|E_y|^2\right)+|E_z|^2\right). \tag{B.7b}$$

These full-vectorial perturbation terms can be directly included into the third term in the formulation of Eq.(3.14b) and using similar procedure as in section B.0.1.1, both effective propagation constant and mode distortion correction can be calculated through Eq.(3.17b) when SPM nonlinearity is induced due to the electric field intensity.

In order to test the validity of the proposed approach, the effective refractive index by using the HFHE method is calculated for a nonlinear waveguide with the same parameters reported in Ref. [49], where an iterative method was used for finding the effective propagation constant based on the input power. Optical fiber parameters are defined as follows: radius $a = 0.5\mu m$, wavelength $\lambda = 1.55\mu m$, linear refractive indexes $n_{co} = 1.45$, $n_{cl} = n_{air} = 1.00$, and the nonlinear Kerr coefficient is given by $n_2 = 3.2 \times 10^{-20}[m^2/W]$.

Figure B.2 shows the calculation of the effective refractive-index for a single-mode fiber as a function of the optical power. The results are compared to those obtained with the iterative solution reported in [49]. Effective refractive index is presented for the E_x field component of the fundamental mode HE_{11}. As can be seen from Fig. B.2, a very good agreement is found for a wide input-power range. In addition, the maximum absolute error is about 0.5% at the highest optical excitation power.

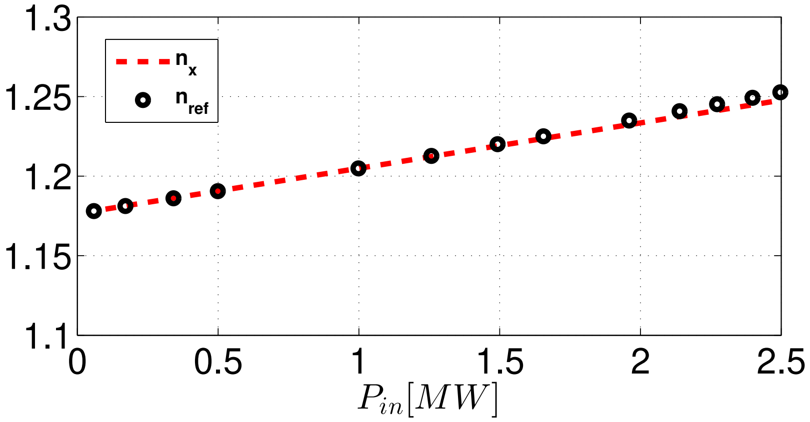

Figure B.2: Effective refractive index n_{eff} for a silica rod as a function of the input optical power. The dashed line is the n_{eff} given by the HFHE formulation, whereas the dots represent the results calculated by a full-vectorial iterative approach (FVI) [49].

This result shows the validity of the proposed method for dealing with vectorial perturbation terms in single-mode fibers. It is worth noting that for single-mode fibers, hermiticity analysis of Eq. (B.2) is not required because there is only one propagating mode. Birefringence analysis are typically performed under the assumption of two orthogonal polarized-modes, but in that particular case the analysis is more suitable to be performed through the formulation in Ref. [45].

B.0.1.3 Nonlinear Parameter Calculation

Nonlinear parameter γ is defined in the analysis of optical pulse propagation when solving the nonlinear propagation equation [43]; particularly for fiber-optics γ is related mainly with the SPM effect. It is worth noting that Refs. [1, 49, 14] have proposed different expressions for extending the calculation of γ in order to take into account all full-vectorial Kerr-type perturbation. Indeed, different definitions of γ are still under discussion and research [31]. Typical definition of the nonlinear parameter in single-mode fiber relates the propagation constant change due to the nonlinear effects and the optical power that carries the transverse electromagnetic field [3]. However, when multimode fibers are under analysis mode interactions due to nonlinearities must be considered [1]. These propositions have been derived based on the power-orthogonality relation discussed in Eq.(3.12) and, though they can include full-vectorial properties of the waveguide such as anisotropies and losses, these definitions remain on the perturbation expansion associated to power independence, and as it was discussed in section 3.2.1.1, external perturbations in multi-mode fibers can cause also spatial-mode distortions when perturbative terms enable the interaction between propagating modes as stated in Eq.(3.17). A simple extension of the definition for γ in Ref.[3] can be achieved based on the HFHE method, in which the distortions on spatial distribution can be included into the calculation of the optical power carried by the perturbed mode, and consequently in the nonlinear parameter evaluation. With the aim to take into account these possible mode distortion for each j-th propagating mode, nonlinear parameter γ_j can be written by:

$$\gamma_j = \frac{2\Delta\beta}{\iint \Re\{\tilde{\mathbf{S}}\} \cdot \hat{i}_z dA} \tag{B.8a}$$

$$\gamma_j = \frac{\langle e_{\alpha j}|\hat{\mathbf{W}}_\mathbf{t}|e_{\alpha j}\rangle}{c\varepsilon_0 \beta_j A_{mj} \langle \tilde{e}_{\alpha j}|n(x,y)|\tilde{e}_{\alpha j}\rangle}, \tag{B.8b}$$

where $\tilde{\mathbf{S}} = \tilde{\mathbf{E}} \times \tilde{\mathbf{H}}^*$ is the complex Poynting's vector for the perturbed propagating mode, with $\tilde{\mathbf{E}}$ and $\tilde{\mathbf{H}}$ the perturbed fields calculated from Eq.(3.17). Magnetic field components can be determined directly from the perturbed electric field by using the Maxwell's equations [38]. For single-mode fibers, and considering that the usual nonlinearities are only in the core region, Poynting's vector $\tilde{\mathbf{S}}$ can be simplified under the assumption of dominant electric field components as: $\tilde{\mathbf{S}}_\mathbf{z} = |\tilde{E}_x|^2/\eta$, being η the intrinsic impedance $\eta = 1/(nc\varepsilon_0)$. This simplification allows to write the optical power for the resultant field in terms of perturbed kets, leading to the expression in Eq.(B.8b). This latter is similar to that proposed in Ref. [1] and presents the same advantages in the analysis of the nonlinearity separated into parts, namely, contributions of linear and nonlinear regions. Besides, Eq.(B.8b) allows associating the inter-mode interaction effects through the inclusion of perturbed kets in the denominator. From

Eq.(B.8b), it is also possible to reproduce the expression proposed in Ref. [3] for the nonlinear parameter. This can be achieved under the following considerations: 1) No modal interactions are considered and only the x-component of the electric field is propagating, i.e. $|\tilde{e}_{xj}\rangle \approx |e_{xj}\rangle$; 2) Kerr-effect is induced due to x-polarized field, thus the perturbation operator can be written as $\hat{\mathbf{W}}_{\mathbf{t}} = (\omega^2/c^2)2n(x,y)\bar{n}_2(x,y)|E_x(x,y)|^2$; 3) nonlinear effects occur only in the core region; 4) the propagation constant for single-mode fiber can be approached by $\beta \approx n\omega/c$.
Under these assumptions Eqs.(B.8) for the nonlinear parameter calculation leads to:

$$\gamma = \frac{\omega}{c}\frac{2\bar{n}_2}{\varepsilon_0 n}\frac{\iint |E_x(x,y)|^4 dxdy}{\left(\iint |E_x(x,y)|^2 dxdy\right)^2} \tag{B.9a}$$

$$\gamma = \frac{\omega n_2}{cA_{\text{eff}}} \tag{B.9b}$$

$$A_{\text{eff}} = \frac{\left(\iint |E_x(x,y)|^2 dxdy\right)^2}{\iint |E_x(x,y)|^4 dxdy}, \tag{B.9c}$$

where A_{eff} is the standard definition of the effective area [3].

In order to show the accuracy of the derived expression in Eq.(B.8) for calculating nonlinear parameter when full-vectorial Kerr-nonlinearity is considered, a set of step-index rod configurations with a high index contrast were considered. Rod configurations were the same as those analyzed in Ref. [1] by using the expression for γ in Ref.[14]. Figure B.3 displays the comparison between γ obtained with Eq. (B.8) and from those reported in Ref. [1]. As it can be seen in Fig. B.3, the calculation through Eq.(B.8) allows to reproduce the nonlinear parameter with relatively good accuracy. Maximum differences were found when higher refractive contrasts were considered, which could be due to the overestimation of the optical power transported in the core region of the rods with high refractive contrasts, which affects the calculation of the intensity-dependent perturbation. Experimental tests reported in Ref. [2] show that effectively high nonlinearities are expected when full-vectorial Kerr effect description is included.

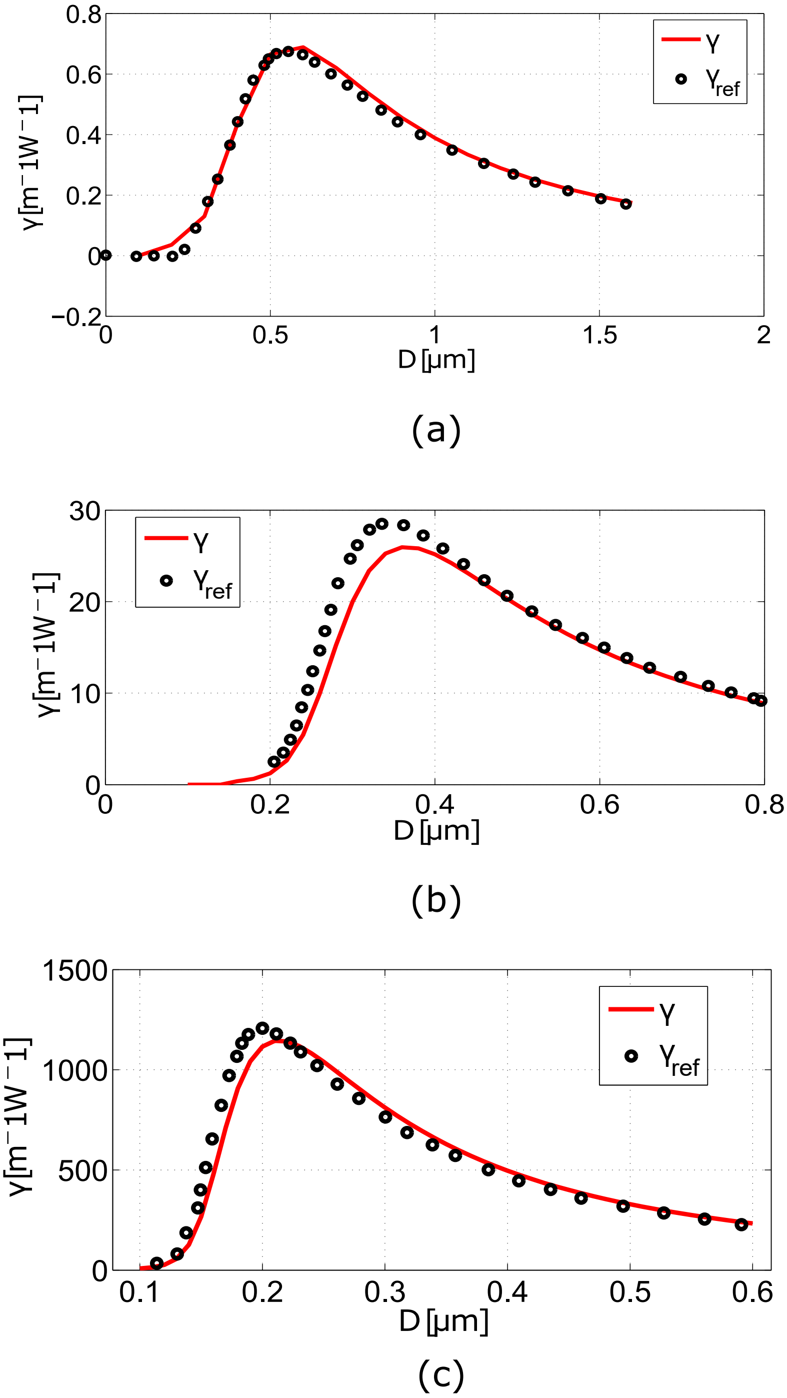

(a)

(b)

(c)

Figure B.3: Nonlinear parameter γ at $\lambda = 800nm$ as a function of the core diameter obtained by the HFHE formulation (continuous line) and results given in Ref.[1, 14] (dots). (a) Silica Rod: $n_c = 1.45$, $n_{cl} = 1.0$, $n_2 = 2.6 \times 10^{-20} m^2/W$ (b) Bismuth Rod: $n_c = 2.05$, $n_{cl} = 1.0$, $n_2 = 3.2 \times 10^{-19} m^2/W$ (c) Silicon Rod: $n_c = 3.45$,$n_{cl} = 1.45$, $n_2 = 4.5 \times 10^{-18} m^2/W$

Appendix C

Coupling coefficients in a Fiber Bragg Grating

As it is mentioned in the **chapter 3** a Fiber Bragg Gratings (FBGs) is modeled assuming a perturbation of the effective refractive index given by [13]:

$$\delta n_{\text{eff}}(z) = \overline{\delta n}_{\text{eff}}(z)\left[1 + v\cos\left(\frac{2\pi}{\Lambda}z + \phi(z)\right)\right] \tag{C.1}$$

which can be also related with the refractive index of the core assuming that power is almost confined to the core region and the wave "sees" only one refractive index. Based on this argument $\delta n_{\text{eff}}(z) = \delta n_{co}(z)$. Additionally, we can make the Taylor series expansion for the permittivity in terms of the refractive index, to write $\Delta\varepsilon_t \approxeq 2n_{co}\delta n_{co}$. Then, considering a z-dependence of this perturbation we can have:

$$\Delta\varepsilon_t(z) = 2n\overline{\delta n}_{co}(z)\left[1 + v\cos\left(\frac{2\pi}{\Lambda}z + \phi(z)\right)\right] \tag{C.2}$$

we can plug this into the coupling coefficient to obtain:

$$K^t_{\nu\mu}(z) = \omega 2n_{co}\overline{\delta n}_{co}(z)\left[1 + v\cos\left(\frac{2\pi}{\Lambda}z + \phi(z)\right)\right]\iint \hat{e}^*_{t\mu}(x,y)\hat{e}_{\nu t}(x,y)dA \tag{C.3}$$

Since the perturbation does not depend on the transversal direction, this integral equation relates the coupling between transversal modes. We can obtain for the integral $\iint \hat{e}^*_{t\mu}(x,y)\hat{e}_{\nu t}(x,y)dA$. Then, we can define two new coefficients to simplify the writing by:

$$\sigma_{\nu\mu}(z) = \omega n_{co}\overline{\delta n}_{co}(z)\iint \hat{e}^*_{t\mu}(x,y)\hat{e}_{\nu t}(x,y)dA \tag{C.4}$$

$$\kappa_{\nu\mu}(z) = \frac{v}{2}\sigma_{\nu\mu}(z) \tag{C.5}$$

then we can write:

$$K^t_{\nu\mu}(z) = \sigma_{\nu\mu}(z) + 2\kappa_{\nu\mu}(z)\cos\left(\frac{2\pi}{\Lambda}z + \phi(z)\right) \tag{C.6}$$

this last expression can be re-written by:

$$K^t_{\nu\mu}(z) = \sigma_{\nu\mu}(z) + \kappa_{\nu\mu}(z)\left[e^{j\left(\frac{2\pi}{\Lambda}z+\phi(z)\right)} + e^{-j\left(\frac{2\pi}{\Lambda}z+\phi(z)\right)}\right] \tag{C.7}$$

this exponential form for the z-dependence is much more convenient for the coupled-mode equations in Eq.A.131. We can plug this equations to have:

$$K_{11} = \sigma_{\nu\mu}(z) + \kappa_{\nu\mu}(z)\left[e^{j\left(\frac{2\pi}{\Lambda}z+\phi(z)\right)} + e^{-j\left(\frac{2\pi}{\Lambda}z+\phi(z)\right)}\right] \tag{C.8}$$

$$K_{12} = \sigma_{\nu\mu}(z)e^{j(2\beta_o)z} + \kappa_{\nu\mu}(z)\left[e^{j2\left((\beta_o+\frac{\pi}{\Lambda})z+\frac{\phi(z)}{2}\right)} + e^{j2\left((\beta_o-\frac{\pi}{\Lambda})z-\frac{\phi(z)}{2}\right)}\right] \tag{C.9}$$

Here we apply the "synchronous approximation", which consist in neglecting all rapid variations with z. Those rapid variations are: variations associated with the refractive index change, i.e. $e^{\pm j\left(\frac{2\pi}{\Lambda}z+\phi(z)\right)}$, because our interest is to determine the slow variation along the total perturbation length. Based on the same argument, we will neglect terms that have: $e^{j(2\beta_o)z}$ and $e^{j2\left((\beta_o-\frac{\pi}{\Lambda})z-\frac{\phi(z)}{2}\right)}$. We will keep slow variation terms only. Therefore, let's define a parameter $\delta = \beta_o - \frac{\pi}{\Lambda}$

$$K_{11} = \sigma_{\nu\mu}(z) \tag{C.10}$$

$$K_{12} = \kappa_{\nu\mu}(z)e^{j2\left(\delta z-\frac{\phi(z)}{2}\right)} \tag{C.11}$$

$$\frac{d}{dz}\begin{bmatrix} A_\nu \\ B_\mu \end{bmatrix} = \begin{bmatrix} -j\sigma_{\nu\mu}(z) & -j\kappa_{\nu\mu}(z)e^{j2\left(\delta z-\frac{\phi(z)}{2}\right)} \\ j\kappa_{\nu\mu}(z)e^{-j2\left(\delta z-\frac{\phi(z)}{2}\right)} & j\sigma_{\nu\mu}(z) \end{bmatrix}\begin{bmatrix} A_\nu \\ B_\mu \end{bmatrix} \tag{C.12}$$

We to obtain:

$$A'_\nu = -j\sigma_{\nu\mu}(z)A_\nu - j\kappa_{\nu\mu}(z)e^{j2\left(\delta z-\frac{\phi(z)}{2}\right)}B_\mu \tag{C.13}$$

$$B'_\mu = j\kappa_{\nu\mu}(z)e^{-j2\left(\delta z-\frac{\phi(z)}{2}\right)}A_\nu + j\sigma_{\nu\mu}(z)B_\mu \tag{C.14}$$

following the same procedure as for the general case. Let's begin defining $\mathbb{A}_\nu = A_\nu e^{j\sigma_{\nu\mu}(z)z}$, we obtain:

$$A'_\nu + j\sigma_{\nu\mu}(z)A_\nu = -j\kappa_{\nu\mu}(z)e^{j2\left(\delta z-\frac{\phi(z)}{2}\right)}B_\mu \tag{C.15}$$

$$\mathbb{A}'_\nu = -j\kappa_{\nu\mu}(z)e^{j2\left(\delta z+\frac{\sigma_{\nu\mu}(z)}{2}z-\frac{\phi(z)}{2}\right)}B_\mu \tag{C.16}$$

doing the same procedure for the back-propagating mode. Defining $\mathbb{B}_\mu = B_\mu e^{-j\sigma_{\nu\mu}(z)z}$, we have:

$$B'_\mu - j\sigma_{\nu\mu}(z)B_\mu = j\kappa_{\nu\mu}(z)e^{-j2\left(\delta z - \frac{\phi(z)}{2}\right)}A_\nu \tag{C.17}$$

$$\mathbb{B}'_\mu = j\kappa_{\nu\mu}(z)e^{-j2\left(\delta z + \frac{\sigma_{\nu\mu}(z)}{2}z - \frac{\phi(z)}{2}\right)}A_\nu \tag{C.18}$$

After this procedure, we can make use again of the new definitions,$A_\nu = \mathbb{A}_\nu e^{-j\sigma_{\nu\mu}(z)z}$ and $B_\mu = \mathbb{B}_\mu e^{j\sigma_{\nu\mu}(z)z}$. Then, replacing into their corresponding equations we can write:

$$\mathbb{A}'_\nu = -j\kappa_{\nu\mu}(z)e^{j2\left(\delta z + \sigma_{\nu\mu}(z)z - \frac{\phi(z)}{2}\right)}\mathbb{B}_\mu \tag{C.19}$$

$$\mathbb{B}'_\mu = j\kappa_{\nu\mu}(z)e^{-j2\left(\delta z + \sigma_{\nu\mu}(z)z - \frac{\phi(z)}{2}\right)}\mathbb{A}_\nu \tag{C.20}$$

defining $\Delta = \delta + \sigma_{\nu\mu}(z)$, we can write:

$$\mathbb{A}'_\nu = -j\kappa_{\nu\mu}(z)\mathbb{B}_\mu e^{j2(\Delta z - \frac{\phi(z)}{2})} \tag{C.21}$$

$$\mathbb{B}'_\mu = j\kappa_{\nu\mu}(z)\mathbb{A}_\nu e^{-j2(\Delta z - \frac{\phi(z)}{2})} \tag{C.22}$$

An additional substitution by:

$$\mathbb{A}_\nu = Re^{j(\Delta z - \frac{\phi(z)}{2})} \tag{C.23}$$

$$\mathbb{B}_\mu = Se^{-j(\Delta z - \frac{\phi(z)}{2})} \tag{C.24}$$

replacing we have:

$$R'e^{j(\Delta z - \frac{\phi(z)}{2})} + j\left(\Delta z - \frac{1}{2}\frac{d\phi(z)}{dz}\right)Re^{j(\Delta z - \frac{\phi(z)}{2})} = -j\kappa_{\nu\mu}(z)Se^{j(\Delta z - \frac{\phi(z)}{2})} \tag{C.25}$$

$$S'e^{-j(\Delta z - \frac{\phi(z)}{2})} - j\left(\Delta z - \frac{1}{2}\frac{d\phi(z)}{dz}\right)Se^{-j(\Delta z - \frac{\phi(z)}{2})} = j\kappa_{\nu\mu}(z)Re^{-j(\Delta z - \frac{\phi(z)}{2})} \tag{C.26}$$

which simplifies to:

$$R' + j\left(\Delta z - \frac{1}{2}\frac{d\phi(z)}{dz}\right)R = -j\kappa_{\nu\mu}(z)S \tag{C.27}$$

$$S' - j\left(\Delta z - \frac{1}{2}\frac{d\phi(z)}{dz}\right)S = j\kappa_{\nu\mu}(z)R \tag{C.28}$$

where we can write:

$$R' + j\left(\delta + \sigma_{\nu\mu}(z) - \frac{1}{2}\frac{d\phi(z)}{dz}\right)R = -j\kappa_{\nu\mu}(z)S \tag{C.29}$$

$$S' - j\left(\delta + \sigma_{\nu\mu}(z) - \frac{1}{2}\frac{d\phi(z)}{dz}\right)S = j\kappa_{\nu\mu}(z)R \tag{C.30}$$

this result is the same presented in [13], where a new parameter $\hat{\sigma}$ and κ given by:

$$\hat{\sigma} = \delta + \sigma_{\nu\mu}(z) - \frac{1}{2}\frac{d\phi(z)}{dz} \tag{C.31}$$

$$\kappa = \kappa_{\nu\mu}(z) \tag{C.32}$$

based on this definitions we can re-write the equations as:

$$R' + j\hat{\sigma}R = -j\kappa S \tag{C.33}$$

$$S' - j\hat{\sigma}S = j\kappa R \tag{C.34}$$

we showed the solutions for this set of equations before. With initial boundary conditions: R(0)=1 and S(L)=0), solution is given by:

$$S(0) = \frac{-j\kappa}{\sqrt{\kappa^2 - \hat{\sigma}^2}\coth(L\sqrt{\kappa^2 - \hat{\sigma}^2}) + j\hat{\sigma}} \tag{C.35}$$

$$R(L) = \frac{\sqrt{\kappa^2 - \hat{\sigma}^2}}{\sqrt{\kappa^2 - \hat{\sigma}^2}\cosh(L\sqrt{\kappa^2 - \hat{\sigma}^2}) + j\hat{\sigma}\sinh(L\sqrt{\kappa^2 - \hat{\sigma}^2})} \tag{C.36}$$

Based on this expression we can find the magnitude of the reflected spectrum by $S(0)$:

$$\rho(\kappa, \hat{\sigma}, L) = \frac{-j\kappa}{\sqrt{\kappa^2 - \hat{\sigma}^2}\coth(L\sqrt{\kappa^2 - \hat{\sigma}^2}) + j\hat{\sigma}} \tag{C.37}$$

Figures C.1 presents the reflection spectrum for different parameters κL [13][52].

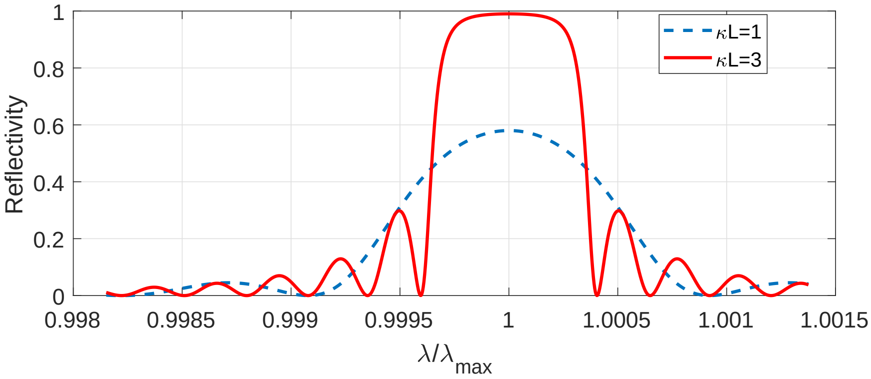

Figure C.1: Reflection spectrum calculated for different parameters κL. (It can be compared to Fig12.19 in [52])

Appendix D

Geometry Effect in the Magnetization Vector $\vec{M}$

In as much magnetic field from magnetization vector will produce a net magnetic field different from zero, it is expected that induced magnetizations modify the magnetic field intensity in both inside and outside the magnetic material. Consider a magnetic dipole moment per unit volume and its corresponding vector potential:

$$d\vec{m} = \vec{M} dv' \tag{D.1}$$

$$d\vec{A}_{\text{dmg}}(\vec{r}) = \frac{\mu_0}{4\pi} \frac{d\vec{m}(\vec{r'}) \times \left(\vec{r} - \vec{r'}\right)}{|\vec{r} - \vec{r'}|^3}, \tag{D.2}$$

where the subindex (dmg) has been included to make explicit the dependence to the magnetization distribution that leads to demagnetization field. Total vector potential at some determined point can be calculated by integrating over the volume of the magnetized material to obtain:

$$\vec{A}_{\text{dmg}}(\vec{r}) = \frac{\mu_0}{4\pi} \iiint \frac{\vec{M}(\vec{r'}) \times \left(\vec{r} - \vec{r'}\right)}{|\vec{r} - \vec{r'}|^3} dv' \tag{D.3}$$

having in mind the vectorial identity:

$$\nabla' \frac{1}{|\vec{r} - \vec{r'}|} = \frac{\vec{r} - \vec{r'}}{|\vec{r} - \vec{r'}|^3}, \tag{D.4}$$

vector potential can be written as:

$$\vec{A}_{\text{dmg}}(\vec{r}) = \frac{\mu_0}{4\pi} \iiint \vec{M}(\vec{r'}) \times \nabla' \frac{1}{|\vec{r} - \vec{r'}|} dv'. \tag{D.5}$$

By using vector identity in $\nabla \times (G\vec{a}) = G\,(\nabla \times \vec{a}) + (\nabla G) \times \vec{a}$, and with the aim to apply divergence theorem upon the resultant integral $\iiint_{v'} \nabla' \times \left(\vec{M}(\vec{r}')/|(\vec{r} - \vec{r}')| \right) dv'$, one can write the argument of the integral as a divergence by using the vectorial identity: $\nabla \cdot (\vec{a} \times \vec{n}) = \vec{n} \cdot (\nabla \times \vec{a}) - \vec{a} \cdot (\nabla \times \vec{n})$ with $\vec{n}$ the normal vector to the surface, this allows to write the vector potential as:

$$\vec{A}_{\mathrm{dmg}}(\vec{r}) = \frac{\mu_0}{4\pi} \iiint_{v'} \frac{\nabla' \times \vec{M}(\vec{r'})}{|\vec{r} - \vec{r'}|} dv' + \frac{\mu_0}{4\pi} \oiint_{s} \frac{\vec{M}(\vec{r'}) \times \vec{n}'}{|\vec{r} - \vec{r'}|} ds', \tag{D.6}$$

which means that vector potential due to magnetized bodies is produced by volumetric: $\vec{J}_m$ and surface $\vec{K}_m$ "magnetic currents", allowing to replace the magnetized body for those equivalent sources during the magnetic field calculation. Finally, magnetic flux density associated to the demagnetization field can be found from Eq.(D.6) by taking the curl upon $\vec{A}_{\mathrm{dmg}}(\vec{r})$ as: $\vec{B}_{\mathrm{dmg}}(\vec{r}) = \nabla \times \vec{A}_{\mathrm{dmg}}(\vec{r})$ which leads to the Biot-Savart law.

$$\vec{B}_{\mathrm{dmg}J_m}(\vec{r}) = \frac{\mu_0}{4\pi} \iiint_{v'} \frac{\vec{J}_m(\vec{r'}) \times (\vec{r} - \vec{r'})}{|\vec{r} - \vec{r'}|^3} dv' \tag{D.7}$$

$$\vec{B}_{\mathrm{dmg}K_m}(\vec{r}) = \frac{\mu_0}{4\pi} \iint_{s} \frac{\vec{K}_m(\vec{r'}) \times (\vec{r} - \vec{r'})}{|\vec{r} - \vec{r'}|^3} ds'. \tag{D.8}$$

These fields $\vec{B}_{\mathrm{dmg}J_m}(\vec{r})$ and $\vec{B}_{\mathrm{dmg}K_m}(\vec{r})$ are produced by magnetization $\vec{M}$ of the body and will interact with any external field. As it is stated in Eqs.(D.7) and (D.8), magnetic induction due to the demagnetization field can be found in general over any known magnetic volume. There is an alternative way to find the demagnetization field from a **scalar potential** to simplify, in some of the cases, the complexity of the resultant integrals. Following examples show the accuracy of the analytical approximation for different geometries.

D.0.0.1 Magnetized Sphere

A very well known problem in literature is the constant magnetized sphere. This particular scenario considers a sphere of radius R located at the origin of coordinates with constant magnetization $\vec{M}(\vec{r'}) = M_0\hat{i}_z$. The idea is to calculate the magnetic field magnitude and the magnetic flux density generated by the constant magnetization. In order to address this problem, we take advantage of the magnetic scalar potential that should satisfy:

$$\nabla^2\phi_m(\vec{r}) = \nabla \cdot \vec{M}(\vec{r}), \tag{D.9}$$

As discussed before, the magnetic scalar potential for a constant magnetization will be generated by the equivalent surface charges at the sphere shell, $\sigma_m(\vec{r'}) = \vec{a}_n \cdot \vec{M}(\vec{r'})$. Therefore, magnetic scalar potential can be calculated by integrating the corresponding expression:

$$\phi_m(\vec{r}) = \frac{1}{4\pi} \iint \frac{\vec{a}_n \cdot \vec{M}(\vec{r'})}{|\vec{r} - \vec{r'}|} ds', \tag{D.10}$$

Or by using the solution of the Laplace equation $\nabla^2 \phi_m(\vec{r}) = 0$ and apply the boundary conditions that apply for the magnetic scalar potential at the body surface. In spherical coordinates the Laplace equation for axial symmetrical geometries can be solved by the Legendre polynomials $P_l(\cos\theta)$. Since inside the sphere and outside the sphere the Laplace equation should be satisfied, we can write for the magnetic scalar potential:

$$\phi_m(\vec{r}) = \begin{cases} \sum_{l=0}^{\infty} A_l r^l P_l(\cos\theta) & r \leq R \\ \sum_{l=0}^{\infty} \frac{C_l}{r^{l+1}} P_l(\cos\theta) & R \leq r \end{cases}, \tag{D.11}$$

then, we impose the boundary conditions: first one corresponds to the continuity of the magnetic scalar potential at $r = R$:

$$\sum_{l=0}^{\infty} A_l R^l P_l(\cos\theta) = \sum_{l=0}^{\infty} \frac{C_l}{R^{l+1}} P_l(\cos\theta), \tag{D.12}$$

leading to:

$$C_l = A_l R^{2l+1}, \tag{D.13}$$

Simplifying for the magnetic potential as:

$$\phi_m(\vec{r}) = \begin{cases} \sum_{l=0}^{\infty} A_l r^l P_l(\cos\theta) & r \leq R \\ \sum_{l=0}^{\infty} \frac{A_l R^{2l+1}}{r^{l+1}} P_l(\cos\theta) & R \leq r \end{cases}, \tag{D.14}$$

At this point, A_l coefficients remain unknown. In order to find them we should make use of the relationship of the scalar potential derivative and the surface charge (in the exact analogous manner as dealing with the electric field generated by surface charges), then we have:

$$\left[\frac{\partial \phi_m(\vec{r})}{\partial r}\right]\Bigg|_R = -\sigma_m(\vec{r'}), \tag{D.15}$$

Since the derivate is respect to r, and their dependence is polynomial, its analytical expression can be found easily by:

$$\sum_{l=0}^{\infty} - \left[(l+1)\frac{R^{2l+1}}{r^{l+2}} + lr^{l-1}\right]\Bigg|_R A_l P_l(\cos\theta) = -\vec{a}_n \cdot \vec{M}(\vec{r'}) \tag{D.16}$$

$$\sum_{l=0}^{\infty} \left[(l+1)\frac{R^{2l+1}}{R^{l+2}} + lR^{l-1}\right] A_l P_l(\cos\theta) = M_0 \cos\theta, \tag{D.17}$$

In order to satisfy the equation, $l = 1$ is the only polynomial order that should be taken into account, i.e. $P_1(\cos\theta) = \cos\theta$. Therefore, we can write:

$$A_1 = \frac{M_0}{3}, \tag{D.18}$$

Finally, magnetic scalar potential due to constant magnetization is given by:

$$\phi_m(r,\theta) = \begin{cases} \dfrac{M_0}{3} r\cos\theta & r \leq R \\ \\ \dfrac{M_0}{3}\dfrac{R^3}{r^2}\cos\theta & R \leq r, \end{cases} \tag{D.19}$$

Once the potential is known everywhere in the space, we can calculate the demagnetization magnetic field, $\vec{H}_{\text{dmg}}$, by taking the corresponding derivative $\vec{H}_{\text{dmg}} = -\nabla\phi_m(r,\theta)$. Thus, potential inside the sphere $\phi_m(r,\theta) = (M_0/3)r\cos\theta$, can be written in terms of the cartesian z-coordinate $z = r\cos\theta$, leading to an internal field, in the region $r \leq R$, caused by the magnetization given by:

$$\vec{H}_{\text{dmg}}(z) = -\frac{M_0}{3}\hat{i}_z, \tag{D.20}$$

which indicates a constant demagnetization magnetic field inside the sphere. Corresponding magnetic flux density associated to the demagnetization field inside the sphere can be calculated from the constitutive equation by $\vec{B}_{\text{dmg}} = \mu_0\left(\vec{H}_{\text{dmg}} + \vec{M}\right)$. In this case, associated magnetic flux density due to this demagnetization field can be written by:

$$\vec{B}_{\text{dmg}} = \mu_0\left(-\frac{M_0}{3} + M_0\right) \tag{D.21}$$

$$\vec{B}_{\text{dmg}} = \mu_0\frac{2M_0}{3}\hat{i}_z, \tag{D.22}$$

At this point we are able to describe the magnetic field inside and outside a sphere as an uniform magnetization. Therefore, once M_0 is given, we can calculate their corresponding magnetic fields (flux density and magnetic field intensity) everywhere in the space. Initial magnetization, M_0, was assumed as known and it was not related to any external field. However, in practice, this magnetization is induced by an external magnetic field (H_{ext}) and depends on the magnetic susceptibility, and it is not known a priori. External field in vacuum will have a magnetic induction field given by $B_{\text{ext}} = \mu_0 H_{\text{ext}}$. In other materials we should look into the B-H curve properties of the corresponding material. An important case is when the magnetization M_0 follows a linear relation with the magnetic field intensity by $M_0 = \chi_m H_{\text{total}}$, being χ_m the magnetic susceptibility. This relationship will cause that total fields will be written by:

$$B_{\text{total}} = B_{\text{ext}} + \mu_0 \frac{2\chi_m H_{\text{total}}}{3} \tag{D.23}$$

$$H_{\text{total}} = H_{\text{ext}} - \frac{\chi_m H_{\text{total}}}{3}, \tag{D.24}$$

Therefore, the total magnetic field intensity will be given by:

$$H_{\text{total}} = \frac{H_{\text{ext}}}{1 + \frac{\chi_m}{3}}, \tag{D.25}$$

Then, magnitude of the magnetic field intensity allows to calculate the magnitude of the magnetization by:

$$M_0 = \chi_m H_{\text{total}} \tag{D.26}$$

$$M_0 = \frac{3\chi_m}{3 + \chi_m} H_{\text{ext}}. \tag{D.27}$$

In order to show the distribution of the magnetic flux density, as well as to validate the implementation of the Finite Element Method (FEM) for computing the magnetic flux density inside a sphere, characterized by $\chi_m = \mu_r - 1$ and placed in a uniform external magnetic field B_{ext}. Figure D.1 shows the distribution of the magnetic flux density and the azimuthal component of the magnetic vector potential.

D.0.0.2 Magnetized Cylinder

Second case is a finite length cylinder exposed to an external uniform magnetic field, $\vec{H}_{\text{ext}} = H_0 \hat{i}_z$. Consider a cylinder of radius b and height L which is orientated along the z-axis as shown in Fig. D.2.

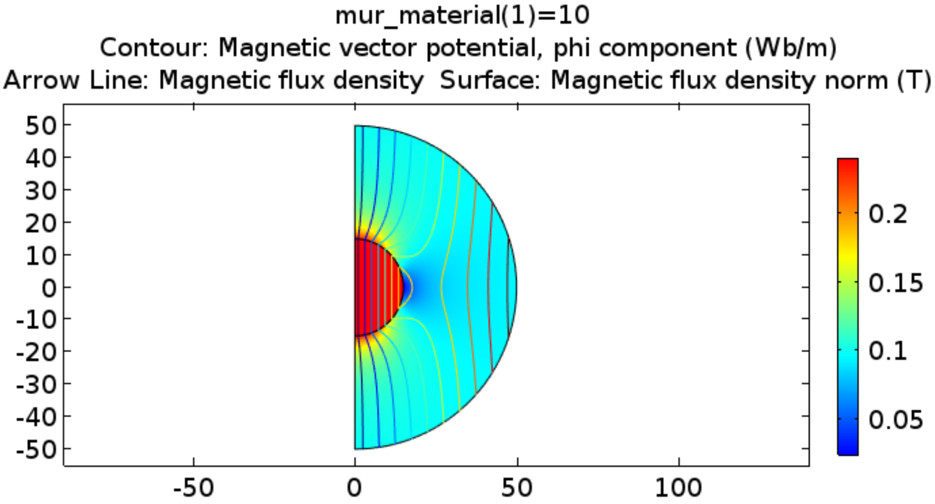

Figure D.1: Magnetic flux density of an uniform Magnetized sphere, radius $R = 15$[mm]. $\mu_r = 10$, $B_{\text{ext}} = 0.1T\hat{i}_z$

An initial approximation is to assume that the external magnetic field will induce inside the cylinder a constant magnetization pointing in the same direction as the external field, i.e. $\vec{M} = M_o\hat{i}_z$. Therefore, demagnetization field due to this magnetization can be calculated by the two methods presented before: vector magnetic potential and scalar magnetic potential.

Demagnetization field through vector magnetic potential In this particular case where magnetization is constant, no volumetric magnetic currents exist because derivatives are null, i.e. $\vec{J}_m = \nabla' \times \vec{M} = 0$. However current magnetic surface on the side wall of the cylinder is not zero, i.e. $\vec{K}_m = \vec{M} \times \hat{i}_r = M_o\hat{i}_z \times \hat{i}_r = M_o\hat{i}_\varphi$. Unitary vector can be written by:

$$\hat{u}_r = \frac{\vec{r} - \vec{r'}}{|\vec{r} - \vec{r'}|} = \cos\alpha(-\hat{i}_r) + \sin\alpha(\hat{i}_z), \tag{D.28}$$

where

$$\cos\alpha = \frac{b}{\sqrt{(z - z')^2 + b^2}} \tag{D.29}$$

$$\sin\alpha = \frac{z - z'}{\sqrt{(z - z')^2 + b^2}}. \tag{D.30}$$

Contribution of the equivalent magnetic surface currents will be given by:

$$\vec{K}_m \times \hat{u}_r = \frac{M_0 b}{\sqrt{(z - z')^2 + b^2}}\hat{i}_z + \frac{M_0(z - z')}{\sqrt{(z - z')^2 + b^2}}\hat{i}_\varphi, \tag{D.31}$$

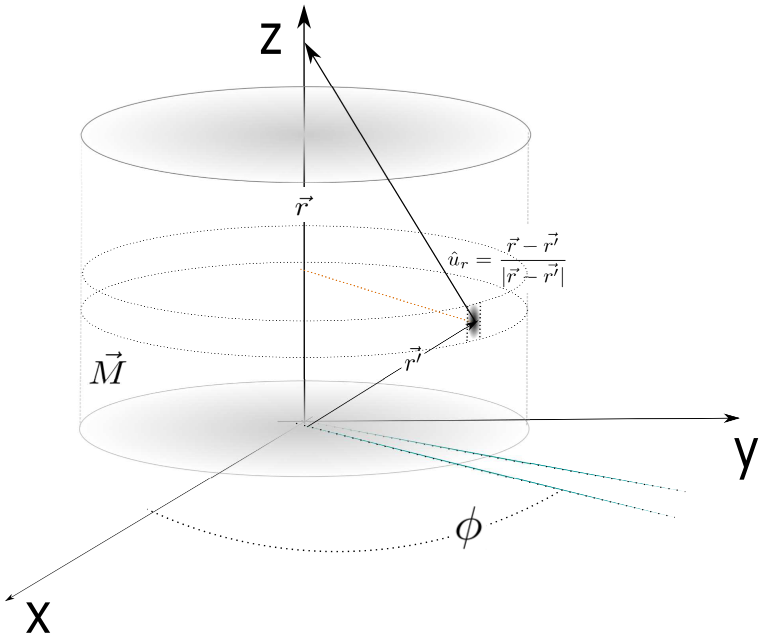

Figure D.2: Uniform Magnetized Cylinder

Owing to the symmetry properties, contributions from radial components $\hat{i}_r$ are null when integration over $\int d\varphi$. Finally, magnetic induction along the z-axis is given by:

$$B_{\mathrm{dmg}}(z) = \frac{\mu_0}{4\pi} \int_0^{2\pi} \int_0^L \frac{M_0 b^2 dz' d\varphi}{\left[(z - z')^2 + b^2\right]^{3/2}} \hat{i}_z, \tag{D.32}$$

which after integration leads to:

$$B_{\mathrm{dmg}}(z) = \frac{-\mu_0 M_0}{2} \left[\frac{z - L}{\sqrt{b^2 + (z - L)^2}} - \frac{z}{\sqrt{b^2 + z^2}} \right] \hat{i}_z \tag{D.33}$$

Once the magnetic induction field due to the magnetization is found, one can calculate for the magnetic field intensity associated to this particular distribution of magnetization by using the constitutive equation:

$$H_{\mathrm{dmg}}(z) = \frac{B_{\mathrm{dmg}}(z)}{\mu_0} - M_0 \tag{D.34}$$

Replacing from the result obtained for the magnetic flux density, we have:

$$H_{\mathrm{dmg}}(z) = \frac{-M_0}{2} \left[\frac{z - L}{\sqrt{b^2 + (z - L)^2}} - \frac{z}{\sqrt{b^2 + z^2}} \right] - M_0 \tag{D.35}$$

which can be written by:

$$H_{\mathrm{dmg}}(z) = -M_0 \left[1 + \frac{1}{2} \frac{z - L}{\sqrt{b^2 + (z - L)^2}} - \frac{1}{2} \frac{z}{\sqrt{b^2 + z^2}} \right]. \tag{D.36}$$

Once the magnetic field produced by the magnetization of the magnetic body is found. Total internal magnetic field can be calculated by summing up the demagnetization field and the external field.

$$H_{\text{int}}(z) = H_{\text{ext}}(z) + H_{\text{mg}}(z). \tag{D.37}$$

In the linear case, magnetization can be written in terms of the internal field by $M_0 = \chi_m H_{\text{int}}(z)$. Therefore, we can write:

$$H_{\text{int}}(z) = H_{\text{ext}}(z) - M_0 \left[1 + \frac{1}{2}\frac{z-L}{\sqrt{b^2+(z-L)^2}} - \frac{1}{2}\frac{z}{\sqrt{b^2+z^2}} \right] \tag{D.38}$$

$$H_{\text{int}}(z) = H_{\text{ext}}(z) - \chi_m H_{\text{int}}(z) \left[1 + \frac{1}{2}\frac{z-L}{\sqrt{b^2+(z-L)^2}} - \frac{1}{2}\frac{z}{\sqrt{b^2+z^2}} \right] \tag{D.39}$$

Rearranging the expression, we can solve for the internal field by:

$$H_{\text{int}}(z) = \frac{H_{\text{ext}}(z)}{1 + \chi_m \left[1 + \frac{1}{2}\frac{z-L}{\sqrt{b^2+(z-L)^2}} - \frac{1}{2}\frac{z}{\sqrt{b^2+z^2}} \right]}. \tag{D.40}$$

Figure D.3 shows the internal magnetic field intensity along the z-axis of a cylinder with magnetic susceptibility $\chi_m = 9$ under several external magnetic fields. The cylinder has a radius of $r = 5$[mm] and height $L = 18.5$[mm]. Numerical solution by using the Finite Element Method (FEM) has been compared with the analytical approach to ensure the consistency of the approximation.

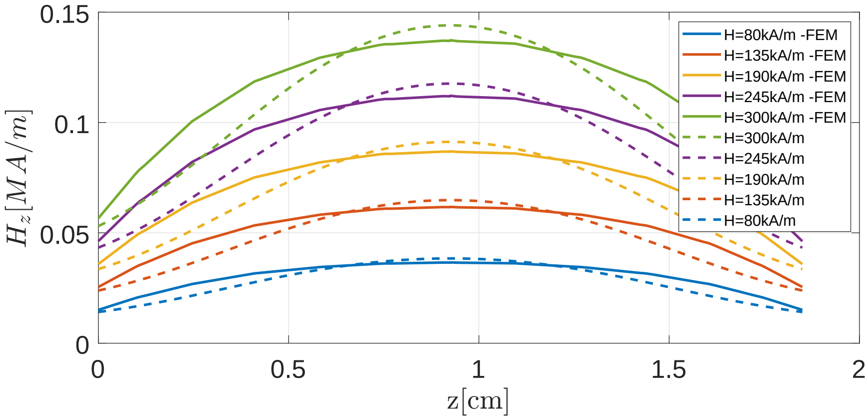

Figure D.3: Internal magnetic field intensity along the axis. Comparison of the approach of an uniformly magnetized cylinder (in dashed lines) and the Finite Element Method (FEM) solution (in solid lines)

As it can be seen from Fig. D.3, cylindric geometry presents a quasi uniform magnitude of the internal magnetic field along the axis of the cylinder. In contrast, the approximation based on a constant magnetization over-estimates the field and predicts a steeped distribution of the field along the axis. Once the internal magnetic field is calculated, magnetization along the axis can be calculated by $M(z) = \chi_m H_{\text{int}}(z)$.

Demagnetization field through scalar magnetic potential A second strategy for computing the demagnetization field is through the scalar magnetic potential formulation. In this particular case we assume constant magnetization, leading to: $\nabla' \cdot \vec{M}(\vec{r'}) = 0$. Therefore, second term of the integral in Eq.(4.4) contributes to the scalar potential $\phi_m(\vec{r})$. Considering the case of the uniformly magnetized cylinder in Fig. (D.2), we have:

$$\phi_m(\vec{r}) = \frac{1}{4\pi} \iint \frac{\vec{a}_n \cdot \vec{M}(\vec{r'})}{|\vec{r} - \vec{r'}|} ds', \tag{D.41}$$

where the surface differential of area is given by $ds' = r'dr'd\varphi$ in both top and bottom faces. We will have $\sigma_{\text{top}} = M_0$ and $\sigma_{\text{top}} = -M_0$ because of the vectorial dot product at each surface. Considering the calculation of the scalar potential along the axis $\vec{r} = z\hat{i}_z$, we can write for the scalar magnetic potential:

$$\phi_m(z) = \frac{M_0}{4\pi} \iint \frac{r'}{\sqrt{r'^2 + (z-L)^2}} dr'd\varphi - \frac{M_0}{4\pi} \iint \frac{r'}{\sqrt{r'^2 + z^2}} dr'd\varphi, \tag{D.42}$$

In this case the integration can be performed simply. Therefore, integrating respect to the angular variable, it reduces to:

$$\phi_m(z) = \frac{M_0}{2} \int_0^b \frac{r'}{\sqrt{r'^2 + (z-L)^2}} dr' - \frac{M_0}{2} \int_0^b \frac{r'}{\sqrt{r'^2 + z^2}} dr', \tag{D.43}$$

which leads to:

$$\phi_m(z) = \frac{M_0}{2} \left(\left[\sqrt{r'^2 + (z-L)^2} \right] \Big|_0^b - \left[\sqrt{r'^2 + z^2} \right] \Big|_0^b \right), \tag{D.44}$$

evaluating at the respective limits:

$$\phi_m(z) = \frac{M_0}{2} \left(\sqrt{b^2 + (z-L)^2} - |(z-L)| - \sqrt{b^2 + z^2} + |z| \right), \tag{D.45}$$

For the case inside the cylinder, $0 < z < L$, absolute values can be changed for their respective sings to obtain:

$$\phi_m(z) = \frac{M_0}{2}\left(\sqrt{b^2 + (z-L)^2} - \sqrt{b^2 + z^2} + 2z - L\right), \tag{D.46}$$

Finally, magnetic field can be found by taking the gradient of the scalar potential, in this case respect to z:

$$H_{\text{dmg}} = -\frac{d\phi_m(z)}{dz}\hat{i}_z \tag{D.47}$$

$$H_{\text{dmg}} = -M_0\left(1 + \frac{1}{2}\frac{(z-L)}{\sqrt{b^2 + (z-L)^2}} - \frac{1}{2}\frac{z}{\sqrt{b^2 + z^2}}\right)\hat{i}_z, \tag{D.48}$$

that is an identical result of that found by using the magnetic flux density approach in Eq.(D.36).

Appendix E

Cantilever beam analysis for a piezoelectric bimorph

The cantilever beam analysis constitutes a very important case of study in this section because it describes the physics of one the most common actuators in piezoelectric applications, i.e. the piezoelectric bimorph.

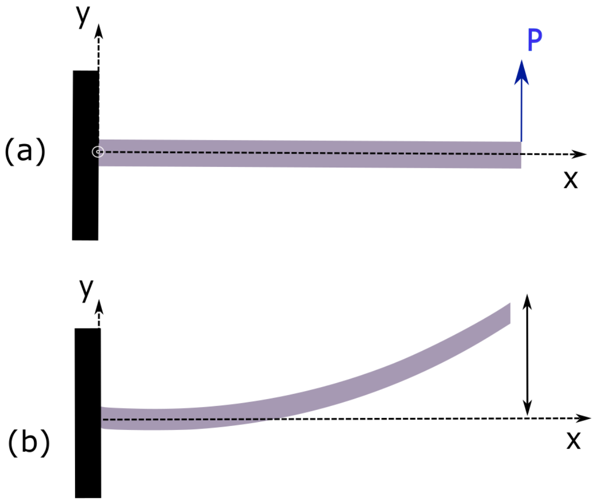

Figure E.1: Cantilever beam deformed by an external force

As it will be discussed in coming sections, the cantilever set-up is frequently used in bimorph and unimorph actuators to generate bending actions from external electric or magnetic fields through the piezoelectric and magnetostrictive effect. Cantilever actuator is shown in Fig. (E.1). If an external force is applied in the XY plane, it will lead to a bending of the cantilever beam axis. $\nu(x)$ is called the deflection curve and describes the bending magnitude of the beam axis. Fig. E.2 shows the variables associated to the cantilever beam deflection. The curvature $\kappa = 1/\rho$ can be expressed assuming an external point O' that ables to write the deflection length by $\rho d\theta = ds$. Besides, the angle θ can be written by:

$$\tan\theta = \frac{d\nu}{ds} \tag{E.1}$$

$$\kappa = \frac{1}{\rho} = \frac{d\theta}{ds} \tag{E.2}$$

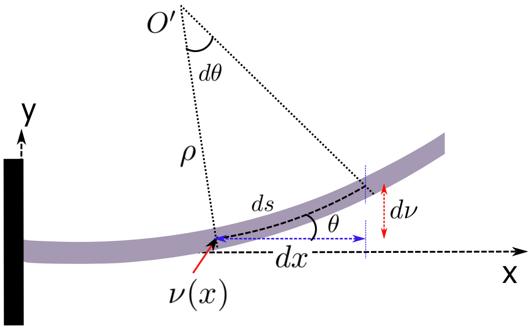

Figure E.2: Definition of the differential variables in terms of the deflection curve and curvature

If the deflection is small, we can consider $ds \approxeq dx$, then $\tan\theta \approxeq \theta$. So, we can simplify the expressions above to write:

$$\theta = \frac{d\nu}{dx} \tag{E.3}$$

$$\kappa = \frac{1}{\rho} = \frac{d\theta}{dx} \tag{E.4}$$

Now, taking the derivative of θ regarding x we can write:

$$\frac{d\theta}{dx} = \frac{d^2\nu}{dx^2} \tag{E.5}$$

from the curvature equation we can write a differential equation for the deflection curve $\nu(x)$ by:

$$\frac{d^2\nu}{dx^2} = \kappa \tag{E.6}$$

Curvature magnitude κ is intimate related to the elastic properties of the material. These properties can be described by using the strain-stress relationships of the material. During the bending process, there will exist a curve somewhere in the body that will remain with the same length as in the undeformed condition. That curve is called the neutral axis. However, curves above the neutral axis will shrink and curves below it will stretch. This condition allows us to write an expression for the strain distribution inside the body. Let's consider a line above the neutral axis at a distance y as it is shown in Fig. E.3. We can think that after deformation the distance between both curves will remain the same, even if there positions respect the coordinate system can change.

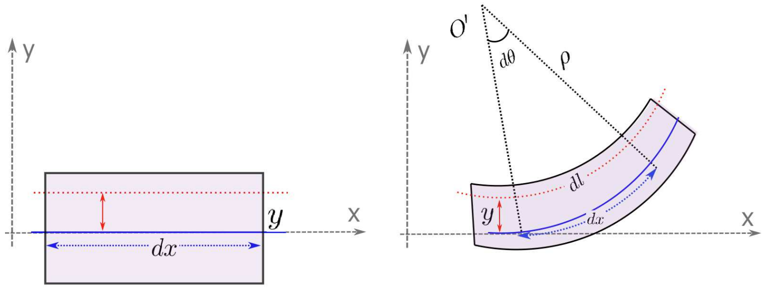

Figure E.3: Determination off the strain distribution based on the definition of the neutral axis

Based on Fig. E.3, it can be seen that total deformation of the curve located at y distance from the neutral axis can be written by:

$$dl = (\rho - y)d\theta \tag{E.7}$$

from the curvature equation, we have:

$$d\theta = \frac{dx}{\rho} \tag{E.8}$$

Based on this result, we can write:

$$dl = (\rho - y)\frac{dx}{\rho} \tag{E.9}$$

$$dl = dx - y\frac{dx}{\rho} \tag{E.10}$$

$$\frac{dl - dx}{dx} = -\frac{y}{\rho} \tag{E.11}$$

Therefore, the definition of the strain can be used to write:

$$\xi_x = \frac{dl - dx}{dx} = -\frac{y}{\rho} = -\kappa y. \tag{E.12}$$

It should be noticed that the measurement of the strain is done over the x-axis. However, there is also a deformation over the cross-section area caused by the Poisson's ratio. This latter deformation is being neglected in the analysis, since it has been shown to be good enough to describe experimental behavior of cantilever bimorphs [15]. For linear elastic materials, we can write a linear relationship between the stress and the strain given by the Young's module $\mathcal{Y}$. Thus, we can write:

$$\sigma_x = \mathcal{Y}\xi_x \tag{E.13}$$

$$\sigma_x = -\mathcal{Y}\kappa y. \tag{E.14}$$

So far we have defined y as the distance between the neutral axis (up to now, it is still unknown) and any other curve above or below it. Therefore, we should determine the exact location of the neutral axis such that we can solve for any point in the solid respect to the global coordinate system. In order to accomplish this, we should write the equations of force equilibrium and momentum equilibrium in the solid.

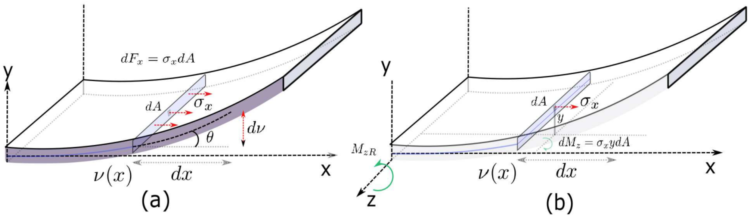

Figure E.4: Calculation of forces and momentum along the cantilever bimorph

First, we calculate forces and bending moments respect to the z-axis due to the corresponding stress component σ_x. Figure E.4 represents these forces (Fig. E.4 (a)) and moments (Fig. E.4 (b)) acting over the cross section of the cantilever bimorph. Based on this situation, we can obtain the differential expressions for the force and the bending moment respectively:

$$dF_x = \sigma_x dA \tag{E.15}$$

$$dM_z = -\sigma_x y dA \tag{E.16}$$

At the origin there should be the total bending moment reaction, M_{zR}, to equilibrate the moments. Pure bending, means that all the bending is caused by the angular moment acting at each cross section along the beam. Therefore, forces along x should cancel out, $\iint dF_x dA = 0$, and total torque created by the stress component should be equal to the moment reaction at the origin. Based on this argument, we can write:

$$\iint \sigma_x dA = 0 \tag{E.17}$$

$$M_{zR} - \int dM_z = 0 \tag{E.18}$$

given $\sigma_x = -\mathcal{Y}\kappa y$, these results imply:

$$-\mathcal{Y}\kappa \iint y dA = 0 \tag{E.19}$$

$$M_{zR} = \mathcal{Y}\kappa \iint y^2 dA \tag{E.20}$$

First result implies that y should be always located at the centroid, since summation of the stresses over the cross section leads always to zero. Second result, allows to calculate the moment reaction at the origin based on the geometrical characteristics of the cross section, $I_c = \iint y^2 dA$ (where I_c is the moment of inertia of the cross section), the Young's module $\mathcal{Y}$, and the curvature of the bending k. It is worth noting that in the strict sense, curvature of bending could change along x, thus it should be written as $k(x)$, implying that bending moment is also a function of x, i.e. $M_{zR}(x)$. Using these results, we can go back to the differential equation found for the the deflection curve $\nu(x)$, to write:

$$\frac{d^2\nu}{dx^2} = \frac{M_{zR}(x)}{\mathcal{Y}I_c} \tag{E.21}$$

Unknown variable is the bending moment $M_{zR}(x)$ for each position along x and it is the resultant torque at some distance x from the origin (clamping point) of all the stresses distributed over the cross section of the cantilever bimorph. Therefore, its magnitude will depend on the longitudinal distribution of the forces forces that act upon the beam.

Appendix F

Closed solution for a frustum cone

Subsection 7.1.1 showed that side slope $n = 1$ presents the more stepped profile in the internal magnetic field. This result suggests that magnetostrictive effect due to this internal field distribution could be transferred to a nonchirped coaxially embedded FBG, such as depending on the external field magnitude a chirping can be induced in the FBG. Since the axial field profile for the cone is of great interest in the analysis, in the following we show a closed solution for a frustum cone magnetic body by using the magnetic scalar potential approach. Previous attempts for designing current sensors based on magnetostrictive composites have been done in the Laboratory of Smart Composites at the University of Wisconsin-Milwaukee. Particularly, in the case of a frustum cone a previous work used the geometry among others to induce frequency chirping in the embedded FBGs[30]. Although, some optical power dependence were achieved in the initial results for different external magnetic fields, spectral broadening was not fully obtained and several aspects of the frustum cone modeling were not considered. Consider a frustum cone to evaluate the magnetic flux density along the z-axis as shown in Fig. F.1. As it was discussed in **chapter 4**, a first approximation for finding the internal magnetic field distribution due to geometric effects is to consider a constant magnetization directed along the external magnetic field. In this case, external field points along the z-direction, $\vec{H}_{\text{ext}} = H_0\hat{i}_z$ which implies an assumption for magnetization given by $\vec{M} = M_0\hat{i}_z$. This constant magnetization inside the magnetic body implies: $\nabla' \cdot \vec{M}(\vec{r'}) = 0$. Therefore, only surface magnetic sources contribute to the scalar potential as discussed in **chapter 4**. For this particular geometry, radius at any height z' in Fig. (F.1) is given by:

$$r(z') = b_0 - \tan\theta z'. \tag{F.1}$$

where $\tan\theta = (b_0 - a_0)/L$. Surface charge densities at the top and bottom of the cone will be same magnitude but opposite signs, $\sigma_{mt} = \pm M_0$, depending on the surface

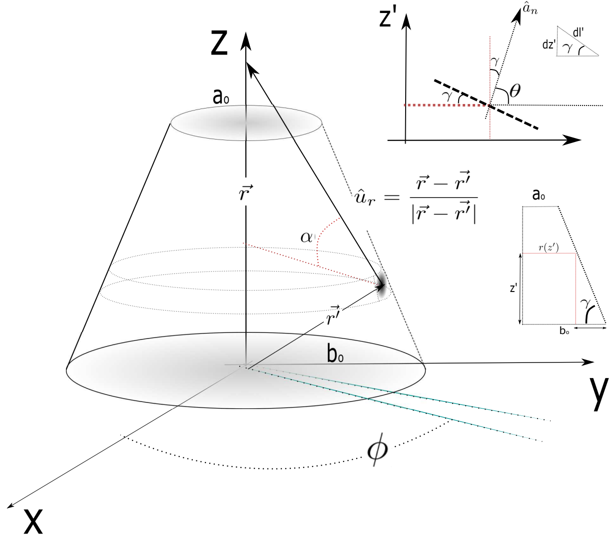

Figure F.1: Uniformly magnetized frustum cone

normal vector. Integration regarding angle φ can be performed easily leading to:

$$\phi_{a_0}(z) = \frac{M_0}{2}\int_0^{a_0} \frac{r'}{\sqrt{r'^2 + (z-L)^2}} dr' \tag{F.2}$$

$$\phi_{b_0}(z) = -\frac{M_0}{2}\int_0^{b_0} \frac{r'}{\sqrt{r'^2 + z^2}} dr', \tag{F.3}$$

performing the integrals we obtain:

$$\phi_{a_0}(z) = \frac{M_0}{2}\left(\left[\sqrt{r'^2 + (z-L)^2}\right]\Bigg|_0^{a_0}\right) \tag{F.4}$$

$$\phi_{b_0}(z) = \frac{-M_0}{2}\left(\left[\sqrt{r'^2 + z^2}\right]\Bigg|_0^{b_0}\right) \tag{F.5}$$

evaluating the expressions at the corresponding limits, we have:

$$\phi_{a_0}(z) = \frac{M_0}{2}\left(\sqrt{a_0^2 + (z-L)^2} - |(z-L)|\right) \tag{F.6}$$

$$\phi_{b_0}(z) = \frac{-M_0}{2}\left(\sqrt{b_0^2 + z^2} - |z|\right) \tag{F.7}$$

If $0 < z < L$ we can write:

$$\phi_{a_0}(z) = \frac{M_0}{2}\left(\sqrt{a_0^2 + (z-L)^2} + (z-L)\right) \tag{F.8}$$

$$\phi_{b_0}(z) = \frac{-M_0}{2}\left(\sqrt{b_0^2 + z^2} - z\right) \tag{F.9}$$

the sum of the scalar magnetic potential due to the top and bottom surface can be written by:

$$\phi_{a_0}(z) + \phi_{b_0}(z) = \frac{M_0}{2}\left(2z + \sqrt{a_0^2 + (z-L)^2} - \sqrt{b_0^2 + z^2} - L\right). \tag{F.10}$$

Now we should account for lateral surface charge density, $\sigma = \vec{a}_n \cdot \vec{M}$. Outward normal vector to the surface can be found from the normal vector to the surface $\vec{a}_n = \cos\theta\hat{i}_r + \sin\theta\hat{i}_z$, which leads to a surface magnetic charge density determined by $\sigma = M_0 \sin\theta$. From geometry $\sin\theta$ is given by:

$$\sin\theta = \frac{b_0 - a_0}{\sqrt{(b_0 - a_0)^2 + L^2}} \tag{F.11}$$

which finally allows us to write for the equivalent surface charge density:

$$\sigma = M_0 \frac{b_0 - a_0}{\sqrt{(b_0 - a_0)^2 + L^2}}. \tag{F.12}$$

Surface differential will be given by $ds' = r(z')\, d\varphi\, dl'$, which written in terms of z' leads to the expression:

$$ds' = r(z')\, d\varphi \frac{dz'}{\cos\theta}. \tag{F.13}$$

In order to test the validity of the surface differential, surface area of the frustum cone can be calculated by:

$$A_s = \int_0^{2\pi}\int_0^L ds' = \int_0^{2\pi}\int_0^L r(z')\, d\varphi \frac{dz'}{\cos\theta} \tag{F.14}$$

$$A_s = 2\pi \frac{\sin\theta}{\cos^2\theta}\int_0^L \left[\cot\theta b_0 - z'\right] dz' \tag{F.15}$$

$$A_s = 2\pi \frac{\tan\theta}{\cos\theta}\left[\cot\theta b_0 z' - \frac{z'^2}{2}\right]\Bigg|_0^L \tag{F.16}$$

$$A_s = 2\pi \frac{1}{\cos\theta}\left[b_0 L - \frac{\tan\theta L^2}{2}\right], \tag{F.17}$$

From geometry of the frustum cone shown in Fig. F.1, we can write for $\tan\theta$ and $\cos\theta$:

$$\tan\theta = \frac{b_0 - a_0}{L} \tag{F.18}$$

$$\cos\theta = \frac{L}{\sqrt{L^2 + (b_0 - a_0)^2}} \tag{F.19}$$

Thus, total surface area can be written by:

$$A_s = \frac{2\pi b_0 L}{\cos\theta} - \left[\frac{\pi\left(b_0 - a_0\right)L}{\cos\theta}\right] \tag{F.20}$$

$$A_s = \frac{\sqrt{L^2 + (b_0 - a_0)^2}}{L}\left[2\pi b_0 L - \pi\left(b_0 - a_0\right)L\right], \tag{F.21}$$

which leads to the known formula for finding the surface area of a frustum cone:

$$A_s = \pi(b_0 + a_0)\left(\sqrt{L^2 + (b_0 - a_0)^2}\right). \tag{F.22}$$

Once surface differential ds' has been tested to reproduce the total surface area correctly after integration, scalar potential along the z-axis associated to the lateral surface charge density can be written by:

$$\phi_s(z) = \frac{M_0 \sin\theta}{4\pi}\frac{1}{\cos\theta}\int_0^{2\pi}\int_0^L \frac{(b_o - \tan\theta z')}{[(z - z')^2 + (b_o - \tan\theta z')^2]^{1/2}}dz'd\varphi \tag{F.23}$$

after simplification we have:

$$\phi_s(z) = \frac{M_0 \tan\theta}{2}\int_0^L \frac{(b_o - \tan\theta z')}{[(z - z')^2 + (b_o - \tan\theta z')^2]^{1/2}}dz', \tag{F.24}$$

Let be $u = b_o - \tan\theta z'$, then $z' = -(u - b_o)/\tan\theta$. Calculating the corresponding derivative regarding u, we have $du = -\tan\theta dz'$. Therefore, limits of the integral become $u_o = b_o$ to $u_L = b_o - \tan\theta L$. Writing the integral in terms of the new variable:

$$\phi_s(z) = \frac{-M_0}{2}\int_{u_o}^{u_L} \frac{u}{[(z + (u - b_o)/\tan\theta)^2 + u^2]^{1/2}}du, \tag{F.25}$$

after some algebra manipulations we can write:

$$\phi_s(z) = \frac{-M_0}{2}\int_{u_o}^{u_L} \frac{u}{[au^2 + bu + c]^{1/2}}du, \tag{F.26}$$

which can be solved analytically to obtain:

$$\phi_s(z) = \frac{-M_0}{2}\left[\frac{1}{a}\sqrt{au^2 + bu + c} - \frac{b}{2a^{3/2}}\ln\left(\frac{2au + b}{\sqrt{a}} + 2\sqrt{au^2 + bu + c}\right)\right]\Bigg|_{u_o}^{u_L}, \tag{F.27}$$

Total scalar potential can be found by summing the respective contributions of the magnetic scalar potential from each surface, which leads to:

$$\begin{aligned}\phi_m(z) = \frac{M_0}{2}&\left(2z + \sqrt{a_0^2 + (z - L)^2} - \sqrt{b_0^2 + z^2} - L\right)\\ \frac{-M_0}{2}&\left[\frac{1}{a}\sqrt{au^2 + bu + c} - \frac{b}{2a^{3/2}}\ln\left(\frac{2au + b}{\sqrt{a}} + 2\sqrt{au^2 + bu + c}\right)\right]\Bigg|_{u_o}^{u_L}\end{aligned} \tag{F.28}$$

where

$$a = 1 + \cot^2\theta \tag{F.29}$$

$$b = \frac{2}{\tan\theta}\left(z - \frac{b_0}{\tan\theta}\right) \tag{F.30}$$

$$c = \left(z - \frac{b_0}{\tan\theta}\right)^2. \tag{F.31}$$

Finally, magnetic field intensity can be calculated taking the derivative respect to z of the scalar potential by:

$$\vec{H}_{\mathrm{dmg}}(z) = -\frac{d\phi_m(z)}{dz}. \tag{F.32}$$

Once the internal field is known, magnetization can be calculated based on the magnetic susceptibility as presented in **chapter 4**. In this case we are assuming $\chi_m = 9$ immersed in an external magnetic field H_{ext}=255[kA/m]. Figure F.2 presents the magnetic field along the axis by using the scalar potential method. As it is shown in the figure, contribution of top and bottom surfaces generates some kind of non symmetric distribution of the axial field. However, lateral surface contribution enhances the asymmetric profile when it is considered. This issue validates the fact that proposed geometry has interesting potential for controlling the steepness of the induced magnetization and consequently the corresponding magnetostriction. FigureF.3 shows the comparison of the calcualtion of internal magnetic field by using the magnetic vector potential method and the scalar potential formulation that allows to write a closed solution for the internal field. As it can be seen from Fig.F.3 there is an equivalence between both methods. Therefore, the use of the analytical approach obtained from the scalar potential formulation can be used in the following analysis for the sake of simplicity in the coming calculations.

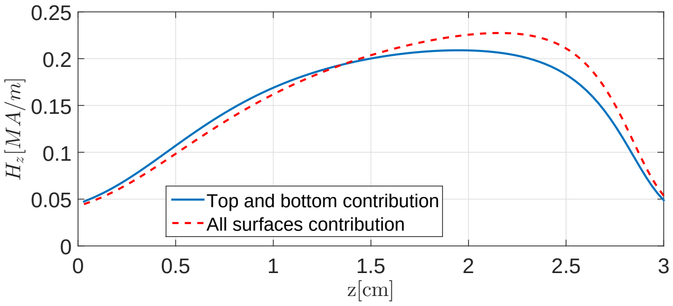

Figure F.2: Contribution to the internal magnetic field from top, bottom and lateral surface in the scalar potential formulation.

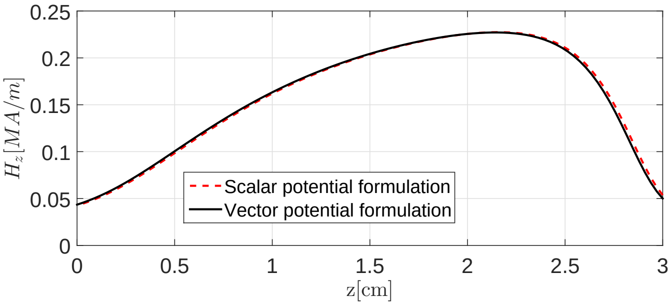

Figure F.3: Internal magnetic field along the frustum cone axis calculated by scalar potential and vector potential formulations.

Results presented above assume only one component of the magnetization that points in the same direction as the external magnetic field. In practice, once a body is exposed to an external field the magnetization distribution inside the body will present full vectorial components that will depend on the geometry and the relative position against the external field direction. Figure F.4 presents the comparison of the calculation of the internal magnetic field along the axis of the cone between COMSOL and the analytical approximation.

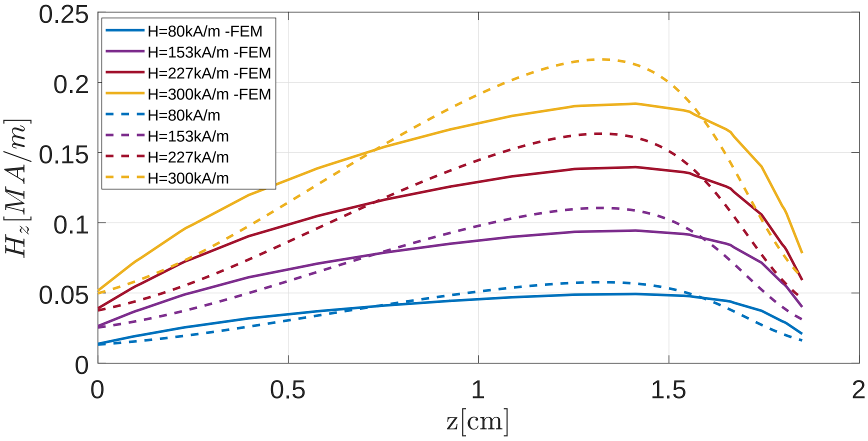

Figure F.4: Magnetic Flux density along z-axis for a uniformly magnetized Cone $\vec{M} = M_0\hat{i}_z$

As it can be seen from Fig.F.4 analytical approximation over estimates the maximum internal magnetic field, this is caused due to the assumption that there are not transverse components of the magnetization. Figure F.5 shows the distribution of the vector magnetic potential A_ϕ inside the material for a frustum cone of bottom and top radius $b_0 = 5$[mm] and $a_0 = 2$[mm] of $L = 3$[cm] in length and relative magnetic permeability of $\mu_r = 10$, immersed into an external magnetic field $\vec{B}_{\text{ext}} = 0.1[T]\hat{i}_z$.

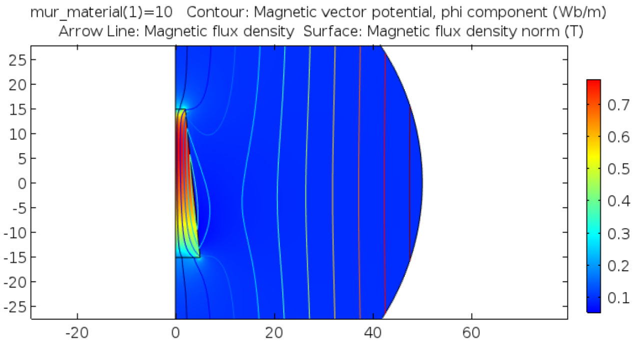

Figure F.5: Magnetic Flux density along z-axis for a uniformly magnetized Cone $\vec{M} = M_0\hat{i}_z$

As it is showed in the numerical simulation, there is an spatial distribution of the internal field that could lead to transverse magnetization components. Based on the solutions for the magnetic field flux density $\vec{B}(r, z)$, magnetization vector inside the material can be found for each component by using the constitutive equation $\vec{B} = \mu_0(\vec{H} + \vec{M})$. Radial and z component for the magnetization vector are plotted in Fig. F.6.

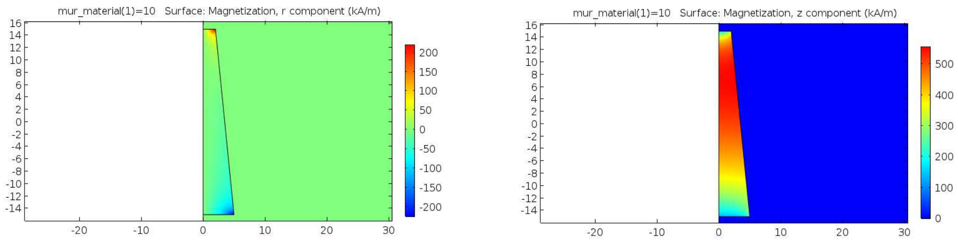

(a) (b)

Figure F.6: Magnetization components. (a) radial component. (b) axial component

As it is shown in Fig.F.6 radial component of the magnetization vector is almost null inside the cone except at the corners, this causes the mismatch of the analytical approach with the numerical FEM results in Fig.F.4 near to the cone ends. However, z-component of the magnetization vector is the dominant component along the middle of the cone, thus central region pattern of the internal magnetic field is well predicted by the analytical approximation.

Bibliography

[1] S. Afshar and T.M. Monro. A full vectorial model for pulse propagation in emerging waveguides with subwavelength structures part i: Kerr nonlinearity. *Opt. Express*, 17:2298–2318, 2009.

[2] V. Afshar, W. Zhang, H. Ebendorff-Heidepriem, and T. Monro. Small core optical waveguides are more nonlinear than expected: experimental confirmation. *Opt. Lett.*, 34:3577–3579, 2009.

[3] G. Agrawal. *Nonlinear Fiber Optics.* Academic Press, 2013.

[4] Abdullah Al Amin, An Li, Simin Chen, Xi Chen, Guanjun Gao, and William Shieh. Dual-lp11 mode 4x4 mimo-ofdm transmission over a two-mode fiber. *Opt. Express*, 19(17):16672–16679, Aug 2011.

[5] G.B. Arfken, H. J. Weber, and F.E. Harris. *Mathematical Methods for Physicists.* Wiley, 1966.

[6] Giorgio Bertotti. *Hysteresis in magnetism: for physicists, materials scientists, and engineers.* Academic press, 1998.

[7] D Bloomberg and V Castelli. Reformulation of nonlinear integral magnetostatic equations for rapid iterative convergence. *IEEE transactions on magnetics*, 21(2):1174–1180, 1985.

[8] R. Boyd. *Nonlinear Optics.* Academic press, 2008.

[9] C. Cohen-Tannoudji, B. Diu, and F. Laloë. *Quantum mechanics.* Quantum Mechanics. Wiley, 1992.

[10] Alcides Oliveira Cremonezi, Elnatan C Ferreira, JAS Dias, et al. A fiber bragg grating rms current transducer based on the magnetostriction effect using a terfenol-d toroidal-shaped modulator. *IEEE Sensors Journal*, 13(2):683–690, 2013.

[11] TA Duenas and GP Carman. Large magnetostrictive response of terfenol-d resin composites. *Journal of Applied Physics*, 87(9):4696–4701, 2000.

[12] TA Duenas, L Hsu, and GP Cakman. Magnetostrictive composite material systems analytical/experimental. *MRS Online Proceedings Library Archive*, 459, 1996.

[13] Turan Erdogan. Fiber grating spectra. *Journal of lightwave technology*, 15(8):1277–1294, 1997.

[14] M. Foster, K. Moll, and A. Gaeta. Optimal waveguide dimensions for nonlinear interactions. *Opt. Express*, 12:2880–2887, 2004.

[15] James M Gere and Barry J Goodno. Mechanics of materials 5th. *Brooks Cole*, 2001.

[16] Richard Hamming. *Numerical methods for scientists and engineers.* Courier Corporation, 2012.

[17] Jiahui Han, Haofeng Hu, Hui Wang, Bowen Zhang, Xiaowei Song, Zhenyang Ding, Xuezhi Zhang, and Tiegen Liu. Temperature-compensated magnetostrictive current sensor based on the configuration of dual fiber bragg gratings. *Journal of Lightwave Technology*, 35(22):4910–4915, 2017.

[18] S Huang, M LeBlanc, MM Ohn, et al. Bragg intragrating structural sensing. *Applied optics*, 34(22):5003–5009, 1995.

[19] John David Jackson. *Classical electrodynamics.* AAPT, 1999.

[20] D Jiles and D Atherton. Ferromagnetic hysteresis. *IEEE Transactions on Magnetics*, 19(5):2183–2185, 1983.

[21] D C Jiles. Theory of the magnetomechanical effect. *Journal of Physics D: Applied Physics*, 28(8):1537, 1995.

[22] David Jiles. *Introduction to magnetism and magnetic materials.* CRC press, 2015.

[23] David C Jiles and JB Thoelke. Theory of ferromagnetic hysteresis: determination of model parameters from experimental hysteresis loops. *IEEE Transactions on magnetics*, 25(5):3928–3930, 1989.

[24] DC Jiles and DL Atherton. Theory of the magnetisation process in ferromagnets and its application to the magnetomechanical effect. *Journal of Physics D: Applied Physics*, 17(6):1265, 1984.

[25] DC Jiles and DL Atherton. Theory of ferromagnetic hysteresis. *Journal of magnetism and magnetic materials*, 61(1-2):48–60, 1986.

[26] L. Jin, Weigang Zhang, Hao Zhang, Bo Liu, Jian Zhao, Qinchang Tu, G. Kai, and Xiaoyi Dong. An embedded fbg sensor for simultaneous measurement of stress and temperature. *IEEE Photonics Technology Letters*, 18(1):154–156, Jan 2006.

[27] S. Johnson, M. Ibanescu, M. Skorobogatiy, O. Weisberg, J. D. Joannopoulos, and Y. Fink. Perturbation theory for maxwell's equations with shifting material boundaries. *Physical Review E*, 65:1143–1149, June 2002.

[28] H. Kogelnik. *Theory of Optical Waveguides*, pages 7–88. Springer Berlin Heidelberg, Berlin, Heidelberg, 1988.

[29] Herwig Kogelnik. Theory of dielectric waveguides. In *Integrated optics*, pages 13–81. Springer, 1975.

[30] S. Lasassmeh. Design and modeling of fiber optical current sensor based on magnetostriction. *Thesis Dissertation*, pages 1–137, 2017.

[31] Guangyuan Li, C Martijn de Sterke, and Stefano Palomba. General analytic expression and numerical approach for the kerr nonlinear coefficient of optical waveguides. *Optics Letters*, 42(7):1329–1332, 2017.

[32] J Maclean and G Wu. *Radiowave propagation over ground.* Springer, 1993.

[33] Isaak D Mayergoyz. *Handbook of giant magnetostrictive materials.* Elsevier, 1999.

[34] R.M. Measures. Smart composite structures with embedded sensors. *Composites Engineering*, 2(5-7):597–618, 1992.

[35] Nimrod Moiseyev. *Non-Hermitian quantum mechanics.* Cambridge University Press, 2011.

[36] Ji Mora, A Diez, JL Cruz, and MV Andres. A magnetostrictive sensor interrogated by fiber gratings for dc-current and temperature discrimination. *IEEE Photonics Technology Letters*, 12(12):1680–1682, 2000.

[37] D.J. Newman. Many-body perturbation theory for non-orthogonal basis states. *Journal of Physics and Chemistry of Solids*, 31(5):1143–1149, 1970.

[38] K. Okamoto. *Fundamentals of Optical Waveguides.* Academic press, 2006.

[39] Joseph E Pasciak. An iterative algorithm for the volume integral method for magnetostatics problems. *Computers & Mathematics with Applications*, 8(4):283–290, 1982.

[40] Clayton R Paul. *Analysis of multiconductor transmission lines.* John Wiley & Sons, 2008.

[41] K Peters, M Studer, J Botsis, A Iocco, H Limberger, and R Salathé. Embedded optical fiber bragg grating sensor in a nonuniform strain field: measurements and simulations. *Experimental Mechanics*, 41(1):19–28, 2001.

[42] F. Poletti and P. Horak. Description of ultrashort pulse propagation in multimode optical fibers. *J. Opt. Soc. Am. B*, 20:1645–1654, March 2008.

[43] A. Saleh and M. C. Teich. *Fundamental of Photonics.* John Wiley & Son, 2007.

[44] M. Skorobogatiy, M. Ibanescu, S. Johnson, O. Weisberg, T. Engeness, M. Soljačić, S. Jacobs, and Y. Fink. Analysis of general geometric scaling perturbations in a transmitting waveguide: fundamental connection between polarization-mode dispersion and group-velocity dispersion. *J. Opt. Soc. Am. B*, 19:2867–2875, March 2002.

[45] M. Skorobogatiy, S. Johnson, S. Jacobs, and Y. Fink. Dielectric profile variations in high-index-contrast waveguides, coupled mode theory, and perturbation expansions. *Phys Rev E Stat Nonlin Soft Matter Phys.*, 67:2867–2875, Apr 2003.

[46] M. Skorobogatiy and J. Yang. *Fundamentals of Photonic Crystal Guiding.* Cambridge University Press, 2009.

[47] A. W. Snyder and J. D. Love. *Optical Waveguides Theory.* Chapman and Hall, 1983.

[48] V.P. Tzolov and M. Fontaine. Nonlinear self-phase-modulation effects: a vectorial first-order perturbation approach. *Optics Letters*, 20(5):1143–1149, March 1994.

[49] V.P. Tzolov, M. Fontaine, N. Godbout, and S. Lacroix. Nonlinear modal parameters of optical fibers: a full-vectorial approach. *J. Opt. Soc. Am. B*, 12(10):1143–1149, October 1995.

[50] Qing-Ming Wang and L Eric Cross. Performance analysis of piezoelectric cantilever bending actuators. *Ferroelectrics*, 215(1):187–213, 1998.

[51] Zhanxione Wei, Yongsen Yu, Hua Xing, Zhongchuang Zhuo, Yuanda Wu, Liang Zhang, Wei Zheng, and Yushu Zhang. Fabrication of chirped fiber grating with adjustable chirp and fixed central wavelength. *IEEE Photonics Technology Letters*, 13(8):821–823, 2001.

[52] Amnon Yariv and Pocji Yeh. *Photonics: optical electronics in modern communications.* Oxford Univ., 2006.